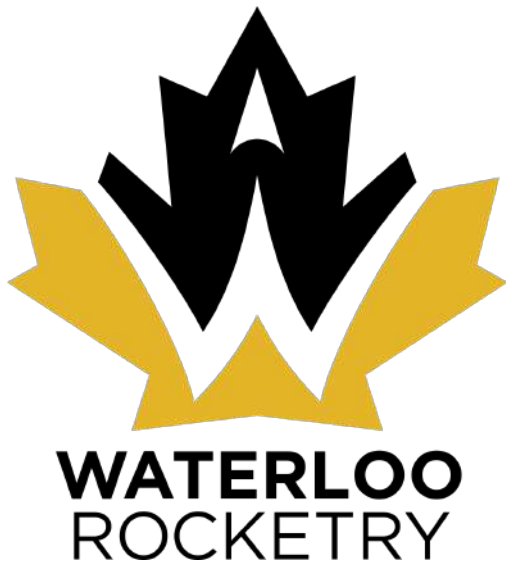


# LAUNCH CANADA 2025 CHALLENGE



Final Design Report for Aurora  
Competing Team 24 - Waterloo Rocketry

# TABLE OF CONTENTS

<b>1</b>	<b>INTRODUCTION</b>	<b>12</b>
1.1	Team History . . . . .	12
1.2	Team Organization . . . . .	13
1.3	Outreach Activities . . . . .	13
<b>2</b>	<b>MISSION REQUIREMENTS</b>	<b>14</b>
<b>3</b>	<b>MISSION CONCEPT OF OPERATIONS</b>	<b>15</b>
<b>4</b>	<b>CYCLE BASED DESIGN APPROACH</b>	<b>18</b>
4.1	Linear vs Cyclical Design . . . . .	18
4.2	Advantages of Cyclical Design . . . . .	19
4.3	Aurora Execution . . . . .	20
4.4	Impact On Aurora Project . . . . .	21
<b>5</b>	<b>SYSTEM ARCHITECTURE</b>	<b>22</b>
<b>6</b>	<b>FLIGHT DYNAMICS</b>	<b>26</b>
6.1	Aurora Design Goals . . . . .	26
6.2	Engine Thrust and Burn Time . . . . .	27
6.3	Cycle-Based System Design . . . . .	27
6.4	Simulation Approach . . . . .	27
6.4.1	OpenRocket Drag Override Plugin . . . . .	30
6.4.2	OpenRocket Thrust Override Plugin . . . . .	30
6.4.3	OpenRocket Monte Carlo Plugin . . . . .	31
6.5	RSE File Generation . . . . .	31
6.6	Loads Analysis . . . . .	31
6.7	Aerodynamic Design and Optimization . . . . .	32
6.7.1	Rocket Diameter Changes . . . . .	33
6.7.2	Nosecone Optimization . . . . .	34
6.7.3	Fin Can Considerations . . . . .	34
6.7.4	Flutter Analysis . . . . .	36
6.7.5	Coning Analysis . . . . .	42
6.7.6	Aero thermal Heating Analysis . . . . .	42
6.8	Canards Aerodynamic Design . . . . .	43
6.8.1	Canard Design Requirements and Safety Concerns . . . . .	43
6.8.2	Aerodynamic Approach and Methodology . . . . .	48
6.8.3	Estimated Roll Rate . . . . .	49
6.8.4	Calculating Lift . . . . .	49
6.8.5	Sizing Canards . . . . .	53
6.9	Painting . . . . .	56
6.10	Current Simulation Results . . . . .	58
6.11	Dispersion Zone Analysis . . . . .	58
6.12	Launch Commit Criteria . . . . .	59

<b>7 AEROSTRUCTURE</b>	<b>60</b>
7.1 Overview . . . . .	60
7.2 Moulds . . . . .	61
7.3 Nosecone . . . . .	61
7.4 Bodytubes . . . . .	62
7.5 Parachute and Avionics Bays . . . . .	62
7.6 Oxidizer Tank Aft Skirt . . . . .	64
7.6.1 3D Printed Longerons . . . . .	64
7.6.2 Fill Disconnect Hatch . . . . .	67
7.7 Fincan . . . . .	68
7.7.1 Fin Manufacturing . . . . .	69
7.7.2 Fin Bonding and Filleting . . . . .	70
7.7.3 Tip-to-Tip Layup and Post-Processing . . . . .	70
7.7.4 Boattail and Spin Can . . . . .	72
7.8 Couplers . . . . .	75
7.8.1 Geometry . . . . .	76
7.8.2 Structure . . . . .	77
7.8.3 Manufacturing and Bonding . . . . .	78
<b>8 PROPULSION</b>	<b>79</b>
8.1 Overview . . . . .	79
8.2 Combustion Chamber . . . . .	80
8.2.1 Combustion Chamber Layout . . . . .	80
8.2.2 Nozzle Exit . . . . .	80
8.2.3 Custom Ablative Development . . . . .	82
8.2.4 Ignition Puck . . . . .	84
8.3 Injectors . . . . .	85
8.3.1 Injectors . . . . .	85
8.3.2 Injector Bulkhead . . . . .	87
8.4 Feedsystem . . . . .	89
8.4.1 Tanks and Couplers . . . . .	89
8.4.2 Piston . . . . .	91
8.4.3 Fill Bulkhead . . . . .	93
8.4.4 Vent Bulkhead . . . . .	94
8.5 SRAD Valves . . . . .	95
8.5.1 Pneumatic Vent Valve . . . . .	95
8.5.2 Fill Disconnect . . . . .	96
8.5.3 Injector Valve Block . . . . .	101
8.5.4 Pyrotechnic Vent Valve . . . . .	103
8.6 Engine Data and Simulation . . . . .	109
8.6.1 Flight Static Fire Data . . . . .	110
<b>9 AVIONICS AND TELEMETRY</b>	<b>113</b>
9.1 RocketCAN . . . . .	113
9.1.1 Harness Design . . . . .	114

9.1.2	Common Hardware . . . . .	115
9.1.3	Common Software . . . . .	116
9.1.4	Message Format . . . . .	118
9.1.5	Telemetry Architecture . . . . .	119
9.1.6	Power Architecture . . . . .	120
9.1.7	Payload Secondary Bus . . . . .	121
9.2	SRAD Avionics Boards . . . . .	122
9.2.1	Rocket Power Board . . . . .	122
9.2.2	Injector Sensor Board . . . . .	123
9.2.3	GPS Board . . . . .	123
9.2.4	Live Telemetry Transmitter . . . . .	124
9.2.5	Camera/Logger Board . . . . .	124
9.3	BigRedBee GPS . . . . .	124
<b>10</b>	<b>RECOVERY SYSTEM</b>	<b>127</b>
10.1	Overview . . . . .	127
10.2	Past Failures and New Changes . . . . .	128
10.3	Structural Design . . . . .	128
10.3.1	Recovery Bulkhead and Camera . . . . .	128
10.3.2	Peak Load Calculations . . . . .	129
10.4	Parachute Design . . . . .	132
10.4.1	Drogue Parachute . . . . .	132
10.4.2	Main Parachute . . . . .	134
10.4.3	Rigging . . . . .	136
10.5	Nosecone and Drogue Deployment . . . . .	139
10.5.1	CO2 Ejectors . . . . .	139
10.5.2	Vent Hole sizing . . . . .	140
10.5.3	Drag Separation . . . . .	141
10.5.4	Pilot Extraction Force . . . . .	141
10.5.5	Testing and Flight Test . . . . .	142
10.6	Main Deployment and Two-ring Release . . . . .	142
10.6.1	Testing . . . . .	144
10.7	Recovery Electronics . . . . .	144
10.7.1	Failing Safely . . . . .	145
10.7.2	Remote Arming ConOps . . . . .	146
10.7.3	Power Management . . . . .	147
10.7.4	Altimeter Control . . . . .	148
10.7.5	Telemetry . . . . .	148
10.7.6	Remote Arming Testing . . . . .	148
10.7.7	Recovery Electronics Sled . . . . .	150
10.8	Risks and Failure . . . . .	151
<b>11</b>	<b>GROUND SUPPORT EQUIPMENT</b>	<b>153</b>
11.1	EGSE Network . . . . .	153
11.2	Remote Launch Control System . . . . .	153

11.2.1	Clientside . . . . .	154
11.2.2	Towerside . . . . .	154
11.2.3	Towerside Power Board . . . . .	155
11.2.4	RLCS Relay Board . . . . .	155
11.2.5	System Safety . . . . .	155
11.3	Data Acquisition System . . . . .	156
11.3.1	DAQ Power Board . . . . .	157
11.3.2	DAQ Patch Panel . . . . .	157
11.4	Omnibus . . . . .	158
11.5	Ground Side Power Distribution . . . . .	158
11.5.1	48 V Boost Board . . . . .	159
11.6	Tank Heating . . . . .	159
11.6.1	Tank Heating Relay Board . . . . .	160
11.7	Electrical Umbilical . . . . .	160
11.7.1	Ground-Side Charging Board . . . . .	161
11.7.2	Pyro Valve Igniter . . . . .	162
11.7.3	Payload Umbilical . . . . .	162
11.8	Launch Tower . . . . .	163
11.9	Antenna Towers . . . . .	164
11.10	Fill Plumbing . . . . .	165

## **12 CONTROLS** 166

12.1	Canard Mechanism . . . . .	166
12.1.1	System Location . . . . .	167
12.1.2	Mechanism Design Details . . . . .	167
12.1.3	Final System and updates since Testflight . . . . .	169
12.2	Flight Simulation . . . . .	170
12.2.1	Simulation Architecture . . . . .	171
12.2.2	Implementation Details . . . . .	171
12.2.3	Comparison with OpenRocket . . . . .	172
12.3	Controller and Estimator design . . . . .	173
12.3.1	Controller architecture . . . . .	173
12.3.2	Controller roll model . . . . .	174
12.3.3	Roll control law design . . . . .	175
12.3.4	Estimator architecture . . . . .	177
12.3.5	Estimator models . . . . .	178
12.3.6	EKF algorithm . . . . .	182
12.3.7	Simulation results . . . . .	183
12.4	Motor Control Board . . . . .	184
12.5	Processor Board . . . . .	185
12.5.1	Electrical . . . . .	185
12.5.2	Firmware . . . . .	186
12.5.3	Testing . . . . .	188
12.6	Results . . . . .	190
12.6.1	hardware-in-the-loop . . . . .	190

12.6.2 Testflight . . . . .	191
<b>13 PAYLOAD</b>	<b>193</b>
13.1 Payload Experiment . . . . .	193
13.2 Deployable Payload Recovery System . . . . .	193
<b>14 TESTING</b>	<b>194</b>
14.1 Engine tests . . . . .	194
14.2 Wet Dress Rehearsal . . . . .	195
14.3 Competition Simulator . . . . .	195
14.4 Testflight . . . . .	196
<b>15 PROGRAMMATIC/TECHNICAL RISKS AND MITIGATION STRATEGIES</b>	<b>197</b>
<b>REFERENCES</b>	<b>199</b>
<b>A APPENDIX - Calculations</b>	<b>203</b>
A.1 Coupler Loads Analysis . . . . .	203
<b>B APPENDIX - Electrical References</b>	<b>204</b>
B.1 Electrical Architecture . . . . .	204

# LIST OF FIGURES

Figure 3.1	Aurora CONOPS Flowchart	17
Figure 4.1	Linear design approach	18
Figure 4.2	Cyclical design approach	19
Figure 5.1	Mechanical assemblies of Aurora	22
Figure 5.2	Outer structure of Aurora	22
Figure 5.3	Complete Aurora vehicle architecture	24
Figure 5.4	Functional architecture map of Aurora	25
Figure 6.1	Aurora cycle 3 mass and length breakdown	28
Figure 6.2	$C_D$ vs. Mach comparison between OpenRocket and RASAero	31
Figure 6.3	Cycle 2.5 takeoff upper bound loads	32
Figure 6.4	Cycle 2.5 MaxQ upper bound loads	33
Figure 6.5	Common fin parameters; Aurora fin shape and size	35
Figure 6.6	Fincan test setup	39
Figure 6.7	Fin torsional testing results; displacement vs force	39
Figure 6.8	Fin torsional testing results; torsional rigidity $JG$ vs time	40
Figure 6.9	Mach cone half angle	46
Figure 6.10	Subsonic and supersonic leading edges	46
Figure 6.11	Wing tip vortices	47
Figure 6.12	Supersonic flat plate	47
Figure 6.13	Subsonic leading edge components	51
Figure 6.14	Lift coefficient vs Mach number	52
Figure 6.15	Comparison of lift coefficient models as a function of Mach number	53
Figure 6.16	Modifiable sizing parameters	54
Figure 6.17	Predicted lift and angular acceleration	55
Figure 6.18	Time-to-roll-rate minimum and average values	55
Figure 6.19	Proposed canard designs	56
Figure 6.20	Selected paint design for Aurora	57
Figure 6.21	Preliminary Monte Carlo dispersion analysis	59
Figure 7.1	Composites in curing oven	61
Figure 7.2	Completed nosecone and bodytube moulds	61
Figure 7.3	SRAD composite parts	63
Figure 7.4	Avionics and parachute bays	63
Figure 7.5	LOTS fill bulkhead	64
Figure 7.6	Fill bulkhead longeron lattice	65
Figure 7.7	Aurora injector section assembly	65
Figure 7.8	Printed longeron stress simulations	67
Figure 7.9	Printed longerons on the build plate after de-powdering.	67
Figure 7.10	Quick disconnect hatch	68
Figure 7.11	Fin plate infusion	69
Figure 7.12	Fins	69
Figure 7.13	Bonding jigs	70
Figure 7.14	Sanded fillets	71
Figure 7.15	Tip-to-tip layup	72

Figure 7.16 Vacuum bagged tip-to-tip . . . . .	73
Figure 7.17 Spin can initial design . . . . .	73
Figure 7.18 Candidate bearing race profiles . . . . .	74
Figure 7.19 Iteration 2 assembly cross-section . . . . .	74
Figure 7.20 Iteration 2 boattail . . . . .	75
Figure 7.21 Spin can final cross-section . . . . .	75
Figure 7.22 Recovery Aft/Avionics Forward Interface . . . . .	76
Figure 8.1 Aurora P&ID . . . . .	79
Figure 8.2 Combustion chamber cross-section . . . . .	81
Figure 8.3 Split retaining ring . . . . .	81
Figure 8.4 Regression of ELSF4 ablative . . . . .	82
Figure 8.5 Phenolic fibreglass layup after room temperature cure . . . . .	83
Figure 8.6 Post-ELSF5 phenolics and nozzle exit . . . . .	83
Figure 8.7 Aluminum CC casing after 9s burn . . . . .	84
Figure 8.8 Initial brazed injector concept . . . . .	85
Figure 8.9 CT scan results for small diameter fluid channels . . . . .	86
Figure 8.10 CFD flow visualization of printed injector . . . . .	87
Figure 8.11 CFD simulation of pressure drop throughout injector fuel channels . . . . .	88
Figure 8.12 Printed injectors . . . . .	88
Figure 8.13 Eridium injector testing . . . . .	89
Figure 8.14 Injector bulkhead cross-section . . . . .	89
Figure 8.15 Spincan running surface on injector bulkhead . . . . .	90
Figure 8.16 Undercut on countersunk tank bolt . . . . .	91
Figure 8.17 Hoop failure of burst test tank . . . . .	92
Figure 8.18 Piston with wear rings . . . . .	92
Figure 8.19 Cross-section of propellant feedlines in fill bulkhead . . . . .	93
Figure 8.20 Cross-section of angled holes on fill bulkhead . . . . .	93
Figure 8.21 Displacement of fill bulkhead at MEOP . . . . .	94
Figure 8.22 Stress concentration on fill bulkhead . . . . .	94
Figure 8.23 Vent section assembly . . . . .	94
Figure 8.24 FEA results of vent bulkhead. . . . .	95
Figure 8.25 Centering plate on vent bulkhead. . . . .	95
Figure 8.26 Pneumatic vent valve cross-section . . . . .	96
Figure 8.27 Cross-section of QD valve in open position . . . . .	97
Figure 8.28 Old and new latch and valve body design . . . . .	98
Figure 8.29 Ground-side mechanism and pneumatic actuator . . . . .	99
Figure 8.30 Cross section of pneumatic actuator . . . . .	99
Figure 8.31 QD arm assembly CAD . . . . .	100
Figure 8.32 Cross-section of the linear section of the QD arm . . . . .	100
Figure 8.33 The ratcheting mechanism of the QD arm . . . . .	101
Figure 8.34 Space optimization in injector section . . . . .	102
Figure 8.35 Cross-section of cross-drilled QD face seal flange . . . . .	102
Figure 8.36 Valve body stress concentration . . . . .	104
Figure 8.37 Developed stress in valve block washers . . . . .	104
Figure 8.38 Developed stress in valve body bolts . . . . .	105

Figure 8.39	Developed stress in valve body nuts . . . . .	105
Figure 8.40	QD flange stress concentration . . . . .	106
Figure 8.41	Developed stress in QD flange washers . . . . .	106
Figure 8.42	Developed stress in QD flange bolts . . . . .	107
Figure 8.43	Pyro valve cross-section . . . . .	108
Figure 8.44	Flight-like thrust curve . . . . .	111
Figure 8.45	Flight-like pressure data . . . . .	111
Figure 8.46	Flight-like mass flowrate data . . . . .	112
Figure 8.47	Flight-like O/F ratio data . . . . .	112
Figure 9.1	Aurora avionics architecture diagram . . . . .	113
Figure 9.2	Male and female Gecko cable assemblies . . . . .	114
Figure 9.3	Female and male Datamate connectors . . . . .	115
Figure 9.4	Tefzel jacketed cable . . . . .	115
Figure 9.5	Standard PIC18 connections . . . . .	116
Figure 9.6	PIC18 oscillator layout . . . . .	117
Figure 9.7	Schematic of CAN transceiver and programming header . . . . .	117
Figure 9.8	RocketCAN bus connection and current sensing . . . . .	118
Figure 9.9	CAN 2.0B Extended ID message format . . . . .	118
Figure 9.10	SRAD dipole antenna . . . . .	120
Figure 9.11	2025 standard battery charge circuit . . . . .	121
Figure 9.12	Rocket Power Board e-fuse circuit . . . . .	123
Figure 9.13	Injector Sensor Board 2-wire and 3-wire sensor connections . . . . .	124
Figure 9.14	Nosecone BRB mounting . . . . .	125
Figure 9.15	Main rocket BRB mounting . . . . .	126
Figure 10.1	Rigging diagram . . . . .	127
Figure 10.2	Recovery bulkhead detailed view . . . . .	129
Figure 10.3	FEA results of recovery bulkhead . . . . .	130
Figure 10.4	Recovery harnessing protector . . . . .	131
Figure 10.5	Recovery camera assembly . . . . .	131
Figure 10.6	Opening force reduction factor vs ballistic parameter . . . . .	132
Figure 10.7	Completed drogue parachute . . . . .	133
Figure 10.8	Drogue parachute during truck test . . . . .	134
Figure 10.9	Drogue parachute bag lengths . . . . .	135
Figure 10.10	Packed drogue parachute inside drogue parachute bag . . . . .	136
Figure 10.11	Rigging stitching pattern tensile test samples . . . . .	137
Figure 10.12	Rigging stitching pattern tensile test samples . . . . .	137
Figure 10.13	Final stitch pattern . . . . .	138
Figure 10.14	Energy modulator stitching pattern prototype . . . . .	138
Figure 10.15	Energy modulator tensile test . . . . .	139
Figure 10.16	Cross-section of the SRAD CO <sub>2</sub> ejectors . . . . .	140
Figure 10.17	2-ring release mechanism . . . . .	143
Figure 10.18	SRAD pyrocutter . . . . .	143
Figure 10.19	Line cutters and 2-ring release testing . . . . .	144
Figure 10.20	Remote Arming block diagram . . . . .	145
Figure 10.21	Complete Remote Arming system . . . . .	145

Figure 10.22 Remote Arming power circuit for one of two batteries . . . . .	147
Figure 10.23 Recovery battery current sensing circuit . . . . .	147
Figure 10.24 Stratologger telemetry level shifting circuit . . . . .	149
Figure 10.25 Recovery electronics sled . . . . .	150
Figure 10.26 Antenna mounting exploded view . . . . .	151
Figure 11.1 Proposed site layout . . . . .	153
Figure 11.2 RLCS Clientside . . . . .	154
Figure 11.3 RLCS Towerside . . . . .	155
Figure 11.4 Patch Panel star-shaped voltage headers . . . . .	157
Figure 11.5 Omnibus dashboard . . . . .	158
Figure 11.6 Tank heater flex PCB . . . . .	159
Figure 11.7 Rocket electrical disconnect . . . . .	160
Figure 11.8 GSCB boost converter . . . . .	161
Figure 11.9 GSCB charge controller . . . . .	162
Figure 11.10 Payload disconnect internal pass-through . . . . .	163
Figure 11.11 Launch tower base stress analysis . . . . .	164
Figure 11.12 Assembled nitrous oxide fill panel . . . . .	165
Figure 12.1 Controls architecture diagram . . . . .	166
Figure 12.2 Canard mechanism top view . . . . .	167
Figure 12.3 Canard shaft sub-assembly section view . . . . .	168
Figure 12.4 Canard aerodynamic surface mounting and profile . . . . .	168
Figure 12.5 Shim adjustment force path . . . . .	169
Figure 12.6 Servo shaft sub-assembly section view . . . . .	169
Figure 12.7 Assembled canards . . . . .	170
Figure 12.8 Simulation architecture diagram . . . . .	172
Figure 12.9 Controls simulation compared to OpenRocket . . . . .	173
Figure 12.10 Control loop block diagram . . . . .	174
Figure 12.11 Controller gain scheduling surfaces . . . . .	175
Figure 12.12 Open loop Bode plot for different dynamic pressures . . . . .	177
Figure 12.13 Closed-loop controller responses . . . . .	178
Figure 12.14 Controlled roll angle . . . . .	183
Figure 12.15 Simulated vs. estimated states . . . . .	184
Figure 12.16 Simulation estimation error . . . . .	185
Figure 12.17 Monte-Carlo controlled roll angle, 200 simulations . . . . .	186
Figure 12.18 Monte-Carlo estimated vs simulated state, 200 simulations . . . . .	187
Figure 12.19 Monte-Carlo estimation state error, 200 simulations . . . . .	188
Figure 12.20 Assembled processor board . . . . .	189
Figure 12.21 Flight phase states and transitions . . . . .	189
Figure 12.22 Flowchart of the hardware-in-the-loop process. . . . .	191
Figure 12.23 Testflight telemetry, estimated state . . . . .	192
Figure B.1 Aurora electrical architecture diagram . . . . .	204

# LIST OF TABLES

Table 2.1	Primary vehicle requirements . . . . .	14
Table 4.1	Aurora design cycles . . . . .	20
Table 6.1	Expected vs upper-bound flight profile comparison for loads analysis . . . . .	32
Table 6.2	6-inch vs 8-inch simulation results . . . . .	33
Table 6.3	Final fin parameters . . . . .	36
Table 6.4	Canard design requirements and considerations . . . . .	44
Table 6.5	Cycle 2.5 Nominal launch OpenRocket simulation results . . . . .	58
Table 7.1	Overview of composite aerostructure components . . . . .	60
Table 7.2	Coupler geometries and safety factors . . . . .	77
Table 8.1	Key engine parameters . . . . .	80
Table 8.2	Tank Structural Safety Factors . . . . .	91
Table 9.1	RocketCAN colour code . . . . .	114
Table 9.2	RocketCAN message ID format . . . . .	119
Table 9.3	Summary of SRAD avionics . . . . .	122
Table 10.1	Extraction force values . . . . .	142
Table 12.1	FreeRTOS tasks and descriptions . . . . .	190
Table 15.1	Likelihood and severity categories . . . . .	197
Table 15.2	Team-wide programmatic risks . . . . .	197
Table A.1	Sample Calculation for Avionics Forward Coupler . . . . .	203

# 1 INTRODUCTION

Waterloo Rocketry is a student team representing the University of Waterloo, from Waterloo, Ontario, Canada. The team is competing in the 2025 Launch Canada Challenge with a high-altitude liquid bipropellant rocket. The primary mission goal is a nominal ascent, followed by a successful recovery. The secondary mission goal is to deploy a payload equipped with a hyperspectral camera to investigate greenhouse gas concentrations at varying altitudes in the atmosphere. This year's rocket also features canards designed for roll control, marking a key advancement in the team's active-control capabilities.

The primary objective of the team is to provide students with hands-on learning opportunities by tackling practical engineering challenges. Team growth and continuity hinge on the team's ability to maintain an atmosphere of learning and collaboration while remaining competitive and striving for year-to-year improvements. Many past and present members have dedicated significant time and effort to the team, and continued success is a recognition of this commitment. Additionally, the team owes much to the support and resources offered by the University of Waterloo, which enriches the team's experience. The team's advisors, both from the University and industry, share valuable insights as the team develops more complex and sophisticated systems.

## 1.1 Team History

Waterloo Rocketry was founded in 2009 and has competed in events like the Intercollegiate Rocket Engineering Competition (IREC) and Launch Canada since 2011. The team has historically focused on SRAD hybrid rockets, but in 2024 made a significant transition to liquid bipropellant systems, achieving Canada's first student liquid rocket launch with Borealis. Below is a summary of the team's recent competition achievements:

- 2017: Successful launch of Vidar III hybrid rocket; winner of the 10,000ft SRAD hybrid/liquid category; awarded the Jim Furfaro award for technical excellence.
- 2018: Successful launch of Unexploded Ordnance hybrid rocket; winner of the 10,000ft SRAD hybrid/liquid category.
- 2019: Successful launch of Shark of the Sky hybrid rocket; 2nd place in the 30,000ft SRAD hybrid/liquid category.
- 2021: Kraken of the Sky hybrid rocket; 30,000ft SRAD hybrid/liquid category; awarded the Gil Moore award for innovative design.
- 2023: Successful launch of Leviathan of the Sky hybrid rocket; 2nd place in the 30,000ft SRAD hybrid/liquid category.
- 2023: Successful launch of Mini KotS solid rocket; 3rd place in the basic category of Launch Canada.
- 2024: Successful launch of Borealis liquid rocket; winner in the advanced category of Launch Canada.

For more information on the team's past rockets, please visit the team's website:  
[waterloorocketry.com](http://waterloorocketry.com).

## 1.2 Team Organization

Waterloo Rocketry currently consists of approximately 100 members from a wide range of faculties, including Engineering, Math, Arts, and Science. The active members are primarily undergraduate students, though the team regularly consults with graduate students and alumni.

The team's faculty advisor, Dr. Andrew Milne, an engineering professor specializing in thermofluids, provides insight as the team develops more complex systems and assists with high-level administrative decisions. The team is co-led by Jeremy Schnellhardt and Luca Scavone, who are responsible for overall project management and team direction, overseeing all technical, administrative, and operational activities necessary to achieve team objectives. The team leads also function as the Chief Engineers. Chief Safety Officers Rhea Scollie, Ben Pickens, and Ash Lang work closely with team members on practices and procedures to ensure safety remains a top priority. While safety is directly overseen by the Chief Safety Officers, every team member is responsible for maintaining safe practices.

Organizationally, the team is structured into both technical and administrative systems. These are led by system leads, who coordinate timelines and communication for each project undertaken. Each technical project is overseen by a project lead, who is responsible for managing all aspects of the project including, but not limited to, design, manufacturing, testing, and integration. Team members are encouraged to work on any project, or projects, that interest them, and there is often collaboration and significant overlap between project teams and systems.

## 1.3 Outreach Activities

Waterloo Rocketry actively participates in University and community outreach each year. These activities serve to recruit new members and promote awareness of student rocketry and Canadian aerospace. Annual outreach activities include:

- Open House: The University of Waterloo hosts two annual open houses for prospective students, where the team showcases its rocket and the benefits of joining student teams.
- Giving Tuesday: The team participates in the University's Giving Tuesday, a university-wide fundraising event, raising funds to support the Student Design Centre.
- Model Rocket Event: Since 2014, the team has hosted an annual model rocket event in the fall. Participants design, assemble, and launch their own model rockets, introducing new recruits to the design process.
- Aviation Fun Day: Since 2018, the team has engaged in the Region of Waterloo's Aviation Fun Day, allowing the team to interact with the community and support local food banks.
- High School Outreach: Team members conduct outreach at local high schools to promote rocketry and STEM education.

## 2 MISSION REQUIREMENTS

The primary mission goal of Aurora is to have a nominal flight with a successful recovery in a reflyable state. The flight also has two secondary goals. The first is to carry a payload containing a hyperspectral imagery experiment to understand the emission spectra of atmospheric gases. The second is to validate a new active roll-control system, with the success criteria being that they effectively eliminate roll induced by the vehicle and to demonstrate an ability to control the vehicle's roll via a short roll program. This rocket embodies the spirit of SRAD, with a design goal of having as many components as possible be student designed and fabricated. It is with these success criteria in mind that the primary rocket requirements can be found in Table 2.1.

There are many requirements for the establishment of a successful vehicle. Below are only the requirements that are unusual or differ from previous vehicles. Requirements that are obvious (such as the vehicle must ascend under its own thrust) have been omitted.

Requirement	Notes
The rocket and GSE shall never create significant increased risk for any personnel	This includes off-nominal cases
The rocket shall comply with the Launch Canada DTEG	The vehicle can violate the DTEG with permission from the LC judges
The rocket should be retrieved in a re-flyable state	
All load bearing components shall be able to withstand the expected loads throughout all phases of flight and descent to a minimum FOS of 2	
The rocket should be able to be fully assembled the night before flight	Many launch attempts from 2024 were made more complicated by some required day-of assembly. Aurora will be designed to remove that need
The rocket should be able to operate at all expected temperatures	For the majority of the vehicle, this is -20C to 30C. For components in contact with nitrous oxide, this range extends down to -40C
All charged components shall be replaceable within 1 hour	
The rocket shall be able to hold in the raised state for a minimum of 6h and in the aborted state for 6h	These two criteria are not required to be satisfied one after the other (i.e. raised for 6h, aborted for 6h in one 12h stretch is not required)

Table 2.1: Primary vehicle requirements

As always, all requirements can be questioned and changed if required.

## 3 MISSION CONCEPT OF OPERATIONS

The mission concept of operations (CONOPS) for Aurora is made up of 11 distinct phases, beginning with preparing for transportation and ending with post-flight. The primary mission objective is a nominal flight. The apogee target for Aurora is 50 000 ft, which will give the team the appropriate technical challenges while remaining inside the boundaries of the Launch Canada waiver. The concept of operations will define the various assembly phases of the vehicle as well as its recycle path if required. A schematic summarizing the phases of the CONOPS for Aurora is included below in Figure 3.1.

### 1. Transportation

This is the state the vehicle is in from when it is packed into the trailer to when the team arrives at the conference centre. All electronics are powered off with batteries removed, propellant tanks are empty, and the rocket is in several pieces.

### 2. Display at Poster Day

This is the state the vehicle is in from when it is being displayed at poster day. The rocket is in several pieces for display at the conference centre. Components which contain energetics, such as the combustion chamber, are assembled and stored outside the conference centre. This is also the state the vehicle is in for judging. Some avionics may be powered on, but all power sources will be replaced before flight.

### 3. Flight Assembly

This is the state the vehicle is in when it is being assembled for the final time before flight, at the launch site. It is in several pieces being assembled, with remaining energetics being loaded and batteries being installed. The payload is mounted into the nosecone, the canards are powered on, and the vehicle is made ready to rail.

### 4. Rocket is Railed

This is the state of the vehicle when the rocket is on the launch rail, before it has been raised. At this time, all avionics are powered on, final checkouts are being performed, and fuel is being filled.

### 5. Rocket is Raised

This is the state of the vehicle when the rocket is raised on the launch rail. At this time, all systems are ready to fly. Final umbilicals to the vehicle are being attached and preparations for operations have begun. This phase ends when clearance for opening of the first nitrous oxide cylinder is given from the Launch Control Officer.

## 6. Fill and Press

The vehicle is now being filled with nitrous oxide and holding on the pad. Once the vehicle is full, final preparations to launch are made (such as turning on the cameras and activating the payload). This phase ends when clearance to fly is given from the Launch Control Officer.

## 7. Ignition

The vehicle's ignition puck is burning. At this point, all active umbilicals are removed from the vehicle, and all systems are ready for flight. This phase ends when the fill disconnect system separates from the rocket.

## 8. Ascent

This phase is broken into three sections. 8.a Takeoff, where the rocket is ascending on the launch rail. Once the first launch button clears the launch rail, phase 8.b Boost begins, where the vehicle is ascending unsupported under its own thrust. Finally, on engine burnout, phase 8.c Coast begins. This phase lasts from when the vehicle is ascending due to inertia all the way until apogee is reached.

## 9. Descent and Landing

This phase is also broken up into three sections. 9.a Drogue Descent begins when the vehicle reaches apogee and the nosecone separates from the rocket. The rocket's drogue parachute is deployed at the same time and the rocket descends under the drogue parachute until a predetermined apogee, after which it releases its main parachute. 9.b Main Descent begins when the main parachute is released approximately 1 500 ft AGL until contact with the ground. 9.c Awaiting Recovery begins when the rocket contacts the ground until the avionics are disarmed. For the entirety of this phase, the vehicle is transmitting telemetry including GPS position, which will be used to recover the vehicle.

### 9.5 Payload Descent and Landing

This phase is broken into three sections. 9.5.a Flat Spin Descent begins when the vehicle reaches apogee and the nosecone separates from the rocket. The nosecone and payload assembly will experience free fall from approximately 50 000 ft to 5 000 ft during which it will reach approximately 150 ft/s and experience a flat spin. 9.5.b Main Descent begins when the payload main parachute is deployed approximately 5 000 ft AGL and continues until contact with the ground. 9.5.c Awaiting Recovery begins when the payload contacts the ground and continues until the avionics are disarmed. For the entirety of this phase, the vehicle is transmitting GPS position, which will be used to recover the vehicle.

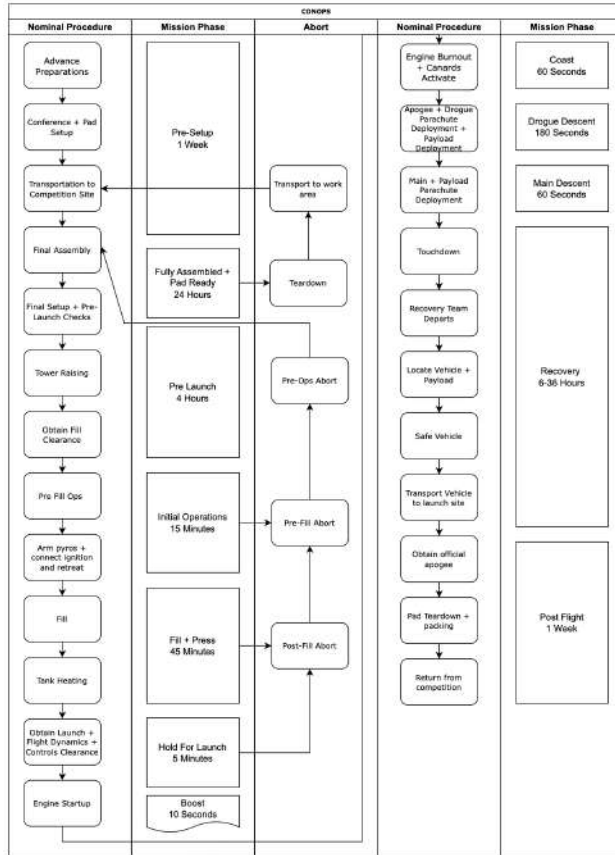


Figure 3.1: Aurora CONOPS Flowchart

## 10. Rocket Retrieval

Rocket Retrieval begins when the avionics are disarmed and ends when the vehicle is returned to its original transportation location. At this time the avionics are powered off, the rocket is largely disassembled, and the vehicle systems are safed. The vehicle is then transported back through the forest to where it will be disassembled and inspected.

## 11. Post-Flight

The vehicle is then disassembled, all relevant logs are pulled, and any relevant failure analysis can begin. This phase also involves the storage of the vehicle for future analysis or testing if required.

## 4 CYCLE BASED DESIGN APPROACH

### 4.1 Linear vs Cyclical Design

As discussed in a retrospective report on 2023's hybrid rocket, the team developed a cycle-based design approach [1]. This replaced the linear approach the team had previously used. This typical linear design approach is shown in Figure 4.1.

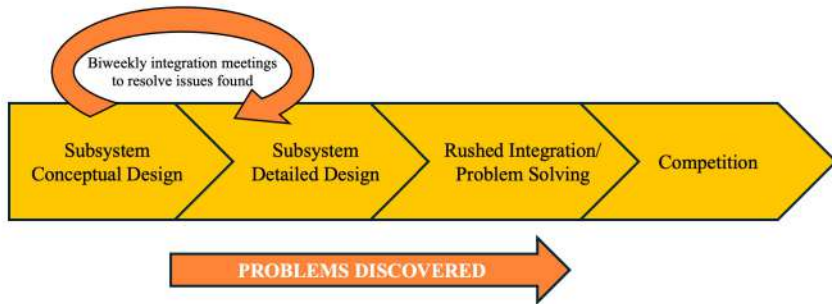


Figure 4.1: Linear design approach

In this linear approach:

"individually, each subsystem would create a conceptual design of what they were considering. Next each subsystem would create a detailed design and work out interfaces with other subsystems through bi-weekly integration meetings. These meetings were intended mainly to fight major issues being discovered throughout the design process. As issues were found and competition grew closer, the team entered into rushed integration and problem solving. Bringing many components designed in relative isolation together resulted in major issues being found very close to competition. An infamous team example happened when assembling the payload into the rocket a few weeks prior to competition. It was found that the payload did not fit through the opening in the rocket. While this issue was resolved, it raises serious concerns about this approach and how robust it is for integration purposes" [1].

To replace the linear design approach, a cyclical approach was created shown in Figure 4.2. The nominal use of this system is that:

"design work is completed as before, individually by each designer. Then periodically, this design data (mainly mass and position data) is collected into a large spreadsheet. Based on this data, OpenRocket simulations are completed. This provides the key flight characteristics of the current rocket as it exists in each designer's mind. Based on the outputs of the OpenRocket simulation, loads analysis is completed. This enables each designer to know what the limiting load scenario is for their parts. After each of these steps is complete, the relevant data is collected and presented in a 10- to 20-page mini report. This cycle was repeated throughout the design

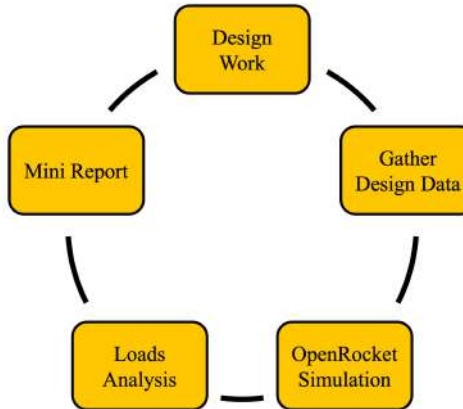


Figure 4.2: Cyclical design approach

process at key project milestones to ensure the information remained recent enough to be representative. This also has a side benefit of driving design progress and keeping each subsystem aligned in terms of design progress" [1].

## 4.2 Advantages of Cyclical Design

Some of the key advantages of the cyclical design approach, in no particular order, are:

- Early architecture decisions such as engine performance targets, rocket diameter, or section locations can be decided earlier with data driven confidence that the decided path is the most efficient.
- The deadlines for submitting design data act as checkpoints in the development of the rocket, improving timeline adherence.
- Architecture and timeline problems/inefficiencies can be spotted and proactively corrected before components are fully designed to improve performance based on simulation data.
- Provides design history documentation recorded in a trustworthy and accessible location.
- Enables the entire team to be on the same page about design priorities and overall system design. Everyone pulling in the same direction.
- Through the team regularly completing cycles, the data collection and simulation processes are optimized and familiar. This means that if schedules slip, the team is capable of incredibly quick data collection and simulation with high quality control. The team follows the philosophy that nothing being done at competition should be done for the first time, and mass collection and simulation is no different.
- Reduction of team stress levels due to deep understanding of the current and desired states of the rocket.

There are also many other benefits of this design approach that are less tangible.

### 4.3 Aurora Execution

In practice, the items in each cycle are not always completed in order or for every cycle. As an example, for some cycles in Aurora's development, a competition report was being written at the end of the cycle. In this case, a mini-report was not needed. For cycles without a competition report, a Slack message was deemed sufficient to communicate the learning's without the engineering resources required for a formal report.

As discussed in the retrospective report, a key consideration of the project was how many cycles to complete, and when [1]. The rationale was that a cycle should be completed when:

- New data is available that significantly changes the flight profile (i.e. completing a static fire test).
- A major architecture design needs to be made and data is required to make that decision (i.e. fin sizing or thrust requirement definition).
- A major competition deliverable is required and updated numbers are desired (i.e. competition final design report).

The cycles completed for Aurora are listed in Table 4.1.

Cycle	Date	Purpose
Cycle 0	September 2024	Early architecture decisions, set project goals and engine requirements, define scope.
Cycle 1	N/A	Due to fall 2024 static fire failure and lack of sufficiently designed parts, Cycle 1 was never conducted.
Cycle 2	April 2025	Finalize fin design using somewhat detailed subsystem designs, RSE based on first engine static fire.
Cycle 2.5	May 2025	Addition of several weighed components following a successful test flight launch, goal to validate fin design.
Cycle 3	July 2025	Integration of detailed subsystem designs, most components weighed.
Cycle 4	August 2025	Assembly-based mass measurements to include smaller components, new RSE based on static fire data.
Cycle 5	August 2025	Assembly-based mass measurements including paint mass that may have been missed in previous cycles.
Cycle 6	August 2025	Final simulations at competition to verify weather launch commit criteria or adjust to any problems discovered at competition.

Table 4.1: Aurora design cycles

At the time of writing, mass collection for Cycle 3 has been completed, with a full breakdown of the mass and length of the vehicle found in subsection 6.3. A detailed explanation of loads analysis is provided in Section 6.6.

## 4.4 Impact On Aurora Project

Unlike LOTS and Borealis which followed more organized cycles and timelines, many aspects of this cycle-based design approach were adapted throughout the year. Some key changes were:

- Cycle 1 typically based on early CAD models and designs, was never conducted on Aurora due to an unsuccessful static fire in late November 2025. Furthermore, the team had very few designed components to reference. Conducting this mass-collection cycle would have likely resulted in similar results to Cycle 0.
- Cycle 2 typically conducted in March to size the fins, was delayed significantly to the end of April. Following a lengthy and unsuccessful cold flow campaign during March 2025, the team's 3D-printed injectors had yet to be fully characterized. As such, there was little confidence in the accuracy of the team's simulations and the team made the decision to delay fin sizing to May 2025, allowing the fins to be sized using data from a successful static fire in early May.
- An intermediate Cycle 2.5 was conducted in late May 2025 following the successful launch of a test flight rocket built to validate several novel systems flying on Aurora (including a single-separation dual-deploy recovery system, a deployable payload, and roll-control canards). The launch of this vehicle significantly benefited mass collection by forcing many systems to manufacture and weigh flight hardware significantly earlier in the design cycle.

The introduction of this design approach is a significant part of why the team has been able to consistently produce innovative and capable rockets for three years in a row and it is expected to serve the team well in the future. Additionally, it more closely approximates a true industry development approach helping students to learn in a realistic engineering environment. The team recommends this type of design approach to all student teams, even those not focused on rocketry. An easily digestible presentation on this approach and its use in LOTS was done at the TMU Rocketry Conference which is an easy way to share the method [2].

## 5 SYSTEM ARCHITECTURE

Aurora is decomposed into a physical architecture, which is a representation of the mechanical assembly of the system. This architecture is used as the structure for the CAD assembly of the vehicle, for mass data management, and to plan assembly order and procedures. The physical architecture breaks the vehicle into 5 major physical sections: the nosecone, the recovery bay, the avionics bay, the feed system (including the propellant tanks and injector section), and the combustion chamber and fin body. A simplified overview of the physical architecture can be seen in Figure 5.1. A more detailed view of the physical shape of the vehicle is shown in Figure 5.2. For clarity, the canards assembly for active roll control has been identified in purple, but falls under the feedsystem subassembly.

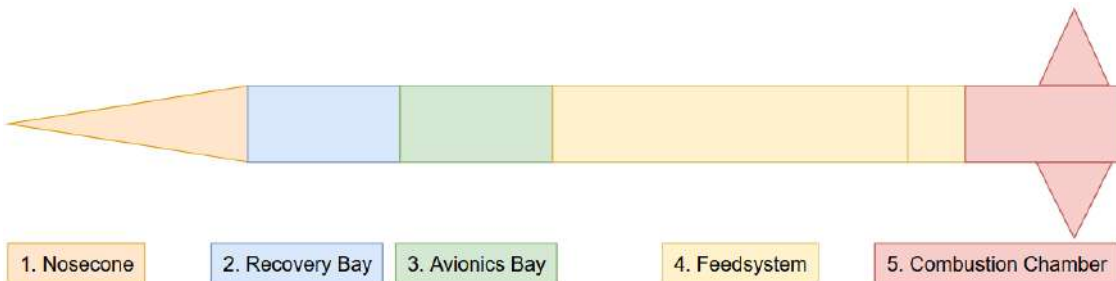


Figure 5.1: Mechanical assemblies of Aurora



Figure 5.2: Outer structure of Aurora

### 1. Nosecone

The nosecone is the region of the vehicle that contains the payload, which separates at apogee and descends independently. It mates to the recovery bay using a bonded aluminum lap joint with shear pins that separate at apogee. The nosecone measures approximately 40 in long.

### 2. Recovery Bay

The recovery bay contains the majority of the recovery system. It is short 8 in diameter tube that mates to the nosecone on the forward end and to the recovery bulkhead on the aft end. A smaller 5.5 in fibreglass tube is bonded to the aft end of the recovery bulkhead and contains the main parachute. The recovery bulkhead hermetically seals the entire section such that it can be pressurized using CO<sub>2</sub> canisters, for ejection. The outer tube measures 9.5 in in length and the inner tube measures 9 in in length.

### **3. Avionics Bay**

The avionics bay is another 8 in diameter straight tube that mates to the recovery bulkhead on the forward end and the top of the propellant tanks on the aft end. The majority of electronics on the vehicle are located in this section, with the recovery wiring running upward to the recovery bulkhead passthrough, and the avionics harness running down to the canards and injector section. This tube physically covers the avionics sled, canards assembly, and vent section. This section measures 24.375 in in length.

### **4. Feedsystem**

The feedsystem contains (from forward to aft) the vent bulkhead, the concentric oxidizer and fuel tanks, the fill bulkhead, as well as the main propellant valves, the fill and vent valves, engine instrumentation, the longerons, and other engine-critical hardware. This section is fully assembled internally and to the combustion chamber before being mounted to the rest of the vehicle. The tanks measure 101.375 in in length and the OTAS portion of the feedsystem measures 5.1 in.

### **5. Combustion Chamber/Spincan Section**

Finally, the combustion chamber section contains the combustion chamber, the spincan (fincan mounted on ball bearings), and the boattail. It serves to contain the combustion chamber and direct the thrust produced by the engine. This is also the part of the vehicle which rests on the base of the launch rail and is the first part of the vehicle to contact the ground on descent. The spincan section measures 19.25 in.

It is critical that the rocket system integrates properly with its ground support equipment (GSE) at the launch site. The team's GSE performed well at IREC in 2023, and a similar layout is intended for Launch Canada 2025. The GSE consists broadly of the launch tower, rocket fill disconnect arm, electrical umbilical, plumbing GSE panel, the Remote Launch Control System, the Data Acquisition System, Ground Side Power Distribution, the antenna towers, and the nitrous oxide tank inverters.

A full breakdown of Aurora's assemblies and sub-assemblies is shown below in Figure 5.3. A complete view of the mechanical, electrical and ground-side interfaces of the rocket is shown in Figure 5.4.

1. Nosecone Assembly
  - 1.1. Payload Assembly
    - 1.1.1. Payload Experiment
    - 1.1.2. Experiment Sled
    - 1.1.3. Payload Rigging
  - 1.2. Payload BRB
    - 1.2.1. BRB Board & Antenna
    - 1.2.2. Nosecone BRB 3D Print
2. Parachute Bay Assembly
  - 2.1. Recovery Bulkhead Assembly
    - 2.1.1. Recovery Bulkhead
    - 2.1.2. CO2 Ejectors
    - 2.1.3. Pyrocutters
    - 2.1.4. Main Parachute Tube
  - 2.2. Recovery Rigging
    - 2.2.1. Drogue Parachute
    - 2.2.2. Shock Cord
    - 2.2.3. Two Ring Release
    - 2.2.4. Main Parachute
3. Avionics Bay Assembly
  - 3.1. Vent Section
    - 3.1.1. Vent Valve
  - 3.2. Canards
    - 3.2.1. Canards Mechanical Assembly
    - 3.2.2. Canards Harness
  - 3.3. Recovery Electronics Sled
    - 3.3.1. Avionics Bay Raceway
  - 3.4. Rocketside BRB
    - 3.4.1. BRB Board & Antenna
    - 3.4.2. Rocketside BRB 3D Print
4. Tanks & Feedsystem
  - 4.1. Oxidizer & Fuel tank
    - 4.1.1. Oxidizer Tank
    - 4.1.2. Fuel Tank
    - 4.1.3. Vent Bulkhead
    - 4.1.4. Fill Bulkhead
  - 4.2. Injector Block
    - 4.2.1. Integrated Valve Block
    - 4.2.2. Pyro Valve
  - 4.3. Oxidizer Tank Aft Skirt
    - 4.3.1. Longerons
    - 4.3.2. OTAS Pannels
    - 4.3.3. Injector Section Data Hub
    - 4.3.4. Feedsystem Harness (Raceway)
5. Spincan Assembly
  - 5.1. Combustion Chamber Assembly
    - 5.1.1. Injector Bulkhead
    - 5.1.2. Injector Element
    - 5.1.3. Combustion Chamber Internals
    - 5.1.4. Combustion Chamber Casing
  - 5.2. Spincan
    - 5.2.1. Spincan Forward Interface
    - 5.2.2. Spincan Aft Interface
    - 5.2.3. Boattail

Figure 5.3: Complete Aurora vehicle architecture

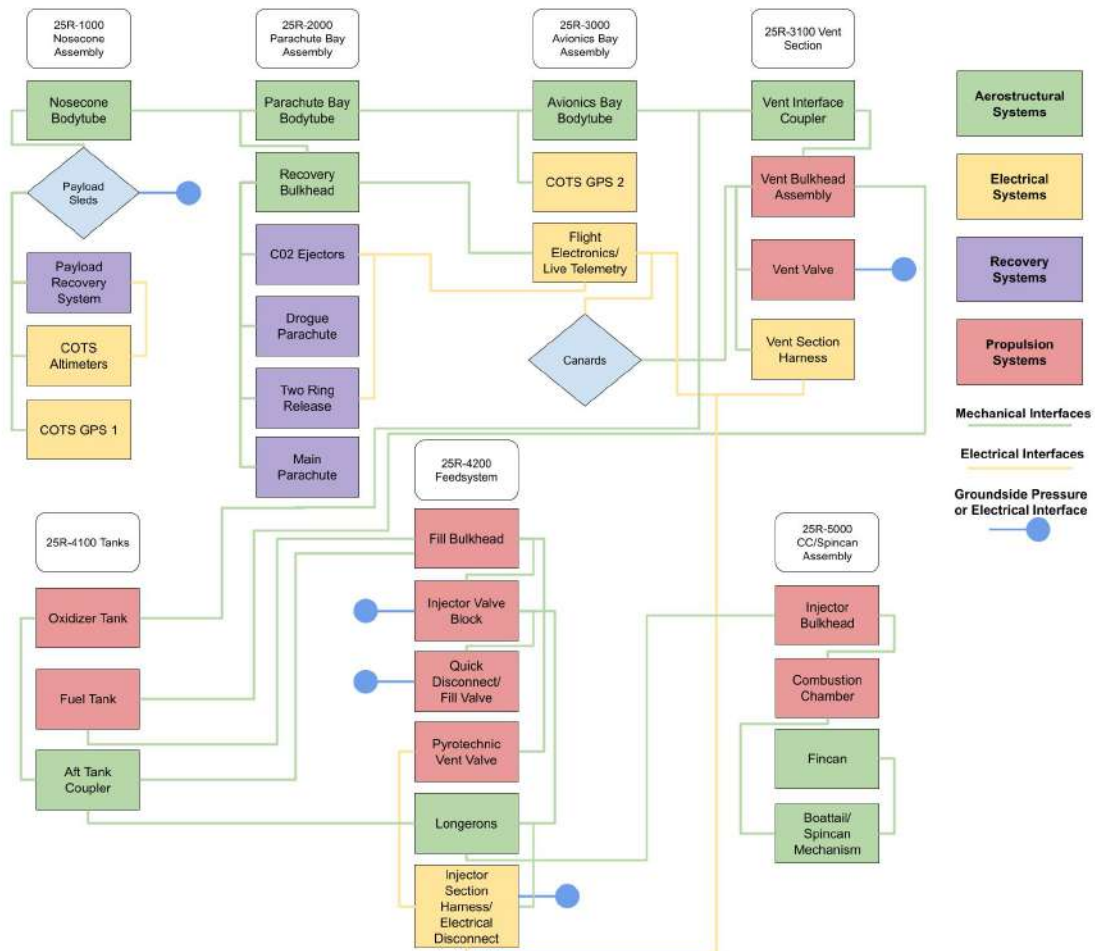


Figure 5.4: Functional architecture map of Aurora

## 6 FLIGHT DYNAMICS

The flight dynamics subsystem was created in response to increasing complexity and the need for a dedicated branch to oversee simulations and aerodynamic design. Most notably, the subsystem introduced a cycle-based design system for Leviathan of the Sky (LOTS) in 2023, which led to a 23% increase in apogee by improving engine efficiency, system integration, dry mass optimization, and much more. The team saw similar success in 2024 through the use of this system.

The subsystem's recurring responsibilities include mass, length, and CG tracking throughout the design process to inform general rocket architecture, fin design, and apogee prediction. As the team aims to go higher and faster, the subsystem's focus has expanded to include rocket optimization for high altitudes and aerodynamic support for current and future active control projects.

### 6.1 Aurora Design Goals

Building on the success of Borealis, the team is aiming to fly higher this year, with a target apogee of 50 000 ft. The architecture of this year's rocket is driven by the requirements and project goals as set out in section 2. The primary flight goal is to fly a nominal ascent and recovery with several new innovative design elements. A secondary design goal is to develop systems and components that are designed for potential future flights to even higher altitudes. Significant design changes and system modifications are listed below:

- A larger 8 in diameter airframe
- A canards active roll-control system designed to minimize roll during ascent and prevent destructive coning
- A new single-separation, dual-deployment recovery system
- A deployable payload that will separate from the rocket at apogee and land under its own recovery system
- A rotating fincan to minimize vehicle roll due to external forces on the rocket, and to prevent roll reversal induced by the canards

The increase in technical scope on this year's rocket presents several design and integration challenges. These difficulties are compounded by more optimistic apogee targets that complicate general system design. In 2024, with Borealis, higher apogee was sacrificed in favour of better passive stability to increase the probability of a successful launch. Given the technical challenges of developing a liquid bipropellant engine, much of Borealis' architecture was borrowed from LOTS. Since the team was focused on validating new designs, less emphasis was placed on mass-optimization, which played a major role in LOTS' success. This year, the team is pushing its limits by targeting a high-altitude flight with new, unproven hardware. As such, this year's design approach has been adapted to mitigate risks, improve chances of success, and provide the team with more flexibility in terms of timelines. A few examples are:

- Larger diameter airframe enables greater flexibility in designs and reduces time spent on size optimization. This decision (discussed further in subsubsection 6.7.1) also reduces fuel tank length, preventing high length-to-diameter (LD) ratios given the increase in required fuel.

- Large targeted apogee range between 50 000 ft and 55 000 ft allowing the team to focus on system success and testing, rather than precise altitude goals that require optimization and careful mass tracking.
- Fuel and oxidizer concentric tank design similar to the design used on Borealis reduces technical scope and integration challenges

## 6.2 Engine Thrust and Burn Time

Preliminary engine thrust and burn time targets were set in Cycle 0 and further refined throughout the design cycle. Initial engine performance targets focused largely on the off-rail velocity of the rocket. As specified in Launch Canada's DTEG, minimum off-rail velocity is 100 ft/s and a 20% safety margin gives 120 ft/s as the chosen minimum target for off-rail velocity. Based on initial simulations that were conducted to evaluate the decision of moving to an 8 in airframe, minimum thrust was set to 8 kN and a subsequent trade study between thrust and burn time was conducted to minimize propellant mass. Simulations were run both in OpenRocket to evaluate off-rail stability and velocity, and in RASAero for apogee prediction.

Due to an unsuccessful static fire in November 2024, the team pivoted to 3D-printed injectors that were characterized through an extensive cold flow testing campaign during the winter semester. As mass estimates were refined, minimum thrust was pushed to 10 kN due to insufficient off-rail thrust-to-weight ratio (TWR).

Following a successful static fire in April 2025, expected thrust is approximately  $10 \pm 1$  kN with a steady-state 8-second burn time. Considering the initial thrust spike and current mass estimates, this corresponds to a more acceptable TWR equal to 12 and an off-rail velocity equal to 152 ft/s.

## 6.3 Cycle-Based System Design

As discussed in section 4, the mass and CG of each component of the rocket, and the length of each section are tracked throughout the design and development of the rocket in several distinct cycles. This data is used to create more accurate models that are fed into OpenRocket simulations to calculate relevant flight characteristics such as apogee, off-rail velocity and stability. The results inform future design iterations and general optimization. The mass and length breakdown of Aurora is outlined below in Figure 6.1.

## 6.4 Simulation Approach

The team has mainly used OpenRocket (version 24.12.RC.01) in the past with excellent accuracy and has continued to do so this year. In 2023, the team's apogee prediction using OpenRocket was off by only 1,096 ft. Similarly in 2024, OpenRocket's prediction was off by 2,638 ft. OpenRocket is extremely well documented, user friendly, and trustworthy. However, it is known among the rocketry community that the program's accuracy generally decreases past Mach 1.5. Therefore, the team also conducted simulations using RASAero II which has been developed using wind tunnel testing data up to Mach 25. Research conducted in the fall semester revealed several key differences between the two simulation programs:

2025 ROCKET LENGTHS – Cycle 3			Mass Breakdown (lb)
Section	Sec. Length	Top plane distance	
<b>Nosecone</b>	<b>40</b>	<b>0</b>	<b>18.19</b>
<b>Recovery</b>	<b>9.5</b>	<b>40</b>	<b>12.44</b>
<b>Avionics Bay</b>	<b>24.375</b>	<b>49.5</b>	<b>12.22</b>
> Canards	4	-	<b>3.62</b>
<b>Feedsystem</b>	<b>106.475</b>	<b>74</b>	<b>53.53</b>
Ox Tank	101.375	-	
OTAS	5.1	-	
<b>Engine Bay</b>	<b>19.250</b>	<b>180.35</b>	<b>33.06</b>
Injector Bulkhead Lip	0.125	-	
Fin Can	17.5	-	
Boattail	1.625	-	
<b>DRY MASS</b>		<b>199.60</b>	<b>133.06</b>
Propellant Mass			119.92
<b>WET MASS</b>			<b>252.98</b>
Length in ft		16.63	
Length L/D		24.95	

Figure 6.1: Aurora cycle 3 mass and length breakdown

- CG simulation in RASAero is insufficient to model liquid engines as it assumes the rocket is using a solid motor. Thus, the CG drifts progressively upward during boost and does not allow the user to provide custom CG locations for the motor through its custom thrust curve file (unlike OpenRocket). On that same line, RASAero does not have an input for dry mass. The software effectively "guesses" the mass flow rate of the rocket during boost, resulting in inaccurate mass and CG simulations.
- RASAero accounts for increases in thrust as the rocket increases in altitude during boost [3]. However, when calculating this increase in thrust, it assumes the thrust curve is normalized to sea-level pressure. This may cause inaccurate simulations if the engine is fired at a high enough elevation such that the initial pressure difference is already significant. Thrust is modified according to Equation 6.1 below:

$$F_\alpha = F_{ref} + (p_{\infty_{ref}} - p_\infty) \cdot A_e \quad (6.1)$$

Where:  $F_\alpha$  = thrust corrected for altitude and nozzle divergence

$F_{ref}$  = thrust at reference altitude condition

$p_\infty$  = atmospheric pressure

$p_{\infty_{ref}}$  = atmospheric pressure at reference altitude condition

$A_e$  = nozzle exit area

- RASAero calculates different drag coefficient curves that account for when the rocket is in boost and once engine cutoff occurs. This partially explains the more accurate simulations that RASAero produces.
- RASAero uses the Rogers Modified Barrowman method for calculating body forces and moments, and centre of pressure at high-supersonic and hypersonic speeds [3].

Given the differences outlined above, the team adopted a hybrid approach to simulations that combines the best of both programs. OpenRocket is primarily used for launch analysis where it provides greater clarity regarding off-rail stability and dispersion zone analysis. OpenRocket's user interface and customizability are also powerful tools. Meanwhile, RASAero is primarily used for apogee prediction due to more advanced simulation capabilities regarding drag coefficient calculations and thrust correction. This is not, however, a viable long-term method. Switching back and forth between programs is not efficient, and at times, there were significant apogee discrepancies between the two programs (predicted apogee sometimes differed by 10 000 ft).

Investigating these apogee differences further over the course of a couple months, a few meaningful tweaks to the simulation settings allowed the team to narrow the apogee prediction significantly. Some of the changes listed below, while self-evident, are included as useful documentation and a reminder for future team members regarding the importance of attention to detail when it comes to simulations:

- Ensuring the surface finish settings are as similar as possible in both OpenRocket and RASAero can vary the apogee by several thousand feet. It is important to note that OpenRocket, by default, measures surface finish in micrometers ( $\mu\text{m}$ ) whereas in RASAero, surface finish is selected from a qualitative drop-down menu with each option corresponding to a specific finish in inches (the exact values associated to each option are included in the RASAero user manual [3]).

- Fin thickness can also affect simulation results quite drastically. However, ensuring the fin thickness in both programs are equal is not quite enough. Fin flutter must also be taken into account in order to design fins with a realistic thickness. Initial simulations using both OpenRocket and RASAero assumed fins with 1/4 in thickness, which resulted in significant apogee discrepancies. When flutter calculations were completed later in the design cycle, simulations were again conducted, this time with a more realistic thickness of 0.375 in. It was found that the apogee predictions were much more similar between the two programs.
- As mentioned earlier, RASAero employs the Rogers Modified Barrowman equations which predicts a slightly more accurate center of pressure (CP) position. While this option should be enabled for true apogee prediction, it should not be selected if one is trying to minimize the apogee discrepancies between OpenRocket and RASAero.
- In the simulation settings, the nozzle exit diameter is distinct from the boattail aft diameter. Care should be taken in ensuring the correct nozzle exit diameter is inputted properly.

It is unclear how significant of an impact each specific fix had on reducing the apogee discrepancies between the two simulation programs. The combined impact resulted in much closer apogee predictions between the two programs that only differed by approximately 1 500 ft, as opposed to the initial 10 000 ft.

Due to the inefficiency of switching between programs, the team developed three OpenRocket plugins in an attempt to minimize apogee differences even further, to take advantage of the high-speed simulation capabilities of RASAero, and to amplify the simulation features of OpenRocket. These plugins were developed with joint contributions from both the flight dynamics and software subsystems. All three projects are freely accessible on Waterloo Rocketry's GitHub page.

#### 6.4.1 OpenRocket Drag Override Plugin

Building off of the OpenRocket airbrakes plugin [4], developed to simulate Borealis' control system, this plugin overrides the drag coefficient ( $C_D$ ) values computed by OpenRocket with values exported from RASAero's lookup tables. For a given rocket model in RASAero,  $C_D$  values are exported as a function of Mach number ( $M$ ) and angle of attack (AoA). A Python script scrapes the relevant values and formats them into a lookup table which is used by the plugin to interpolate a  $C_D$  at each time step.

While nice to have, the predicted  $C_D$  as a function of  $M$  is similar in both programs. Given that a new lookup table must also be created every time the rocket design changes, the plugin was not heavily used. The predicted  $C_D$  values for both programs are plotted below in Figure 6.2, with OpenRocket predicting slightly higher values in the transonic flight regime. RASAero also predicts significantly higher supersonic drag values during the boost phase. The GitHub repository for this plugin can be found [here](#).

#### 6.4.2 OpenRocket Thrust Override Plugin

As mentioned in subsection 6.4, RASAero accounts for the slight increase in thrust generated by the engine at higher altitudes where the ambient pressure is lower. This increase in thrust has been neglected in the past because the team's previous rockets had relatively short burn times, and thus the atmospheric pressure could be considered constant over the boost phase. However,

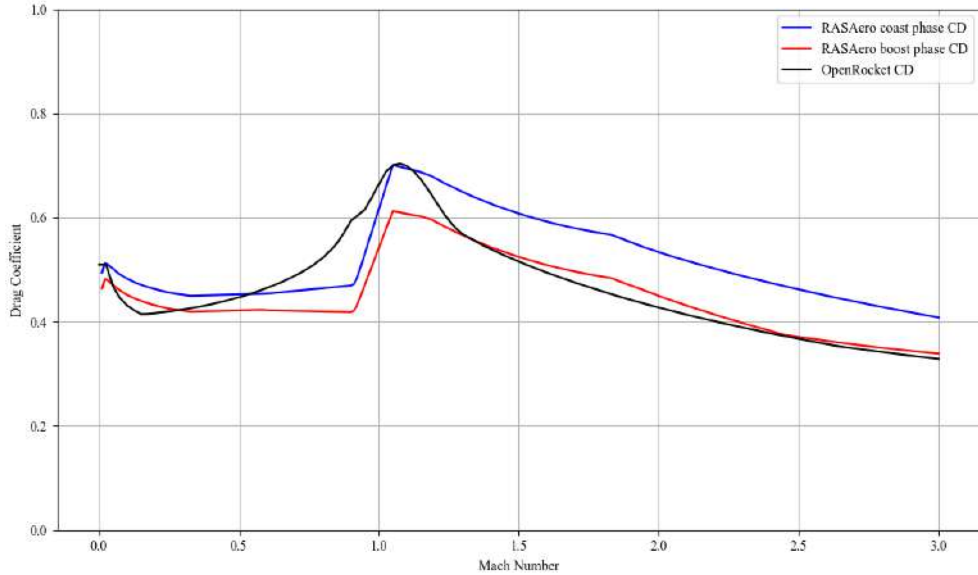


Figure 6.2: Drag coefficient vs Mach number comparison between OpenRocket and RASAero

given the longer burn time the team is targeting this year, the rocket is likely to see a difference in atmospheric pressure of nearly 0.4 atm between liftoff and the end of the boost phase. As confirmed by the OpenRocket developers, the program does not account for this increase in thrust. The plugin utilizes the same Equation 6.1 to adjust the thrust of the rocket for every time step. The GitHub repository for this plugin can be found [here](#).

#### 6.4.3 OpenRocket Monte Carlo Plugin

Building off of an existing Monte Carlo simulator developed by the team in the past, the improved version incorporates the two aforementioned plugins and is updated to the newest OpenRocket release candidate, which supports multi-level wind simulations. An export feature has also been added allowing the user to post-process the simulation results for dispersion zone analysis and to highlight low-stability cases. The GitHub repository for this plugin can be found [here](#).

### 6.5 RSE File Generation

Modelling the engine properly is critical to the accuracy of our simulations which inform general rocket design throughout the year. It can also be challenging due to the complex fluid dynamics involved. Custom RSE files informed by cold flow and static fire data allow the team to simulate the rocket in OpenRocket. Further details can be found in subsection 8.6 regarding the simulation of the engine and RSE development.

### 6.6 Loads Analysis

The team continues to use the BENDIT7 Excel calculator [5] for calculating load cases at maximum acceleration (takeoff) and at maximum dynamic pressure (MaxQ). The relevant inputs for

the calculator are obtained through OpenRocket simulations based on the current design cycle. Shear, bending, and axial moments are calculated along the rocket's length, as well as bending and axial moments along the fin span. These results are crucial for the structural design of the airframe, ensuring that couplers, body tubes, and internal components can withstand the expected loads without failure.

As further explained in subsubsection 8.3.1, the team's decision to utilize 3D-printed injectors and the significant ablative regression observed during the April Static Fire resulted in more uncertainty regarding the characterization of the engine. As such, a over-optimistic engine RSE file was created specifically for load calculations allowing joint design to proceed with upper-bound load estimates. Simulating the rocket with this new RSE file the following results listed in Table 6.1 below as compared to the expected flight profile. The calculated takeoff loads from this upper-bound simulation are included in Figure 6.3. Expected loads at MaxQ are found in Figure 6.4

Parameter	Flight Profile	
	Expected	Upper-Bound
Altitude (ft)	50 000	57 000
Max. Velocity (ft/s)	2 400	2 665
Max. Mach Number	2.2	2.5
Max. Acceleration (Gs)	10	13

Table 6.1: Expected vs upper-bound flight profile comparison for loads analysis

Takeoff, Summarized - Cycle 2.5 Aurora				
	Body Station, in	Design Body Shear Force, lb	Design Body Bending Moment, lb-in	Pi, Axial Force, lb
0	0.0	0.0	0.0	0.0
Nosecone	40.0	0.8	10.7	-613.7
Recovery	49.0	0.8	17.9	-1049.8
Avionics Bay	70.0	0.8	34.7	-1308.3
Fuel tank	74.0	0.8	37.8	-1308.3
Ox tank 1	95.9	0.5	52.5	-2374.3
Ox tank 2	112.3	0.2	58.7	-3079.4
Ox tank 3	128.7	-0.2	58.8	-3690.5
Ox tank 4	145.2	-0.7	51.5	-4207.5
Ox tank 5	161.6	-1.3	34.9	-4630.5
OTAS	178.0	-2.0	7.7	-4959.4
Engine Bay	184.0	-2.0	-4.5	-4963.0
Boattail	201.4	0.1	-17.4	1085.5
	203.5	0.0	0.0	924.2
				0.0

Figure 6.3: Cycle 2.5 takeoff upper bound loads

## 6.7 Aerodynamic Design and Optimization

In 2023, LOTS reached a team-best 31 476 ft and a maximum velocity of Mach 1.5. The team's goal this year to reach 50 000 ft with a top speed above Mach 2 represents a significant departure from the flight conditions the team has worked with in the past. Given the increases in altitude

MaxQ, Summarized - Cycle 2.5 Aurora				
	Body Station, in	Design Body Shear Force, lb	Design Body Bending Moment, lb-in	Pi, Axial Force, lb
0	0.0	0.0	0.0	0.0
Nosecone	40.0	32.6	477.7	-154.4
Recovery	49.0	24.2	734.2	-270.2
Avionics Bay	70.0	18.6	1185.6	-341.7
Fuel tank	74.0	18.6	1260.1	-341.7
Ox tank 1	95.9	6.1	1533.0	-484.3
Ox tank 2	112.3	-4.0	1551.3	-589.1
Ox tank 3	128.7	-14.7	1399.4	-693.8
Ox tank 4	145.2	-26.0	1066.6	-798.6
Ox tank 5	161.6	-38.0	541.7	-903.4
OTAS	178.0	-50.7	-186.2	-1008.1
Engine Bay	184.0	-51.1	-491.8	-1011.3
Boattail	201.4	7.1	-1051.9	414.5
	203.5	0.0	0.0	400.6
				0.0

Figure 6.4: Cycle 2.5 MaxQ upper bound loads

and velocity, a host of aerodynamic studies were conducted to design and optimize the vehicle and mitigate against various aerodynamic phenomenon.

### 6.7.1 Rocket Diameter Changes

Historically, the team has flown 6 in diameter rockets since 2019. Given the team's aspirations to fly to 50 000 ft this year and over 100 000 ft in the future, a rocket diameter trade study was conducted in September 2024 to evaluate several potential rocket diameters that would be suitable for the team's goals in the next few years. The team compared highly-optimized versions of both a theoretical 6 in and 8 in diameter rocket in terms of expected apogee, cost, manufacturing and long-term versatility. Simulations were conducted in both OpenRocket and RASAero resulting in upper and lower bound apogee estimates for both optimized rockets.

In a first round of simulations, rocket models with a length-to-diameter ratio (LD ratio) of 30 were simulated, representing the absolute longest rocket the team is willing to launch. In a second round of simulations, models with an LD ratio of 25 were simulated, representing a more realistic rocket length. Table 6.2 outlines the results for both rounds of simulations.

Software	6 in Diameter	8 in Diameter
<b>LD = 30</b>		
OpenRocket	79 611 ft	170,058 ft
RASAero	120 196 ft	326 337 ft
<b>LD = 25</b>		
OpenRocket	51 526 ft	119 506 ft
RASAero	72 325 ft	<i>not simulated</i>

Table 6.2: 6-inch vs 8-inch simulation results

As shown in Table 6.2, based on RASAero results, while both models with an LD ratio of 30 would likely clear 100,000 ft, a 6 in diameter rocket with an LD ratio of 25 would likely not. Given the team's ambitions for high-altitude rockets in the future, an 8 in diameter was selected as the team's rocket diameter moving forward, as it provides greater flexibility in terms of the team's apogee targets without requiring excessive optimization. It is noteworthy that the significantly higher apogee predictions by RASAero are likely due to inexact simulation inputs as described in subsection 6.4 which had not been identified yet by the team.

### 6.7.2 Nosecone Optimization

Early results from the simulations described in Table 6.2 showed that Aurora would likely reach speeds above Mach 2.0, even higher for future rockets. This prompted a trade study of various nosecone designs that were optimized for high supersonic regions of flight. In the past, the team has used a Von Karman nosecone design with a 4:1 fineness ratio. However, as the team's current moulds were quite old and required extensive repairs, this presented an opportunity to create new moulds with a design better suited for future projects.

An exhaustive literature review yielded three potential options:

- A power series ( $x = 0.75$ ) nosecone design was found to be best suited for high supersonic speeds, yet generates significantly more drag at transonic speeds compared to the Von Karman nosecone.
- A conic nosecone design is similar to the power series nosecone, with slightly higher drag values overall.
- The Von Karman nosecone design is generally best suited for transonic speeds, but drag values for supersonic speeds are not significantly higher than the previous two options, making it a viable alternative.

While the power series nosecone generally has the smallest drag values at high supersonic speeds, the design decision ultimately came down to manufacturing preferences. While the team has experience making complex composite shapes such as the Von Karman nosecone, the conic nosecone design was chosen given its relative manufacturing ease compared to the other geometries. An analysis of fineness ratio showed little drag decrease for fineness ratios past 5:1. Thus, the team selected a 5:1 conic nosecone design moving forward.

### 6.7.3 Fin Can Considerations

Fin design must be preceded by a good model of the rocket in OpenRocket. Any major inaccuracies in the model may render any simulation results useless and lock the team into a poor design. Cycle-based data collection ensures that key rocket information is kept up-to-date. Unfortunately, due to delays in the April 2025 static fire and large uncertainty associated with the 3D-printed injectors, fin design was only finalized at the beginning of May 2025. Despite the significant lead time associated with the SRAD fin can manufacturing process, delaying this design decision allowed the fins to be sized using a static-fire-informed RSE file and provided more time for in-depth flutter analysis discussed further in subsubsection 6.7.4. Key fin parameters are defined in Figure 6.5.

The fin parameters found to most affect flight results include the semi-span, sweep length, fin thickness, and fin positioning. Some common fin designs such as rectangular, clipped delta, swept, and trapezoidal are generally easier to manufacture and are often used as a starting point.

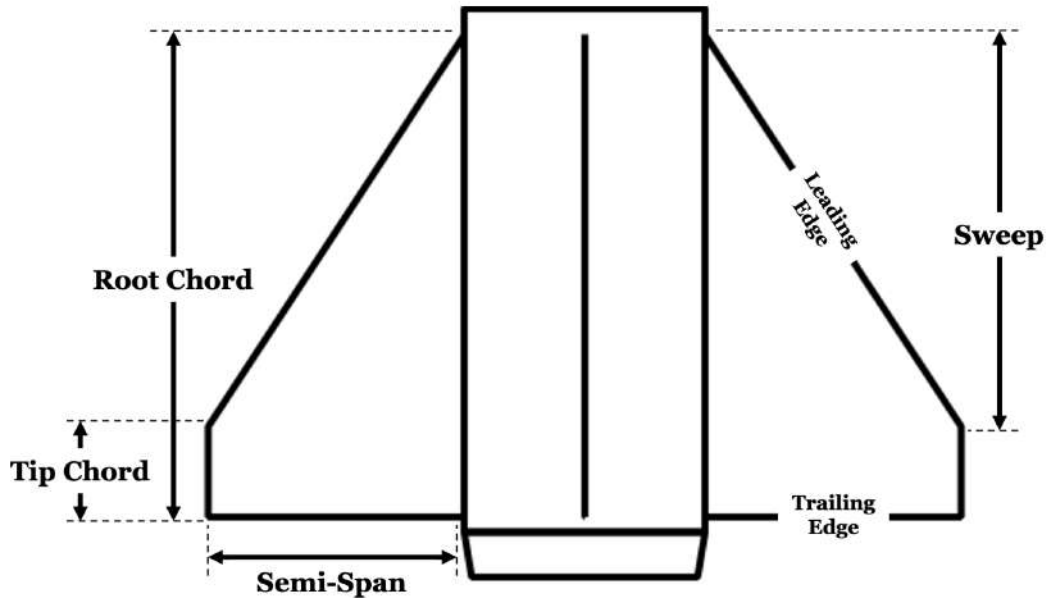


Figure 6.5: Common fin parameters; Aurora fin shape and size

As set by the team, the primary criteria for determining fin size and shape is to maintain a minimum launch stability of 1.5 cal in 15 mile per hour winds. Secondary requirements, in descending order of importance, call for:

- A maximum root chord length of 16 in, set by the combustion chamber length, which itself is sized based on injector characterization.
- A maximum sweep length equal to the difference between the root chord and tip chord. This ensures that the fin is not swept back past the end of the root chord, thereby avoiding damage on landing and reducing the risk of flutter.
- A maximum semi-span length of 8.5 in, set by the size of the team's curing oven.
- A minimum 0.5 in clearance on both sides in the root chord direction for the composite manufacturing process.
- Rounded edges which are easier to manufacture than airfoils and decrease aerothermal heating on the leading edges
- A fin size and shape that minimizes apogee losses due to stability gains.

Fin sizing for Aurora proved more challenging than in previous years. Not only is the team flying higher and faster than ever before, but the overall diameter increase of the rocket coupled with the minimal increase in length of the combustion chamber severely restricted the fin sizing process. Notably, the combustion chamber was resized to be 2 in longer to allow the root chord length to be 16 in long (2 calibres). Similarly, it is considered good practice among the rocketry community for the fin semi-span to be at least 1 calibre in length. This left little room to play with in terms of fin optimization, especially given that fin semi-span is the easiest way to increase static stability without suffering drastic losses in apogee.

Based on previous fin sizing analyses conducted by the team, a four-fin design was selected, which typically results in smaller apogee losses for a gain in stability. Furthermore, fin thickness was set based on extensive flutter analysis described in the following section. Lastly, weighed rocket component masses following a successful test flight launch in May 2025 informed an updated OpenRocket model to which additional weight was added at the bottom of the rocket to account for unforeseen increases in mass that could negatively affect the rocket's static stability margin. Following these requirements and constraints, fin parameters were iterated over 50 times in OpenRocket until an optimal fin shape was determined. The resulting shape is presented above in Figure 6.5 and the exact dimensions are included in Table 6.3.

Number of fins	4
Fin cant	0°
Root chord	16 in
Tip Chord	3 in
Sweep length	13 in
Semi-span	8.5 in
Thickness (avg)	0.34 in
Fin cross section	Rounded

Table 6.3: Final fin parameters

Given the tight constraints on fin sizing in order to meet the stability requirements, little optimization was conducted on the boattail. Over the years, the team has found that having a longer boattail and a more aggressive taper is beneficial for apogee due to a decrease in base drag. However, a significantly increased taper angle was found to decrease stability, and a longer boattail pushes the fins upwards, also hurting stability. When stability is decreased through these methods it forces the fins to be larger which results in lower apogee and decreased fin flutter FOS. Following initial iterations of the boattail design, it became evident how sensitive the overall stability and apogee of the vehicle was to any change in the boattail design. Considering the distance from the bottom of the injector bulkhead to the end of the combustion chamber is 19.125 in and the fin can length is 17.5 in, the boattail length was simply set to 1.625 in with an aft diameter of 7.5 in.

Lastly, Aurora's increased speed and target apogee could also increase the amount of roll that the rocket is expected to experience, compared to the team's previous rockets. Rockets experience roll due to small manufacturing defects in a rocket's fins and/or external factors such as wind and angle of attack. As velocity increases, these effects can increase roll rate drastically and lead to coning, where the pitch-yaw oscillations create a destructive helical flight path (described further in subsubsection 6.7.5). To mitigate this risk, and prevent roll reversal caused by the canards system, the team decided to mount the fincan on ball bearings allowing it to rotate freely about the rocket. Further discussion of roll reversal can be found in subsection 6.8. The mechanical design of the spin can is outlined in subsubsection 7.7.4.

#### 6.7.4 Flutter Analysis

Fin flutter is a destructive aeroelastic phenomenon that occurs at high speeds and caused by the coupling of aerodynamic forces with pitching moments acting on the fins. Historically, the team

has calculated fin flutter FOS using an empirical formula widely used in amateur rocketry derived by D. J. Martin in 1956 [6]. However, given that Aurora is expected to reach Mach 2.3, the team conducted extensive research and fin torsional testing to quantify the structural integrity of last year's Borealis composite fins and to begin adapting flutter analysis methods for higher Mach regimes. This included a reassessment of the existing flutter modelling approach in order to establish a safer and more technically robust methodology moving forward.

## Review of Previous Flutter Modelling Techniques

In both 2023 and 2024, the team used the following Equation 6.2 below from [6] to calculate fin flutter velocity, which is compared to the rocket's simulated MaxQ conditions to obtain a fin flutter FOS. During fin sizing, the fin thickness was varied such that a minimum flutter FOS of 1.5 was obtained using inputs from the most up-to-date simulations. Once the shape was finalized, the fins were water jet cut out of carbon fibre plate stock and additional thickness was added via a carbon fibre tip-to-tip wet layup until the specified thickness was reached.

$$V_f = a \times \sqrt{\frac{G_E}{\frac{39.3 \times AR^3}{(t)^3 \times (AR+2)} \times \left(\frac{\lambda+1}{2}\right) \times \left(\frac{p}{p_0}\right)}} \quad (6.2)$$

- where       $V_f$  = flutter velocity  
 $a$  = speed of sound at MaxQ local pressure  
 $G_E$  = shear modulus  
 $AR$  = aspect ratio  
 $t$  = thickness ratio [thickness ÷ root chord]  
 $\lambda$  = taper ratio [tip chord ÷ root chord]  
 $p$  = MaxQ local pressure  
 $p_0$  = sea level pressure

While both LOTS and Borealis flew successfully without experiencing flutter-related incidents, several limits to the accuracy of this model were identified:

- Martin's original paper was based on wind-tunnel testing of various missile designs that were known to have reached approximately Mach 1.5 without experiencing flutter-related failures. Furthermore, Martin's work is an extension of a previous paper by Theodorsen and Garrick who developed an empirical formula from fins with aspect-ratios larger than 7 [7]. Since Aurora is expected to reach Mach 2.3, and given that the team typically designs fins with low aspect-ratios smaller than 1, the predicted flutter velocity using Equation 6.2 must be interpreted with a significant grain of salt.
- Equation 6.2 was derived from an empirical equation that torsional rigidity  $JG$  instead of shear modulus  $G_E$ . Martin's equation using  $G_E$  is popular because the shear modulus of a material is independent of the material's dimensions or shape. However, to isolate  $G$  from  $JG$ , Martin made the assumption that the torsional constant  $J = \frac{ct^3}{6}$ . Critically, as will be discussed shortly, this formula for the torsional constant yielded unreasonably high shear modulus values when the team conducted torsional testing in May 2025.

- The denominator constant  $DN = 39.3$  in Equation 6.2 is calculated based on Equation 6.3 below where  $\gamma$  is the ratio of specific heats, and  $\epsilon$  is the distance between the fin's centre of gravity and quarter-chord, expressed as a fraction of chord length. In Martin's derivation, a symmetrical fin is chosen such that  $\epsilon = 0.25$ . However, given the highly swept nature of the team's past and current fin designs, this value was found to nearly double in some cases, and resulted in fin flutter velocity being overestimated by a factor of 1.37 for LOTS and 1.34 for Borealis.

$$DN = \frac{24 \times \epsilon \times \gamma \times p_0}{\pi} \quad (6.3)$$

- The shear modulus used in previous flutter analyses is based on the average shear modulus of carbon fibre (598 ksi) [8]. However, this value fails to account for the added shear strength through the tip-to-tip wet layup process. In Peak of Flight Issue 615, J. K. Bennett suggests that a tip-to-tip doubles the shear modulus of the fin, however, this claim is un-referenced [9].
- A literature review found that if flutter occurs during flight, the fins often break off at the root of the fin. As such, epoxy fillets are typically added to reinforce the root chords. The added strength of these fillets is not accounted for in Martin's equation and the team has arbitrarily set the fillet diameter to 0.5 in.

## Fin Torsional Testing

In May 2025, to characterize the strength of the carbon fibre fins the team manufactures, testing on Borealis' fin can was conducted in an effort to facilitate and inform fin sizing for this year's rocket.

As described in subsubsection 6.7.4, the effects of fin flutter were investigated more thoroughly this year, prompting the need to quantify the stiffness of the fins. In previous years, the team had attempted to find the material properties of the fins by testing coupons of similar material. The accuracy of these previous tests were deemed questionable and therefore, more elaborate processes were investigated.

The test was conducted to obtain the torsional rigidity of the fins, which was calculated using Equation 6.4 below from [10]. By dividing the experimental value obtained by the torsional constant  $J$ , the shear modulus  $G$  can be obtained and directly inserted into Equation 6.2.

$$JG_E = \frac{TL}{\theta} \quad (6.4)$$

Where	$JG$ = torsional rigidity
	$J$ = torsional constant
	$G_E$ = shear modulus
	$T$ = torque ( $N \cdot m$ )
	$L$ = length of structure (m)
	$\theta$ = deflection (rad)

The test was conducted using a MTS322 compression-tension machine to induce a torsional moment on the fin. Additional aluminum extrusion was used to extend the moment arm during the test. This test setup is similar to fin torsional testing conducted by both UOttawa (internal document available upon request) and Georgia Tech. The fincan was fastened down to the worktable using a custom-made jig. Linear variable differential transformers (LVDTs) were positioned at the leading and trailing edges of the fin and were used to measure the linear deflection. The complete setup is shown in Figure 6.6. As the moment applied on the fin increases, the LVDT on the left detects the region of the fin moving upwards while the LVDT on the right detects the region of the fin moving downwards. Using the known locations of the LVDTs and the resulting linear deflections, an axis of revolution and the rotational deflection of the fin were calculated.



Figure 6.6: Fincan test setup

Using Equation 6.4 and the applied force and deflection data from the test, the torsional rigidity was calculated to be approximately  $2\ 500\ N \cdot m^2$ . Figure 6.7 below shows the displacement of both LVDTs as recorded during the test as a function of applied force. Figure 6.8 plots  $JG$  vs time.

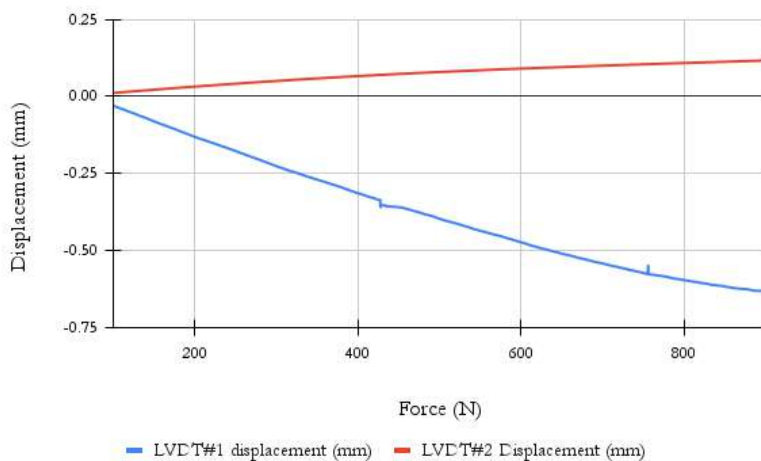


Figure 6.7: Fin torsional testing results; displacement vs force

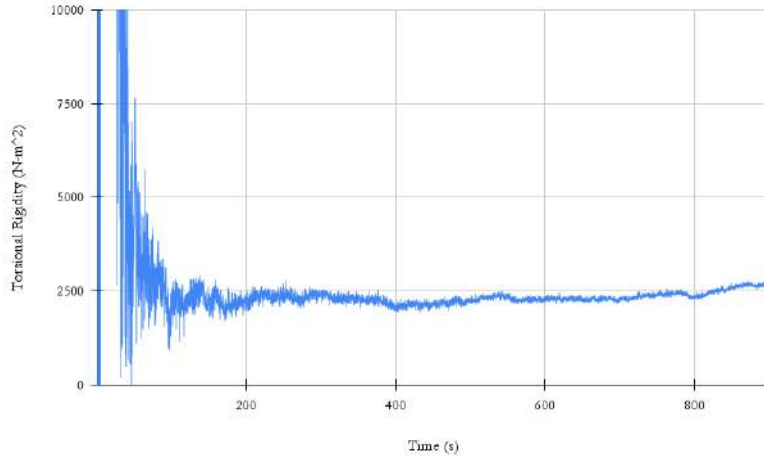


Figure 6.8: Fin torsional testing results; torsional rigidity  $JG$  vs time

As shown in Figure 6.8, the measured torsional rigidity remains relatively constant throughout the test, as expected. However, dividing by the torsional constant  $J$  to get shear modulus is not as simple as it may seem since the fin is an asymmetric body under torsion. For a uniform beam with rectangular cross-section, shear modulus  $G_E$  is proportional to  $ct^3$  where  $c$  is the chord length and  $t$  is the thickness of the cross-section [10]. In his paper, Martin further suggests approximating the torsional constant of a solid, thin airfoil according to Equation 6.5 below [6].

$$J = \frac{ct^3}{6} \quad (6.5)$$

Given the highly swept nature of the fins, Equation 6.5 results in a unrealistically high shear modulus equal to 17 226 ksi compared to carbon fibre's average shear modulus around 598 ksi. Nonetheless, recalculating the flutter safety factor for Borealis' fin can using  $G_E = 17\ 226$  ksi results in FOS 4.288. However, Martin provides a second method, Equation 6.6 below, for calculating flutter velocity as a function of torsional rigidity  $JG$ .

$$\frac{V_f^2}{a^2} = \frac{\pi c_{3/4}^2 f_1^2 JG}{4 \epsilon c^4 L^2 \rho a^2} \quad (6.6)$$

$c$  = root chord length

$c_{3/4}$  = chord length at the three-quarter-span location

$f_1 = 1 + 1.87(1 - \lambda)^{1.6}$

$JG$  = torsional rigidity

$L$  = fin span

$\rho a^2 = \gamma p$

Using Equation 6.6, the flutter safety factor for the Borealis fin can was found to be 3.094, a more reasonable value reaffirming the claim that Equation 6.5 is not applicable to the Borealis fins and by extension, Equation 6.2.

## Updated Flutter Modelling Approach

Given the limitations of Martin's equation mentioned earlier, and the results from torsional testing, the team followed the approach outlined below to mitigate flight failure risks associated with fin flutter:

1. First, the team researched other high-altitude flights that reached similar velocities to obtain an approximate range for the thickness that Aurora's fins would likely have to be. From these results, the team set a preliminary targeted fin thickness of 0.375 in. Specifically, Georgia Tech's Fire on High sounding rocket launched in July 2024 reached Mach 1.89 with airfoiled 0.346 in carbon fibre fins reinforced with a tip-to-tip layup. While that rocket unfortunately experienced destructive coning shortly after, the fins were not destroyed due to flutter and provided the team with a valuable reference point in setting a preliminary fin thickness target.
2. Second, the team updated Equation 6.2 to Equation 6.7 below and created a spreadsheet to automatically calculate the denominator constant as per (Equation 6.3) for the team's highly swept fin designs. The team also made the assumption suggested by J. K. Bennett that adding a tip-to-tip layup doubles the shear modulus of the fin. Using this updated model, output parameters from OpenRocket simulations and the preliminary targeted fin thickness of 0.375 in, the team calculated a fin flutter FOS of 0.832 (well below the FOS 1.5 requirement).

$$V_f = a \times \sqrt{\frac{G_E}{\frac{DN \times AR^3}{(t)^3 \times (AR+2)} \times \left(\frac{\lambda+1}{2}\right) \times \left(\frac{p}{p_0}\right)}} \quad (6.7)$$

3. Third, using a conservative torsional rigidity value of  $2000 \text{ N} \cdot \text{m}^2$  obtained from torsional testing and inputting Borealis' fin dimensions into Equation 6.6, the team calculated a new fin flutter FOS for the Borealis fin can equal to 3.094.
4. Fourth, the flight conditions were changed to reflect the expected pressure and velocity at MaxQ for Aurora to obtain a hypothetical fin flutter FOS for the scenario where the Borealis fin can was flown on Aurora. This yielded a fin flutter FOS equal to 2.462, demonstrating that Borealis' 0.235 in fins would have likely survived in conditions upwards of Mach 2.3. Given that Aurora's fins are 1.45 times thicker and considering the 8-layer tip-to-tip added to the fins, the team is confident that fin flutter risks have been mitigated.
5. Lastly, to further mitigate fin flutter risks, the team moved to 1.5 in diameter fillets, reinforcing the fin bond at the root chord.

While the team ultimately fell short of its goal to develop and research a better way to model fin flutter, torsional testing conducted in May 2025 allowed the team to tackle fin flutter from a largely empirical approach that will be refined over the following years as the team is able to conduct further composites testing.

### 6.7.5 Coning Analysis

Coning is a destructive aerodynamic phenomenon caused by the coupling of roll, pitch, and yaw oscillations, which can occur when the rocket's roll rate aligns with its natural pitch frequency. As Aurora is expected to exceed Mach 2.0, this risk was investigated in October 2024. To mitigate the potential for coning, an analysis of roll rate and pitch frequency was conducted. An extensive literature review also revealed the following factors as potential contributors to coning occurrences:

- Fin misalignment
- Low number of fins
- Aerodynamic imbalances (from non-uniform fins, or external wind gusts or turbulence)
- Flexible rocket sections and joints
- Uneven propellant burning
- Large LD ratios
- Inertial spin axis being displaced from the vehicle centre-line
- Centre-of-gravity offsets

The team used mass estimates from Cycle 0, OpenRocket simulations and formulas from [11] [12] to estimate the natural pitch frequency and roll rate of the rocket. The pitch frequency was calculated according to Equation 6.8 below:

$$w_n = \sqrt{\frac{0.5pV^2A_rC_{N_a}[cp - cg]}{I_L}} \quad (6.8)$$

where       $w_n$  = natural frequency  
 $p$  = density of air  
 $V$  = velocity of rocket  
 $A_r$  = reference area  
 $C_{N_a}$  = normal force coefficient  
 $cp$  = centre of pressure location  
 $cg$  = centre of gravity location  
 $I_L$  = longitudinal moment of inertia

During the boost phase, roll rate is estimated to be between 0.5 and 2 Hz, with a pitch frequency ranging from 0.0058 Hz at takeoff to 0.055 Hz at burnout. With the potential implementation of a spin can, the roll rate is expected to decrease further, significantly reducing the likelihood of coning. These early results suggest coning is unlikely to occur during flight.

### 6.7.6 Aerothermal Heating Analysis

As the team embarks on new projects moving at higher speeds, considering aerodynamic heating increases in importance. Based on preliminary research as well as examining similar projects from other organizations, the team is not taking steps to create high-temperature resistance composites at the moment. Multiple factors are included in this decision, including but not limited to the size/length of the nosecone tip, the shape of the fin tips and the time spent during boost.

It was decided to include a 2 in gap at the top of the nosecone moulds in order to maintain access during infusions. This, along with the 5:1 fineness ratio of the nosecone results in a metal nosecone tip a minimum of 10 in long. This will contribute heavily to reducing the heat experienced by composites on the rocket. Additionally, the team's current fin designs have rounded leading edges on the fins as opposed to sharp leading edges, which avoids concentrating large amounts of heat flux in the fin tips, which would occur if they were to have a thin leading edge. Finally, the inside of the airframe will be lined with temperature indicating stickers to obtain data on heating during flight.

## 6.8 Canards Aerodynamic Design

### 6.8.1 Canard Design Requirements and Safety Concerns

The canard system being developed for Aurora is subject to several mechanical, aerodynamic, electrical and software design requirements established by both the team and the Launch Canada body. The primary requirements and considerations relevant to the aerodynamics, sizing and safety of the canards are listed along with their justification in Table 6.4. Requirements are defined using the term "shall" while considerations and suggestions are defined using the term "should".

As the canards are intended to actively modify the rocket's roll rate during flight, naturally several safety concerns and risks emerge that have been summarized and addressed below.

### Positioning

The positioning of the canards on the rocket can greatly affect its stability. Two positions were considered by the team: placing the canards above the propellant tanks, or integrating them within the injector section. The former offers a significantly easier design footprint to work with, but decreases the passive stability margin of the rocket by shifting the centre of pressure (CP) forward and closer to the centre of gravity (CG). This can be mitigated by increasing fin size to regain the loss in passive stability, but would lower their flutter velocity (this effect is likely negligible, but was still considered). The latter option of placing the canards in the injector section is significantly more difficult from a system integration perspective, but does not affect the CP nearly as much since the canards are already located behind the CP. In September 2024, initial designs placed the canards in the injector section, but as designs for both the canards and the injector valves increased in complexity over the following months, the team decided to mount the canards above the propellant tanks.

### Yaw and Pitch Control

To induce a rolling moment about the rocket's rotational axis, the canards located on opposite sides of the rocket must rotate in opposite directions. Doing so generates lift in opposite directions, which cancel, but produce a rotational moment without affecting the vehicle's yaw and pitch. However, in a scenario where the system were to malfunction or fail such that both canards actuate in the same direction, the lift forces generated would not cancel, which would cause a pitching moment about the vehicle's CG. This possible failure mode was of particular concern to the team, and was mitigated through a mechanically-linked canard design where the actuating shafts are

Requirement	Justification
Canards shall be locked to explicitly roll control	The system will not control the yaw or pitch of the vehicle which presents significantly more technical challenges and safety risks
Canards should reduce the roll rate of the rocket to 0 deg/s	To avoid destructive coning behavior and produce better image quality
Canards shall not actuate (remain in neutral position) unless the rocket is at least 20,000 ft AGL, after boost phase or after flight has reached maxQ	As per Launch Canada's Design, Test & Evaluation Guide (DTEG) (Pending a successful test flight of this system in May, the team hopes to obtain permission from Launch Canada to activate the system from lift-off)
Each of the canard fins shall not operate independent of each other	No other moment shall be created other than roll moment on the flight vehicle
Canards shall be designed to take all the loading from directly impeding the airflow	The system must be strong enough to not break or fail in transonic and supersonic airflow; canards shall transmit all the moment and drag it induces to the rocket
Selected actuators shall be electrically driven	Generally simpler and more reliable
Canards shall not deploy when any of the rocket's yaw or pitch exceeds 30 degrees according to an IMU. It must abort and return to neutral state for the remainder of the flight	As per Launch Canada's DTEG
Canards should not induce roll reversal	Roll reversal can be destructive and could lead to the system losing control authority
Canards should be sized to mitigate roll in the region of flight most likely to experience roll	Due to the large altitude and velocity range during flight, the canards will not have control authority in some regions of flight
Canards should be shaped to minimize risks associated with parachute tangling upon drogue deployment at apogee	This could lead to a ballistic landing and total loss of the vehicle
Canards should be sized to minimize drag	This decreases expected loads on the system
Canards mounting mechanism should minimize protuberances on or near the control surfaces	This encourages non-turbulent airflow around the system

Table 6.4: Canard design requirements and considerations

connected such that rotating one canard causes an opposite rotation in the other. Furthermore, the axis of rotation of the canard was placed above the expected CP of the canard, providing some degree of passive stability to the canards and forcing them back to a more neutral position in the event where the actuating servo were to lose power. A detailed review of the canards' mechanical system can be found in subsubsection 12.1.2.

## Maximum Actuation Angle

Historically, the team has little experience manufacturing and designing lifting surfaces with airfoils. As such, the canards were chosen to have an uncambered uniform cross-section with rounded leading and trailing edges. The rounded edges provide a smoother surface to deflect airflow while the uncambered cross-section ensures no lift is generated when the canards are in their neutral position (0-degree angle of attack). Furthermore, this allowed the canards to be modelled as flat plates that only produce lift when positioned at a given angle of attack (AoA) relative to the oncoming airflow. According to flat plate theory, wake separation occurs around an AoA of 12 degrees, resulting in a sharp drop-off in lift being generated. This is a significant concern from an aerodynamic standpoint that would also result in excess drag, turbulent airflow and potential loss of control for the controller. While this can be mitigated by implementing a maximum actuation angle, this limit comes at a loss of precision for the controller since the number of steps that the servo can make is decreased. For a flat plate in normal conditions, lift is proportional to AoA and canard surface area. Thus, for a canard limited to a 5-degree actuation angle, the canard itself must be quite large to produce the same lift as a canard limited to a 10-degree AoA with a smaller area. Furthermore, a 5 degree limit results in half as many servo steps, each step producing a larger difference in lift from the previous due to the canard's larger size. The finalized design was limited to a 10-degree actuation angle in either direction, with a mechanical stop at 12 degrees.

## Canard Size and Shape

The team explored swept wing designs that minimize drag at supersonic speeds. As the rocket reaches supersonic speeds, shockwave cones are likely to form around the canards. This cone extends outwards with a half angle  $\mu$  as a function of mach number  $M$  according to Equation 6.9. Figure 6.9 illustrates the behaviour of the Mach cone as a function of Mach number.

$$\mu = \arcsin \frac{1}{M} \quad (6.9)$$

For a swept canard with sweep angle  $\Lambda$  as shown in Figure 6.10, significantly more drag is created if the leading edge intersects the Mach cone when the vehicle is supersonic (i.e. when  $90 - \Lambda > \mu$ ). As the Mach number increases,  $\mu$  gradually decreases causing the cone to become sharper. Thus, choosing a design that ensures the canards are permanently swept behind the shockwave (referred as a subsonic leading edge) is important to decrease the expected loads on the canards caused by wave drag in the transonic region. A subsonic leading edge also results in smoother airflow over the canards which helps create more lift. These design features help address concerns about failure modes where one or both canards could be ripped off during flight due to unexpectedly high loads caused by wave drag. Flutter is also an area of concern given that the

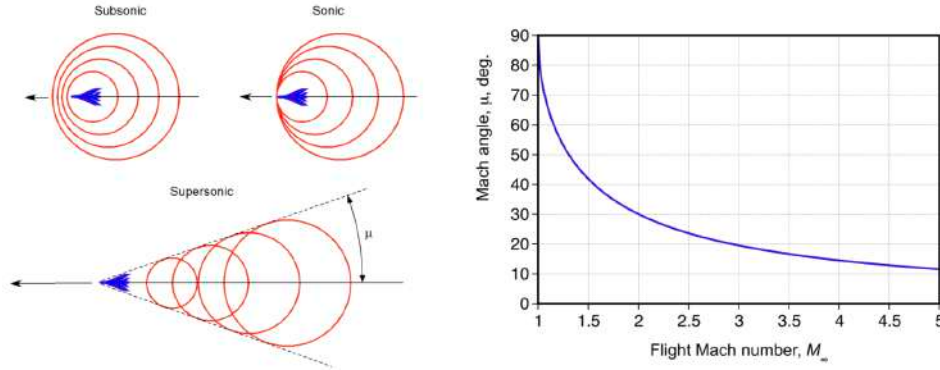


Figure 6.9: Evolution of the Mach cone half angle  $\mu$  as a function of Mach number [13]

canard's root chord is not attached to the rocket's body tube. Further flutter analysis is being conducted on both the canard itself and the axis of rotation to determine mechanical manufacturing constraints in terms of minimum axle and flutter thickness.

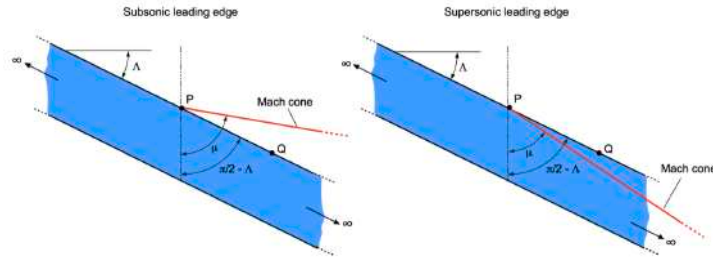


Figure 6.10: A swept wing with subsonic and supersonic leading edges. Limiting the buildup of wave drag on the wing requires that the leading edge be swept behind the Mach cone [13]

## Canard Wake Interference and Roll Reversal

Lifting surfaces generate lift by creating pressure differences between the top and bottom surfaces, disturbing the airflow in the process. The disturbances extend behind the lifting surface's trailing edge in the form of wakes which can interfere with other surfaces. Canard wake interference is likely caused by wingtip vortices, shown in Figure 6.11. While these vortices are relatively small just behind the canards, they can quickly grow in size and affect the stability of the rocket if they intersect any other control surfaces. Wake interference can also be caused by shock waves that asymmetrically intersect the rocket. This occurs when the canards are positioned at an angle of attack relative to the airflow, resulting in shockwave-expansion-fan pairs at the leading and trailing edges, illustrated in Figure 6.12. If the canards are positioned too closely to other control surfaces, the asymmetrical shockwaves cause uneven pressure distributions on said surfaces. Both shock waves and wing tip vortices may result in roll reversal, an aerodynamic phenomenon that causes the rocket to rotate in the opposite direction than what is commanded. An extensive literature review conducted by the team revealed that no amateur rocket has successfully flown a canard roll-control system without additional mitigative measures such as a spin can (fin can placed on ball bearings allowing the fins to rotate freely without causing the rest of the rocket to roll).

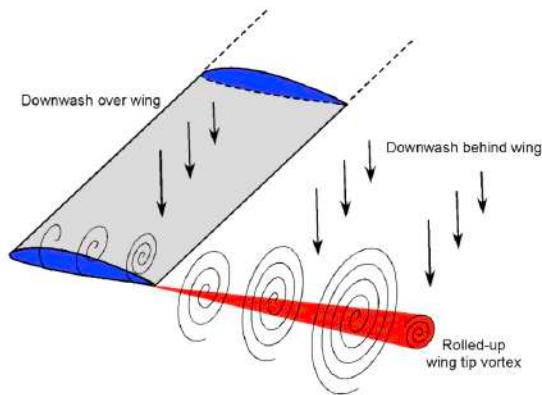


Figure 6.11: Wing tip vortices extend and grow in size behind the wing [13]

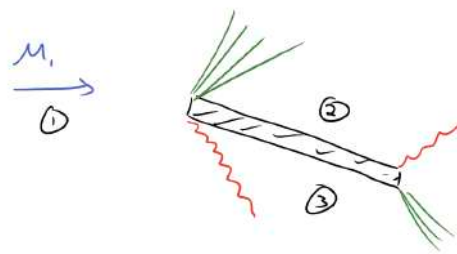


Figure 6.12: A flat plate at an angle of attack creates shockwave-expansion-fan pairs at the wing's leading and trailing edges

## 6.8.2 Aerodynamic Approach and Methodology

In 2024, the aerodynamic design of Borealis' airbrakes system was disorganized and relied too heavily on computer-based analysis. Several key issues were identified after launch including:

- Communication breakdown between the controls and flight dynamics subsystems, resulting in disorganized timelines and a general lack of understanding of the various technical aspects by different project owners.
- Over-reliance on computational fluid dynamics (CFD) for aerodynamic analysis and aerodynamic properties that were crucial for the controller system to function properly. CFD is extremely time- and energy-intensive and requires reliable real-world data to verify and support its results. Notably, the system crashed several times during crucial simulations and compressible flow was omitted from the final simulation due to human error.
- Insufficient preliminary aerodynamic analysis proving the safety of the system due to decreased time commitments from the flight dynamics subsystem and no prior established methodologies within the team for conducting comprehensive aerodynamic studies.

To avoid a similar situation with Aurora's roll-control system, key meetings in early September and October outlined subsystem roles and responsibilities, defined realistic scope and complexity, and established a rough outline of required aerodynamic analysis to demonstrate the system's safety and to size the canards for the expected flight conditions. The following is a rough timeline of decisions and events throughout the development of Aurora's roll-control system. The rest of the report is similarly structured according to the timeline.

1. **Initial design phase (September early October 2024):** Initial design meetings defined technical scope for both the flight dynamics and controls subsystems; control authority was limited to the roll axis, mechanically-linked canards were suggested, and canards were tentatively positioned in the injector section.
2. **Early aerodynamic studies (October 2024):** Aerodynamic investigations began to assess expected flight conditions, focusing on key stability and control challenges:
  - Expected roll rate study to estimate the rocket's maximum roll during flight.
  - Destructive coning study to understand pitch-roll coupling and identify contributing factors.
  - Roll reversal study to assess its causes, effects, and the potential need for a spin can as a mitigation strategy.
3. **Refinement of aerodynamic studies (end of October 2024):** The roll rate study was completed, and the spin can investigation evolved into a detailed wake interference analysis. This analysis focused on roll reversal issues caused by wing-tip vortices and shockwave interactions.
4. **Spin can requirement (end of November 2024):** The coning study was finalized; findings from the wake interference analysis confirmed the requirement of a spin can to mitigate roll reversal, regardless of canard placement on the rocket.
5. **Further aerodynamic analyses (December 2024):** Work began on calculating the lift generated by the canards and their induced angular acceleration.

6. **Repositioning of the roll-control system (January 2025):** In response to the wake interference findings and increasing integration challenges in the injector section, the roll-control system was relocated above the fuel tank to simplify assembly and reduce complexity.
7. **Finalizing canard design (mid-March 2025):** Lift and induced angular acceleration calculations were completed; canard shape was finalized. A preliminary design review was conducted to evaluate and refine the canard's size.
8. **Completion of canard sizing (mid-March 2025):** Following revisions from the design review, the canard sizing for both the Aurora rocket and its test flight vehicles was finalized.

### 6.8.3 Estimated Roll Rate

Rockets experience roll due to small manufacturing defects in a rocket's fins and/or external factors such as wind and angle of attack. With Aurora's increased speed and higher apogee, the maximum roll rate that the rocket will experience is also expected to increase.

#### Retrospective Roll Rate Analysis

In October 2024, a survey of other high-altitude rocket launches showed that most nominal launches experience roll rates between 0.5 and 2 Hz. Based on an analysis of on-board video from past Waterloo Rocketry projects, LOTS experienced a maximum roll rate around 1 Hz during boost which decreased to approximately 0.67 Hz by burnout, while Borealis experienced a steady 0.2 Hz roll rate over the first 10 seconds of flight which was exceptionally low due to its high passive stability margin.

For the purposes of sizing canards, a factor of safety equal to 3 was applied to the 2 Hz upper bound determined previously. This is due to uncertainty associated with launching a rocket into the jet stream, potential fin misalignment during manufacturing, and the risk that the spin can may not function as intended. Thus, a loose requirement was set that when the canards are set to their maximum actuation angle, they must be able to spin the rocket to 6 Hz in approximately 0.5 seconds under MaxQ conditions (an arbitrarily set time interval that ensures that the canards have sufficient control authority through the first 40 seconds of flight). This high factor of safety ensures that the canards maintain control authority under all flight conditions, including any unexpected aerodynamic behaviours the rocket may experience.

### 6.8.4 Calculating Lift

When the canards are actuated to some angle of attack, they produce lift perpendicular to the longitudinal axis of the rocket. This moment induces an angular acceleration to counter any roll the rocket is experiencing. Recall that generated lift is a function of air density  $\rho$ , velocity  $v$ , canard area  $A$  and lift coefficient  $C_L$  defined in Equation 6.10.

$$L = \frac{1}{2} C_L \rho v^2 A \quad (6.10)$$

## Subsonic Flow

Accurately calculating the lift produced by the canards is important for canard sizing. Specifically, extensive research was conducted to determine a decently accurate  $C_L$  value for the canards such that this sizing can occur. Since the controller itself does not specifically reference this lift coefficient during flight and will determine its own approximations, the focus was not on determining the most accurate  $C_L$  value, but rather on a sufficiently accurate value that captures the aerodynamic behaviour of the canard through subsonic, transonic and supersonic regions of flight as a function of angle of attack  $\alpha$ . As the canards are uncambered, early research pointed to  $C_L$  models for flat plates derived from flat plate airfoil theory and linearized subsonic flow to account for the compressibility effects of the atmosphere as velocity approaches Mach 1.0. Equation 6.11 describes  $C_L$  for subsonic compressible flow [13]:

$$C_L = \frac{2\pi}{\sqrt{1 - M^2}} \alpha \quad (6.11)$$

Given the nature of the Prandtl-Glauert factor  $\sqrt{1 - M^2}$  in Equation 6.11, this results in an asymptote at Mach 1. However, given the swept nature of the canards, flat plate theory is not necessarily accurate. Stengel's textbook on flight dynamics provides alternatives in Equation 6.12, Equation 6.13 and Equation 6.14 that account for both aspect ratio  $AR$  and compressibility effects [14].

$$C_L = \frac{\pi AR}{2} \alpha \quad (6.12)$$

for  $AR < 1$  according to slender-wing theory for any Mach number

$$C_L = \frac{\pi AR}{1 + \sqrt{1 + (\frac{AR}{2} \cos \Lambda_{1/4})^2 (1 - M^2 \cos \Lambda_{1/4})^2}} \alpha \quad (6.13)$$

for  $M < 1$  according to Hembold's equation for subsonic flow

where  $\Lambda_{1/4}$  is the sweep angle at the canard's quarter-chord

$$C_L = \frac{1.8 + AR}{1.8 + \sqrt{1 - M^2} AR} \cdot \frac{5.65}{1 + \frac{1.8}{AR}} \cdot \alpha \quad (6.14)$$

for  $M < 1$  according to Prandtl-Glauert-Gothert-Ackeret similarity rules [15]

## Supersonic Flow

Regarding supersonic flight, thin airfoil theory predicts lower  $C_L$  values that decrease as a function of the supersonic Prandtl-Glauert factor according to Equation 6.15 below. This equation however assumes a supersonic leading edge, which the team has decided against in the interest of reducing wave drag on the canards [14].

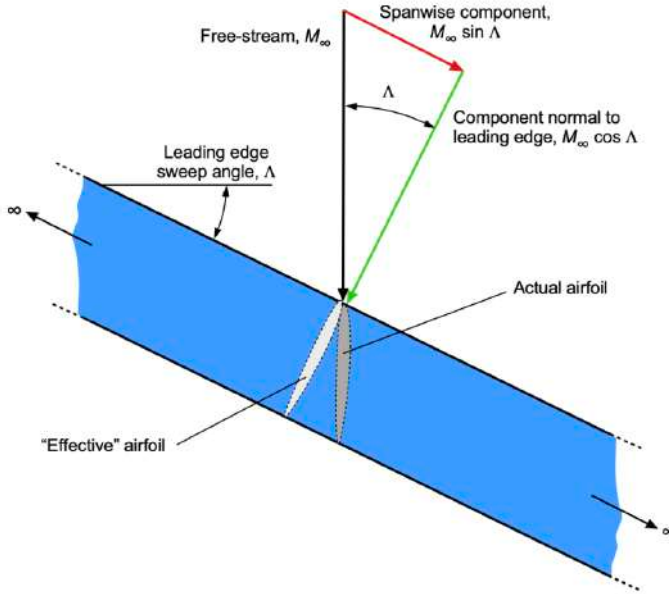


Figure 6.13: The independence principle states that only the Mach number acting normal to the leading edge affects the aerodynamics [13]

$$C_L = \frac{4}{\sqrt{M^2 - 1}} \alpha \quad (6.15)$$

For a subsonic leading edge, the supersonic flow over the canard often behaves more similarly to subsonic flow due to the independence principle that decomposes the velocity vector of the airflow into span wise and chord wise components, as shown in Figure 6.13. If the chord wise component of Mach number is smaller than 1, the canard is described as having a subsonic leading edge. Again, Stengel provides Equation 6.16 derived empirically for  $C_L$  as a function of angle of attack, sweep angle and Mach cone half-angle [14]:

$$C_L = \frac{2\pi^2 \cot \Lambda}{\pi + m(0.38 + 2.26m - 0.86m^2)} \alpha \quad (6.16)$$

$$m = \frac{\cot \Lambda}{\cot \sigma}$$

$$\sigma = \arccos \frac{1}{M}$$

It should be noted that Equation 6.16 does not explicitly account for aspect ratio or compressibility effects. However, the equation implicitly accounts for some compressibility effects through the half-angle of the Mach cone  $\sigma$  and the sweep angle  $\Lambda$ , which influence the aerodynamic load. Since delta wings have a high sweep angle and low aspect ratio, the flow generally remains more attached, and shock-induced separation is less significant, reducing the overall impact of compressibility effects. The canards were sized according to this subsonic leading edge equation because it is continuous along the Mach number range Aurora is expected to fly in. Specifically, it does

not produce the asymptote at Mach 1 which is the case for several of the equations presented earlier. Figure 6.14 plots Equation 6.16 for delta wings with varying sweep angles across multiple Mach numbers. As can be seen, this equation is also valid for subsonic flow where  $\sigma = 0$ . It is also continuous with Equation 6.15 that predicts  $C_L$  for a supersonic leading edge. No other combination of equations investigated provided a smooth transition across the subsonic, subsonic leading edge, and supersonic leading edge regimes. Other equations the team investigated, plotted in Figure 6.15, illustrate the discontinuities or abrupt changes in predicted  $C_L$  when transitioning between these flow regimes, making them less reliable.

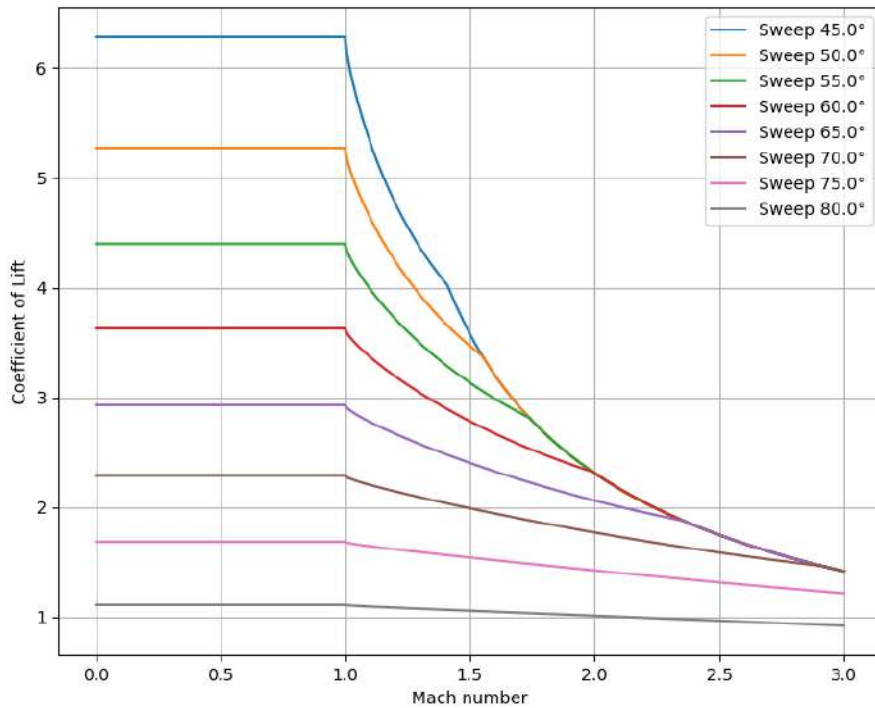


Figure 6.14:  $C_L$  as a function of Mach number and sweep angle according to Equation 6.16

The limit to Equation 6.16 is its behaviour at subsonic speeds. It is widely accepted that the lift coefficient is at least partially influenced by compressible flow as the flow approaches Mach 1. Since Equation 6.16 is constant for any velocity below Mach 1, this constitutes a small inaccuracy. Thus, to model the lift created by the canards, the team chose a hybrid approach, utilizing Equation 6.13 for subsonic flow, Equation 6.16 for supersonic flow with a subsonic leading edge, and Equation 6.15 for supersonic flow with a supersonic leading edge. Lastly, while a discontinuity is still present at Mach 1, as shown in Figure 6.15, the difference was considered acceptable given the relatively short time frame the rocket spends travelling at speeds around Mach 1.

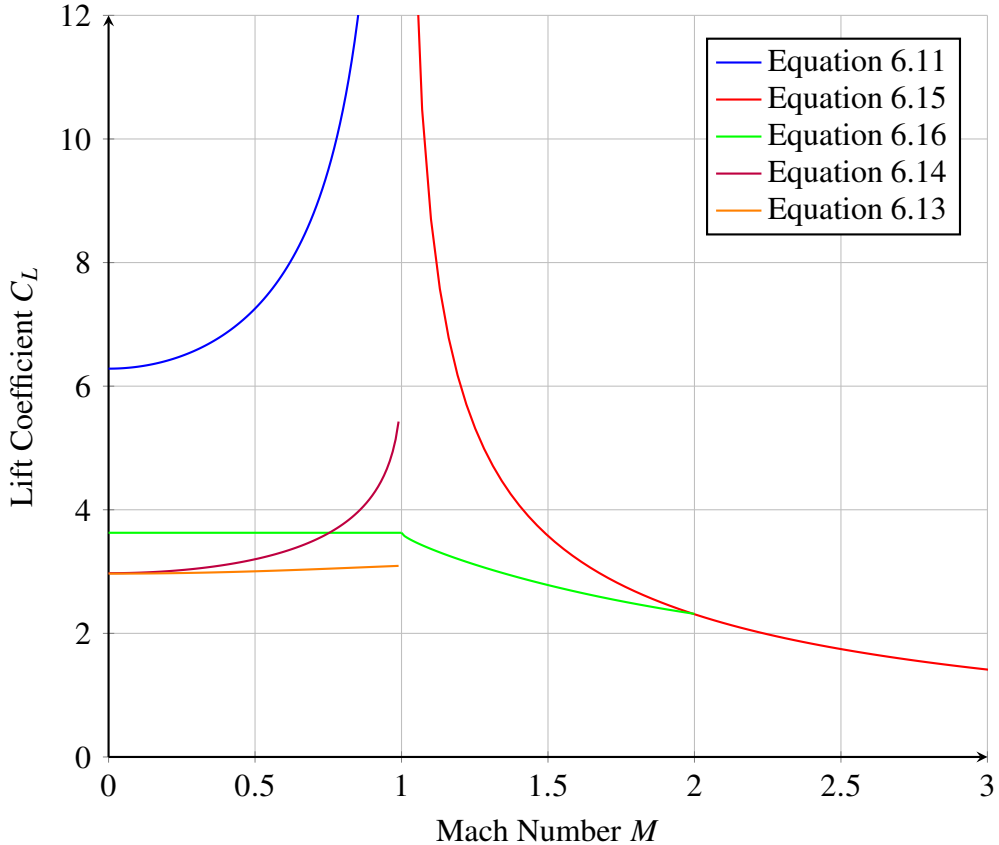


Figure 6.15: Comparison of lift coefficient models as a function of Mach number

### 6.8.5 Sizing Canards

#### Final Design Configuration

The final canard configuration is a mechanically-linked canard design positioned above the propellant tanks. The fins will have rounded leading and trailing edges with a swept delta wing design ensuring a subsonic leading edge to reduce wave drag effects. The maximum actuation angle has been set to 10 degrees, thus providing more precision to the controller. As per Launch Canada's DTEG, the canards will be activated after boost phase ends.

#### Sizing and Control Authority

Using trajectory data from an OpenRocket simulation of Aurora (time step, altitude, velocity, Mach number and atmospheric density), the estimated lift produced by the canards was plotted as a function of time. From Cycle 2 Aurora mass and CG estimates, an approximate value for the rotational moment of inertia of the rocket,  $I$ , was determined allowing the resulting angular acceleration of the vehicle,  $\dot{\omega}$ , to also be calculated according to Equation 6.17 below. The parameters in Figure 6.16 were iteratively modified until Figure 6.17 was obtained, which shows the expected duration of flight where the canards are expected to have meaningful control authority.

$$M_x = L \cdot d = I \cdot \dot{\omega}$$

$$\Rightarrow \dot{\omega} = \frac{L \cdot d}{I} \quad (6.17)$$

Using basic kinematics, the time it takes to accelerate a rocket to a given roll rate can be calculated. To minimize safety risks but ensure sufficient control authority, the canards were sized by calculating this time-to-roll-rate value for the rocket at MaxQ (highest value in Figure 6.17) assuming full canard actuation to 10 degrees. Given how quickly the rocket accelerates and decelerates, this is by far the worst-case scenario in which the canards must maintain control of the vehicle. The rocket also reaches MaxQ at motor burnout, corresponding to the region of flight where the rocket is most likely to experience roll. As shown in Figure 6.18, an average time interval was also computed to provide further context into average expected control authority over the first 30 seconds of flight (the atmosphere is too thin and the rocket is not travelling fast enough to maintain control authority after the first 30 seconds of flight). The parameters from Figure 6.16 result in a minimum time-to-roll-rate value of 0.562 s and an average value of 1 s. At first glance, this amount of control authority may seem excessive, but considering the nominal case where the canards are actuating by just a few degrees at a time, this time-to-roll-rate value quickly increases to over 5 seconds on average.

Parameter	Value	Units
Angle of attack	10	deg
Angle of attack (rad)	0.1745	rad
Chord (in)	3	in
Span (in)	3	in
Surface area	4.5	in <sup>2</sup>
Aspect ratio	2	
Lambda (rad)	1.107	rad
Lambda (deg)	63.426	deg
Surface area (m <sup>2</sup> )	0.002903	m <sup>2</sup>
Number of canards	2	
Rotational moment of inertia (dry mass)	1078.236	lb-in <sup>2</sup>
Canard distance from center	4.5	in
Canard distance from center (m)	0.1143	m

Figure 6.16: Modifiable sizing parameters

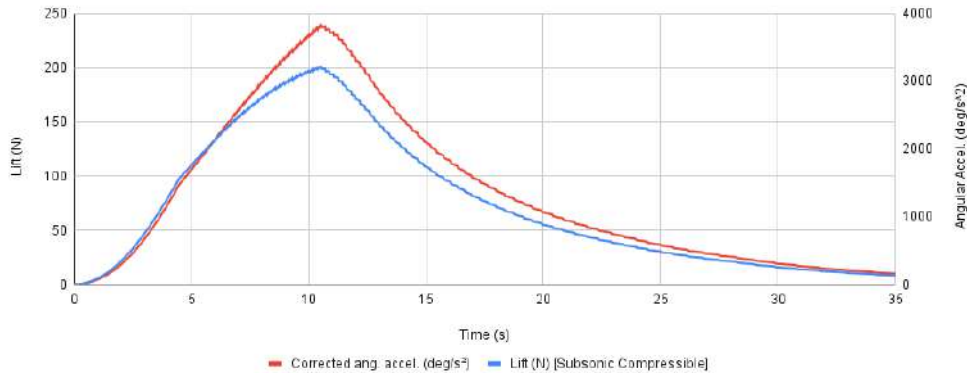


Figure 6.17: Predicted lift produced by the canards and resulting angular acceleration of the rocket as a function of time

Parameter	Value	Units
Given roll rate	6	Hz
Angle of attack	10	deg
Choose angular acceleration (AVG)	2073.4005	deg/s <sup>2</sup>
Time to dampen roll rate	1.042	s
Choose angular acceleration (MAX)	3840.13	deg/s <sup>2</sup>
Time to dampen roll rate	0.562	s

Figure 6.18: Time-to-roll-rate minimum and average values

Following a design review where the aforementioned control authority was approved internally by the team, four design variants were proposed that modified root chord length and sweep to varying degrees. The selected design for Aurora is shown below in Figure 6.19. The standard delta-wing design was slightly modified by slanting the trailing edge, making it less likely for the parachute rigging to get caught on the canards in the event that the rocket tips over before the recovery system is deployed. The centroid and 60% root-chord-line are also indicated.

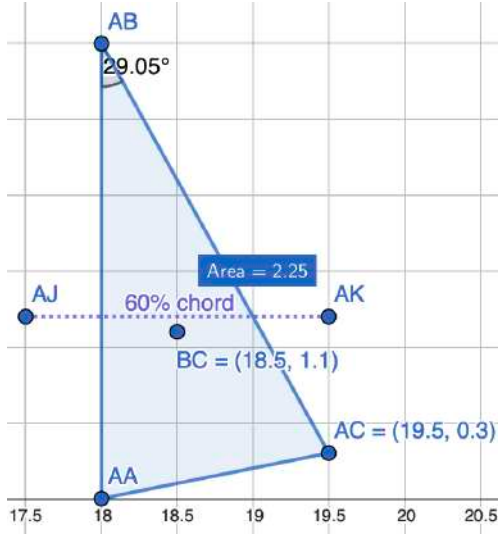


Figure 6.19: Proposed canard designs

Lastly, flutter analysis was also conducted on the design to determine the minimum thickness required for the canards. To improve manufacturing timelines, the analysis was conducted using 0.125 in and 0.1875 in aluminum plate that can be easily water jet. Using Equation 6.7, a flutter FOS was calculated for both thickness options. To account for the fact that the canards are mounted to a shaft with a 0.67 in diameter, a requirement was imposed that the flutter FOS be larger than the root chord-to-shaft diameter ratio. Considering the dimensions of the final design, this ratio is equal to  $3 \text{ in} / 0.67 \text{ in} = 4.5$  and the predicted FOS for the 0.1875 in aluminum plate is 6.144, thus satisfying this requirement.

## 6.9 Painting

The effect of surface finish on the apogee of the rocket was first considered in 2023 when optimizing the rocket for a 30 000 ft apogee was a primary requirement. At the time, going from a regular paint finish (0.787 mil) to a smooth paint finish (2.36 mil) could result in an apogee difference of 2 200 ft. While intuitive in retrospect, this is an astronomical difference. For comparison, a similar apogee increase would require a vehicle dry mass reduction of 13% (11lbs).

For LOTS, the painting process was extremely time- and labour-intensive, but yielded extremely successful results. As such, Borealis required a new approach. The previous procedure involved using diluted paint to paint one layer, then sanding it smooth with 800-grit sand paper, and repeating that for anywhere from three to five coats per colour. Due to the large surface area of the airframe, this was a very time consuming process. In total around a 150 working hours were

spent on painting with a few team members solely dedicated to this for a few weeks. Sanding was by far the most time-consuming operation of this process. This is obviously not desirable.

With this in mind, the team focused on minimizing the amount of sanding involved in painting for the current rocket. After multiple rounds of testing methods, it was concluded that spray paint was an acceptable way to paint the rocket. With spray paint, each layer could be applied evenly and thick enough that there was no need to sand in between each layer, nor was there a need for more than 2 coats of each colour. This significantly reduced the amount of drying time and halved the number of days it took to finish painting each part. With these results in mind, the painting team drew up a procedure for the entire process, detailed as follows:

1. Sand all the body tubes to 800 grit to ensure a smooth surface for paint application.
2. Apply a base coat of white paint of around 5 layers. Wait for 30 to 40 minutes between each layer of base coat.
3. Apply the first layer of base coat as a tack. No need to cover the entire surface of the body tube. Just enough so that the next layer has a surface to stick to.
4. Apply next 4 layers until a thick finish is achieved.
5. Wait 24 hours for the base coat to cure.
6. Sand last layer of base coat with increments from 800 grit to 2000 grit to obtain smooth base for further application of colour layers.
7. Apply colours coat and use stencils as per the paint scheme. Each colour should have 5 to 6 layers but if they seem inadequate and there is fear of sanding chipping away the paint to reveal base coat, then add 1 to 2 more layers as a precaution.
8. Wait for 24 hours for the colour coat to cure.
9. Remove any stencils. You should feel a subtle bump when you run your finger along the seam where the stencil was placed. This is expected.
10. Sand from 800 grit to 2000 grit to obtain a smooth and lustrous surface finish. Pay extra attention at the seams where the stencils were placed, intend to make them uniform.

The process outlined above yielded successful results for Borealis while noticeably decreasing labour time. This year, Aurora will be painted following the same procedure. However, more emphasis was placed on the complexity of the paint design in order to decrease labour time even further. Notably, the gradient designs on Borealis took several days to perfect. As such, the selected design for Aurora, shown below in Figure 6.20, utilizes several stripe patterns to mimic gradients while simplifying the painting process.

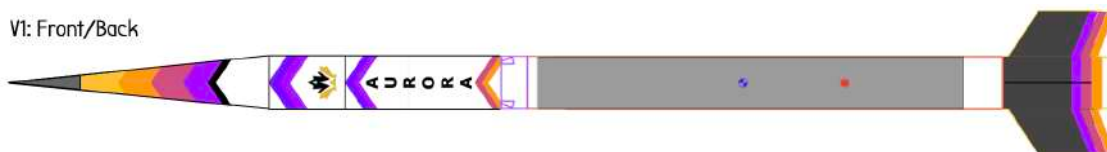


Figure 6.20: Selected paint design for Aurora

## 6.10 Current Simulation Results

Following a successful static fire in May 2025, a new RSE engine file was developed to inform vehicle simulations. Based on the results from Cycle 2.5, the simulation results for a nominal launch are listed below in Table 6.5:

Apogee (ft)	48 282
Off-Rail Velocity (ft/s)	152
Maximum Velocity (ft/s)	2 334
Off-Rail Stability (cal)	2.678
Maximum Stability (cal)	5.738
Apogee Stability (cal)	4.786

Table 6.5: Cycle 2.5 Nominal launch OpenRocket simulation results

The results above are averaged results from over 600 simulations based on compiled historical weather data from August 2023 and August 2024 for Timmins, ON. More information regarding historical weather data and Monte Carlo simulations can be found below in subsection 6.11. These results were calculated for temperatures between 5°C and 25°C with an average pressure of 990 mbar. Similar results are obtained when simulating the rocket with a constant wind speed of 15 mph.

Following a successful flight-representative static fire on July 19, 2025, the team is in a position to develop a more accurate and representative RSE file. Unfortunately, this RSE file was not developed in time for this report. Based on preliminary data, the results show a lower peak thrust of approximately  $11 \pm 1$  kN which will likely result in a lower apogee. Propellant mass will also be adjusted such that the rocket's off-rail velocity, stability and TWR are suitable for launch.

## 6.11 Dispersion Zone Analysis

The OpenRocket plugin developed internally and described in subsubsection 6.4.3 is capable of running both Monte Carlo simulations of the rocket and exact simulations based on historical data.

The historical data was obtained from [16], an open-source weather API that uses historical data from thousands of weather stations and sensors around the world to interpolate accurate weather conditions for nearly any region of the globe. Hourly wind data from August 2023 and August 2024 was collected and processed into a .csv file, each line containing the relevant parameters to describe a unique simulation. Data was filtered to exclude weather conditions outside of the typical launch window and data points where cloud cover was higher than 50%. The resulting .csv file contains over 600 multi-level wind simulations with 17 different wind layers from 110 m to 22 000 m.

Using this data, all 623 entries were simulated for all three launch cases: nominal, main-at-apogee, and ballistic. Unfortunately, due to an unresolved issue as of the writing of this report, dispersion for the two off-nominal cases could not be simulated. Additionally, an error in the initial launch coordinates has caused an offset in the data. However, Monte Carlo simulations were successfully simulated for all three cases, and the results are plotted below in Figure 6.21. The simulations were run using OpenRocket's multi-level wind function, a launch rail angle set to 5°

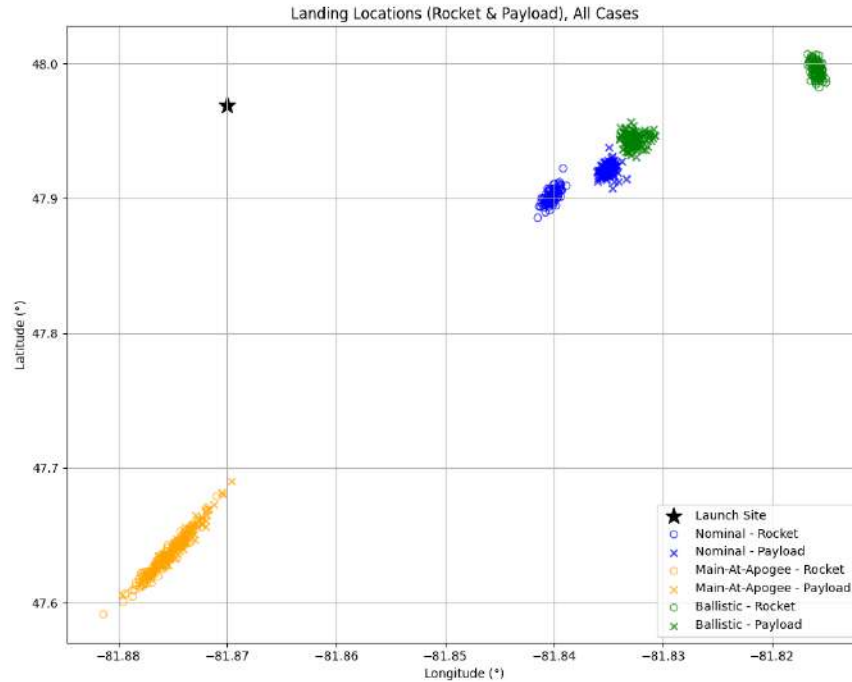


Figure 6.21: Cycle 3 preliminary Monte Carlo dispersion analysis for nominal and off-nominal cases

and a launch rail direction set to  $93^\circ$  relative to North (i.e.  $3^\circ$  south of East). As shown below, both nominal and ballistic cases fall within the Launch Canada boundaries with an average dispersion distance of 7 km and ranging from 5 – 10 km.

The main-at-apogee case is highly dependent on wind direction and the results plotted are not considered entirely accurate because the multi-level wind inputs are based on an average of all 623 historic entries for each layer. As such, the specific historical entries once plotted are expected to be more scattered. Furthermore, the results from Figure 6.21 must be interpreted with a grain of salt as single simulations from OpenRocket also do not line up well with the Monte Carlo simulated dispersion. With that said, preliminary results for the main-at-apogee case indicate a medium-to-high likelihood of the rocket landing outside the Launch Canada's recovery area.

## 6.12 Launch Commit Criteria

As mentioned in subsection 6.10, the team's simulation results are out-of-date as a new static-fire-informed RSE file has not been developed yet. As such, the team is not in a position to include a detailed table of launch commit criteria. However, based on the results from Cycle 2.5, the rocket can safely launch in wind speeds less than 20 mph while ensuring an off-rail stability greater than 1.5 cal. It is of note that RASAero predicts sufficient stability in wind conditions higher than 20 mph.

## 7 AEROSTRUCTURE

### 7.1 Overview

Aerostructures on Aurora can be subdivided into composite and metallic components. The former includes the majority of the outer airframe. The latter includes the oxidizer tank, couplers between bodytubes, and the longerons. The upper composite sections of the airframe (nosecone, recovery bay and avionics bay) are made from fibreglass, allowing radio transparency for the telemetry electronics. The lower sections (oxidizer tank aft skirt and fincan) are made from carbon fibre, as it possesses a higher strength-to-weight ratio allowing for more optimal fin construction. The Aurora aerostructure breakdown can be found in Table 7.1.

Component	Stacking Sequence	Fabric Used
Nosecone	[45/90/-45] <sub>2</sub>	Vectorply E-Glass Weft Triaxial Fibreglass (E-TTX 2300)
Recovery Bay	[45/90/-45] <sub>3</sub>	Vectorply E-Glass Weft Triaxial Fibreglass (E-TTX 2300)
Avionics Bay	[45/90/-45] <sub>3</sub>	Vectorply E-Glass Weft Triaxial Fibreglass (E-TTX 2300)
Oxidizer Tank Aft Skirt (OTAS) Fairings	[90, 0, 45, 0]	10HS Fibreglass Cloth, 2x2 Twill Double Bias A&P Carbon Fibre, Textreme 80 Spread Tow Carbon Fibre
Fincan/Combustion Chamber Bodytube	[45 <sub>3</sub> , 0]	Composites Canada 10HS Fibreglass Cloth, A&P 6" OD Braided Carbon Fibre Biaxial Sleeving, Textreme 80 Spread Tow Carbon Fibre
Fins	[45 <sub>6</sub> , 0]	2x2 Twill Double Bias A&P Carbon Fibre, Textreme 80 Spread Tow Carbon Fibre

Table 7.1: Overview of composite aerostructure components

A vacuum-assisted resin transfer moulding (VARTM) process was used to manufacture all composite parts, with the exception of the fincan tip-to-tip, which uses a wet layup. In this process, flat fibreglass or carbon fibre plies are laid out in a female mould with small amounts of Super 77 adhesive to hold them together. Then, the part is placed under vacuum with resin allowed to flow from one end of the mould to the other. Once the part is entirely soaked in resin, it is left to cure under vacuum.

All SRAD composite parts on Aurora were post-cured after manufacturing. The parts were placed in an insulated oven and held at specific temperatures to increase the glass transition point of the epoxy. Care was taken to not go above the temperature limit prescribed by the data sheet, for Airstone 780E + 786H this is 90°C. The oven and composite parts are shown in Figure 7.1.



Figure 7.1: Composites in curing oven

## 7.2 Moulds

With the change of diameter from 6" to 8", new moulds were required for Aurora. A set of moulds for the nosecone and the bodytubes were necessary to account for this change of diameter, as well as a modified nosecone geometry. The design and construction of these moulds is identical to the previous, smaller set. Layers of medium density fibreboard were attached with wood glue into four separate blocks, creating 4 mould halves. The profile of the parts were cut on a router and sanded until smooth. Finally, the moulds received a coating of Duratec primer to create a durable surface. The moulds were aligned using Polytetrafluoroethylene (PTFE) pins to prevent adhesion. The completed nosecone and bodytube moulds are shown in Figure 7.2.



Figure 7.2: Completed nosecone (left) and bodytube (right) moulds

## 7.3 Nosecone

The nosecone geometry was optimized for the predicted flight regime of the rocket. Aurora is expected to fly in the transonic and supersonic regime, so a conic shape with a 5:1 fineness ratio

was selected, as explained in subsubsection 6.7.2.

The nosecone tip was machined entirely from stainless steel, a decision that was made considering aerodynamic heating concerns, as further explained in subsubsection 6.7.6. This decision was also made to shift the centre of gravity of the nosecone further forward, matching the centre of gravity of a previous nosecone launched on a test flight vehicle in May 2025. Aurora's nosecone houses a deployable payload (section 13) and is designed to separate entirely from the vehicle at apogee. The payload contains its own independent recovery system, and is retrieved with the nosecone separate from the main rocket. The nosecone recovery system was successfully tested on the aforementioned test flight.

The nosecone was manufactured using two plies of E-TTX 2300 fibreglass sheeting inserted into the female nosecone moulds, wrapping fully around, before being vacuum bagged and infused with resin. After post-curing, an aluminum tip spacer was bonded to the top of the nosecone and an eye bolt was inserted through the spacer and screwed into the steel nosecone tip, securing the tip.

## 7.4 Bodytubes

The team's SRAD composite bodytubes aim to be superior to COTS bodytubes in four ways: cost, time, geometry and weight. SRAD bodytubes do not need to be shipped, reducing their cost. Removing the need for shipping reduces lead times significantly, allowing for greater flexibility in manufacturing. Furthermore, in-house bodytubes provide the team with more control over their required dimensions. Finally, SRAD bodytubes can be made thinner in accordance with design safety margins, decreasing their weight.

Along with the benefits of SRAD tubes comes uncertainty. Testing was planned this year to characterize the properties of SRAD composites. This was more relevant than in previous years, as this year saw a switch in the main fibreglass fabric used by the team. Unfortunately, due to a compressed schedule, no testing was completed on the flight tubes for Aurora. Consequently, there was a lack of data informing the required thickness for the bodytubes. However, considering the epoxy in the bodytubes was identical to that of past years, and the new fibreglass sheeting showed equal or better strength properties than the previous, the decision was made to consider past years' testing data to inform the thickness of this year's tubes. Additionally, the tubes and nosecone were made much thicker than previously to account for this discrepancy in accurate data (close to 2 mm wall thickness).

With the increased size of the team's newly manufactured moulds, all fibreglass bodytubes for Aurora were cut from the same composite part. Figure 7.3 below shows the carbon fibre tube (used for the fincan and OTAS panels) along with the fibreglass nosecones and bodytube.

## 7.5 Parachute and Avionics Bays

The upper section of the vehicle underwent major changes compared to the team's previous rockets; the payload moved from the upper bodytube to the nosecone, and the control system is attached directly to the vent bulkhead assembly. As a result, the upper body tube was shortened and was renamed to the avionics bay. The parachute bay contains the rocket's parachutes; the main and the drogue. It is located forward of the recovery bulkhead, and is pressurized during recovery deployment. The tube for the parachute bay is pictured alongside the avionics bay in Figure 7.4.



Figure 7.3: SRAD composite parts (from left to right): Fincan tube, nosecones, avionics/parachute bay tube



Figure 7.4: Avionics (left) and parachute (right) bays

## 7.6 Oxidizer Tank Aft Skirt

Similar to previous rockets, the oxidizer tank aft skirt contains three structural aluminum longerons to transfer compressive and tensile loads between the combustion chamber and the rest of the rocket. Specifically, the longerons are designed to transmit loads to the oxidizer tank fill bulkhead and combustion chamber injector bulkhead. The section is enclosed by a non-structural, carbon fibre fairing for aerodynamic performance. The fairing contains an opening for the fill disconnect mechanism. The rocket electrical umbilical connector is also embedded in one of the fairing panels.

### 7.6.1 3D Printed Longerons

The team has worked previously with the Multi-Scale Additive Manufacturing lab (MSAM) at the university to design and manufacture the fill bulkhead for LOTS (Figure 7.5), using a laser powder bed fusion (LPBF) process [17]. Based on the success of this project, MSAM was willing to work with the team again to develop and print both the longerons and injectors (discussed further in subsubsection 8.3.1) for Aurora. Both the longerons and injectors were printed from AlSi<sub>10</sub>Mg, the same alloy used for the fill bulkhead.



Figure 7.5: LOTS fill bulkhead

One important feature of the LOTS fill bulkhead design was the integrated longerons. To shorten the total length of the machined longerons, longeron-like structures were integrated into the bulkhead. Because of the printing process, the internal geometry of these structures could be made much more complex than the uniform cross-section used for the machined version. A lattice structure with further topology optimization on the top face, (Figure 7.6), was selected.

Borealis flew with machined longerons, but the team continued work on an independent printed longeron design for future vehicles. For Aurora, the design was mature enough to be pursued for flight, with machined longerons as a backup. Figure 7.7 shows the injector section, in which the longerons are mounted. Unlike the LOTS longerons, these longerons are asymmetrical along their length, since the upper and lower bulkheads to which they mount have two different diameters and mountings.

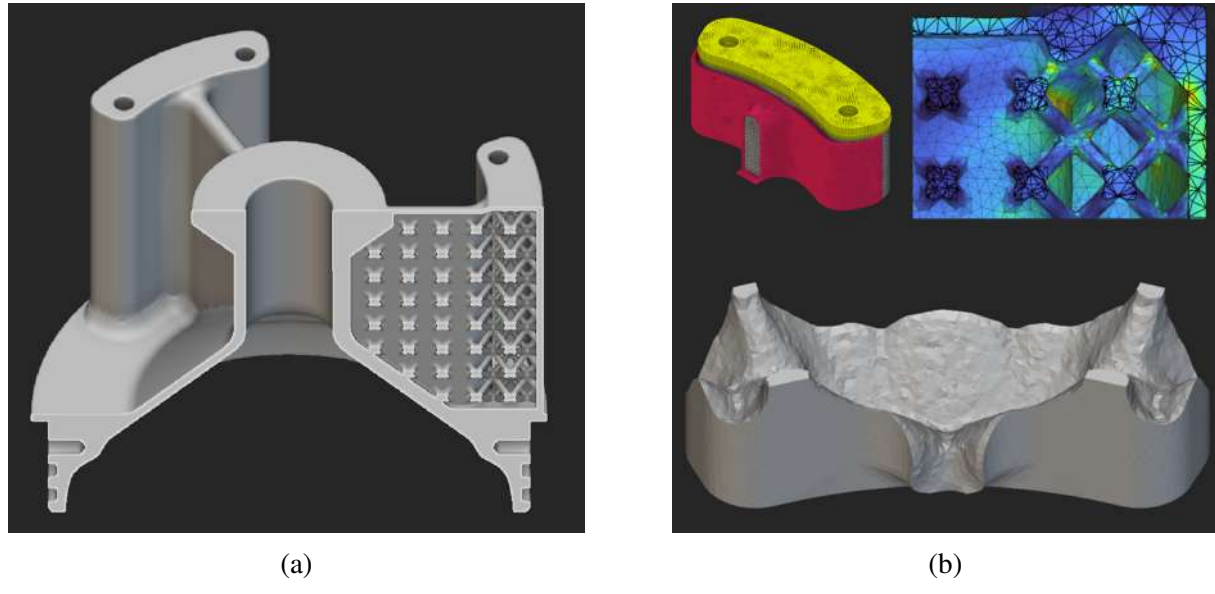


Figure 7.6: Internal longeron structure on the printed fill bulkhead. (a) Initial BCC lattice structure. Stress concentrations and unprintable overhangs are present at the top face. (b) Topology optimization of top face area using a 45-degree overhang constraint resolves the stress and overhang issues of the original lattice.

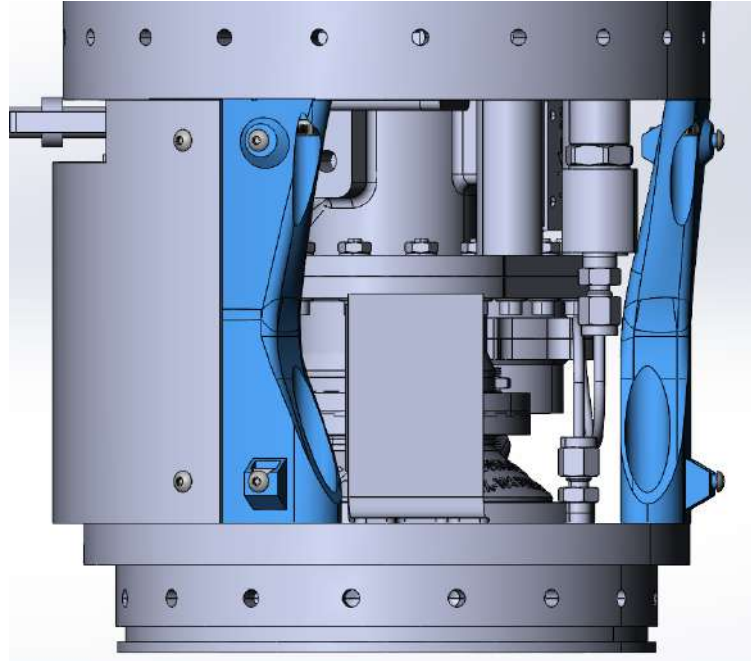


Figure 7.7: Aurora injector section assembly; longerons are highlighted in blue. Note that the top coupler has a wider diameter than the bulkhead at the bottom, resulting in eccentric loading on the longerons.

Slots with T-nuts were used to mount the fairing panels, eliminating the need to thread the longerons. The surface roughness of the print recipe provides an acceptable mounting face as-printed. Combined, this means that no post-machining of the longerons is required, and they can be cut from the build plate and installed directly in the rocket. Because steeper overhangs have been well characterized, these T-nut slots make use of a number of steep, 30 degree overhangs to reduce material use and therefore weight.

The design optimization workflow is based on a research case study completed by Z. Mears [18]<sup>1</sup> and was performed as follows:

- Starting from the initial outer CAD geometry developed for the symmetrical LOTS design case by Mears [18], the design was adjusted to match the new length and mounting locations for Aurora.
- The majority of the design effort was then devoted to design of the fairing mounting features.
- Once the design of the outer geometry was complete, it was imported into nTop [19], a design-for-additive-manufacturing software package. Minor adjustments and fixes were quickly made to inputs to account for the geometry change and new loads.
- The software then automatically followed the procedure of running an initial stress simulation, computing a shell based on those results, applying latticing and design tweaks for printing, and finally simulating the performance of the final design. Minor tweaks were made, such as adjusting reference planes and other features that had not been well generalized to any input. In addition, the stress vs. thickness function used to generate the functionally graded shell is somewhat input dependent, so required a few iterations of tweaking values to produce good results. Despite these minor fixes and adjustments, the majority of the workflow simply re-calculated a new design without intervention, resulting in a manual, iterative optimization process that took many minutes instead of many hours.

Stress and buckling simulations for the final design of the printed longerons are shown in Figure 7.8. The final mass of the Aurora printed longerons is 113 g per longeron, representing a 59% reduction in weight compared to the conventionally machined design.

With the updated design complete, the longerons were then printed. Figure 7.9 shows the longerons after being de-powdered.

---

<sup>1</sup>A detailed description of this workflow has not been included as at the time of writing this research is pre-publication and is under an embargo

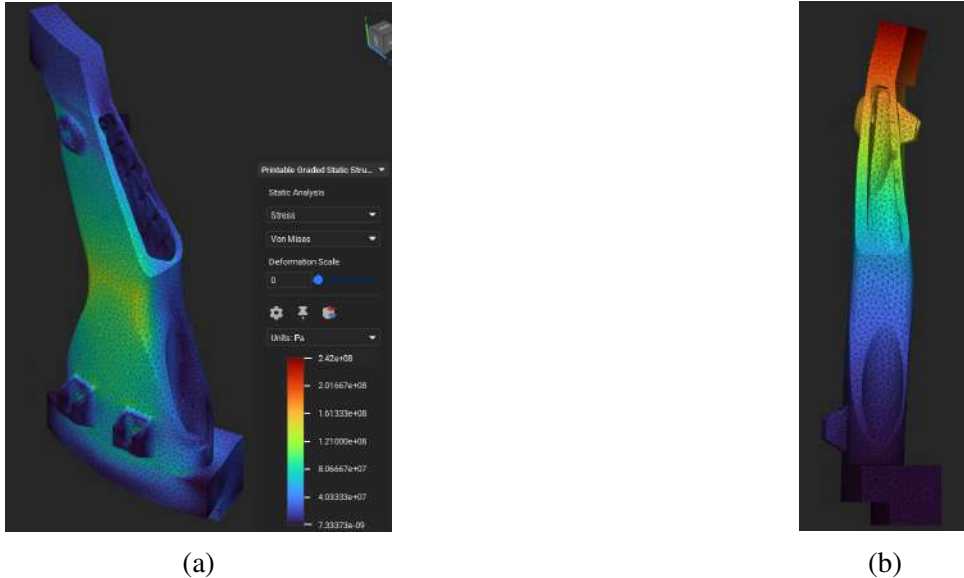


Figure 7.8: Printed longeron stress simulations with section view: (a) Von Mises stress analysis result. (b) First buckling mode based on linear buckling simulation. Buckling load factor is 7.99.



Figure 7.9: Printed longerons on the build plate after de-powdering.

### 7.6.2 Fill Disconnect Hatch

The fill disconnect hatch is a mechanism covering the fill disconnect opening in the OTAS panels. It allows the fill barb to interface with the QD valve and closes after fill disconnect is actuated, immediately before takeoff. The assembly consists of a 3D-printed frame and hatch door, compression springs, guiding dowel pins, and neodymium magnets to hold the panel closed during

flight.

Unlike designs on previous rockets, the hatch does not incorporate hinges, due to limited clearance both internally and externally. Instead, the door is recessed slightly within the rocket's outer profile to better accommodate the mechanism's geometry while minimizing parasitic drag.

The hinged mechanism has been replaced with a vertically actuated spring-based system. During filling, the hatch door remains in a compressed state (Figure 7.10a) beneath the fill disconnect tube. Upon disconnection, the compression springs drive the door upward to seal the opening (Figure 7.10b). Precision dowel pins embedded in the frame guide this vertical motion to ensure alignment and repeatability. As an added precaution, aluminum safety plates were integrated into the design to prevent potential interference between the arms of the fill quick disconnect and the hatch mechanism. To enhance structural integrity, both the interior and exterior surfaces of the 3D-printed hatch door are reinforced with carbon fibre layups, ensuring the assembly can withstand aerodynamic forces during flight. Once deployed, the door sits flush with the top surface of the hatch frame, just beneath the coupler, and is held in place by embedded magnets to maintain closure throughout ascent.

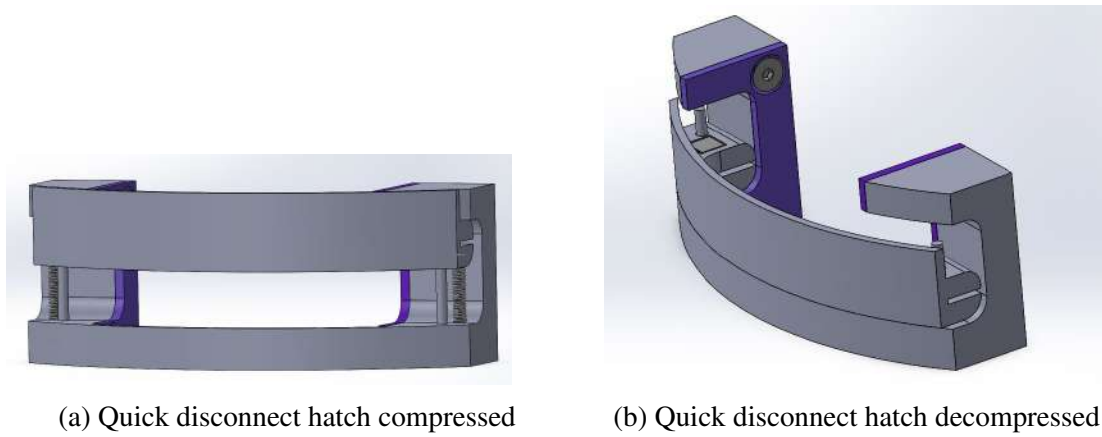


Figure 7.10: Quick disconnect hatch

## 7.7 Fincan

The purpose of the fincan is to provide passive stability to the rocket during flight. It consists of composite fins bonded to a composite tube, with metallic doublers at either end. The fincan is the most complex composite structure on Aurora, in terms of both function and manufacturing. The structure is made up of a carbon fibre bodytube, whose manufacturing process is described in subsection 7.4. The fins were bonded to the base tube using epoxy before being wrapped in additional carbon fibre layers. In previous years, the fincan has been held fixed relative to the surrounding airframe. This year, the fins are able to freely rotate relative to the main structure. Considerations on the purpose and requirements for this joint, as well as the shape and size of the fins, can be found in subsubsection 6.7.3. The remainder of this section discusses the composite structure and metallic joints.

### 7.7.1 Fin Manufacturing

The fins were cut from SRAD 0.25 in carbon fibre plate stock. The number of carbon fibre layers for the plate was determined through examining past infusions and from the layer thickness provided with the material (1 layer = 0.01 in when infused). A 4 ft × 8 ft glass table was used as the moulding surface and was prepped with eight layers of mould release wax. 25 layers of 194 gsm 2x2 carbon fibre twill were sandwiched between peel ply using minimal Super 77 spray adhesive on the moulding surface (Figure 7.11). A top layer of infusion mesh was placed under the vacuum bag, which was then sealed with gum tape. The plate was then infused with Airstone 780E + 786H.



Figure 7.11: Fin plate infusion

The fins were cut from the finished plate using a waterjet, which has historically provided the best results for cutting composite plate. The cut fins are shown in Figure 7.12



Figure 7.12: Fins

## 7.7.2 Fin Bonding and Filleting

After being prepared and cleaned, the fins were bonded to the bodytube using Aeropoxy ES6228. A two-part wooden jig (Figure 7.13) was used to maintain alignment, and was held together using spacer pieces to prevent unintended movement during curing. All fins were bonded in one session and left to cure before sanding.



Figure 7.13: Bonding jigs

The joints between the fins and tube underwent light sanding before epoxy fillets measuring 1.5 in in diameter were added to each root. The fillets form the desired shape around the fin roots, but also provide additional strengthening to the fins to mitigate fin flutter. Airstone 780E + 786H was used to create the fillets, with Cabosil filler used to increase the viscosity of the epoxy. A wooden dowel was used to form the 1.5 in fillets, which were left to cure before hand-sanding (Figure 7.14).

## 7.7.3 Tip-to-Tip Layup and Post-Processing

The tip-to-tip layup is the largest manufacturing step of the fincan, which involves placing layers of fabric from the edge of one fin, across the tube, and to the edge of the next. To achieve the desired fin thickness (0.375 in), the layup consisted of seven layers of 194 gsm 2x2 twill and one layer of Textreme 80 gsm. The twill forms the structure of the layup while the Textreme creates a smoother surface finish. The number of layers in the tip-to-tip is typically only two to three, as the inner plate is stiffer than those added in the layup. However, given the increased thickness of Aurora's fins, it was decided to do a thicker layup on top of a thinner plate. This decision was made to prevent the formation of resin voids and air bubbles that are more likely to form when infusing very thick pieces.

Each layer of fabric was wet out using Airstone 780E + 786H between plastic sheeting and placed onto the fincan (Figure 7.15). The first ply was laid between two fins and care was taken to prevent any bridging or air gaps. The fincan was then rotated 90° and the same process was repeated until all 7 layers had been laid up. Lastly, a layer of Textreme was added at the end. Peel ply, perforated plastic and breather cloth were layered on top. The peel ply acts as an easily removable barrier to the rest of the layup, while the perforated plastic allows for even airflow



Figure 7.14: Sanded fillets

around the part. The breather cloth soaks up much of the excess epoxy that is pulled out. The layup was finally vacuum bagged to pull out any excess epoxy and obtain a better fibre volume fraction, then left to cure for three days. The final part is shown in Figure 7.16.



Figure 7.15: Tip-to-tip layup

After removal from the vacuum bagging, excess material was trimmed from the fincan before sanding. Material on the edge of the fins was sanded until the core plate was reached. Bondo body filler was applied to smooth out any wrinkles in the fabric, before final rounds of sanding to prepare for painting.

#### 7.7.4 Boattail and Spin Can

As discussed in subsubsection 6.7.3, a spin can has been implemented for this year's rocket. To facilitate this, an interface was designed between the boattail and the fincan that allowed the components to spin freely relative to one another, hence "spin can". The goal was to mimic a bearing by using the boattail and the traditional fincan as bearing races to allow for rotation about the longitudinal axis.

Initial designs developed with a focus on thrust bearings, as the rocket would mainly experience axial loads. An example cross-section is shown in Figure 7.17. The bottom component is the boattail, and it differs from a traditional boattail as it contains a rectangular profile that acts as one of the races. The wall on the right represents the fincan bodytube. A ring is bonded to the inside of the fincan using epoxy (the "interface") and a bolted cap attaches to the interface to fully enclose

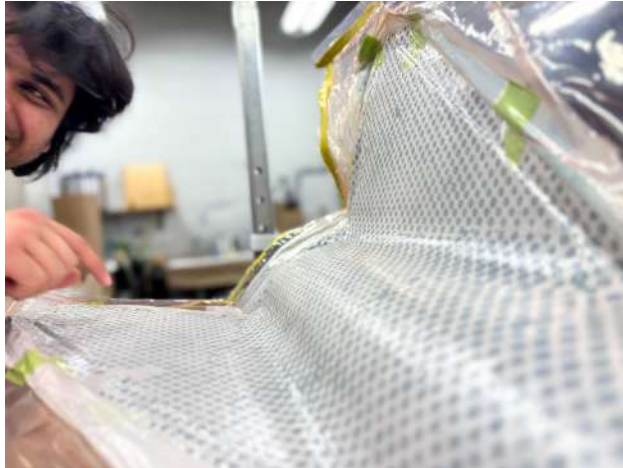


Figure 7.16: Vacuum bagged tip-to-tip

the bearing. Other variations of this design used cylindrical rollers, but it was quickly determined that there was not ample space available to use rollers.

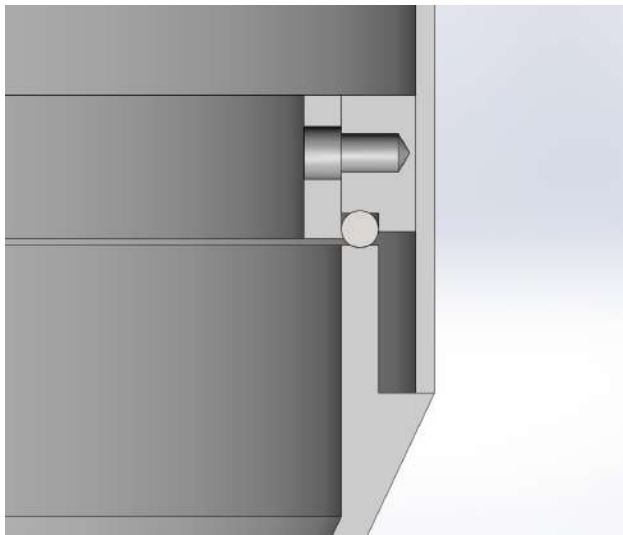


Figure 7.17: Spin can initial design

Another initial consideration was the profile of the races, as shown in Figure 7.18. Traditional bearings use curved race profiles to distribute the load across the contact area, but curved profiles are significantly harder to manufacture. At the time of the initial proposal, it was not clear whether or not the boattail would be machined in-house or could be sponsored. Therefore, other proposed profiles were a flat and chamfered profile. Flat profiles have precedence in spin cans that have been flown previously [20], and chamfered profiles have a larger contact area for force distribution and are not as difficult as curved profiles to manufacture.

After preliminary design review, several design requirements were set:

1. Curved profile to allow to prevent stress concentrations
2. Geometry to prevent clumping of bearings

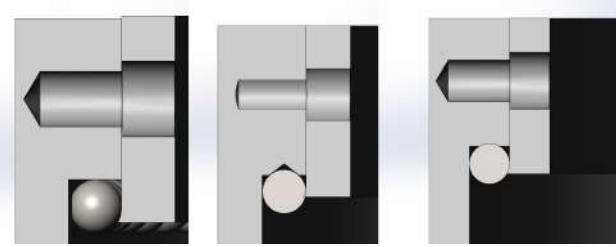


Figure 7.18: Candidate bearing race profiles

3. Bearings must be fully enclosed in boattail
4. Bearing must support some (lesser) shear load in addition to axial loads

Having the bearings fully enclosed in the boattail means that the design must be able to house the bearings without the presence of the fincan, and that the bearings should not spill out prior to assembly. With these requirements, a new design was proposed, shown in Figure 7.19. The isolated boattail is shown in Figure 7.20.



Figure 7.19: Iteration 2 assembly cross-section

The boattail in this design contains slots which confine the movement of the bearings to a specific area, preserving the bearing spacing. Slots are also present on the cap component. A cage design was initially considered to accomplish the same goal, but major concerns were present regarding the structural integrity of a potential cage since the bearings were already small at 0.125 in. A cage would have been extremely thin and was considered not viable.

This design, however, had a number of problems after prototyping and testing. A 3D-printed version was created to test the geometry, but the boattail failed to retain the bearings without the presence of the fincan. It was unclear whether this was due to poor design or printing tolerances. At this point, the project timeline was a significant concern. As such, the requirements for the spin can were revisited and the design was greatly simplified to allow for easy manufacturing and integration.

The requirement for having the boattail fully retain the bearings was removed, and a flat race profile replaced the curved one. The resulting design is shown in Figure 7.21.

The cap was removed as it was no longer required for bearing retention. The races remain as the interface and the boattail, but radial movement is confined by the interface and the outer surface of the combustion chamber. Kapton tape was wrapped around the inner circular face of



Figure 7.20: Iteration 2 boattail



Figure 7.21: Spin can final cross-section

the interface to prevent friction during spin with the combustion chamber. The main drawback for this design is the resulting thicker boattail, as the geometry is required for the bearing race surface. However, with aluminum being lightweight, it is not predicted to cause issues with stability.

## 7.8 Couplers

The entirety of the airframe is connected using metal couplers that are bonded to each end of the bodytubes. The team also makes use of machined rings ("doublers") that are bonded into the tube prior to the couplers. The couplers and doublers are made of 6061-T6 aluminum and fastened using 1/4"-28 radial button head cap screws. All joints are fastened using six bolts, except the nosecone-recovery bay joint and avionics aft-tank joint. The former is held together by six plastic shear pins and the latter uses eight bolts rather than six to provide additional stiffness. Having a standard joining interface between bodytubes simplifies the design and also minimizes damage to the parts during assembly and disassembly. Radial patterns are chosen for their simplicity to machine with the tools available in the student machine shop. Other joint types, like radax joints, have been considered but ultimately rejected due to their machining and assembling complexity.

Joint design is driven primarily by two constraints, geometry and structural need. It is also to a lesser extent driven by ease of machining, ease of assembly, and similarity to joints used historically on the team.

### 7.8.1 Geometry

The primary joint type used on the rocket is a composite/metal joint. This involves an outer composite part and an inner aluminum part. Typically, there is also a doubler bonded into the composite. The doubler serves two purposes. The first is to maintain circularity. The second is expanded upon in subsubsection 7.8.2. There is also one joint on the rocket which connects the upper recovery section to the rest of the vehicle. It involves an outer metal ring bonded to the aft end of the joint (Avionics Forward Coupler), a centre aluminum ring bonded to the forward end of the joint (Recovery Aft Coupler), and an inner recovery bulkhead used to hold all recovery electronics and seal pressure inside the recovery bay. This is as seen in Figure 7.22

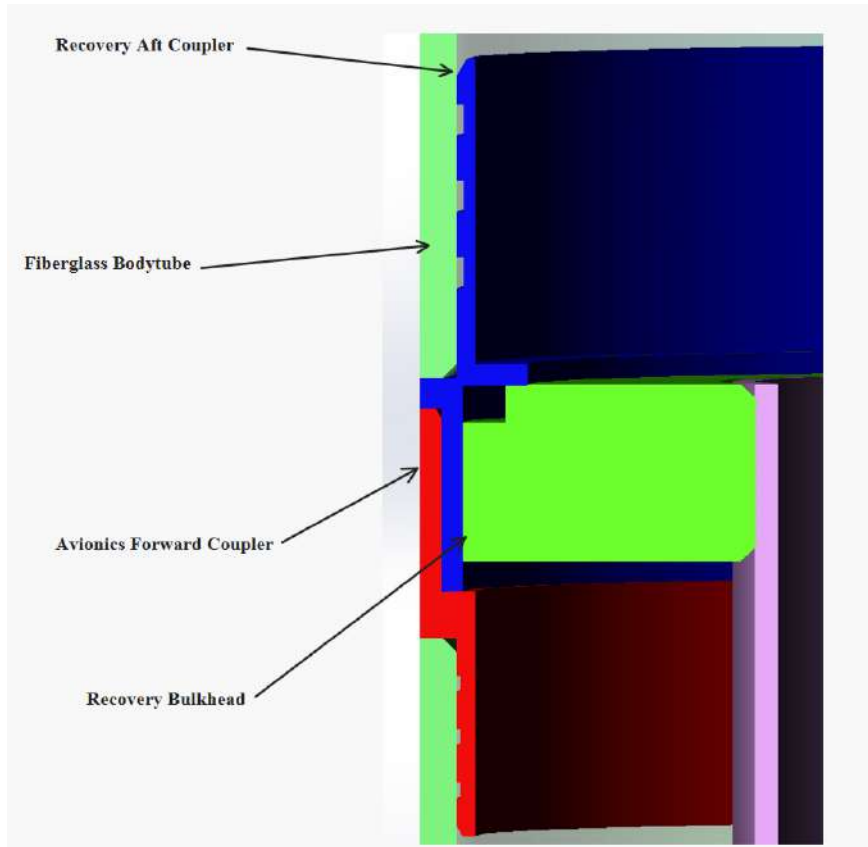


Figure 7.22: Recovery Aft/Avionics Forward Interface

Geometry of a joint is designed first, typically by iterating on sketches. The key parameters to address are:

- What is the diameter of the tube sections, and is there sufficient clearance to mate them?
- Will the designed joint be simple to machine with the available tools?
- Will everything entering through this side of the bodytube be able to fit past the designed joint?
- Does the team have experience or reference material for making this joint?
- If the team decides this joint is unsuitable down the line, how can it be adapted?

- Where can this joint be weight optimized or strength optimized?

After developing the joint profile, structural analysis can begin.

### 7.8.2 Structure

Failure modes of coupler joints are always failure around the bolt circles, due to increased stress concentrations and because the bolt circles have the least amount of material compared to rest of the joint, and therefore bearing failure and tearout failure at takeoff, MaxQ, and recovery deployment are the limiting cases. A minimum of FOS 2.0 is targeted for all cases. For information on how the team develops those load profiles, see subsection 6.6. For metal/metal joints, the analysis is relatively straightforward, as the bearing and shear strengths of aluminum are well understood. However, for bolts bearing directly on composite, the bearing and shear strength of the composite is less well understood or consistent. Therefore, as well as being effective for maintaining circularity, the doubler must be capable of handling the full load of the vehicle independent of the composite in all three load cases.

Inputs to the structural analysis of the joints are the geometry of the joint, as well as the load inputs described in section 6.6. For takeoff and MaxQ, the axial and bending load and the given geometry are converted to a bearing and shear stress, taking the bearing area to be the thickness of the joint multiplied by the minor diameter of the bolt and the shear area to be twice the thickness of the joint multiplied by the distance from the bolt to the edge of the coupler. Dividing the bearing yield strength and shear strength of the material by the bearing and shear stresses experienced by the joint gives the factor of safety, which is kept above 2.0. In the recovery deployment loading case, an axial force of approximately 1050 lbf acting on the entire dry mass below aft of that joint is assumed. The specific geometry of the joint is then designed by tuning the inner and outer diameters of the parts until they are above FOS 2.0 for all load cases. Although the factors of safety are calculated for each kind of loading, shear loads are not considered to be significant since their magnitude is drastically smaller than the axial force and the bending moment that is experienced by the rocket. This can be seen in Figure 6.3. Finally, to conduct the loads analysis, the bending is modelled as an additional axial load in tension/compression.

A complete list of all load-bearing coupler geometries and safety factors can be found in Table 7.2. Note that the failure point of all joints on Aurora is either bearing failure or tearout failure on parachute deployment. The only exception to this is the vent section joint, where the failure point is bearing failure on launch. This is due to the fact that there are 8 bolts at this joint instead of 6. Aerodynamic loads were not considered for the tank bulkheads, since they are negligible compared to the tank pressure. This is expanded on in subsubsection 8.4.1.

Coupler	COD (in)	CID (in)	CED (in)	Position (in)	Min. FOS
Recovery Aft Coupler	7.86	7.72	0.07	49.0	4.24
Avionics Forward Coupler	8	7.86	0.07	49.0	4.24
Vent Doubler	7.75	7.63	0.06	70.0	70

Table 7.2: Coupler geometries and safety factors

### 7.8.3 Manufacturing and Bonding

All couplers were machined on a manual lathe. All mating surfaces were machined to fit wherever possible. Interfaces between metal and composite components were permanently bonded in place using West Systems 105/206 epoxy resin and left to cure for at least 24 hours. Radial holes were then drilled on a rotary table. This machining and bonding process has been used since 2019 and has never seen an in-flight failure since it was implemented (3 total flights).

# 8 PROPULSION

## 8.1 Overview

Eridium V2 is Waterloo Rocketry's second flight-ready liquid bipropellant rocket engine. To attain the apogee target of 50 000 ft, this engine is designed to deliver more thrust and impulse than Eridium V1, which propelled Borealis to 19 212 ft in 2024. It features a larger feedsystem and improved ablative performance. V2 uses the same propellant combination as V1, nitrous oxide ( $N_2O$ ) and ethanol, to reduce the scope of changes to the propulsion system architecture. A P&ID of the Aurora rocket and GSE is shown in Figure 8.1.

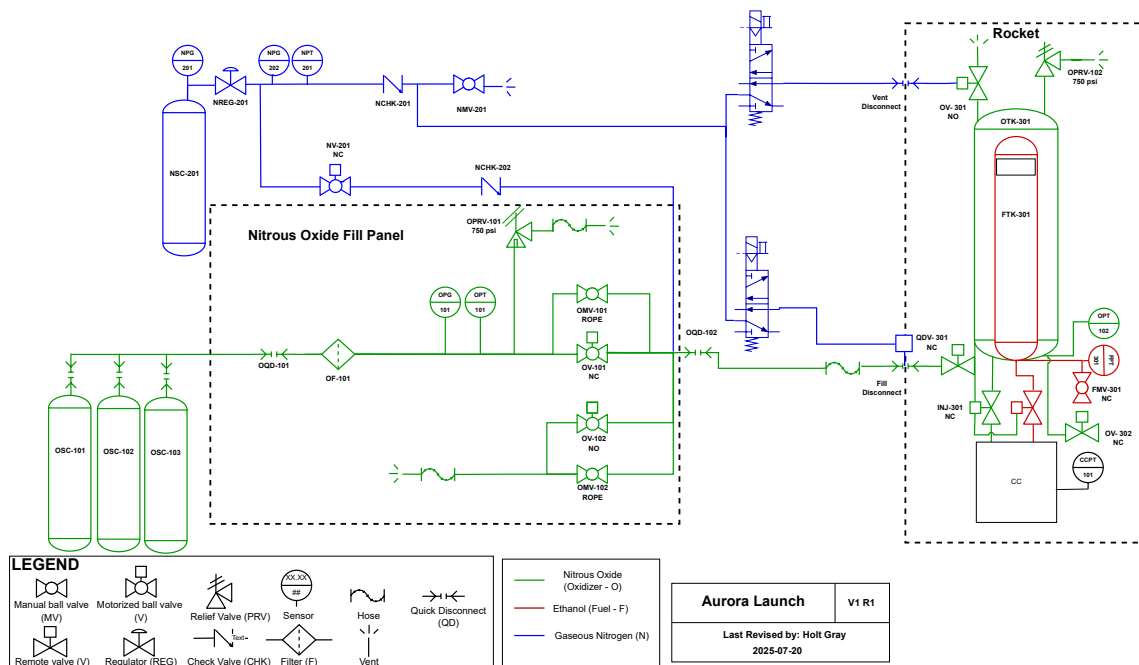


Figure 8.1: Aurora P&ID

The goals of Eridium V2 are to achieve the thrust targets set in subsection 6.2, and to create an architecture that can be scaled up for even larger engines. As such, the focus this year was on improving ablative regression and simplifying feedsystem plumbing. The latter is achieved through nitrous-piloted injector and fill valves, and ground-side actuation of the remaining valves. This improves serviceability while reducing integration complexity and electrical scope. Key engine parameters are summarized in Table 8.1. Experimental parameters are based on the results of the most recent static fire.

Parameter	Value
Oxidizer	44.6 kg N <sub>2</sub> O
Fuel	10.3 kg Ethanol
Impulse	82 000 Ns
$c^*$ efficiency	0.966
Burn averaged $I_{sp}$	194 s
$I_{sp}$ efficiency	0.895 <sup>2</sup>
Thrust (peak)	11 kN
Thrust (sustained)	10 kN
Burn duration	9 s
O/F ratio	3.4 (initial), 2.65 (burn average)
Oxidizer tank pressure	650 psi
Chamber pressure	325 psi (peak), 260 psi (average)
Chamber length	20 in
Chamber OD	6.375 in
Chamber wall	0.125 in
Nozzle geometry	15° Conical
Throat diameter	2.71 in
Expansion ratio	3.75
Characteristic Length ( $L^*$ )	47.5 in

Table 8.1: Key engine parameters

## 8.2 Combustion Chamber

### 8.2.1 Combustion Chamber Layout

The combustion chamber (CC) is made from an ablative liner that slots inside an aluminum tube, which acts as the pressure vessel. The assembly is shown in Figure 8.2. The liner is retained on one end by the injector bulkhead and on the other end by a retaining ring. The nozzle is a graphite insert around which the ablative liner is layered. For mass optimization, the last 1.5 in of the diverging section is also made of ablative material, not graphite. The exit of the CC is post-machined all at once to ensure a smooth nozzle exit and a consistent half-angle of 15 degrees.

### 8.2.2 Nozzle Exit

The nozzle exit was made from COTS Garolite LE flat stock. The exit was bonded onto the graphite, and high-temperature RTV gasket maker (Permatex 26BR) was applied to all interfaces. The main drivers for material selection of the nozzle exit were availability and cost, because of tight timelines and budgets leading up to ELSF5. Of the options available on short notice, linen

---

<sup>2</sup> $I_{sp}$  efficiency is lower than would be expected given the  $c^*$  efficiency and nozzle geometry. This is attributed to nozzle losses from damage to the exit geometry during the burn. Efficiency should increase for the flight engine due to process improvements in the manufacturing of the combustion chamber ablatives



Figure 8.2: Combustion chamber cross-section



Figure 8.3: Split retaining ring

phenolic was the better choice because the linen has a finer weave and thus better pyrolysis for effective charring and removal of heat from the CC. The entire assembly was post-machined to finish the geometry of the nozzle exit. For this design, the retaining ring was a split ring held in by 8 bolts and 8 stainless clearance fit pins, shown in Figure 8.3. It was necessary to split the retaining ring due to space constraints from integration with the spincan assembly.

### 8.2.3 Custom Ablative Development

Initial engine tests for Eridium V2 were conducted with an epoxy-based ablative mixture consisting of phenolic micro-balloons, boric acid, and West Systems epoxy. This mixture, based on Half Cat Rocketry's Chambersafe material [21], regressed 0.125 in throughout a 5 s burn during Eridium Liquid Static Fire 4 (ELSF4). Figure 8.4 shows the residual ablative post-burn. Since the epoxy mixture made up part of the nozzle exit, this dramatic change in geometry resulted in a significant loss of engine efficiency and is not acceptable for longer burns and larger engines than those flown on Borealis.



Figure 8.4: Regression of ELSF4 ablative

The most recent engine test of the Eridium V2 engine, ELSF5, used a 5.5 in ID, 0.063 in wall COTS fibreglass tube bonded to a graphite nozzle insert. A wet layup was done over the tube using 13 plies of triaxial fibreglass and Aerodux Resorcinol resin. It was then cured under vacuum at room temperature. Figure 8.5 shows the state of the phenolic fibreglass post-cure.

The OD of the completed ELSF5 CC was 6.25 in and the SRAD phenolic fibreglass layer was 0.25 in thick. Throughout the burn, pieces of fibreglass melted into beads that were expelled at high speed from the nozzle. Fibreglass residue is visible on the graphite nozzle exit, shown in Figure 8.6a. There was a thin layer of ablative left over at the end of the burn, but a combination of the weak composite structure (due to heat soak into the material and voids formed during the

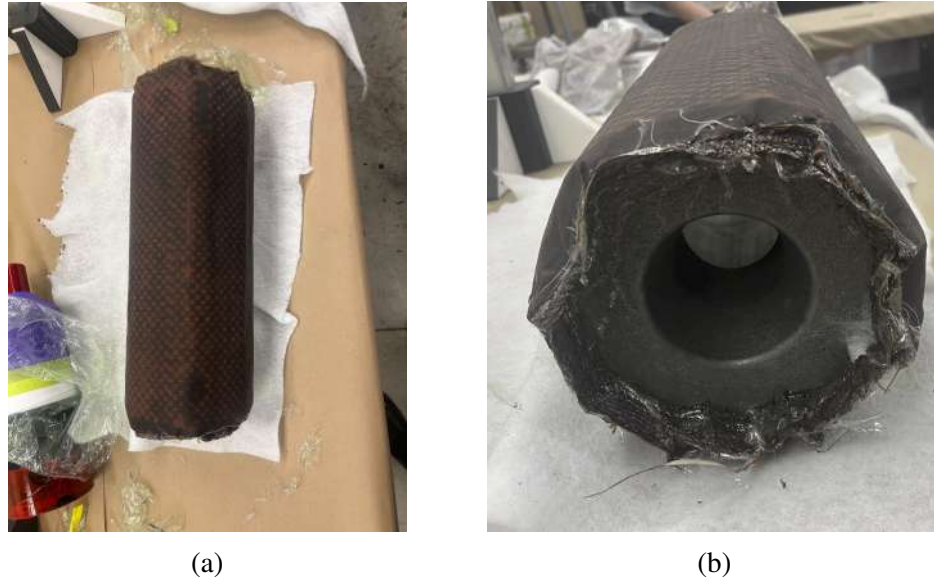


Figure 8.5: Phenolic fibreglass layup after room temperature cure

curing of the layup), sudden loss of chamber pressure and the post-burn CO<sub>2</sub> purge of the system caused the leftover ablative to cave in. The fibreglass matrix that remained after the burn consisted of material that was completely charred through (Figure 8.6b), indicating that the material failure was caused by voids and imperfections from the layup process rather than the phenolic resin being inadequate at the operating temperatures. Additionally, the phenolic exit sheared off at the bottom plane of the retaining ring, as shown in Figure 8.6a. This was a result of there being 0.24 in of ablative material in that area, slightly thinner than other parts of the engine. Despite the issues with ablative performance, the aluminum casing of the combustion chamber survived the 9 s burn intact (Figure 8.7).



Figure 8.6: (a) Fibreglass beads on nozzle exit post-ELSF5; (b) Char formation in phenolic fibre-glass ablative



Figure 8.7: Aluminum CC casing after 9s burn

Further design and process improvements are planned for the flight CC to improve ablative performance. The CC OD will be increased to 6.375 in to accommodate extra ablative thickness. Additionally, the SRAD layup will undergo a heated cure to ensure it cures well. Instead of fibreglass, the plies will be 2x2 Twill Double Bias A&P Carbon Fibre pulled tight over the mandrel to minimize void formation. Carbon fibre has the advantage of a higher strength-to-weight ratio and lower coefficient of thermal expansion. Additionally, whereas fibreglass forms glass beads as it melts, carbon fibre becomes a char layer that insulates the outer layers. These improvements in the ablative design should result in lower ablative regression during flight and lower peak temperature in the aluminum tube, helping to preserve the structural integrity of the fincan.

### 8.2.4 Ignition Puck

The ignition puck borrows heavily from previous hybrid engine igniters. The igniter sits in the combustion chamber and uses a modified version of Richard Nakka's RNX propellant, with the burn rate modifiers removed to keep the burn rate slower. The igniter is bonded directly to the COTS fibreglass tube, approximately 1.5 in below the face of the injectors to minimize heating of that surface. Ignition is achieved through 2 redundant Nichrome wires that are cast directly into the surface of the RNX. Speaker wire is run from the Nichrome out of the nozzle to the ground support equipment. The only significant change that has been made from 2023's ignition system is that the Nichrome was moved from being 2 distinct coils to being wrapped around the inner diameter of the igniter. This style of ignition puck has successfully ignited the last five liquid engine static fires that have been conducted.

## 8.3 Injectors

### 8.3.1 Injectors

For Eridium V1, the team developed a coaxial swirl injector design using modified COTS brass nozzles. While sufficient for that engine, it presented significant manufacturing challenges, and it was difficult to achieve a reliable seal between the elements and the plate they were brazed into. The initial injector design for V2 used a set of hypodermic needles brazed into brass plates to direct the fuel flow, with a small annular gap in the injector face around these needles providing the metering orifice for the oxidizer. The planned assembly, shown in Figure 8.8, was comprised of over 50 parts. While small-scale brazing tests showed some success, no reliable process was achieved that would allow all elements to be brazed successfully into a larger plate without blockages or other defects.

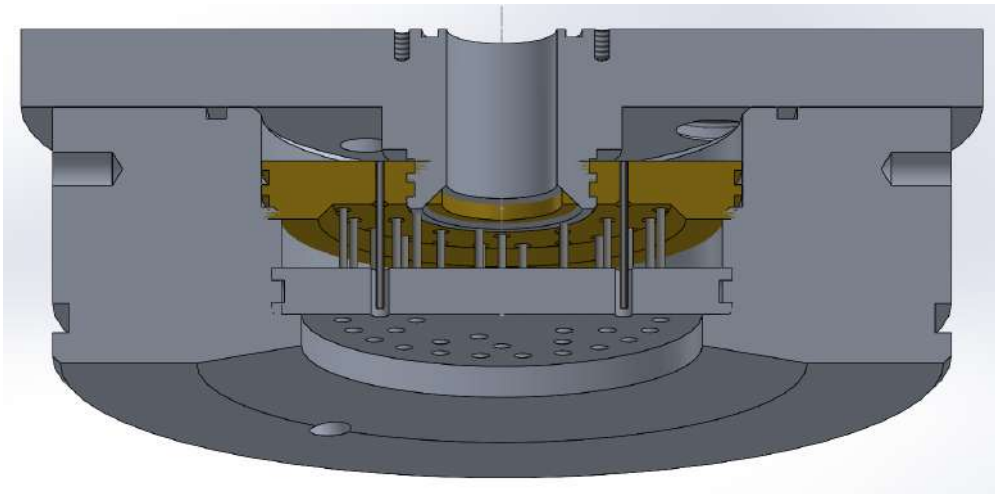


Figure 8.8: Initial brazed injector concept. 55 hypodermic needle tubes are brazed into a brass plate to form the fuel injector. These tubes pass through holes in a lower plate, forming an annular gap for oxidizer to flow through. A series of O-ring seals are used to ensure propellants don't mix.

To mitigate these difficulties, an alternative injector design leveraging metal additive manufacturing was developed with the help of MSAM (see subsubsection 7.6.1).

The injectors are printed from AlSi<sub>10</sub>Mg. The use of an aluminum alloy with a melting temperature of 590 °C for use inside a combustion chamber with temperatures exceeding 2000 °C may seem counterintuitive, but the relatively high thermal conductivity of aluminum alloys combined with the high flow rate of cool propellants through the injector mean that a number of aluminum injectors have been successfully developed for much more powerful rocket engines [22]. This alloy had the best available characterization data on its mechanical properties and surface roughness, which were vital to the project [18]. Crucially, this alloy is also materially compatible with N<sub>2</sub>O.

To achieve the target fuel and oxidizer flow rates, 0.9 mm diameter fluid channels were required. Research into AlSi<sub>10</sub>Mg printing suggested that channels of this size could be printed reliably, within a reasonable tolerance and without significant flow obstructions [18]. Figure 8.9 provides an overview of the channels as designed and printed.

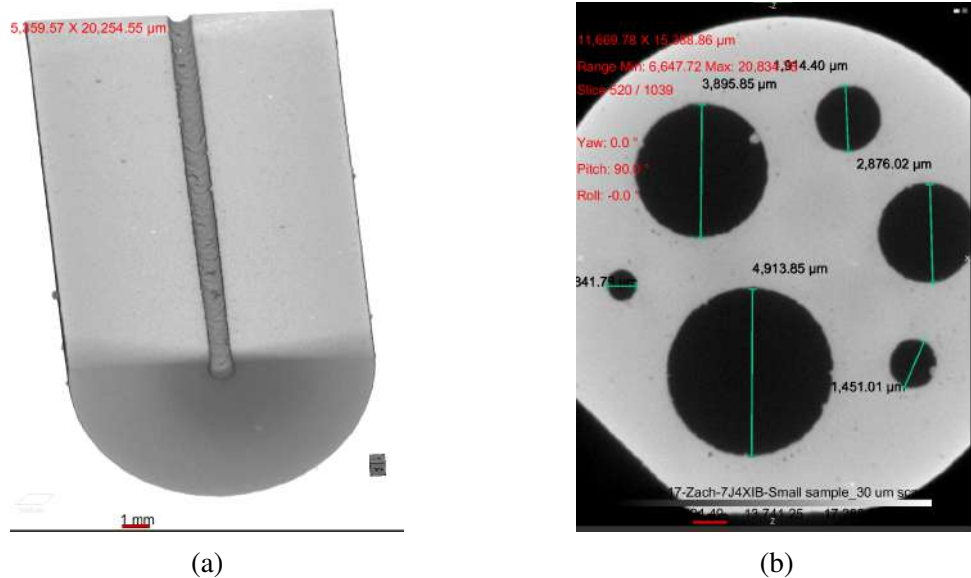


Figure 8.9: CT scan results for small diameter fluid channels. (a) Cross-section of 1 mm as-designed channel 25 mm long. While some spatter is present, overall the channel is very uniform and free of concerning obstructions. (b) CT slice of sample showing measurements of all tested diameters.

A number of design improvements were made to the brazed design to leverage additive manufacturing capabilities. The largest change was switching from a co-axial shear injector to a more efficient like-like impinging injector. In this design, each element consists of two fuel holes and two oxidizer holes. The fuel and oxidizer hole pairs are angled towards themselves, causing the fuel to impinge on itself and atomize, while the oxidizer does the same. The impingement causes the propellants to atomize individually. Each pair of elements is angled inwards, causing the streams of unlike atomized propellants to impinge on each other and mix. Figure 8.10 shows a computational fluid dynamics (CFD) simulation of the injector to help visualize the flow.

The printed injector design consolidates numerous components. The two inter-propellant O-ring seals are eliminated, which removes leak points that could result in premature mixing and the destruction of the engine. A total of 21 injector elements, each with two fuel and two oxidizer holes, are incorporated into the 4 in diameter injector.

The injector experiences considerable heat flux from the combustion gases, and is reliant on the propellant flowing through it to avoid melting. To ensure sections of the injector further from the orifices are well cooled, a series of regenerative cooling channels are incorporated into the design. Fuel flows through the injector as follows: Fuel enters through a port on the side of the injector, where it is split into three streams. One stream runs to the inner ring of the injector where seven of the elements are located. The other two streams run to the outside of the injector to feed the other 14 elements. The outer streams feed into the primary fuel manifold, where the flow is distributed before flowing into 14 cooling channels that run near the injector face. After passing through the outer cooling channels, the flow passes into the secondary outer fuel manifold, before then being injected into the engine via the fuel orifices. Meanwhile, the inner fuel flow is split seven ways into the inner cooling channels, where it runs near the injector face before entering the inner fuel

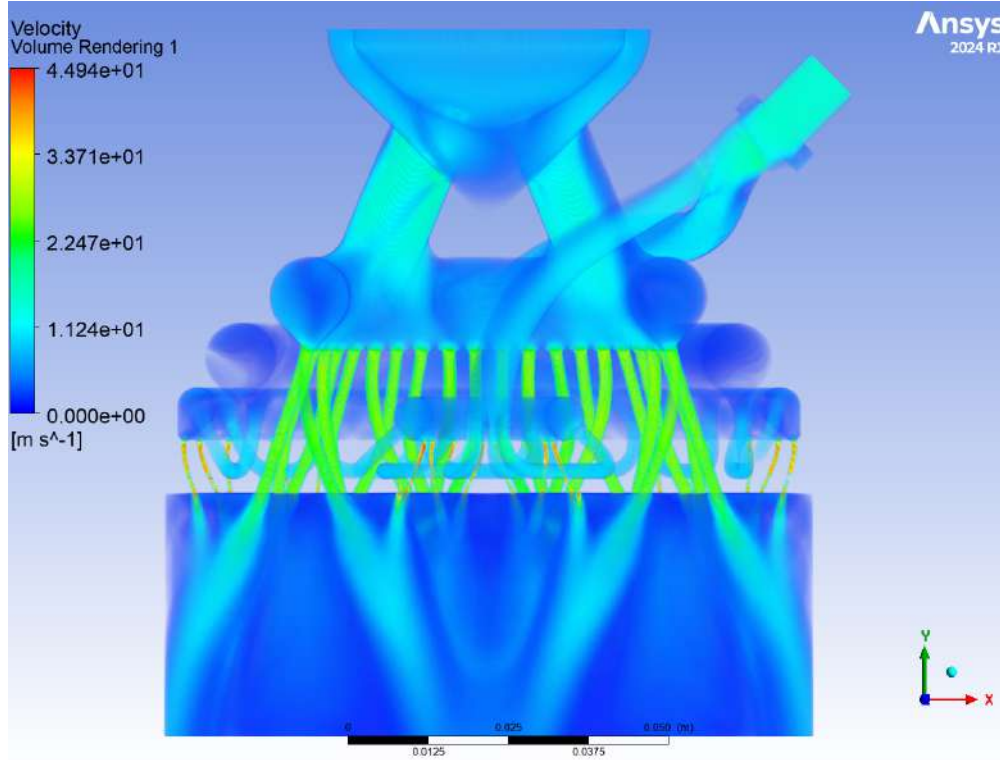


Figure 8.10: CFD flow visualization of printed injector. Oxidizer enters from the top of the injector, while fuel enters from a port in the upper right corner of the image. The rectangular volume at the bottom of the image is the combustion chamber, and the fuel and oxidizer can be observed impinging on one another.

manifold, and is subsequently injected into the engine.

An important secondary effect of these manifolds and cooling channels is to ensure that fuel is evenly distributed to every element to prevent hot spots that could burn through the engine, a potential risk for the brazed design. To ensure that fuel distribution between the inner and outer rings was even, CFD simulation was used to iterate on the fuel inlet geometry as shown in Figure 8.11.

Once the design was completed, two copies of the injector were printed, shown in Figure 8.12. Two slightly different orifice sizes were used to ensure one would provide the required flow rates based on experimental testing. After the injectors were removed from the build plate, they were post-machined to add the required O-ring grooves and threads. A set of cold flow tests (Figure 8.13) were conducted, using liquid CO<sub>2</sub> and water as analogues for nitrous oxide and ethanol, to confirm the flow rates through the injector. The injector was integrated into the engine, and a static fire test (ELSF4) was conducted. The engine performed well, operating smoothly with no significant combustion instability, and achieved high combustion efficiency. The cooling system worked as intended and the injector did not melt. The injectors again performed as expected during ELSF5.

### 8.3.2 Injector Bulkhead

The injector bulkhead holds and seals the injectors against the combustion chamber, shown in Figure 8.14. As such, it features a split ring that bolts in two halves around the injector manifold.

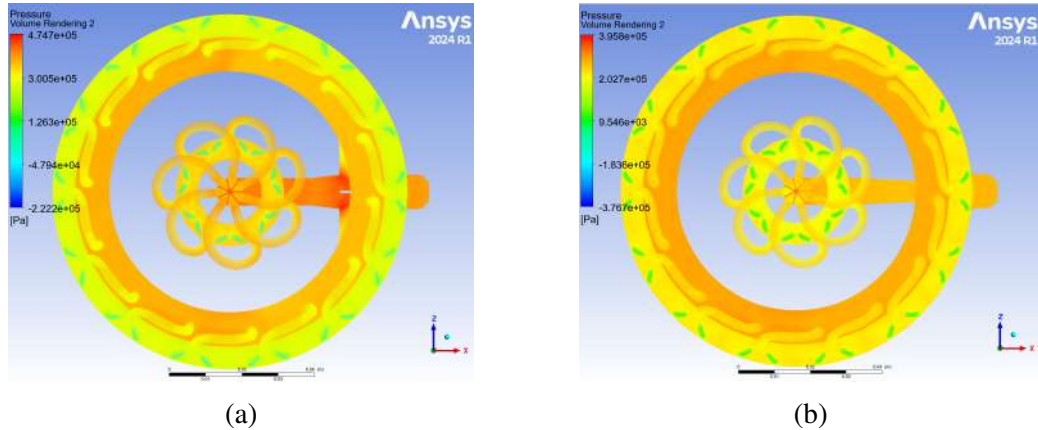


Figure 8.11: CFD simulation of pressure drop throughout the fuel channels of the injector used to refine the flow distribution. The fuel orifices can be seen as a low pressure region in green: (a) Initial fuel flow simulation. It was found that the fuel splitter resulted in uneven flow, with a disproportionate amount of fuel entering the inner fuel manifold. (b) Final fuel flow simulation. The fuel splitter (hidden from view by the outer manifolds) now results in an even pressure distribution between the inner fuel manifold and the secondary outer fuel manifold.



Figure 8.12: Printed injectors after being cut from the build plate but before post-machining.



(a) Cold flow testing of the fuel channels using high-pressure water. The two fuel streams of each element impinge, resulting in atomization of the fuel.

(b) Static fire of the Eridium V2 engine using the printed injector.

Figure 8.13: Eridium injector testing

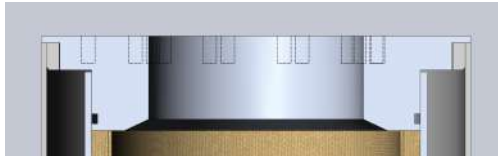


Figure 8.14: Injector bulkhead cross-section

Bending calculations and FEA simulation verify that the ring can withstand bending loads from CC pressure pushing on the injector face.

The bulkhead also includes mounting for a PCB that records sensor data in the injector section and a 1/16 NPT port for a pressure transducer for CC pressure.

The step feature above the bolt circle is a running surface that interfaces with the spincan (Figure 8.15). As such, it is machined smooth and taped with 0.5 in wide polyamide tape to ensure the spincan does not bind. Using polyamide tape is a better choice than using other slippery materials, such as PTFE, because it does not need any retention features, making assembly easier. Additionally, it would not be affected by any fibres shed from the fincan.

## 8.4 Feedsystem

### 8.4.1 Tanks and Couplers

The desire to have a lighter, more optimized propellant tank was one of the key drivers behind the change in airframe diameter from 6 in to 8 in. The wall thickness of the tank is limited by supplier availability for aluminum tube stock; 1/8, 3/16 and 1/4 in. The Borealis (and all previous 6 in rockets') oxidizer tank used 3/16 in 6061-T6 aluminum extruded tube. For Aurora, the oxidizer tank is both a larger diameter and thinner, using only 1/8 in thick wall and an 8 in OD. While this change significantly reduces the safety factor on the tank, the effect is somewhat offset by reducing the nominal engine firing pressure to 650 psi and the tank MEOP to 800 psi. Counterintuitively, reducing the firing pressure actually improves the propulsion system's  $\Delta V$  for a given tank size, as the reduction in ISP from a lower chamber pressure is offset by the increased propellant mass

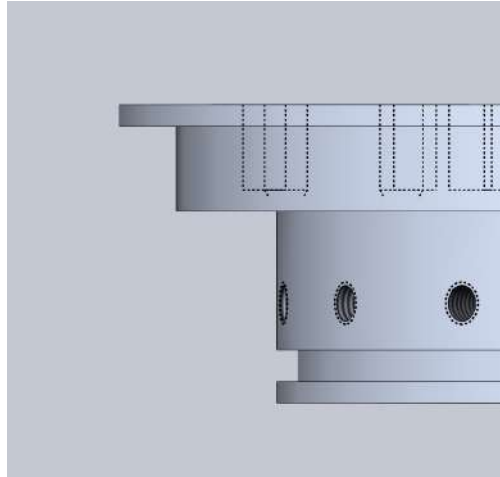


Figure 8.15: Spincan running surface on injector bulkhead

from loading denser nitrous oxide. This change in propellant pressure and tank dimensions allows approximately twice as much propellant to be filled for a fixed tank length, with a 5% decrease in tank mass over that same length.

The 1/8 in thick tubing has a lower margin to failure as compared to previous years, and required significant redesign of the bolted closures. The closures were designed to have a higher safety factor compared to the hoop stress in the tank, because the hoop stress is a simpler and more accurate analysis that does not depend on as many assumptions. This ensures that the tank will fail closer to the predicted pressure, and allows confidence in its performance even if there are minor imperfections in the bolt circles. The largest change to the closures was increasing from one to two bolt circles. This increases the difficulty of lining up all bolts to ensure even loading, which is especially important considering the reduced structural margin. To facilitate this process, the bolts were switched to flat head countersunk screws, and the bolt holes were match drilled through the coupler and the tank at the same time. This allows for the application of minor preload to the countersunk bolts, ensuring all the bearing surfaces are engaged approximately equally. Match drilling the couplers means that holes on the couplers and tanks match exactly.

When machining and tapping a countersink directly into the tank, no undercut was machined for the radius where the bolt countersink meets the thread, because adding the undercut machining operation to the tank was deemed more difficult than machining the undercut into the bolts. The undercuts were mass machined into the shoulder of the bolts using a fixture jig that ensured they were all similar, to within 5 thou. The bolts were then painted to prevent rusting of the exposed structural steel. The length of undercut was determined by the maximum allowable bending stress. Figure 8.16 shows the 0.050 in undercut.

Important structural safety factors are presented below at the MEOP of 800 psi in Table 8.2. Note that for all tank structural calculations, aeroelastic forces were determined to be negligible so are not included in the structural analysis. The expected tank wall failure mode is hoop stress and the expected bolt failure mode is bending at the modified section.

To comply with the DTEG and to verify the validity of the structural calculations, a shorter tank was constructed for hydrostatic burst testing. The tank was made shorter than the full tank due to the reduced costs and lower stored energy, since the bolt circle failure modes are unaffected by



Figure 8.16: Undercut on countersunk tank bolt

Loading	Yield Safety Factor
Bolt Shear	2.88
Bolt Bending	1.95
Tank Edge Tearout	2.68
Tank Wall 2D Bearing	2.33
Tank Wall Tensile	2.11
Tank Hoop	1.56

Table 8.2: Tank Structural Safety Factors

tank length. The tank was manufactured identically to the flight propellant tank at the same time. For burst testing, the tank was taken to failure in 5 increments, at 400 psi (50% MEOP), 800 psi (MEOP), 950 psi (PROOF), 1200 psi (1.5x MEOP) and finally failure. In between each step, the tank was depressurized and inspected for signs of yielding or failure, including removing bolts from the bolt circle to inspect the contact area. No signs of yielding were observed at 1200 psi. The tank failed in hoop stress at 1480 psi, which was 2% higher than predicted. Figure 8.17 shows the way the tank failed in hoop stress.

#### 8.4.2 Piston

Similar to Borealis in 2024, a piston runs inside an aluminum drawn tube that acts as the fuel tank, allowing the nitrous to pressurize the fuel. The drawn tank ensures tight dimensional tolerances along the entire length of the tube. Both ends were measured and the piston was sized to ensure a minimum of 10 percent compression on the entire OD of the o-ring. As shown in Figure 8.18, two PTFE wear rings ensure there is no metal-to-metal contact between the piston and the ID of the fuel tank. This reduces the chance of binding and scratches, which would affect the performance of the dynamic seals. As with all inter-propellant seals, there are two redundant o-rings. The piston is lubricated with oxidizer-safe Krytox synthetic grease to ensure it slides well in the tank. The piston was successfully tested at ELSF5, as well as at cold flows during preparation, and will be further tested at wet dress rehearsals.



Figure 8.17: Hoop failure of burst test tank



Figure 8.18: Piston with wear rings

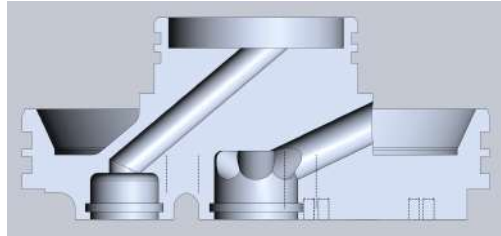


Figure 8.19: Cross-section of propellant feedlines in fill bulkhead

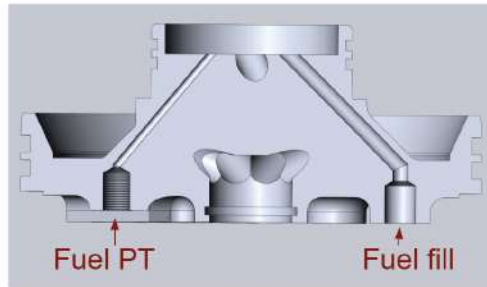


Figure 8.20: Cross-section of angled holes on fill bulkhead

### 8.4.3 Fill Bulkhead

The fill bulkhead is the lower bulkhead, which seals the oxidizer tank to the environment and the fuel tank. It also allows for fuel filling and sensor data acquisition via a fuel pressure transducer (PT) and an oxidizer PT.

Figure 8.19 shows a cross-section of the bulkhead, where the oxidizer and fuel fluid paths are visible. The design is similar to the one flown on Borealis. The positions of propellants are again inverted due to the concentric tank geometry. An angled hole (drilled on a 5-axis CNC) leads to a female o-ring groove which fits around the fuel valve compensator. There are three such grooves, one for each compensator coming off of the valve block (fuel, oxidizer, and oxidizer fill). The geometry of the angled holes avoids complicated tube bends and part geometry in the rest of the feedsystem, which could otherwise result in pressure drop and cavitation. This includes holes for the fuel PT, fuel fill line, and fuel valve inlet, with individual cross-sections shown in Figure 8.20.

The pyrotechnic vent valve (pyro valve) is also mounted to this bulkhead using a bolted flange with two face seals. The tank inlet to the pyro valve is integrated within the bulkhead, as is the outlet for soot from the pyrotechnic charge. The vent orifice for the oxidizer is integrated within the valve body and is not located on the bulkhead.

The bulkhead is made of 6061-T6 aluminum, and is designed to a minimum safety factor of 2.0 at a MEOP of 800 psi. It has been validated via hand calculations, SolidWorks FEA (Figure 8.21 shows the results of the displacement study), and through hydrostatic tests.

Note that SolidWorks Simulation shows a small stress concentration at the thin wall between the angled oxidizer inlet holes that had a FOS below 2 on yield. As shown in Figure 8.22 this is likely a result of the coarse mesh in that thin region of the bulkhead, which led to inaccurate simulation results.

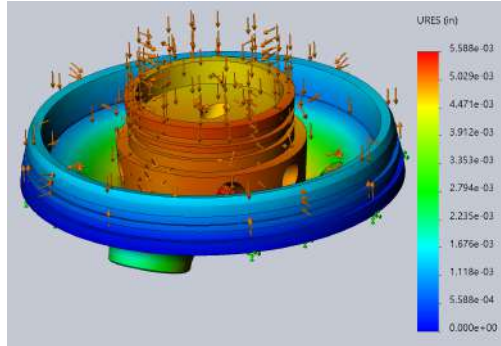


Figure 8.21: Displacement of fill bulkhead at MEOP

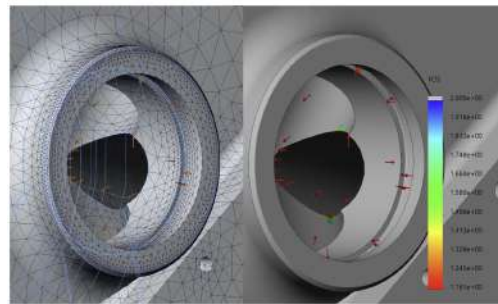


Figure 8.22: Stress concentration on fill bulkhead

#### 8.4.4 Vent Bulkhead

The vent bulkhead caps the top of the concentric tanks. An initial bolted joint analysis for two rows of bolts on the bulkhead revealed tight safety factor margins for net tension failure. Thus, the bulkhead is not directly fastened to the tank. Instead, standoffs at the top of vent bulkhead bolt into the plate shown in Figure 8.23, which is fastened into the coupler via radial bolts. This ensures that loads from the top of the rocket are transmitted into the coupler and tank, rather than the bulkhead. It also axially retains the bulkhead, so nothing pulls on the hard tubing of the diptube.

The bulkhead is machined from 6061-T6 aluminum and designed to withstand an internal pressure of 800 psi with a minimum FOS of 2.0, as validated by FEA (see Figure 8.24).

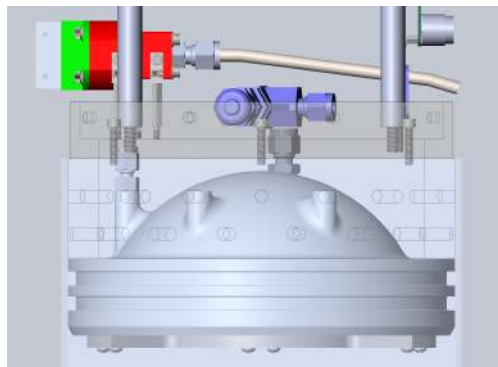


Figure 8.23: Vent section assembly

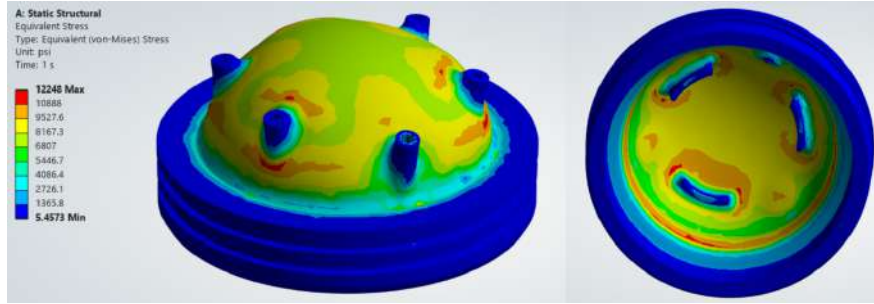


Figure 8.24: FEA results of vent bulkhead.



Figure 8.25: Centering plate on vent bulkhead.

The water jet-cut plate seen in Figure 8.25 uses prongs to centre the tank during assembly and operation. The angle bracket levels the fuel tank and prevents it from sliding upward.

The bulkhead also features a port to allow for gas flow to the vent valve. This port connects to the diptube used to set the fill level for the oxidizer. The diptube is swaged onto the fitting on the bulkhead, and then fastens onto the valve inlet.

## 8.5 SRAD Valves

### 8.5.1 Pneumatic Vent Valve

The pneumatic vent valve is a poppet-style valve that opens the tank to ambient pressure when filling oxidizer into the tank, and vents the tank in case of an abort. The valve design largely follows from previous iterations; however, two modifications to the design were implemented during this design cycle.

Firstly, as outlined in the DTEG, the vent valve must be designed to fail open. As such, the vent valve is actuated by ground-side pneumatic pressure and uses a magnetic quick disconnect to hold it closed on the launch pad. The quick disconnect detaches upon launch of the rocket and opens the valve, leading to a small amount of oxidizer being vented during the flight.

Secondly, the sealing mechanism was slightly adjusted since 2024 such that an aluminum poppet seals onto a PTFE seat, as opposed to an aluminum seat and a PTFE poppet tip. This improves the machinability of the valve, but has led to issues during testing due to wear of the valve seat. This was mitigated by fabricating multiple spare seats. The valve attaches to the vent bulkhead as described previously and is supported by several mounting brackets. Figure 8.26 is a cross-section of the valve, showing the PTFE seat in white near the centre of the valve, and the sealing stem and piston in blue.

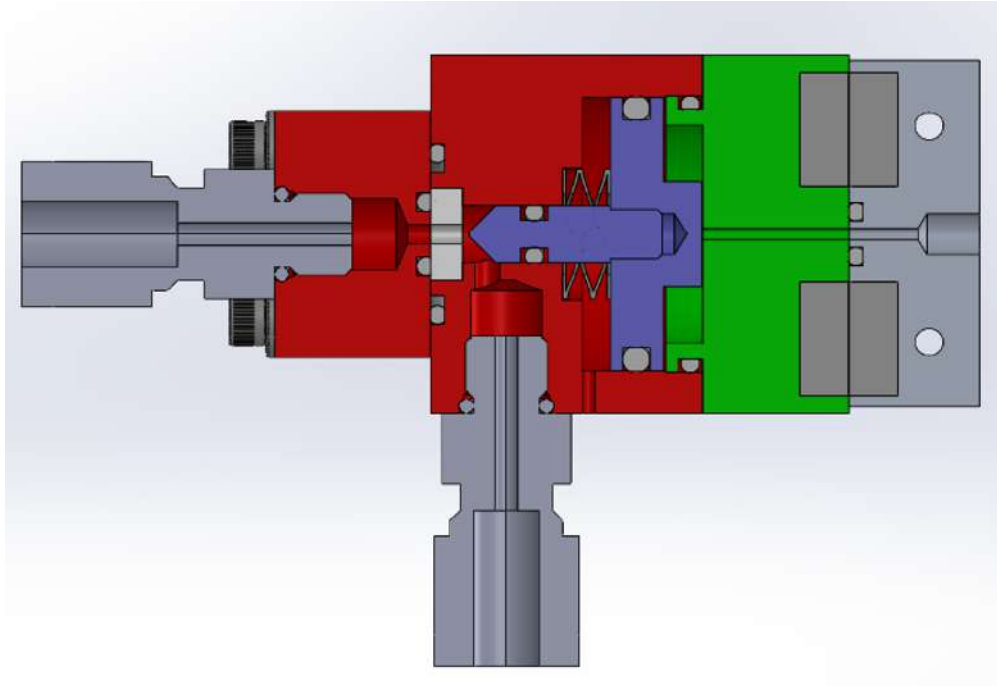


Figure 8.26: Pneumatic vent valve cross-section

### 8.5.2 Fill Disconnect

The fill disconnect is the interface between the ground-side oxidizer fill system and the rocket-side feedsystem. It transports the oxidizer from the fill panel into the oxidizer tank and the injector valve pilot volume. Actuation of the fill-disconnect mechanism releases it from the rocket, which vents the pilot line and opens the injector valves. This is the final step in the engine startup procedure. The fill disconnect assembly is composed of the quick disconnect (QD) valve, the GSE block, and the QD arm mechanism.

#### QD Valve

The QD valve is a normally-closed poppet valve designed to facilitate the filling and sealing of nitrous oxide in the main oxidizer tank. Its development was driven by two primary requirements: relocating all pneumatic control from the rocket to GSE, and reducing the tank fill time to less than 5 minutes. This valve replaces the fill/dump valve used on Borealis [23], which is incompatible with the new requirement to remove onboard pneumatics. The valve is illustrated in Figure 8.27. To

fill the oxidizer tank, a barb from the GSE block is inserted into the valve, displacing the internal poppet against a spring and opening the primary flow path. This orifice is sized for a 0.375 in diameter connection, which was determined to provide an adequate flow rate to meet the fill time requirement of 5 minutes or less. The barb remains connected until the terminal count, at which point the fill disconnect is actuated. This actuation uses fluid pressure to generate an ejection force of 111 lbf, safely retracting the barb from the rocket as the engine starts up. Upon disconnecting, a combination of spring force and internal tank pressure drives the poppet against a PTFE seat to seal the main orifice. Retracting the GSE block vents a pilot orifice on the valve's flange and opens the main injector valves.

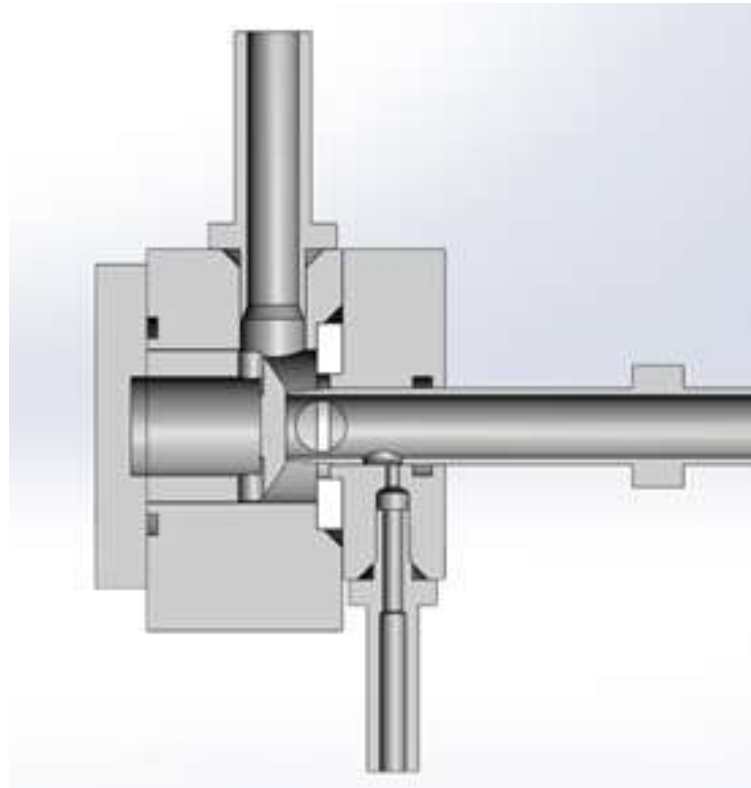


Figure 8.27: Cross-section of QD valve in open position

This design provides robust abort capabilities for multiple scenarios. For aborts initiated while the GSE is still connected, the valve allows the oxidizer tank to be vented through the fill system, significantly reducing abort time. In the event of an abort after the ground-side mechanism has disconnected, a dedicated on-board pyrotechnic valve (subsubsection 8.5.4) is actuated to vent the tank.

The valve's sealing performance and structural integrity were validated through a series of hydrostatic tests. The first test assessed the static poppet seal by pressurizing the valve from the tank-side port, during which a pressure drop of 10 psi over 10 min was observed, meeting the acceptance criteria. A second test validated both the dynamic O-ring seal and the structural integrity of the latching mechanism while the GSE barb was engaged. Following a mid-cycle design change to the latch arms, this test was conducted on both the original and revised configurations. Both versions successfully passed the validation, each demonstrating a pressure drop of 10 psi over 10 minutes.

Three distinct actuation tests were performed to validate the release mechanism throughout the design cycle. The initial test, conducted at a tank pressure of 200 psi, successfully demonstrated the ejection of the GSE barb. However, this test revealed significant pin misalignment and required excessive force to engage the poppet. A subsequent quality inspection identified a machining error, which was fixed. After correcting this error, a second actuation test was performed. In this test, the mechanism failed to release even when pressurized to 800 psi, which is 150 psi above the nominal tank pressure. A design review revealed a flaw in the force analysis: the model had approximated the arm-to-valve interface as a flat surface, but the design was changed in CAD to feature 3/8 in mating radii. This geometry in the CAD resulted in a near-zero degree contact angle, which failed to generate the necessary outward force to overcome friction and release the latch arms. To resolve this issue, the design was modified to incorporate a 55 degree chamfer on both the valve body and the latch arms, as shown in Figure 8.28. This change was calculated to produce a force perpendicular to the valve body equal to 74 lbf. The third and final test validated this revised design. It was confirmed that the spring force alone was sufficient to release the mechanism without tank pressure and the system performed reliably up to the maximum test pressure of 800 psi, demonstrating that the increased outward force both did not impede the retraction of the locking pins and that the latch arms were able to overcome the higher friction forces.

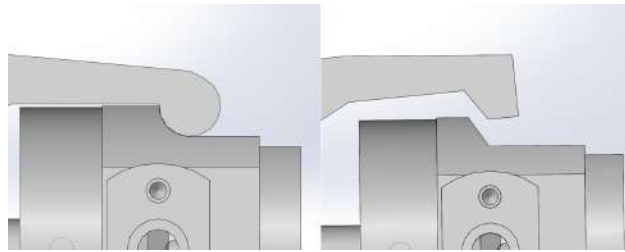


Figure 8.28: Old (left) and new (right) latch and valve body design

In the final flight configuration, the QD valve is integrated directly into the main valve block (subsubsection 8.5.3). This integrated assembly includes a dedicated pilot channel connecting the QD to the main valves. The injector block and fill disconnect arm were validated during ELSF5, and will undergo further testing during wet dress rehearsals.

## GSE Block

The GSE block was designed to transfer as much of the system's mass and complexity from the launch vehicle to the ground support equipment as possible. This approach simplifies the on-board systems and reduces vehicle dry mass. The GSE block consists of two primary components: a mechanism for latch arm retention and pin retraction, and a pneumatic actuator for barb ejection. The complete ground-side assembly, shown both in CAD and during actuation testing, is presented in Figure 8.29.

The arm retention and pin retraction mechanism is constructed from three stacked waterjet steel plates. Bearings are press-fit into the plates to allow the latch arms to pivot and guide the release pins. An aperture in the bottom and middle plates aligns and constrains the barb when engaged. The entire assembly is fastened using a combination of threaded rods, spacers, and nuts.



Figure 8.29: Ground-side mechanism and pneumatic actuator in CAD (left) and during tests (right)

A custom pneumatic actuator was designed and fabricated in-house to reduce procurement costs and meet specific performance criteria. The primary design requirement was to generate a minimum retraction force of 180 lbf, which is the force calculated to overcome static friction and pull the mechanism's release pins. A cross-sectional view of the actuator and an image of the final machined component are presented in Figure 8.30.

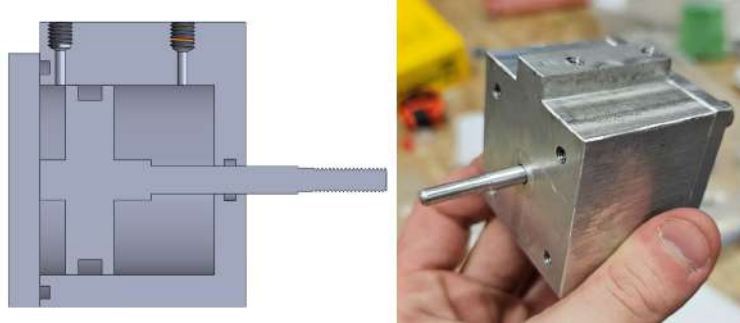


Figure 8.30: Cross section of pneumatic actuator (left) and machined version (right)

To engage the system, the GSE barb is inserted into the QD valve. The latch arms are then manually closed around the valve body, and the mechanism is secured by inserting two release pins through aligned holes in the arms. This action locks the arms in the engaged position. With the mechanical connection established, the pneumatic actuator is connected to its supply line, preparing the system for remote, rapid disengagement.

Validation of the GSE block involved both standalone and integrated testing. The pneumatic actuator was first tested individually and performed as expected before being installed into the main assembly. The subsequent integrated actuation tests were designed to meet two key objectives: ensuring the release pins would not deform under operational shear loads and confirming the actuator could reliably retract the pins. While initial analysis predicted no issues, a design change to the QD valve significantly increased the outward force on the latch arms. This raised concerns that the resulting frictional force on the unlubricated pins, particularly at a tank pressure of 800 psi, might exceed the actuator's capability. The final tests specifically addressed this worst-case scenario. The actuator reliably retracted the pins without issue, thereby validating the structural integrity of the pins and the functional performance of the complete mechanism.

## QD Arm Mechanism

The QD arm is a mechanism designed to enable the controlled retraction of the disconnect ground-side assembly from the rocket body during launch operations. When the pneumatic actuator retracts the pins from the latch arms, tank pressure generates substantial force on the GSE block. The primary design objective of the arm was to mitigate any risk of damage to vehicle-side or ground-side hardware during actuation. CAD of the full assembly can be seen in Figure 8.31

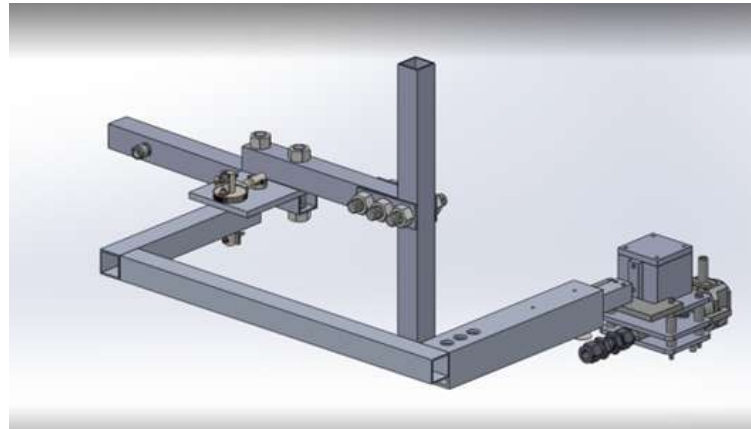


Figure 8.31: QD arm assembly CAD

The arm mechanism is comprised of two integrated sections: a linear segment that retracts the pneumatic actuator and latch arms from the rocket's aerostructure, and a ratcheting arm that ensures the system does not interfere with the fins during ascent. The assembly is mounted to the launch tower for repeatable installation without additional equipment. The linear portion clears the GSE block from the rocket body without damaging the aerostructure. It consists of a smaller inner tube that slides along a rail within a larger outer tube (Figure 8.32). The stroke length of the inner tube is defined by a spring-loaded pin housed in the outer tube. Once the block, attached to the inner tube, has fully retracted beyond the vehicle, the pin engages a slot in the inner tube to lock it in place and prevent further motion.

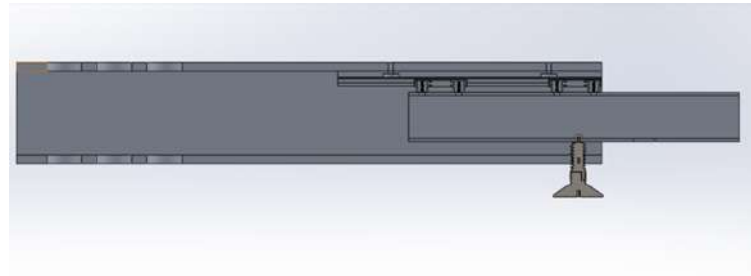


Figure 8.32: Cross-section of the linear section of the QD arm

To ensure clearance from the fins during ascent, the linear segment is connected to a ratcheting arm. The rotational section comprises an arm that pivots about a ratcheting gear, a ratcheting mechanism to control rotation, and a hard stop that limits the range of motion. The hard stop is an aluminum arm equipped with a high-load compression spring to absorb the force of the rotating

arm. The rotating arm is attached to a shaft coupled with the ratcheting gear. A spring-loaded pawl locks the ratchet mechanism, preventing any reverse rotation toward the vehicle, particularly after impact with the hard stop. The ratcheting mechanism can be seen in Figure 8.33.



Figure 8.33: The ratcheting mechanism of the QD arm

The arm mechanism was validated through integrated testing with the rest of the fill disconnect. A tank was filled through the QD valve, and the GSE block was actuated to characterize the performance of the arm mechanism. Through this testing, the arm was validated to meet its performance requirements at a minimum pressure of 400 psi and up to 800 psi (MEOP). The stroke length of the linear section and the total rotational travel of the arm were sufficient to ensure no interference or damage to rocket hardware. Additionally, the compression spring on the hard stop was verified to reliably absorb the kinetic energy of the swinging arm.

### 8.5.3 Injector Valve Block

The injector valve block was created to consolidate the fuel injector valve, oxidizer injector valve, and QD valve into one body. This allows for mass and volume optimization compared to the stacked valve configuration. A comparison between the two configurations is shown in Figure 8.34. Since the valves are too big to be arranged side-by-side, the valve block saves approximately 6 in of height. The bolted flange design has the added benefit of reducing the number of fitting connections in the injector section assembly. Historically, the team has had issues with leaks at fitting and tube connections. During the launch of Borealis in 2024, there was a 3 psi/s leak in the injector section pneumatics that would have caused valve actuation to fail if there was further delay in Borealis' engine startup procedure. Having all of the fluid paths integrated within the body makes the section easier to maintain and results in more consistent performance.

Instead of using fittings and hard tubing for the pilot line, a through hole connects the pilot orifices of both valve bodies and is capped by an NPT plug on one side. The pilot line coming from the QD valve is cross-drilled and seals via face-seal flange to the main valve body, as shown in Figure 8.35. An NPT plug blocks the remaining open orifice. The tank-side inlets of all three valves are compensators (static O-ring piston seals that allow the length of the oxidizer and fuel

Unified valve block design

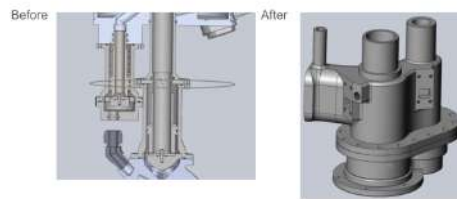


Figure 8.34: Space optimization in injector section

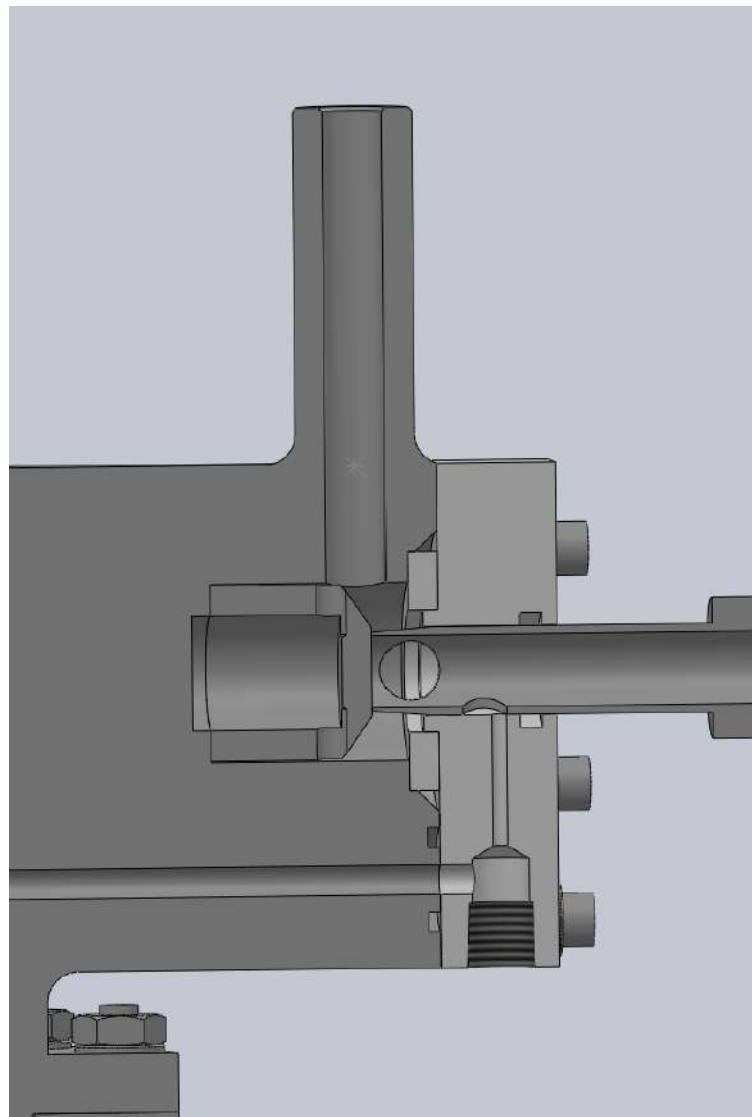


Figure 8.35: Cross-section of cross-drilled QD face seal flange

feedlines to fluctuate about .15" in either direction), which seal with female O-ring grooves within the fill bulkhead. This design ensures that the structural longerons are the only parts defining the length of the section, and therefore take all of the load coming from the engine.

The injector valves leverage the team's experience in designing coaxial sleeve valves, starting with LOTS in 2023. Each valve has a spring to ensure the valve sleeve starts with the knife edge in contact with the PTFE seat, exerting 15.37 lbf for fuel and 60.60 lbf for oxidizer. Crucially, the spring force is not enough to seal the valves. The intent is to ensure the valves open upon venting of the pilot line and remain open for the remainder of the flight, even at low upstream pressure. Both injector valves are sized so that the downstream projected area is larger than the upstream projected area, which keeps the force balance such that the valve stays open with no pilot pressure. Fuel valve is specifically designed to close against 30 psi of head pressure. This allows for the valve to stay closed while fuel is filled from fill bulkhead as the rocket is horizontal on the launch rail.

The valve sleeves seal the pilot orifice against the body via reciprocating seals - one on the valve sleeve and one upstream, integrated within the geometry of the compensator. There are two O-rings for redundancy at every inter-propellant seal. The sleeves seal via deformation of the PTFE seat under the knife-edge geometry at the outlet of the valve sleeve.

The fuel valve is fully self-contained within the valve body, while the oxidizer valve seat is retained by a bolted flange between the valves and the injectors. The face seal flange on the QD side mates directly to the ground-side actuator for the quick-disconnect mechanism, as mentioned previously.

The two halves of the main valve body are bolted together via a 16-bolt asymmetrical flange. Ansys FEA was performed on the flange, taking into account bolt preload and friction between all bolted connections (nuts to washers, washers to valve body, washers to bolt heads). The simulation verified that, with a preload of 800 lbf (higher than the design preload of 666 lbf), a maximum stress of 12 198 psi is developed in the 6061-T6 aluminum body, corresponding to a FOS of 3.27. The bolts, washers, and nuts are made of steel and are subject to maximum stresses that put them above the minimum FOS of 2, defined in the LC DTEG. The results of the simulations are shown in Figure 8.36, Figure 8.37, Figure 8.38, and Figure 8.39. The maximum deflection of the flange at MEOP was also acceptable for ensuring sealing of the triangular O-ring groove on the fuel valve side.

The same analysis was performed on the face seal flange of the QD side and was found to be similarly acceptable. Results are shown in Figure 8.40, Figure 8.41, and Figure 8.42.

Actuation, sealing, and nominal operation of the injector valve block were tested in cold flows and ELSF5, during which it performed nominally. From test data, the delay for the valves opening after the pilot volume vents and the start of the thrust curve is 0.55 s, which is long enough to ensure the ground-side QD mechanism completely exits the airframe before the rocket takes off.

#### 8.5.4 Pyrotechnic Vent Valve

The pyrotechnic vent valve is an emergency vent that allows for rapid draining of the oxidizer tank in case the pilot vents and the injector valves remain closed. At this point in the abort, the ground-side quick-disconnect mechanism would have been disengaged, so the rocket would be pressurized and sealed with no way to vent nitrous oxide from the fill panel. A similar pyrotechnic injector valve flew on Vidar III in 2017.

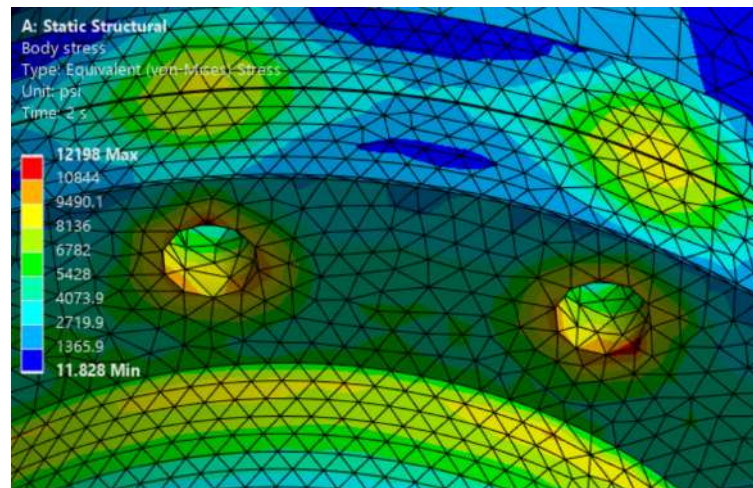


Figure 8.36: Valve body stress concentration

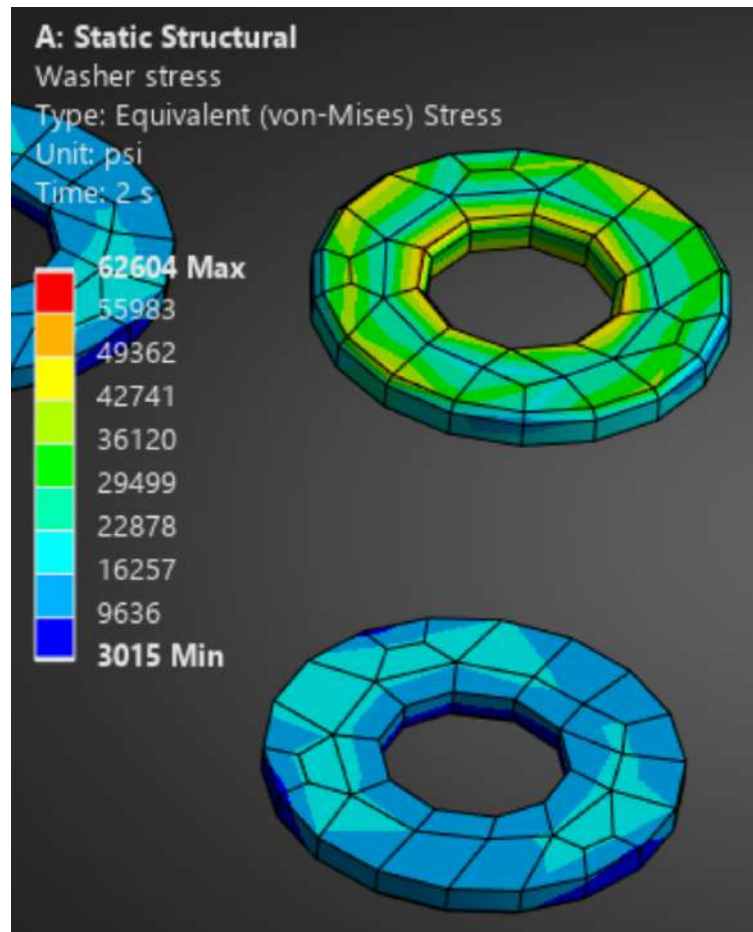


Figure 8.37: Developed stress in valve block washers

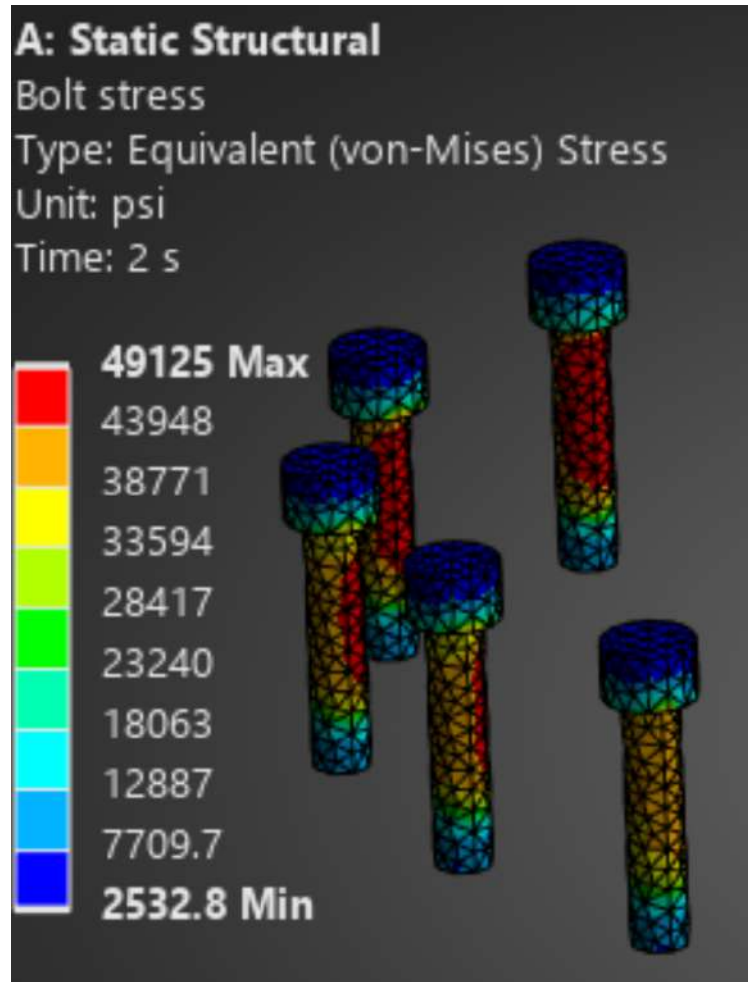


Figure 8.38: Developed stress in valve body bolts

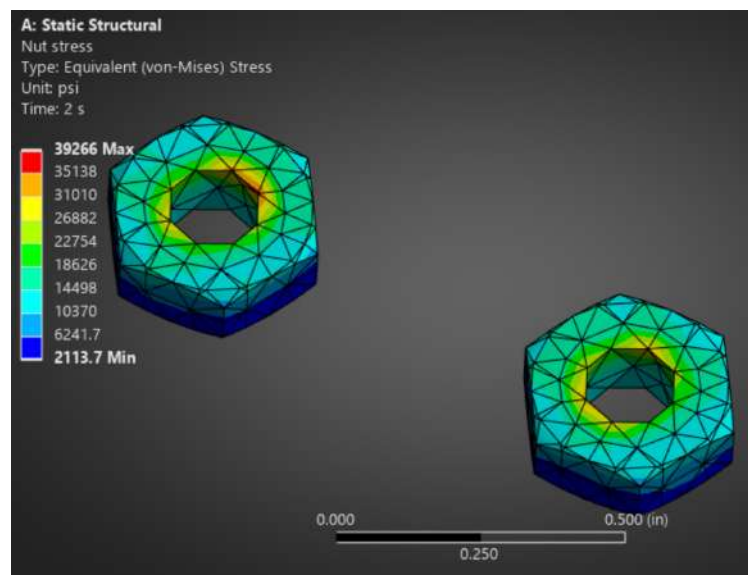


Figure 8.39: Developed stress in valve body nuts

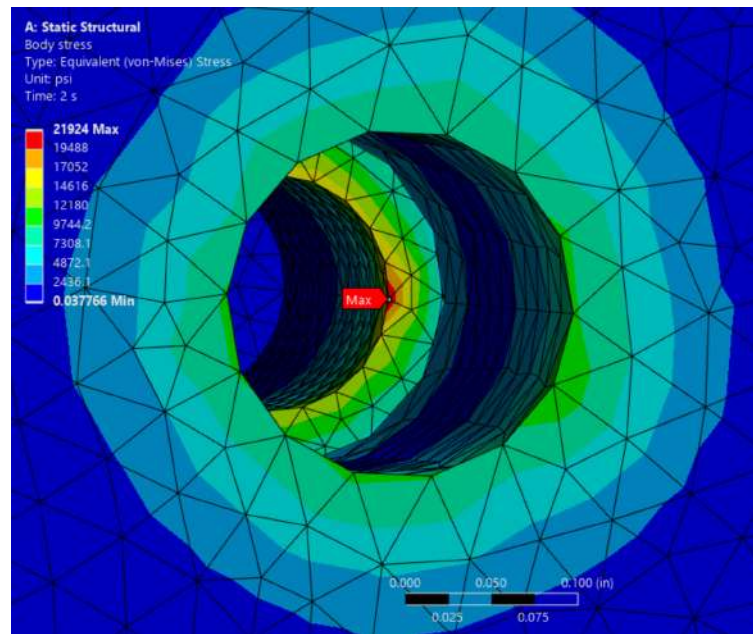


Figure 8.40: QD flange stress concentration

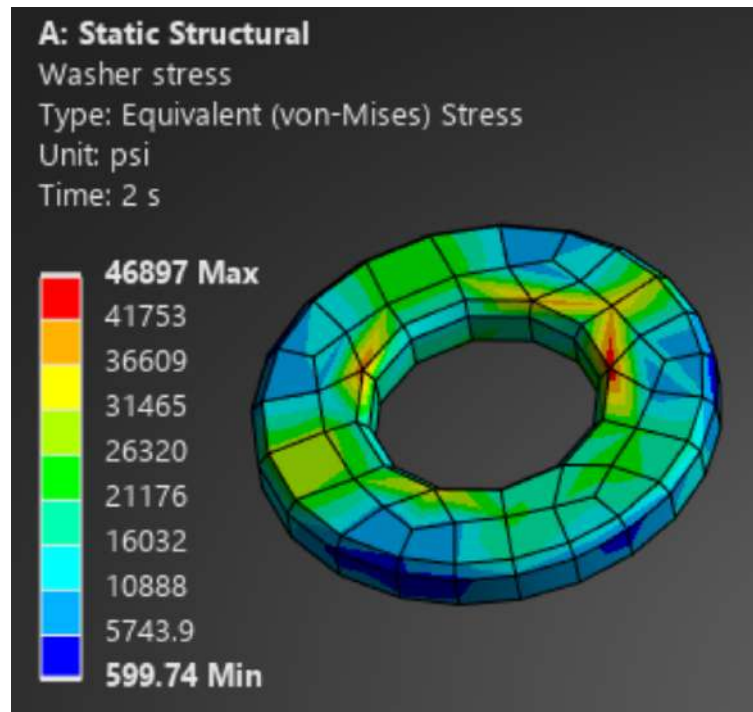


Figure 8.41: Developed stress in QD flange washers

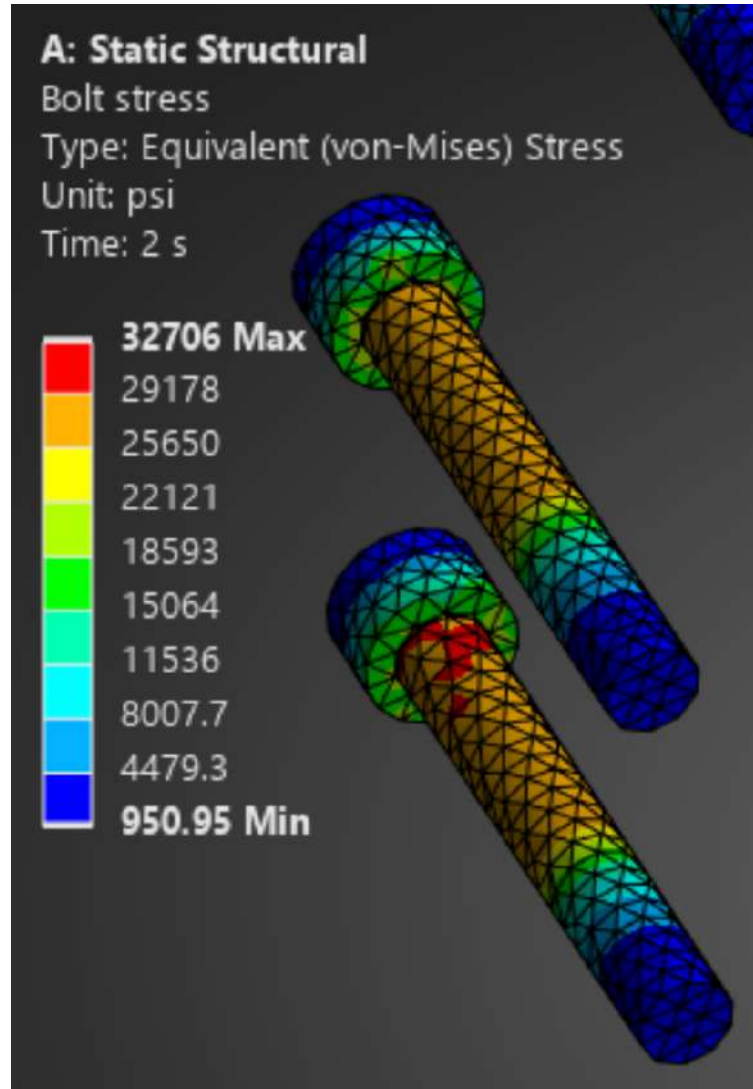


Figure 8.42: Developed stress in QD flange bolts

The pyro valve is a poppet valve that is nominally closed by the RNX cartridge, which acts as a mechanical stop against nitrous oxide pressure pushing down on the top face of the piston. A cross-section of the valve is shown in Figure 8.43, with the pyrotechnic charge colored white. Once the cartridge is ignited, most of the material leaves through the soot outlet. The remaining combusted material gets compacted under the piston as it opens. A fitting going to a swaged tube directs the nitrous oxide out of the injector section airframe through a cutout in the OTAS.

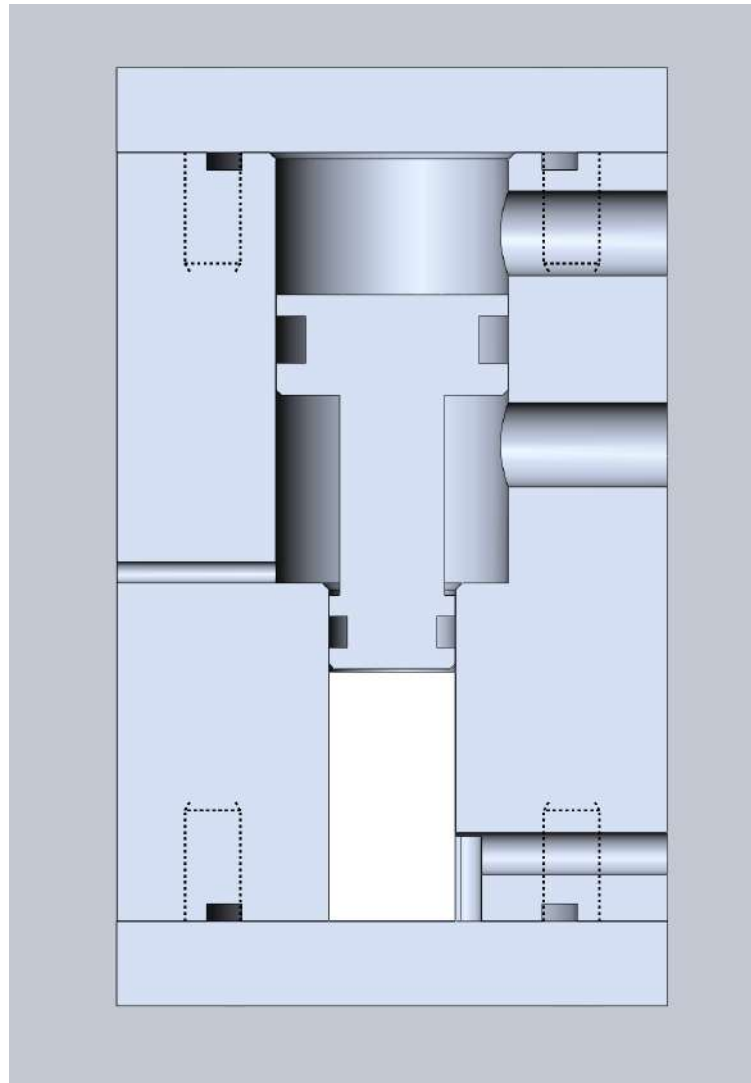


Figure 8.43: Pyro valve cross-section

The design of the pyrotechnic cartridge is based on the team's experience with RNX charges, previously used in the ignition puck. The KNO<sub>3</sub> and resin mixture is cast into a 3D printed mould made of ASA filament which is dissolved in acetone once the RNX cures. Due to the small size of this cartridge, only one ignition coil is used, and the leads are fed out from the exit of the soot port. It is actuated via a current sent from the ground-side electrical infrastructure through a pin in the electrical quick-disconnect. If it remains unused and the rocket takes off nominally, the lead is disconnected when the electrical disconnect tears off.

Although the burning pyrotechnic charge generates heat, there is little concern that it will ignite the nitrous oxide in the propellant tank. On the piston, the combustion gas is separated from the tank volume by an air gap and two redundant dynamic o-ring seals. The soot outlet is isolated from the tank volume by the two o-rings on the fill bulkhead.

The pyrotechnic vent valve's compatibility with nitrous oxide was confirmed through an actuation test in which nitrous oxide was used as the pressurizing fluid. The valve failed to fully actuate as the 3D printed mould interfered with the stroke of the piston. This resulted in the change to dissolvable filament, as discussed previously. However, the valve did actuate and validated its compatibility with nitrous oxide. New charges will be tested during an actuation test with nitrogen as the pressurizing gas.

## 8.6 Engine Data and Simulation

Engine performance is evaluated using static fire data and is predicted for future tests using those values if required. While the major performance values such as thrust, chamber pressure and tank pressure can be directly measured, it is not practical to do so for the propellant flow rate. The tank is hung from a load cell to attempt to measure the mass, but there is considerable swinging and drift of the load cell that makes getting accurate mass values difficult. Mass values are verified using multiple methods independent of the load cell to ensure accuracy. During filling, the tank is generally filled to the diptube if possible, to allow for a calculation of tank filled mass using the equilibrium properties for saturated nitrous oxide. The volume above the diptube is assumed to be vapour, and the volume below is assumed to be liquid, allowing an approximate propellant mass to be calculated. This can be compared to the load cell mass to check for errors. In addition, the fuel is filled by hand using a scale, so the load cell can be verified against those measurements as well.

During the burn, the fuel mass flow rate over time can be determined using an iterative method to calculate the effective  $C_d$  of the injector orifices. The starting fuel mass is known to a high degree of accuracy, as well as the pressure drop between the fuel tank and the combustion chamber over time. The moment the fuel tank runs out of fuel is also easily seen as the instant where the pressure drops sharply, indicating the piston bottoming out. A starting discharge coefficient is assumed and the mass flow rate at each data point is calculated according to Equation 8.1 for single phase incompressible orifice flow.

$$\dot{m} = C_d A \sqrt{2\rho\Delta P} \quad (8.1)$$

where  $\dot{m}$  = mass flow rate

$C_d$  = discharge coefficient

$\rho$  = fluid density

$A$  = flow area

$\Delta P$  = pressure drop

The total fuel mass burned can then be calculated using numerical integration. If the calculated total mass is above/below the known filled mass, the discharge coefficient is adjusted, and the process is repeated until the masses converge. Once a fuel mass flow rate is calculated, the nitrous oxide flow rate can be calculated either by using the load cell mass flow rate, making sure to subtract the fuel mass, or by following a similar procedure to the fuel side. At the point where the liquid nitrous oxide runs out, which can be found by looking for a large slope change of the tank pressure graph or by looking for a large drop in engine thrust, the tank is known to be approximately filled with saturated vapour. The residual nitrous mass at this point can be calculated assuming that the vapour is at saturation. Similar to the fuel side, various discharge coefficients can be iterated to find a mass flow rate over time which matches the total amount of burned nitrous oxide and the measured pressure change over time between the tank and the combustion chamber. For nitrous oxide, the homogeneous equilibrium and Dyer models are also used to attempt to more accurately predict two phase flow behaviour in the injectors, which each yield slightly different mass flow rate over time, but will all give the correct total mass flow rate. This means any average value has significantly more confidence than any instantaneous value, since the exact two phase behaviour of the nitrous oxide in the injector is unknown [24].

Once the mass flow rates over time are known, a .RSE file can be made for flight dynamics analysis. To calculate the propellant COG over time, the nitrous oxide is assumed to be at saturation and the liquid and vapour fraction are calculated using pressure and mass data. The .RSE files used for Aurora only contain propellant mass data and include no dry mass other than the piston, which is modelled since it moves during the burn.

### 8.6.1 Flight Static Fire Data

Important engine performance graphs are shown below. Note that these graphs are real data based on the flight-like static fire, and the actual flight performance may slightly differ depending on propellant loading and shorter feed lines.

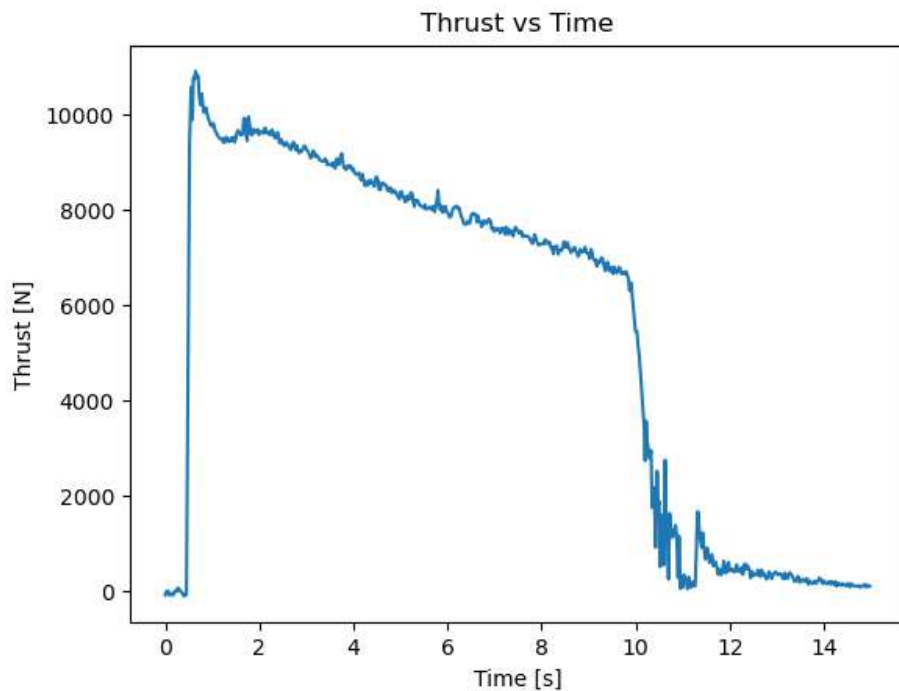


Figure 8.44: Flight-like thrust curve

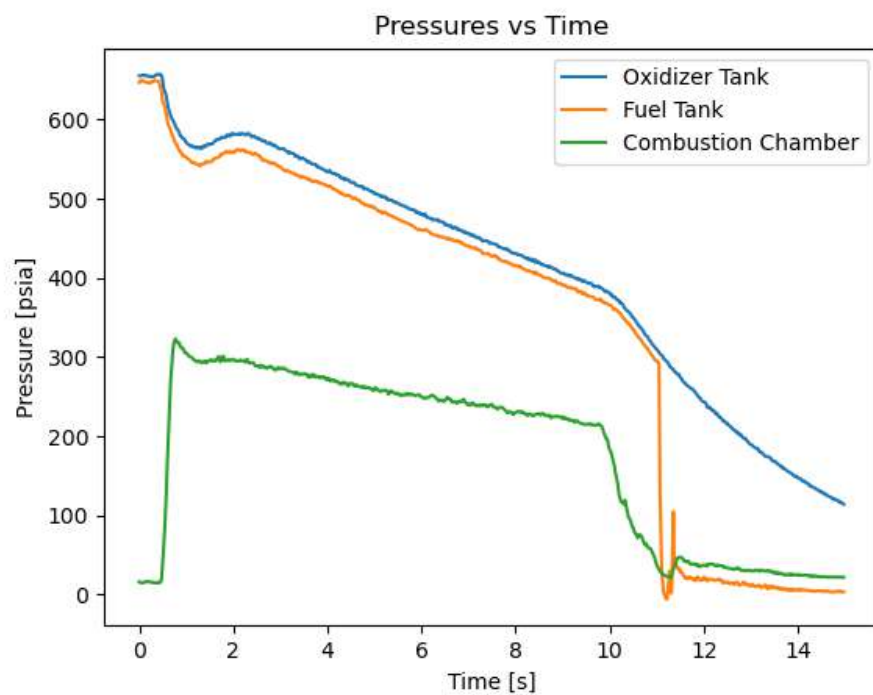


Figure 8.45: Flight-like pressure data

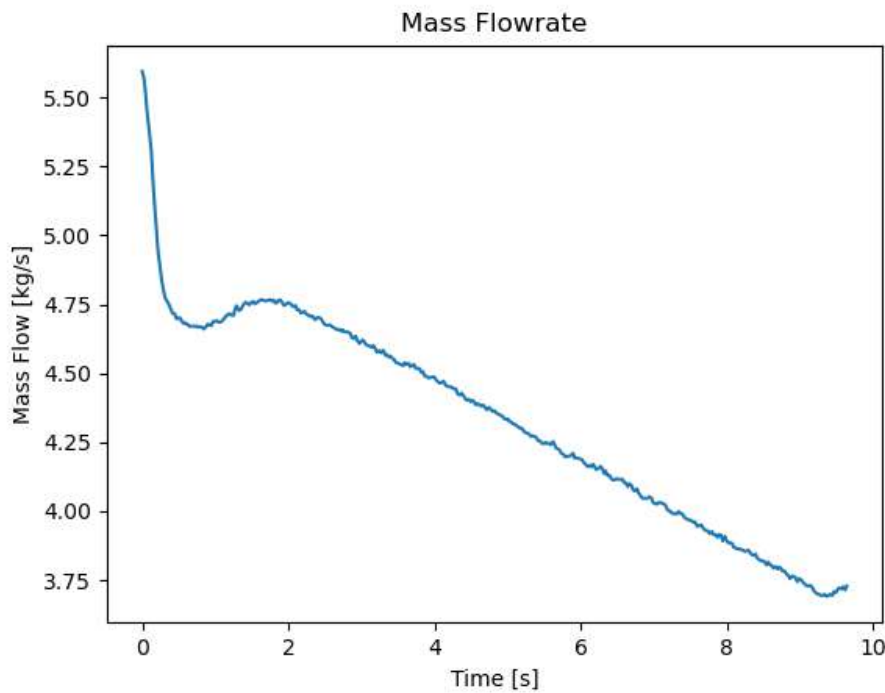


Figure 8.46: Flight-like mass flowrate data

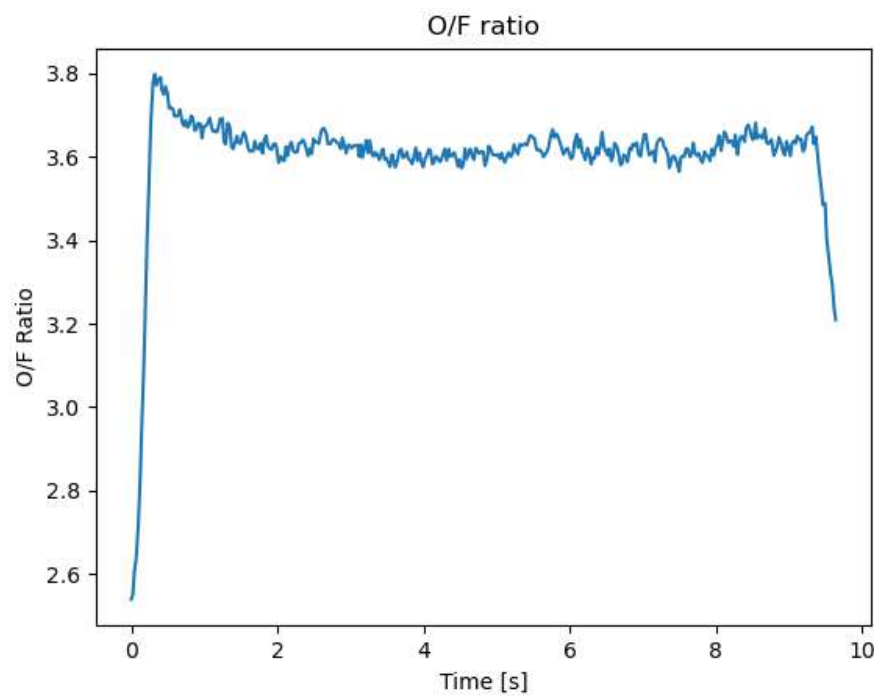


Figure 8.47: Flight-like O/F ratio data

## 9 AVIONICS AND TELEMETRY

Aurora's avionics system is comprised of three main subsystems: the RocketCAN bus, a pair of dissimilar COTS Altimeters, and an independent GPS tracking module from BigRedBee. The RocketCAN network consists of individual boards with single functionalities, which communicate through a Controller Area Network (CAN) bus. This system was initially developed in 2019 for Shark of the Sky (SotS), but has undergone significant updates since then, including new revisions of every board based on lessons learned throughout the previous years. This year, the main changes to the avionics system are a redesigned power architecture and power distribution board, payload boards, and controls boards. Other avionics projects saw significant development over the year, but were not flight-ready for Aurora and have been pushed into the next design cycle.

Figure 9.1 shows the interconnection of all avionics with the RocketCAN bus (below). Appendix B contains a complete block diagram of all electrical systems, both rocket-side and ground-side.

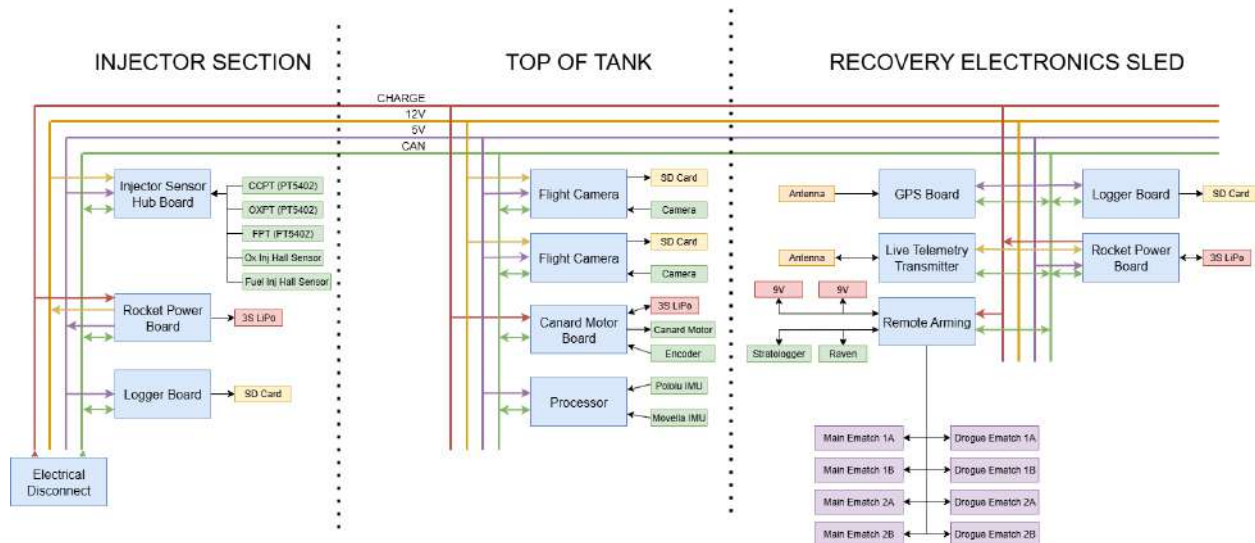


Figure 9.1: Aurora avionics architecture diagram

### 9.1 RocketCAN

The avionics modules on Aurora use a Controller Area Network (CAN) bus to communicate. The CAN protocol was primarily selected for its robustness; it has strong noise resistance and is suitable for safety-critical, outdoor applications. Additionally, CAN is a democratized protocol. There is no 'bus master' or 'slave' and all boards have an equal opportunity to take control of the bus. This aids the fault tolerance of the system, any individual board can fail without affecting the rest of the bus. Each of the modules can send and receive messages independently using the bus. For example, Live Telemetry Board can send a message to Remote Arming Board to arm the altimeters.

The CAN communication network is part of the team's larger RocketCAN standard, which also encompasses the power architecture and higher level communication implementation. This modular, standardized approach maximizes reliability and robustness and reduces coupling between the

different avionics systems. Additionally, if any individual board fails, it can quickly and easily be replaced with an identical spare copy.

### 9.1.1 Harness Design

To allow all the RocketCAN systems to communicate, there is a harness that runs the length of the rocket, connecting the boards in a tree topology. The bus can be separated into multiple sections for disassembly and transport via in-line Harwin Gecko connectors (Figure 9.2), which are reconnected during final assembly.



Figure 9.2: Male (G125-FC10605F1-0150L) and female (G125-MC10605M1-0150L) inline Gecko cable assemblies

Electrically, the RocketCAN bus consists of 6 wires: the CANH/CANL differential signal pair, a common ground line, regulated 5 VDC, unregulated 12 VDC, and the charge line (see Sec. 9.1.6). Each end of the bus is terminated with a  $120\ \Omega$  resistor that ties CANH and CANL together when they are not driven. A standard colour code (Table 9.1) has been developed this year to distinguish each line.

Table 9.1: RocketCAN colour code

Netlabel	Pin Number	26 AWG Colour	Tefzel Colour
CHG	1	Red	Red
CANL	2	Yellow	Orange
CANH	3	Green	Green
GND	4	Black	Black
5V	5	Blue	Blue
12V	6	White	White

The harness is connected to each system using Harwin Datamate and Harwin Gecko connectors. These connectors, shown in Figure 9.3, along with the Geckos, were selected as they are shock resistant and can survive the intense mechanical vibrations experienced during flight due to their screw-locking mechanism. This has been confirmed through testing, including post-flight analysis of the electrical systems on LOTS and Borealis, which both experienced a high-G landing due to failed main parachute deployment.



Figure 9.3: Female Datamate connector assembly (M80-9410642) and male Datamate PCB-mounted connector (M80-5400642)

Since the harness is subject to high loads and wide temperature ranges, particularly the section of the harness which connects the vent and injector sections and runs along the outside of the oxidizer tank, the use of high-quality wire is critical. As such, the CAN bus harness is made primarily from 6 conductor shielded cable with Tefzel jacketing, conforming to MIL-C-27500. This is connected to the COTS pre-crimped contacts provided by Harwin, which also use durable, high-temperature PTFE insulation. All connections are made using suitable butt splices and clear heat shrink complying with the LC DTEG safety-critical wiring guidelines.



Figure 9.4: Tefzel jacketed cable (M27500-22TG6T14)

### 9.1.2 Common Hardware

Most RocketCAN boards are built around the PIC18F26K83 (PIC18) microcontroller (MCU). The PIC18 is an 8-bit MCU running at 12 MHz, selected for its low power draw, expansive I/O capabilities including CAN support, low price, and availability throughout worldwide chip shortages. Most RocketCAN boards do not perform any complicated processing that would require a larger or more powerful processor, allowing cost savings and simpler embedded code. Boards which do significant data processing, such as Camera and Processor, use an STM32H7 series 32-bit MCU, selected for its higher clock speed and data bandwidth.

The PIC18s are wired similarly across all RocketCAN boards (Figure 9.5). OSC1 and OSC2 connect to an external 12 MHz crystal oscillator. In 2023, some PIC18 boards experienced intermittent resets and timing issues. One root cause was determined to be electromagnetic interference (EMI) on the oscillator lines. This led to the standardization of the oscillator circuit to better adhere to manufacturer guidelines and EMI best practices. As Figure 9.6 shows, the ground planes around the oscillator are isolated with an exclusion zone and via fence, and are connected to the rest of circuit ground through the MCU ground pin.

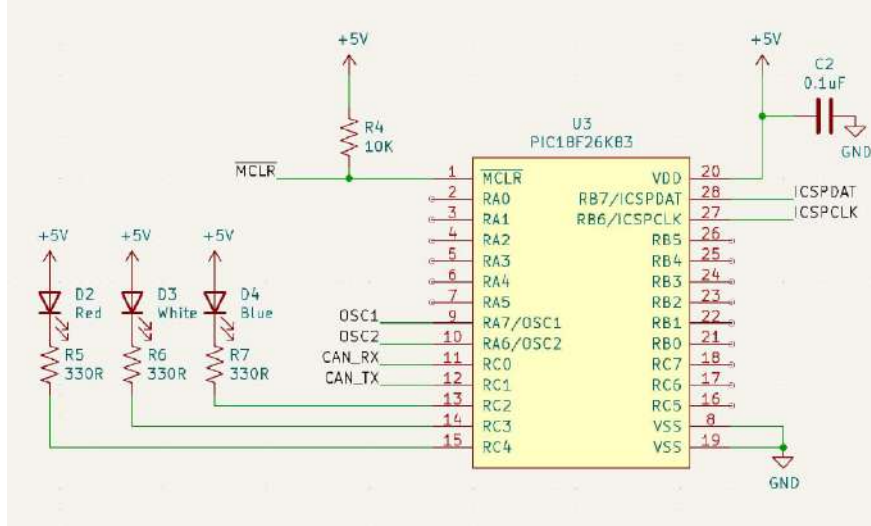


Figure 9.5: Standard PIC18 connections

Another common fixture of RocketCAN boards is the CAN transceiver. This is the chip responsible for converting the differential CANH and CANL signals into digital CAN\_TX and CAN\_RX signals. The MCP2562 (Figure 9.7) was selected for this purpose due to its ease of use and price. Additionally, drop-in replacements are widely available.

The boards are programmed using a PICKit3 which can also act as an in-circuit debugger. It requires three lines to be connected to the MCU: MCLR, ICSPDAT and ICSPCLK. These lines along with power and ground are broken out to a Dupont connector placed on each board for ease of programming.

The last feature, common across all RocketCAN boards, is input current sensing. Each board is equipped with a current sensing resistor on the input power line(s) which allows it to measure and report how much current it is drawing. The voltage drop across the shunt resistor is amplified by a current-sense amplifier (typically an INA180A3) and measured by the MCU using its internal analog-to-digital converter (ADC), as shown in Figure 9.8. This in combination with a suitable fuse allows boards to detect and appropriately react to an internal fault. It is also useful for ground operators to monitor the health of each board on the bus.

### 9.1.3 Common Software

All RocketCAN boards use a common library called canlib to interface with the CAN bus. Canlib performs two main functions. One is to abstract the hardware implementation of CAN for a particular chip. This allows, for example, firmware written for both PIC18 and STM32-based boards to use the same CAN message "send" and "receive" functions. The second is to standardize the format of data sent via CAN. One board can build an analog actuator command just by passing the command value to a function and another can extract that command value, without either having to know how that data is organized in the CAN message payload.

All avionics must fail safely, and software is an important factor in this. Each board periodically produces a nominal status message to indicate that it is still online and functioning correctly. If any of the internal error checks on a board fails, this status message will be replaced with an error

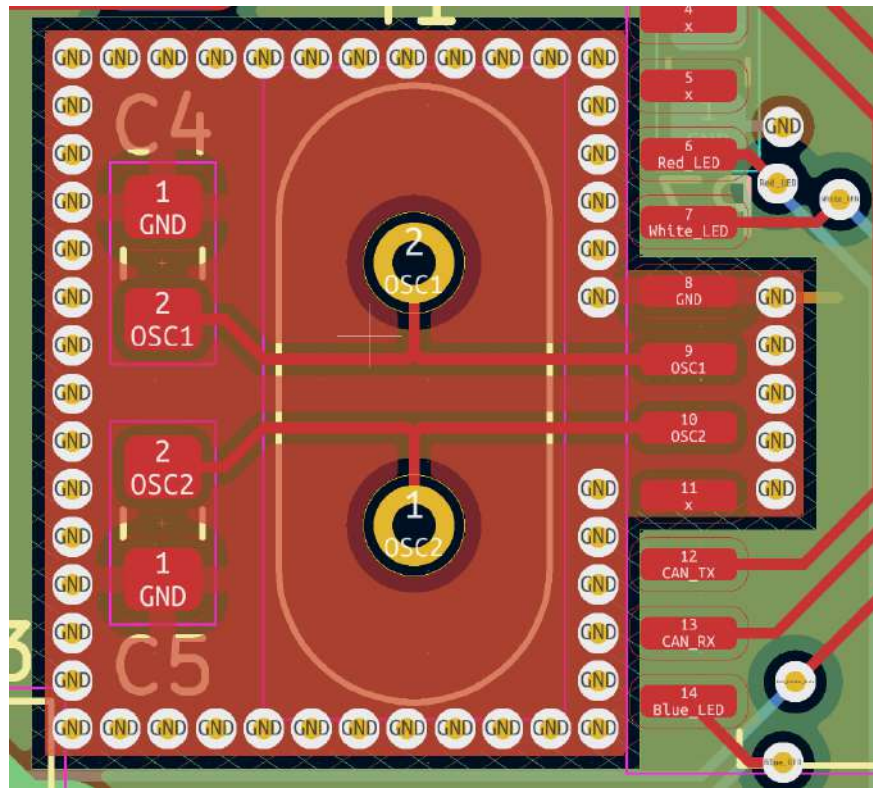


Figure 9.6: PIC18 oscillator layout

message indicating the error(s) detected, which will be relayed to ground operators. Additionally, safety-critical boards will automatically go into an appropriate safe state if an error is detected. The nature of the safe mode depends on the function of each board, but it is generally a state which will minimize hazards to both the rocket and the human operators. The democratized structure of the CAN protocol means that if any of the boards suddenly stops communicating, the bus will remain online and the other boards on the bus can continue functioning normally.

A new addition this year is `rocketlib`, a complement to `canlib` which standardizes code for individual peripherals specifically for the PIC18. This is code to interface with, for example, the ADC or real-time clock, which are used on all boards and would otherwise be copied directly from existing firmware. A mature hardware abstraction layer (HAL) for STM32 MCUs already exists

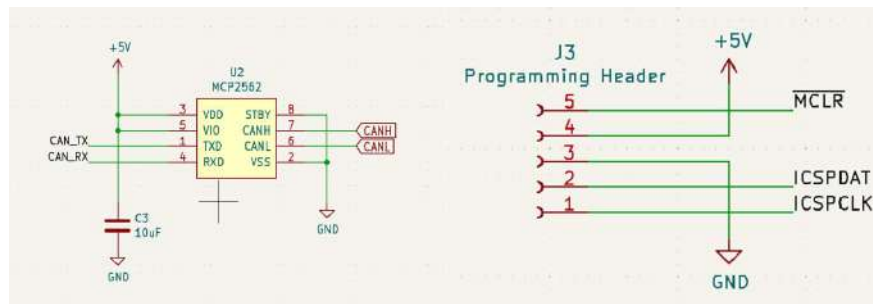


Figure 9.7: MCP2562 CAN transceiver and PICKit3 programming header schematic

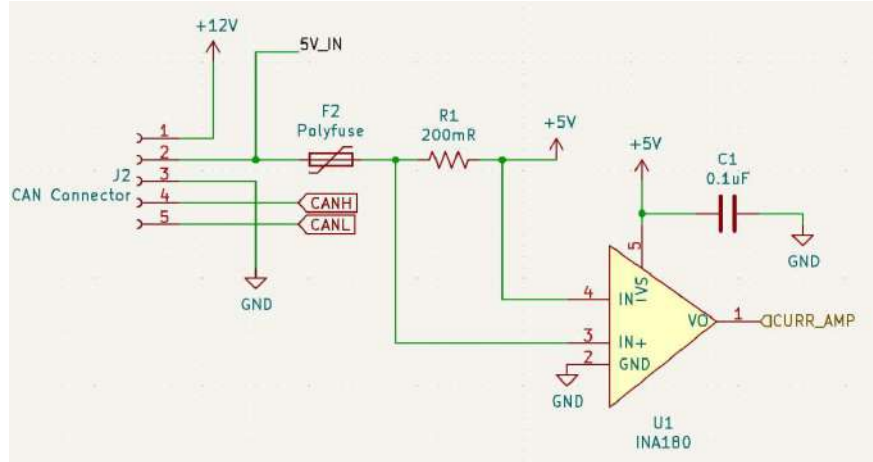


Figure 9.8: RocketCAN bus connection and current sensing

and is actively maintained by ST and this is used for boards based on these MCUs instead.

#### 9.1.4 Message Format

This year, the team has moved to the CAN 2.0B standard, on top of which the RocketCAN message format has been redesigned. An example of a single, generic CAN message is shown in Figure 9.9.

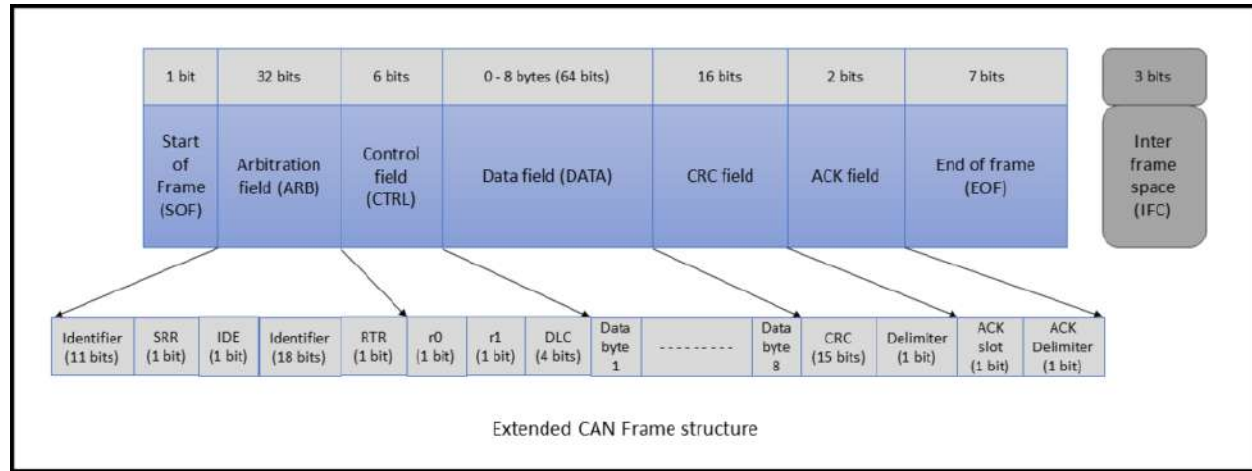


Figure 9.9: CAN 2.0B Extended ID message format [25]

The key fields in the CAN message are Arbitration, Data, CRC, and ACK. The CRC, or Cyclic Redundancy Check, is built into the CAN hardware, and provides robust error detection for each message, ensuring no false data or commands are read, without the need for any software. The ACK bit is asserted by any other controller on the bus to signal a message has been successfully received. The data field of a CAN message can be up to 8 bytes long and carries the information in each message. The 29 identification bits are used to determine the priority level of a message, with all zeros being the highest priority, and all ones being the lowest. RocketCAN splits these bits into four fields: the priority, the message type, the board type ID, and the board instance ID. They are

divided as shown in Table 9.2. Since the most important criteria for prioritizing messages on the bus is typically their purpose, the most significant bits are dedicated to global priority and message type. This means that, for example, valve and altimeter arming commands will always supersede status messages, regardless of where those messages come from.

Table 9.2: RocketCAN message ID format

<b>Bit 28:27</b>	<b>Bit 26:18</b>	<b>Bit 17:16</b>	<b>Bit 15:8</b>	<b>Bit 7:0</b>	
SID (Identifier)		EID (Extended Identifier)			
Priority	Message Type	Reserved	Board Type ID	Board Instance ID	

### 9.1.5 Telemetry Architecture

The primary method of communication between the rocket and mission control is the wireless telemetry system. CAN messages sent on the rocket bus are serialized by Live Telemetry Transmitter Board (LT) as a UART stream and transmitted to mission control through the COTS RFD900x radio modem and an SRAD antenna. In the other direction, LT de-serializes commands from mission control into CAN messages and sends them to the rocket bus. The RFD900x modem was selected for its long range and ease of use as a transparent UART link over radio. It operates on the 900MHz band and has transmit power up to 1 watt.

CAN messages are serialized into ASCII messages consisting of hexadecimal digits and separators. Each serialized message has a CRC8 code attached to ensure the integrity of data. This can prevent cases such as single bit error turning a "close injector" command into an "open injector" command, launching the rocket. While ASCII is not the most optimal format to transfer data in terms of bandwidth, a human readable format makes verifying the radio communication much easier using a FTDI cable and serial terminal. There is enough bandwidth over radio to accommodate for the overhead.

An SRAD antenna setup is used on the rocket side for the telemetry link. Two printed dipole antennas are evenly spaced around the body tube with mounts on the recovery electronics sled. This change allows for an increase in the amount of radiation pattern radially from the rocket, reducing the dead space required in the UBT. This approach also allows the antenna to lay flat inside the rocket, reducing the vertical space required. The two traces are connected to the RFD900x modem individually; the trace with the best received signal is automatically selected for communication. This eliminates blind spots in the radiation pattern, allowing radio communication from any direction regardless of the orientation. The antenna is shown in Figure 9.10.

At mission control side, two antennas are used. During flight, communication occurs through an SRAD helical antenna. This helical antenna is made from light-weight fibreglass, making it easy to move around by hand and aim. Furthermore, its circular polarization helps it maintain connection even when the rocket is spinning. When the rocket is on the pad or has landed, a high-gain COTS Yagi antenna is used in parallel to improve reliability.

Additionally, while the rocket is on the pad, the electrical ground support equipment (EGSE) acts as a backup line of communication via the electrical umbilical. The rocket's main CAN bus lines are routed through the umbilical to the DAQ system, which contains a board that can transmit

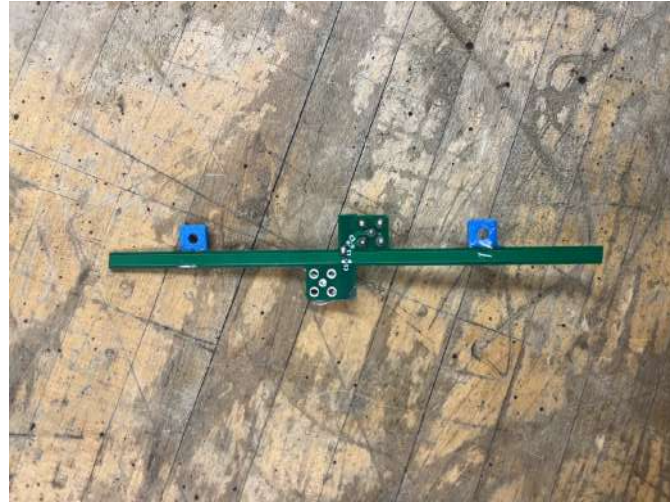


Figure 9.10: SRAD dipole antenna

and receive CAN messages over a USB connection. This data stream is then passed over the EGSE antenna link along with the usual traffic from DAQ and RLCS. Because the electrical umbilical disconnects after liftoff, this backup link is fully sufficient to launch the rocket in the event of a telemetry failure.

### 9.1.6 Power Architecture

The bus contains both a 5 V regulated and 12 V unregulated line. The 5 V regulated line saves on board space, since individual boards which may have limited functionality and thus low power draw (such as GPS board) do not need to include their own power regulation circuits. Boards that use significant amounts of power, such as Live Telemetry or Camera, draw from the 12 V unregulated line, which is connected directly to the main rocket battery (and thus fluctuates from 10 V to 12.6 V during operation).

RocketCAN power rails are provided by a single power distribution board connected to an onboard battery, which powers all avionics except the COTS altimeters (which have isolated 9 V batteries). For mass savings and standardization across the team's electrical systems, this battery is a single 3S Lithium-Polymer (LiPo). It can provide sufficient power during operations and flight, but there is a risk of the battery dropping too low during extended operations post-assembly, as was observed in 2022. In 2023, the team implemented on-pad charging in order to keep the rocket battery topped up during these extended operations. For both LOTS and Borealis, charging was achieved by passing a 24 V line from EGSE through the electrical umbilical to the power distribution board, which was then responsible for charging the rocket battery.

As the rocket electrical system has become more complicated, more boards on the rocket require their own batteries. SRAD Altimeter Board (which was de-scoped from flight this year) has two LiPos, and Motor Control Board for the canards also has a LiPo. Finally, the payload has its own, independent RocketCAN bus (see 9.1.7) with its own copy of Rocket Power Board. For this reason, the 24 V line of the bus has been replaced with Ground-Side Charging Board (GSCB), located in the EGSE. All batteries on the rocket are connected in parallel to a charge line, which connects to EGSE through the rocket umbilical. This new board contains a LiPo charge chip,

similar to what was flown on Charging Board previously. It supplies a constant current of 1A to the charge line, up to the safe charging voltage of the LiPos ( 12.6 V). This current is passively distributed between all the batteries on the rocket. The individual batteries are connected to the charge line through a diode to prevent them attempting to balance each other. The typical battery charge stage is shown in Figure 9.11. Once all batteries on the rocket have reached the maximum charge voltage, the charger shuts off. Although 1 A is little current when split across up to five batteries, batteries are assembled into the rocket fully charged, and charging only serves to keep them topped up.

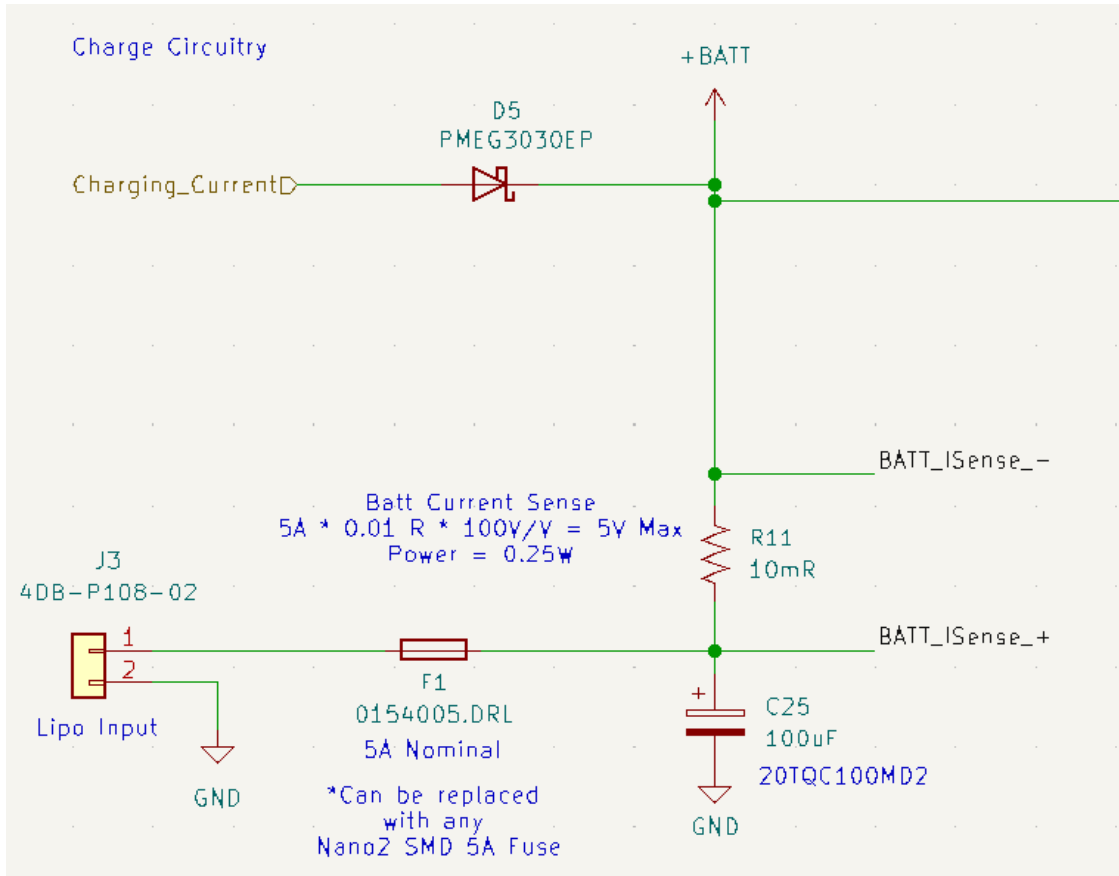


Figure 9.11: 2025 standard battery charge circuit

### 9.1.7 Payload Secondary Bus

Aurora contains a deployable payload, which introduces significant complexity to the electrical connection. The payload must have its own recovery electronics which meet the same safety and redundancy requirements as the main rocket, contain additional electronics to achieve the experiment objectives, and be monitored (and armed) from the ground along with the main rocket avionics. To achieve these requirements, the payload contains its own copies of Remote Arming Board, Rocket Power Board, and the COTS altimeters. To avoid an internal electrical connection with the rest of the rocket, which would need to be severed during payload deployment, the payload has its own independent electrical umbilical.

## 9.2 SRAD Avionics Boards

Per the design philosophy of RocketCAN, many boards are reused from previous design cycles. A more detailed analysis is provided for boards developed this year, while an abridged description is provided for boards that are being re-flown. Table 9.3 provides internal or external references to detailed design information for each board, as applicable. Remote Arming is addressed later in subsection 10.7, alongside the rest of the recovery system wiring.

Table 9.3: Summary of SRAD avionics

Board	Last Revised	Reference for Detailed Design
Rocket Power	2025	subsubsection 9.2.1
Injector Sensor	2025	subsubsection 9.2.2
Live Telemetry Transmitter	2023	[17]
Camera/Logger	2024	[26]
Remote Arming	2024	subsection 10.7
GPS	2022	[27]
Motor Control	2024	subsection 12.4
Processor	2025	subsection 12.5
Payload Motor	2025	??
Payload Sensor	2025	??

### 9.2.1 Rocket Power Board

The power distribution board flown on Borealis, Charging Board, was designed to fill the roles of both power distribution and motor control via reconfigurable solder jumpers. The time spent troubleshooting that board and its different configurations that year was significant, including during final assembly at competition. Again this year, the payload and active control system have motors which require SRAD avionics to control. This year, however, the functions of payload motor control, canard motor control, and power distribution have been split into three distinct boards. This architecture has allowed each board to be simplified, targeting and optimizing for a smaller set of requirements than if they had been combined.

Rocket Power Board fulfills the power distribution requirements of the RocketCAN bus and is designed around the new ground-side charging architecture. It connects to a single 3S LiPo battery (Figure 9.11), and supplies an unregulated 12 V line as well as a regulated 5 V line. Each can be toggled on and off by the board, allowing the entire bus to be shut off to minimize power consumption.

Charging Board was designed with non-resettable fuses on the 12V line. During final electrical integration of Borealis, it was discovered the inrush current due to the capacitance of the bus was high enough to blow this fuse, even though the fuse was appropriately sized for the steady state current draw. To mitigate this and a number of other failure modes, both power lines now run through a TPS25947 electronic fuse (e-fuse). This chip integrates over-current, over-voltage, and under-voltage lockouts, slew rate control to limit inrush current, and fault state feedback. It can also be disabled by the MCU to manually shut off the line and conserve power. The e-fuse circuit

for the 12 V line is shown in Figure 9.12; the 5 V circuit is functionally identical. The remainder of the board uses the RocketCAN common hardware architecture. The MCU monitors the voltage and current draw of the battery, 12 V, and 5 V lines, and raises an error if any values fall outside their specified range.

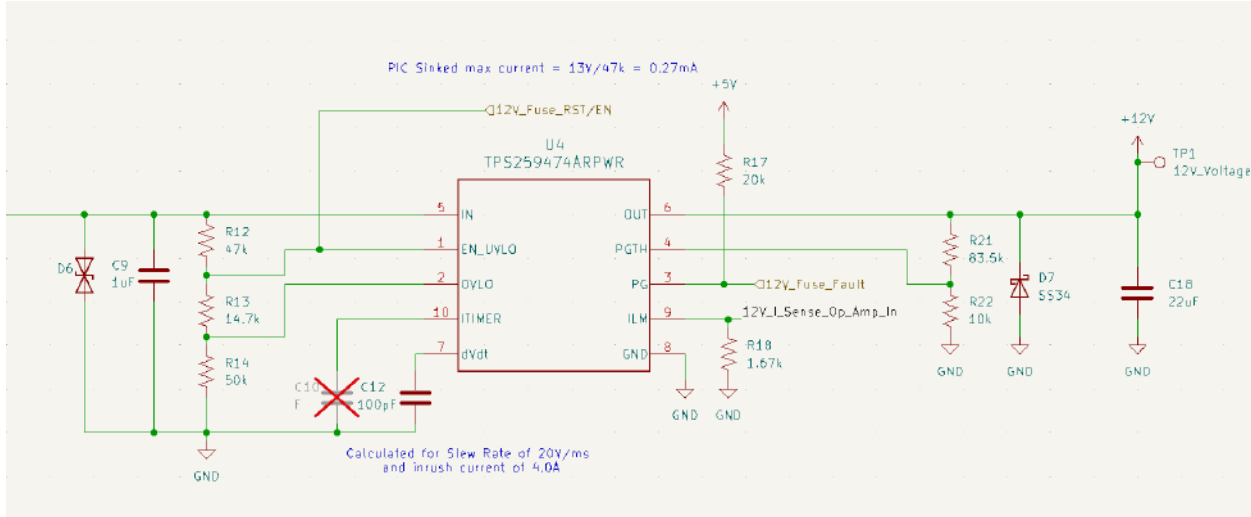


Figure 9.12: Rocket Power Board e-fuse circuit

## 9.2.2 Injector Sensor Board

Propulsion Board, developed for Borealis, had a number of design flaws which made it undesirable to reuse. Since the requirements from propulsion for avionics has decreased significantly on Aurora, it was decided to develop a new, simplified board. For both LOTS and Borealis, onboard valves were controlled with a dedicated pneumatics system and solenoids. Since Aurora runs on entirely ground-actuated valves, there is no requirement for rocket-side actuation. Thermistors, which have been experimented with in the past to infer propellant characteristics, have also been discarded.

The only requirement from the propulsion system is to read four pressure transducers and two hall sensors. Pressure transducers sense the chamber pressure and fuel/oxidizer pressures, and Hall effect sensors are used to measure the displacement of a ring of magnets connected to each of the injector valve sleeves, providing state feedback for those valves.

The board is based mostly on the RocketCAN common architecture. It has eight analog sensor channels which are connected to the PIC18's ADC. These support four pressure transducers: oxidizer, fuel, and two (redundant) for combustion chamber pressure, as well as a Hall sensor for each of the injector valves. A spare channel for each type of sensor is included, which offers flexibility if a channel malfunctions. The typical channel design is shown in Figure 9.13

## 9.2.3 GPS Board

With the use of an M10578-A2 GPS receiver, GPS Board locates the rocket in space and transmits this data over the CAN bus. This data is transmitted to mission control through the telemetry

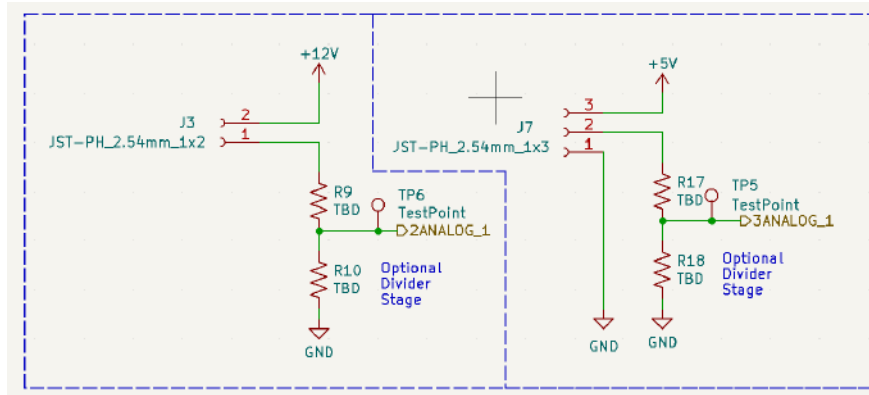


Figure 9.13: Injector Sensor Board 2-wire and 3-wire sensor connections

system to provide a secondary method of tracking the rocket, and is also logged to provide data for post-flight analysis.

#### 9.2.4 Live Telemetry Transmitter

The purpose of the Live Telemetry Transmitter (LTT) is to act as a two-way CAN to UART converter between the RocketCAN bus and the radio modem as described in section 9.2.4. The board uses 12 V as its power source. A switching regulator steps 12 V down to 5 V to supply the radio modem, and a linear regulator produces 3.3 V from 5 V to supply the PIC18. This way, LTT can remain powered up and communicating with mission control while the 5 V line is turned off to conserve power. In addition, power to the radio can be switched off or reset by the MCU, either manually through hard wired RLCS CAN connection or automatically through a timeout timer in the code.

#### 9.2.5 Camera/Logger Board

Camera Board was designed for Borealis as a replacement for COTS FPV camera modules, and is responsible for recording in-flight video from the rocket. It is built around the OV5640 image sensor which provides JPEG frames to an STM32H750 MCU at 720p/30fps. The board includes an SD card for storing footage, a USB port to upload footage to a computer, and a connection to the RocketCAN bus for control.

Additionally, the fast processor and SD card on the board also allows it to be used to log all messages on the CAN bus for post-flight review. In this configuration the image sensor is not connected to the board, and RocketCAN data is instead logged to the SD card. Electrically these two modes are identical, with the only difference being what firmware is flashed to the board.

### 9.3 BigRedBee GPS

In addition to the GPS board, the rocket contains a commercial BigRedBee (BRB) GPS. This board is stored in a mount in the nosecone and has its own independent power supply. In 2022, the team had considerable difficulty with this battery depleting for the duration it was plugged in. In 2023, the chosen mitigation involved charging the BRB through the nosecone tip and shear pin

coupler, which was successful but difficult to work with and required constant contact between the two outer metal surfaces. For Borealis, it was decided to arm and charge via a screw switch in the nosecone surface. Before installation, the BRB is installed into a mount and connected electrically to a screw switch and a Dupont connector underneath the screw switch. The BRB is then armed with a #6-32 screw to the outside, or charged by feeding a solid core wire through a #6-32 which connects to ground, and the #6-32 connects to the positive terminal of the battery. This configuration allows arming and charging of the BRB through only a #6-32 hole in the nosecone, preserving surface finish and accessibility. The mount is partially bonded into the nosecone, and the two mount halves are fastened with double sided tape and two axial M3 screws. This mounting solution was validated at IREC 2023 and LC 2024.

Aurora's nosecone contains a deployable payload. The nosecone fully separates from the rocket at apogee to complete its own, independent recovery with the payload. Since two rocket sections must be recovered, each contains its own independent BRB. Figure 9.14 shows the nosecone BRB mount, which is similar to previous rockets, while Figure 9.15 shows the main rocket BRB, which is mounted in the upper bodytube in the same manner.

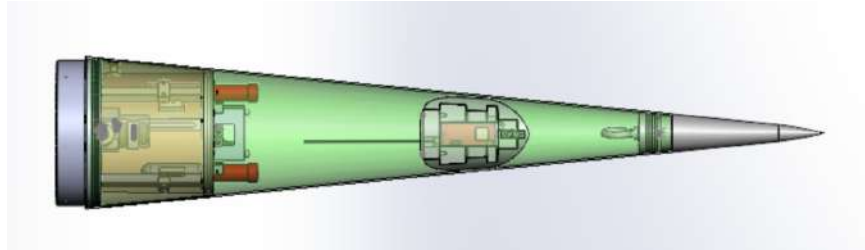


Figure 9.14: Nosecone BRB mounting



Figure 9.15: Main rocket BRB mounting

# 10 RECOVERY SYSTEM

## 10.1 Overview

Aurora is recovered with a single-separation, dual-deployment recovery system. At apogee, a pair of SRAD dual-redundant ejectors punctures two 38 g CO<sub>2</sub> canisters, rapidly pressurizing the recovery bay until the pressure shears six nylon rivets. At this point, a loosely packed pilot chute is released into the air stream. The pilot chute extracts the drogue parachute in its parachute bag in a lines-first deployment. The drogue stabilizes and decelerates the rocket from apogee of 50 000 ft down to 1 500 ft AGL. At 1 500 ft AGL, the drogue is partially released from the rocket by a two-ring release system actuated by dual-redundant SRAD line cutters. The drogue extracts the main parachute out of its canister, allowing a predictable line-first deployment sequence. A rigging diagram is presented in Figure 10.1.

This year, there is a focus on flight data collection of the new dual-deployment system, to better understand how the recovery system functions at high altitudes. An upward-facing camera is integrated into the recovery bulkhead to record the system deployment and descent from apogee. The intention is to aid in the future development of recovery systems and provide a strong base for further mass and volume optimizations.

The addition of a mid-design cycle test flight allowed the recovery system to be tested in a fully integrated and realistic environment. The recovery system performed as designed, with full drogue and main parachute deployment, marking the first successful recovery in the team's history. Furthermore, all four pyrotechnic devices actuated successfully, demonstrating the full functionality of the harnessing and altimeters.

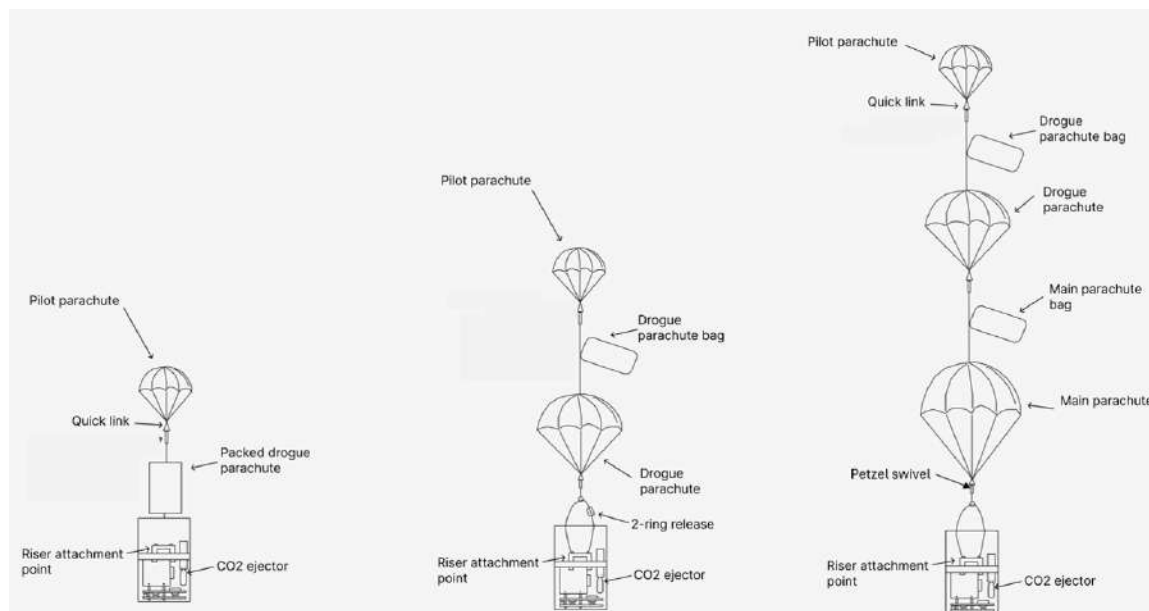


Figure 10.1: Rigging diagram

## 10.2 Past Failures and New Changes

Last year's rocket carried the team's most advanced reefing system. Using pyrocutter located in the parachute canopy, the reefing line was successfully cut, yet the parachute did not fully inflate, marking the third unsuccessful reefing recovery. Due to shifting team objectives towards higher altitude flights, the decision was made to move from a reefing to dual-deploy system. This would permit the drogue parachute to be tailored to the much faster descent rate, increasing its stability and structural integrity.

The change to a dual-deploy system necessitated a major overhaul of the recovery architecture. In order to ensure a high system reliability, and meet tighter deadlines than the subsystem faced before, two key factors were prioritized throughout the entire design.

First, all successful components of previous recovery systems were reused where possible. Certain hardware such as line cutters, which have performed as designed in multiple flights, were reused. The nosecone ejection system and parachute deployment methods were also reused as much as possible from previous flights. This reduced the development time and increased the reliability of the system.

Second, the system was simplified as much as possible. With the exception of the bulkhead camera, every piece of hardware in the recovery system is flight critical. This allowed the team to ensure each component was designed properly and thoroughly, serving the fundamental goal of providing a strong base for future designs to iterate from.

## 10.3 Structural Design

### 10.3.1 Recovery Bulkhead and Camera

The recovery bulkhead, Figure 10.2, is the main structural component of the recovery system. Every component of the recovery system is mounted directly to the bulkhead, reducing part count and simplifying the assembly process. A major component of the recovery bulkhead is a 5.5 in diameter G12 fibreglass tube, which is directly bonded to the bulkhead with West Systems 105. The tube stores the main parachute throughout flight until its deployment. Composite tube was chosen due to its high stiffness and strength-to-weight ratio; the smooth interior surface also facilitates parachute deployment. The main parachute sits below the CO<sub>2</sub> ejectors, protecting it from the blast, and using the available space efficiently. The two ejectors are threaded into mounting holes located in the bulkhead. Attached to the bulkhead with two bolts each are the parachute attachment points.

The bulkhead is made from 6061-T6 aluminum, while the parachute attachment points are made from 7075-T6 aluminum. The structural strength of the bulkhead and parachute attachment points was validated with SolidWorks FEA, as seen in Figure 10.3, with no part of the system yielding under a load two times higher than expected. The bulkhead is secured to the airframe with eight radial bolts. Around the entire edge of the bulkhead is a soft Buna-N O-ring, which creates a hermetic seal reducing the amount of CO<sub>2</sub> needed to successfully eject the nosecone.

To protect the recovery harnessing from damage during parachute packing and regular recovery operations, a 3D printed shroud encloses the screw terminal blocks. As seen in Figure 10.4, the shroud contains three clearance holes for M3 screws that are threaded directly into the bulkhead. The shroud covers the two bulkhead passthroughs, and also has features to facilitate cable

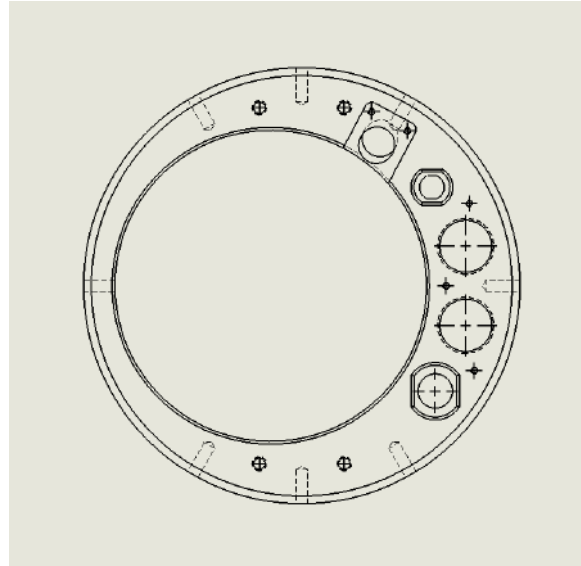


Figure 10.2: Recovery bulkhead detailed view

management.

To capture valuable data on how the recovery system functions in flight, a camera is integrated into the bulkhead, shown in Figure 10.5. The camera assembly consists of 3 parts: the image sensor itself, a copy of Camera Board, and 3D printed mounting hardware. To ensure a good view of the deployment, the camera is angled 5 degrees toward the inside of the bulkhead. The camera is mounted with a 3D printed enclosure which is bolted directly to the bulkhead. Above the lens, there is a thin sheet of polycarbonate which protects the fragile hardware. The PCB is bolted into a 3D print bonded to the main parachute tube.

### 10.3.2 Peak Load Calculations

The opening load forces for both the main and the drogue parachutes were calculated using the Pflanz Method. This method assumes that the drag area of the parachute would increase from a low value to 100% in a given time and in a mathematically definable form. The Pflanz method includes altitude effects but does not take into account gravity effects or drag area overshoot, as described by Knacke [28]. To calculate the parachute opening force load, Equation 10.1 was used.

$$F_{opening} = (C_D S)_p \cdot q \cdot C_X \cdot X_i \quad (10.1)$$

where  $F_{opening}$  = opening load

$(C_D S)_p$  = parachute drag area, fully open,  $ft^2$

$q$  = the dynamic pressure at line stretch

$C_X$  = the opening-force coefficient at infinite mass, dimensionless from Knacke [28]

$X_i$  = force reduction factor, dimensionless

In order to calculate  $X_i$ , a dimensionless ballistic parameter  $A$  is first calculated using Equation 10.2.

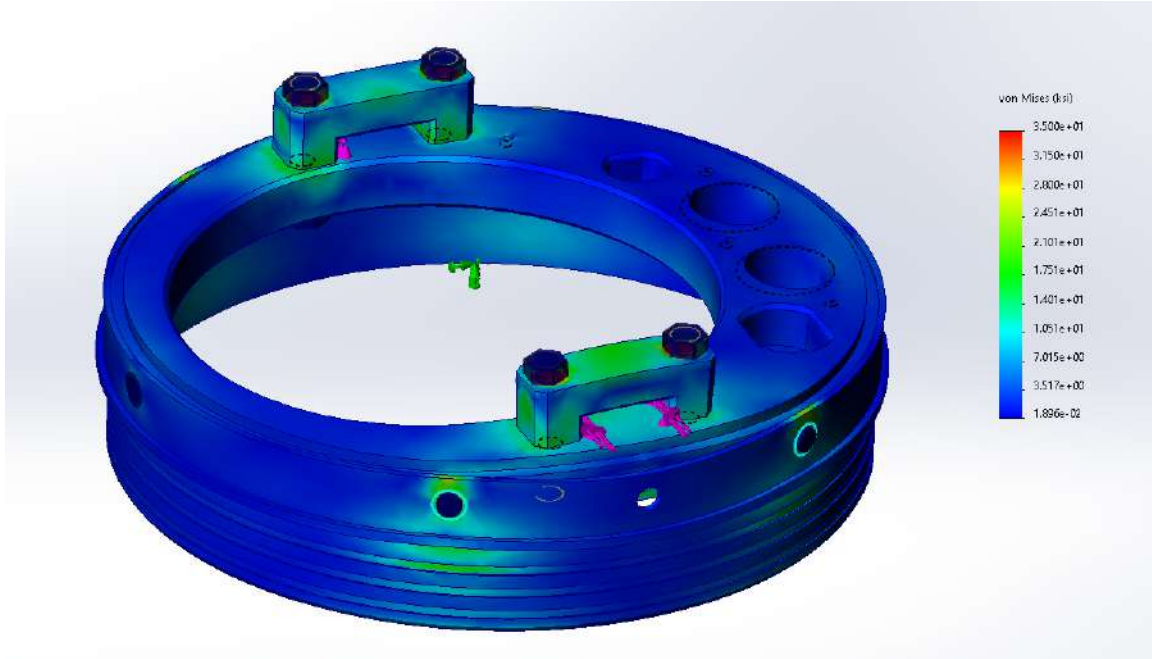


Figure 10.3: FEA results of recovery bulkhead

$$A = \frac{2W}{Cd \cdot S \cdot \rho \cdot g \cdot v \cdot t} \quad (10.2)$$

where       $A$  = ballistic parameter, dimensionless  
 $W$  = weight of rocket  
 $Cd$  = effective drag area constant  
 $S$  = area of chute (flat)  
 $\rho$  = air density  
 $v$  = velocity at line stretch  
 $t$  = time to inflate

The ballistic parameter is calculated to be 76.20 and 0.30 for the drogue and main parachutes, respectively. Using a chart provided by Knacke, Figure 10.6,  $X_i$  is found to be 1 and 0.25 for the drogue and main parachutes, respectively. These values are used with Equation 10.1 to calculate the opening load force.

The drogue parachute is intended to deploy at apogee, nominally 50 000 ft, where air density was found to be  $3.64 \cdot 10^{-4}$  slug · ft<sup>-3</sup> [29]. Remaining values were calculated based on the preliminary weight of the rocket, 130 lb, and the nominal drogue parachute diameter, 3.22 ft. Inputting the respective values into Equation 10.1, the drogue parachute opening load was determined to be 51.95 lbf, or 231.1 N.



Figure 10.4: Recovery harnessing protector

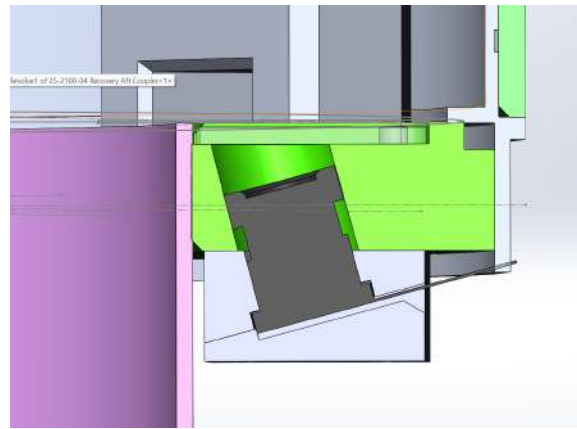


Figure 10.5: Recovery camera assembly

The main parachute is intended to deploy at 1500 ft AGL, and the air density here was found to be  $2.227 \cdot 10^{-3}$  slug · ft<sup>-3</sup> [29]. The same preliminary rocket weight of 130 lbs was used along with the nominal main parachute diameter, 10.66 ft. The main parachute opening load was determined to be 1280.53 lbf, or 5696 N.

There are some sources of error in this calculation. First, the velocity at line stretch was estimated to be 245 ft/s and 160 ft/s for the drogue and main parachutes, respectively. This was based on the team's Cycle 2 OpenRocket simulations, which are not the most current. Secondly, the force reduction factor  $X_i$  is estimated based on a chart it, and thus it is possible for there to be slight error in estimating the values from the figure.

Based on these calculations, the drogue and main opening loads will be within the structural limits of the airframe with a FOS of at least 2.0, indicating that parachute deployment will not compromise the structural integrity of the rocket.

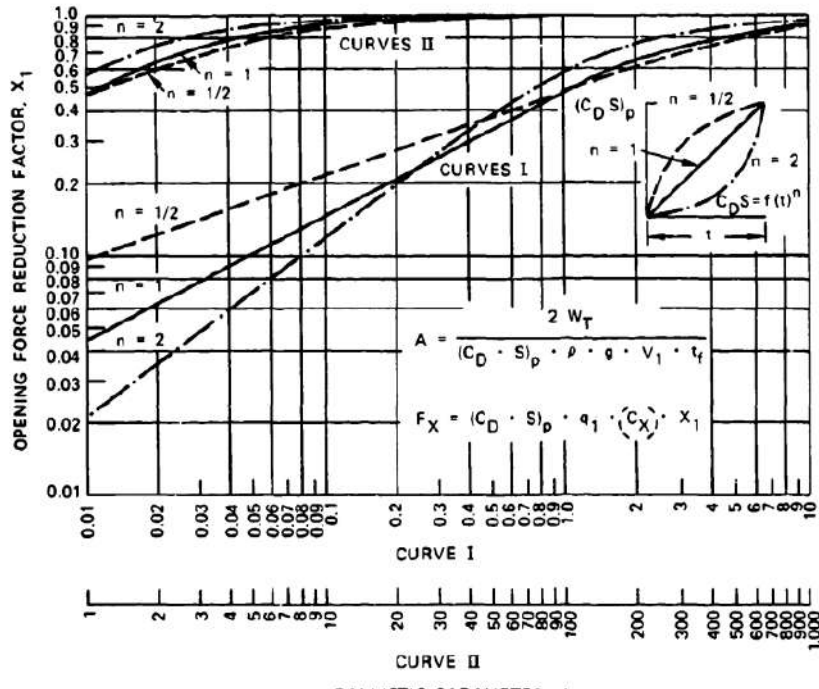


FIGURE 5-51. Opening-Force Reduction Factor,  $X_i$ , Versus Ballistic Parameter,  $A$ .

Figure 10.6: Opening force reduction factor  $X_i$  vs ballistic parameter  $A$  [28]

## 10.4 Parachute Design

### 10.4.1 Drogue Parachute

The drogue chute is a 30 degree conical ribbon parachute, chosen for its extensive flight heritage as a drogue chute for dozens of vehicles [28]. The high stability, as well as proven ability in the super/sub-sonic regime, makes this parachute a good choice for descent from 50 000 ft to 1500 ft AGL. Furthermore, this choice aligns with the team's ambitions to pursue higher altitude flights, by maintaining its properties and structural integrity at very high descent rates. The drogue was designed following design best practices specifically for conical ribbon parachutes as well as a detailed step-by-step conical ribbon design by Knacke [28] ensuring proper inflation and accurate drag.

When the rocket is coming down under drogue, it is also coming down under the pilot parachute, however the drag effects of the pilot parachute were not taken into effect. This is because the structural integrity of the pilot cannot be guaranteed during the entire descent as it is not designed for a high speed descent at low air pressure. In order to protect for the worst case scenario where the pilot shreds on descent, the drogue must provide sufficient drag to adequately decelerate the rocket on its own.

The drogue was designed early in the design cycle, before accurate vehicle masses could be collected. As a result, it was initially designed for a descent rate of 140 ft/s, with a rocket weighing 100 lb and a  $C_D$  of 0.55. The completed drogue parachute design uses 12 gores and has a flat radius of 48 cm. Its deployed canopy has a diameter of approximately 3.2 ft, with a total surface area of

about 8 ft<sup>2</sup>. The parachute was designed to withstand a load of 1 000 lbf. Each gore contains 11 horizontal ribbons, each 1.5 in wide and spaced 0.3 in apart. Additionally, two vertical ribbons are sewn on each gore, 0.5 in wide and spaced 3.75 in apart. All ribbons are constructed from nylon webbing and sewed with nylon thread. Manufacturing of the drogue parachute was completed in early March 2025. See Figure 10.7 for an image of the inflated drogue chute.



Figure 10.7: Completed drogue parachute

The suspension lines are made from CYPRES AAD line ("cypress"), with each line measuring 120 cm from end to end. Each includes a 3 cm loop at each end, which is used for attachment to both the parachute and the carabiner. The length was chosen to be 1.25 times the parachute's diameter, to account for slightly higher rocket mass.

In April 2025, the parachute underwent ground-based truck testing (Figure 10.8), where it inflated nominally. This test validated the parachute's aerodynamic stability and structural performance, despite the turbulent air caused by the truck, it remained remarkably stable. The truck testing also helped gain an insight into how the parachute performed when attached to the deployment bag and pilot parachute. The data collected from the truck test suggested the drogue had a  $C_D$  of 0.27, and the drogue and pilot having a combined  $C_D$  of 0.56. While these coefficients are well below the predicted, the large truck wake effects could reduce the computed  $C_D$  by as much as 30-50%, as that portion of the parachute's area was obstructed by the truck [28].

During the May 2025 test flight, two major discrepancies in the recovery system were discovered. First, the parachute did not inflate as expected. This was determined to be the result of insufficient descent velocity, as the test vehicle was significantly lighter than Aurora. The lower mass resulted in a slower descent rate and inadequate dynamic pressure for full inflation. This is further supported by the parachute inflating properly in the truck test, where the air speed was much higher. Second, the observed descent speed under drogue was approximately 73.4 ft/s, compared to the theoretical design speed of 150 ft/s for a properly loaded system. This allows for a more accurate  $C_D$  of 0.64 to be calculated.

Finally, the data from the test flight could be combined with more up-to-date mass estimates for a final estimated descent rate of 147-160 ft/s under drogue. This is relatively close to the

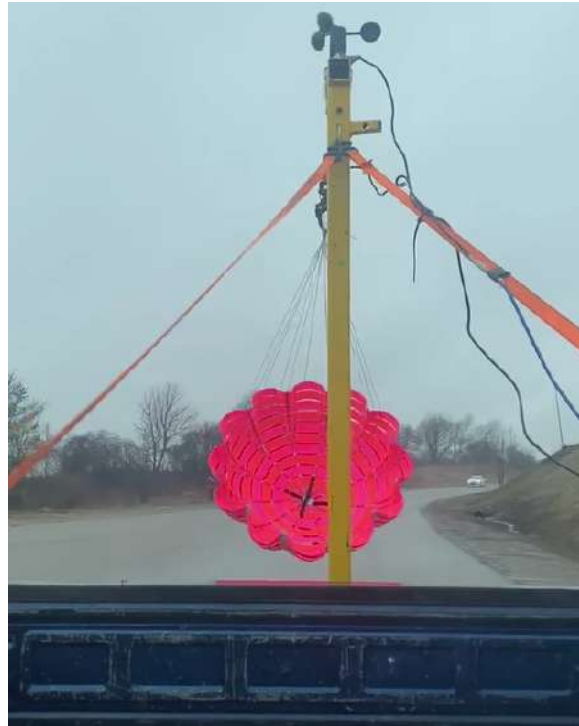


Figure 10.8: Drogue parachute during truck test

targeted descent rate of 150 ft/s, offering high descent rate for a low dispersion while slow enough to produce manageable shock loads upon main deployment.

The drogue parachute bag is manufactured in the shape of a cylinder, with a diameter of 7 in, so that the parachute and bag will easily come out of the body tube. There is a little over 1.5 m between the point of confluence of the pilot parachute to the drogue parachute (see Figure 10.9 for details).

The drogue parachute is packed by first folding the flat canopy in half along its centre line. It is then folded into compact triangular sections. Next, the parachute is folded lengthwise using an accordion-style fold to form a compact bundle. This packing method ensures that the suspension lines exit from one end, while the attachment point to the parachute bag is located at the opposite end. Once folded, the cypress suspension lines are carefully threaded through the elastic loops on the parachute bag to secure them in place and minimize the risk of entanglement during deployment. Figure 10.10 shows the drogue in a packed configuration.

#### 10.4.2 Main Parachute

The main parachute is an SRAD hemispherical design reused from a previous flight. This allowed for more time to be focused on developing the drogue chute, with which the team had less experience due to having used a reefing system previously. The parachute has a diameter of 10.7 ft with an area of 89.2 ft<sup>2</sup>. Previous truck testing placed the  $C_D$  of the parachute at 1.23. The calculated descent rate of the parachute under main using the most recent mass estimates is 30.1 ft/s. While the original target decent rate was calculated early into the design cycle at 25 ft/s, the mass of the



Figure 10.9: Drogue parachute bag lengths

rocket significantly increased as the designs matured. A more accurate descent speed is about 29 ft/s, which meets DTEG regulations.

Given the changes to the recovery sequence, a new parachute bag was designed. The focus was to prevent potential friction damage to the suspension lines during deployment, while maintaining a consistent and reliable deployment order. This is achieved by routing all suspension lines directly underneath the parachute, rather than up the side, as had been done in previous launches. This change in the design also reduces the possibility of suspension lines catching on recovery hardware as the parachute is extracted.

Parachute packing is based on skydiver parachute packing and circular military parachute folding methods. They show an initial dart folding, followed by z-folds to insert the parachute into the bag to make for a smoother deployment. This has the benefit for the parachute exiting the bag ready to deploy, which leads to lower opening shock as the rocket has less time to accelerate. This packing system has been flight tested twice successfully, most notably with the 2025 test flight.



Figure 10.10: Packed drogue parachute inside drogue parachute bag

#### 10.4.3 Rigging

The expected opening load forces on the main parachute are approximately 5 696 N, as determined in subsubsection 10.3.2. While all rigging is rated to a far higher load, it is also critical to ensure that the sewn loops can withstand such a load. A stitching pattern was developed in order to prevent the stitches in the rigging from ripping during deployment. The pattern consists of horizontal bars created by four passes of zigzag stitching. Figure 10.11 shows test patterns.



Figure 10.11: Rigging stitching pattern tensile test samples

Straight stitches were then layered across the bars, running along the length of the shock cord. A tensile test was conducted to determine how many bars are necessary to provide sufficient resistance against the opening load forces. Each sample was clamped at the top and bottom, with the stitched bar secured near the top and its free end left unstitched to replicate the layout used in the final parachute system.



Figure 10.12: Rigging stitching pattern tensile test samples

Results of the test showed that a single bar could withstand more than 10 789 N, about twice the predicted recovery load. The final design incorporated seven bars to ensure sufficient strength and reliability.



Figure 10.13: Final stitch pattern

Energy modulators were also proposed to reduce the high loads experienced during deployment of the main parachute. They were adapted from NASA's design for the Orion spacecraft [30]. They are four folds sewn into the Kevlar shock cord connected to the main parachute in a tested stitching pattern that will break upon deployment and dissipate a targeted total of 10 000 J. Although they were ultimately excluded from the final parachute configuration, they still underwent full design and testing. The energy modulators were intended to be sewn according to the pattern in Figure 10.14.



Figure 10.14: Energy modulator stitching pattern prototype

Cotton thread was stitched over the fold using an alternating pattern of zigzag and straight stitch for a total of four lines of zigzag stitching and three lines of straight stitching. A tensile test

(Figure 10.15) was performed by clamping the samples at both ends to simulate the pull on the shock cord during deployment of the parachute.



Figure 10.15: Energy modulator tensile test

Variations of the proposed pattern were used as samples during the test. While the energy modulators failed as expected, the strongest design was only capable of dissipating 50 J each. This is attributed to the selection of cotton thread which has an average breaking strength of approximately 2 lbf. Initially, cotton was chosen for its predictable failure characteristics and low cost, which made it suitable for intentional stitch breakage. However, it is too weak to dissipate a significant amount of energy. Although the tested configuration did not meet the project goals, results provided valuable insight for future iterations which should incorporate higher strength thread or explore more compact stitching patterns.

## 10.5 Nosecone and Drogue Deployment

The nosecone, and drogue deployment are actuated by the pressurization of the recovery bay with the team's new SRAD CO<sub>2</sub> ejectors. The parachute bay and nosecone are connected via six nylon rivets that act as shear pins to allow the nosecone to separate from the rest of the rocket. The shear pins break when at least one of the two CO<sub>2</sub> cartridges eject their contents into the parachute bay, thereby pressurizing it. This deployment method has been extensively tested through its use on the last six rockets flown by the team, and is tested thoroughly on the ground each year.

### 10.5.1 CO<sub>2</sub> Ejectors

Each CO<sub>2</sub> ejector consists of a puncture-actuated 38 g CO<sub>2</sub> cartridge housed in a machined aluminum body, designed to compactly integrate into the recovery bulkhead. Activation is achieved through a dual-redundant e-match system that ignites a small black powder charge. This charge drives a puncture pin into the sealed end of the CO<sub>2</sub> cartridge, releasing pressurized gas through

the ejector and into the recovery bay. The ejector body is threaded and sealed with a Buna-N O-ring, allowing for direct installation into tapped holes in the bulkhead while maintaining a reliable pressure seal. A cross section of the ejectors can be seen in Figure 10.16.

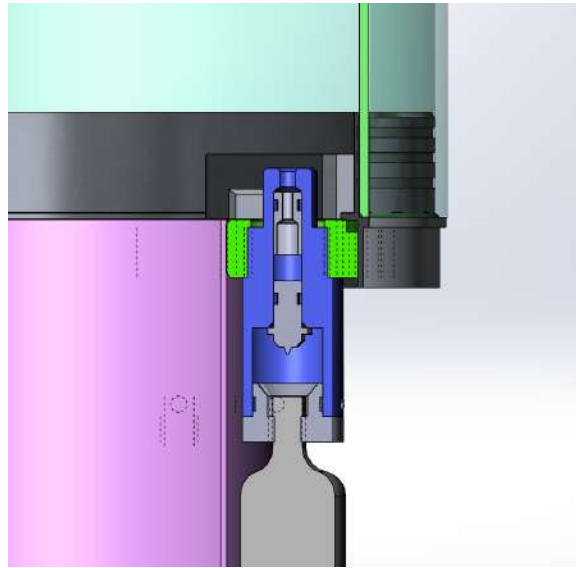


Figure 10.16: Cross-section of the SRAD CO<sub>2</sub> ejectors

These ejectors were tested extensively during subsystem evaluations and integrated test flights. Their compact form factor and threaded mounting simplified assembly, while the use of CO<sub>2</sub> enabled clean, residue-free pressurization. Ground testing confirmed reliable actuation with consistent pressure buildup and controlled nosecone separation. Lessons from earlier designs were incorporated to reduce leak paths, improve O-ring fit, and ensure consistent puncture geometry.

### 10.5.2 Vent Hole sizing

As the rocket ascends rapidly through the atmosphere, it experiences a pressure differential. The pressure of the outer atmosphere drops rapidly, and vent holes are needed to minimize the pressure difference between the inside of the rocket and the outer atmosphere. Given the large diameter of the rocket, even small pressure differences are highly pronounced, and can cause premature separation of the nosecone; such an event would be catastrophic.

To ensure sufficient margin with the shear pins and drag separation, it was decided that the vent hole would need to be sufficiently large to prevent any force greater than 72 lbf of building up. Using time, altitude and pressure data obtained from OpenRocket simulations, along with the length and diameter of the recovery section, the ideal hole size could be determined. An excel spreadsheet based on formulas created by David Schultz allowed for rapid hole sizing [31].

A hole diameter of 0.64 in was chosen as it would keep the force below 72 lb. Instead of one large hole, three holes of a diameter of 0.37 in were chosen. This would allow the pressure to equalize evenly, while also providing resistance against clogging if some rigging were drawn up to one of the holes.

### 10.5.3 Drag Separation

Drag separation occurs when the drag on the rocket body significantly exceeds that on the nosecone. This differential can result in a net pulling force on the coupler joint between the nosecone and the body. If this force is sufficient, it may lead to premature separation of the nosecone during flight, as described by the MIT Rocket Team [32]. To mitigate the risk of drag separation, an analysis was performed using Equation 10.3.

$$N = \frac{M_1 D_2 - M_2 D_1}{M_1 + M_2} \quad (10.3)$$

Where:  $M_1$  = mass of rocket body

$M_2$  = mass of nosecone

$D_1$  = drag force on rocket body

$D_2$  = drag force on nosecone

Using Equation 10.4, the estimated drag forces for the rocket body and the nosecone were calculated.

$$F_d = \frac{1}{2} \cdot \rho \cdot v^2 \cdot C_d \cdot A \quad (10.4)$$

Where:  $F_d$  = drag force

$\rho$  = density of air

$v$  = velocity of rocket

$C_d$  = drag coefficient

$A$  = reference area

Using these values N was found to be -963 N (-216 lb), indicating that without shear pins, a premature nosecone deployment would occur.

To retain the nosecone, nylon shear pins are used at the coupler joint. Based on prior testing, each nylon shear pin can withstand up to 72 lbf. To resist the calculated separation force, at least three shear pins are required. Aurora uses six nylon shear pins, providing a factor of safety of 2 to prevent premature nosecone deployment.

### 10.5.4 Pilot Extraction Force

A critical aspect of the recovery sequence is ensuring that the drogue is extracted immediately at apogee. This is because the pilot chute is not designed to work at very high altitudes and velocities.

The opening load force for the pilot parachute was calculated using subsubsection 10.3.2. The relevant parameters are presented in Table 10.1.

The resulting opening load of the pilot chute is 13.91 lbf or 61.86 N. With a previously measured drogue extraction force of 3.4 lbf, the pilot parachute generates four times more force than needed, ensuring a reliable extraction.

Table 10.1: Extraction force values

Variable	Value	Units
Air Density	0.0002845	slugs/ft <sup>3</sup>
Rocket Weight	118	lbs
Parachute diameter	2.91	ft
Drag area constant	0.75	-
Parachute Area	6.65	ft <sup>2</sup>
Dynamic Pressure	2.7881	lbf/ft <sup>2</sup>

### 10.5.5 Testing and Flight Test

The team plans to conduct a total of five deployment tests to prove the functionality of the system. Two successful deployment tests were performed prior to the test flight. Deployment of the system during the test flight itself was successful, as previously discussed. A flight-like deployment test using Aurora flight hardware was successful. A final deployment test is planned to ensure that the new recently purchased shear pins behave as expected.

## 10.6 Main Deployment and Two-ring Release

Deployment of the main parachute is the second critical phase of recovery operations. It occurs at 1500 ft AGL, and decelerates the rocket from descent rate of 150 ft/s to a descent rate 27 ft/s. When the altimeters detect an altitude of 1500 ft, they actuate a set of dual redundant custom line cutters. These are mounted on a two-ring release, similar to a mechanism that skydivers use. The actuation separates the drogue parachute from the drogue bridle, allowing it to extract the main parachute. The main parachute undergoes a lines first deployment, where the shock cord and suspension lines deploy prior to the parachute coming out of the parachute bag, reducing shock load and increasing the reliability of the system.

The two-ring release was chosen due to its reliability and simplicity. It is heavily based off of the common three-ring release mechanism used in nearly every skydiver's parachute. However, due to the much lower weight of the rocket, it was not necessary to include the 3rd ring, as the effective load was far below the rated strength of cypress line. Furthermore, it allowed the team to reuse the custom titanium line cutters that had been used in previous flights successfully as seen in Figure 10.17.

By extracting the main parachute with the drogue parachute, the reliability and simplicity of the recovery system was improved. While alternative options like a piston or parachute mortar have been used before, they would have required the use of an additional pyrotechnic or electromechanical device to actuate. Furthermore, this would incur a risk of the main parachute tangling with the drogue parachute as it is propelled upwards. Partially releasing the drogue, then using it to extract the main, addresses both of these issues.

The line cutters are designed to increase system reliability; they are machined, disassembled, and cleaned in-house. The line cutters consist of a titanium body, which provides a high degree of strength and longevity through corrosion resistance as seen in Figure 10.18. The tube has threads on each end, which allow for bolts to be inserted and tightened. Two radial holes are placed near the



Figure 10.17: 2-ring release mechanism

middle, one for the line being cut and one for additional venting. The bottommost bolt is machined with a through hole, allowing for two e-matches to fit, increasing reliability and redundancy. The e-matches and black power are placed inside a small 3D printed cup, for easy assembly. A pellet made of hardened tool steel is propelled by the black powder, and is stopped by the second bolt. These cutters have flown on three previous flights, and have successfully cut the line on each occasion.



Figure 10.18: SRAD pyrocutter

### 10.6.1 Testing

The testing of the main deployment system was conducted in three phases. Component testing, system testing and flight testing. In component testing the two ring release was loaded to approximately 1.5 times its maximum expected loads, ensuring its structural integrity. The two-ring release performed very well, as the applied load of approximately 90 lbf was far below the ultimate tensile strength of every component. To verify the function of the system under load, the entire system was tested with a mass simulator as seen in Figure 10.19. A mass of 90 lbf was suspended from the two-ring release in a flight-like configuration, and the line cutters were actuated three times, leading to a successful actuation every time. Finally, the entire system was tested in the test flight. While the test flight underwent much lower loads than expected in Aurora, it validated the system in very similar conditions to the of flight. All components of the system actuated exactly as expected, with both line cutters triggering and deploying the system. The flight test also functioned as a successful deployment test, with the main parachute deploying with no tangles, in the exact order it was designed for. This validated the main parachute deployment system for flight at Launch Canada.



Figure 10.19: Line cutters and 2-ring release testing

## 10.7 Recovery Electronics

Remote Arming is an SRAD board designed to eliminate the need for operators to climb a step ladder and use a magnet attached to a pole to arm the altimeters while standing directly under the rocket. In addition, it provides valuable instrumentation that allows for constant monitoring of the recovery system health before and during flight, allowing a comprehensive check of the system performance immediately prior to launch. The board communicates via RocketCAN, described in subsection 9.1 A block diagram of Remote Arming is presented in Figure 10.20.

Remote Arming is a single SRAD PCB, which all the key components of the recovery system are attached to securely, either with screws or locking Datamate connectors. This reduces the

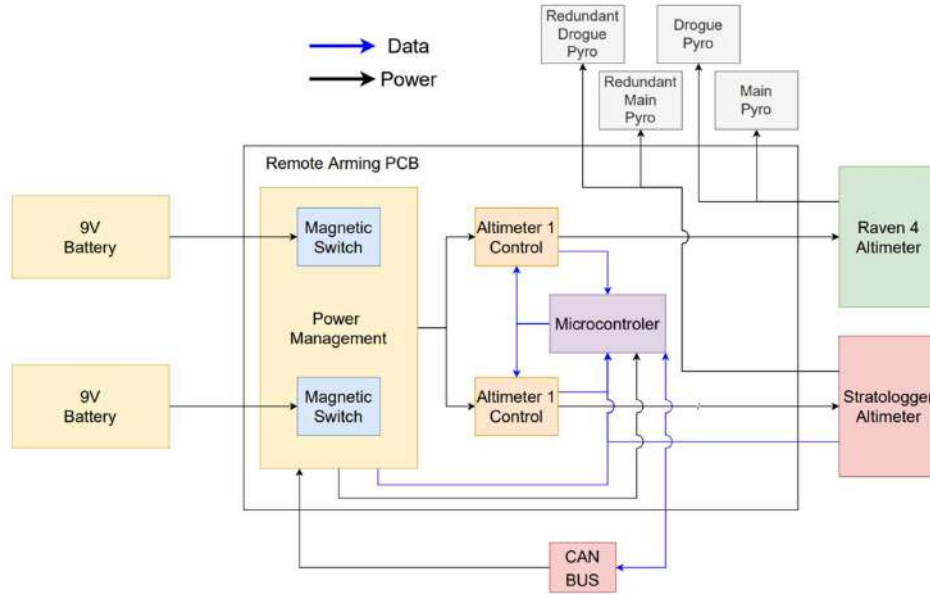


Figure 10.20: Remote Arming block diagram

complexity of the recovery wiring and the subsequent risk of mistakes or faults in the harness, such as bad crimps. The complete system is shown in Figure 10.21.

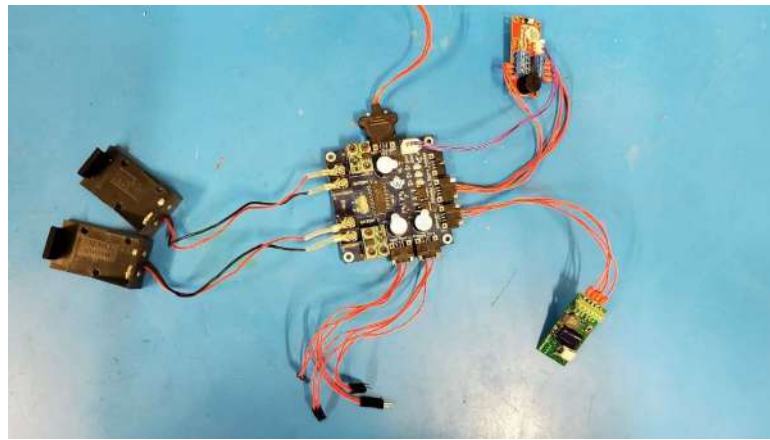


Figure 10.21: Complete Remote Arming system

### 10.7.1 Failing Safely

A core requirement for Remote Arming is to always fail safe. Most systems on the rocket must fail safe, however this usually has a well-defined, single meaning. For example, the vent valve should always fail open so as not to seal an SRAD pressure vessel. For Remote Arming, failing safely is more complex. While the rocket is on the ground it must fail in the disarmed state, as if it fails armed the pyrotechnics could accidentally be triggered, and an operator could be injured. However, once the rocket launches, the altimeters must stay armed, or the recovery system will fail. As such, once in-flight the system must fail armed.

It is not possible to design a system which will always fail armed and will always fail disarmed, so a compromise is made. The system is designed such that it will always fail armed. However, a pair of magnetic switches ensure that the recovery system can always be manually disarmed with a magnetic switch if needed. In addition, buzzers are continuously on whenever the altimeters are powered, to ensure that there is no possibility of personnel approaching the system without knowing it is armed.

Since both arming circuits are controlled by a single microcontroller, several measures have been taken to ensure that it does not cause a single point of failure:

- There is a pull up resistor which ensures that if the microcontroller fails or loses power, the circuit will keep the altimeter powered.
- The code on the microcontroller ensures that its default state on power up is armed, as such any temporary loss of power will not result in the altimeters disarming.
- A watchdog timer is used, such that if the main loop is ever hung up, the microcontroller will be reset.
- The microcontroller is powered both by the recovery batteries, and the RocketCAN bus, which adds redundancy and reduces the chances of a brown out.

### 10.7.2 Remote Arming ConOps

Since the logic of remote arming is designed to default to armed, some care must be taken in setting up the system for launch. The procedure is as follows:

- Since the magnetic switches' default state is closed, during assembly the 9 V batteries should be installed first, the magnetic switches turned off, and then the e-matches should be attached.
- Once the rocket has been full assembled, inspected, and loaded onto the launch rail, but before the rail is raised, the CAN bus should be powered up, Remote Arming should be commanded to disarm the altimeters, and then a magnet should be used to turn on the magnetic switches, checking the Remote Arming telemetry to ensure both switches are functioning correctly. The indicator buzzers will also play a distinct tone to indicate both batteries are functioning correctly.
- The CAN bus can then be powered down, and Remote Arming will continue operating using recovery battery power.
- Once the rocket is vertical on the tower and ready for launch, Remote Arming should be commanded to arm. The telemetry will then be checked to ensure the system is ready for launch. This includes the following:
  - Both battery and magnetic switch voltages are good.
  - Remote arming reports both altimeters armed.
  - Current draw from the recovery batteries matches expected value for all systems armed.
  - Drogue and main line cutter e-match voltages for each altimeter read as expected for the armed state.
  - Altitude data is being received from the Stratologger altimeter.

### 10.7.3 Power Management

Remote arming is powered by two 9 V batteries connected via a 4 A PTC fuse, each with their own voltage sensing and magnetic switch, as shown in Figure 10.22. A SM74611 smart diode is used with each battery to ensure a difference in voltage between the two does not cause issues. These diodes are designed for solar power generation and have a nominal voltage drop of only a few mV thanks to an internal FET and charge pump circuit, ensuring there is minimal power loss through the diode.

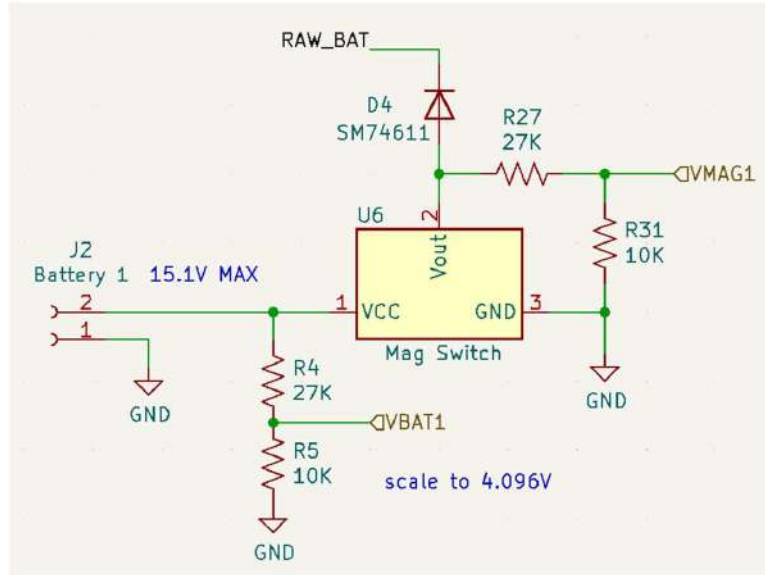


Figure 10.22: Remote Arming power circuit for one of two batteries

The microcontroller is powered by RocketCAN via the standard fuse and current sense amplifier connection, the only difference being a CUS08F30 Schottky diode to prevent Remote Arming from powering the bus with its backup 5V regulator, which draws power from the 9 V batteries. Current sensing from the 9V batteries is achieved using an INA180 amplifier as shown in Figure 10.23.

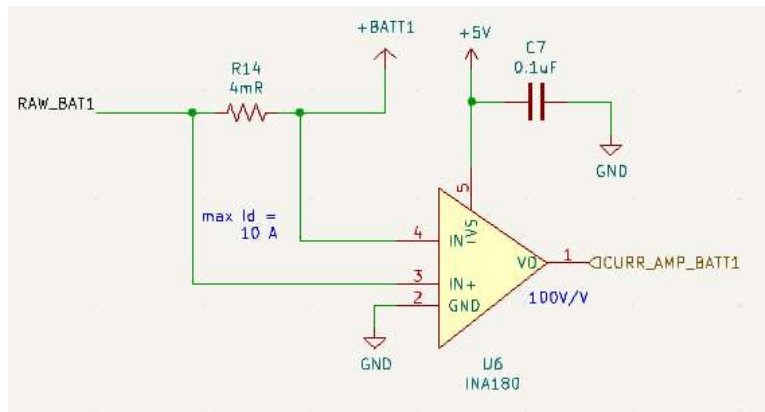


Figure 10.23: Recovery battery current sensing circuit

#### 10.7.4 Altimeter Control

Power to each altimeter is controlled by a P-channel MOSFET, which is in turn controlled by an N-channel MOSFET, to allow power to be switched on and off with the microcontroller's 5 V logic. This high-side switching is slightly more complex than if low-side switching was implemented with a single N-channel MOSFET, but ensuring that the altimeters and remote arming have a shared ground is needed for reading altitude data from the Stratologger. Pull-up solder jumpers are used with the Raven 4 altimeter, which does not have a dedicated positive pin for the drogue or main e-matches, and as such requires that they are externally connected to power. Each power control circuit has a buzzer that is on whenever the altimeter is powered. Two different frequencies are used to make it possible to identify which altimeters are powered.

#### 10.7.5 Telemetry

Remote arming has a total of 11 different sources of telemetry; the telemetry channels are as follows:

- Battery 1 and 2 voltage
- Magnetic switch 1 and 2 output voltage
- Voltage reading for all four of the drogue and main e-matches. This voltage reads close to the battery voltage while the altimeters are powered, and the e-matches connected, and close to zero if not. As such it is easy to verify that the recovery system is entirely functional immediately prior to launch.
- Current draw from the 9V recovery batteries, this has a maximum value of 4A so that the current draw of the e-matches firing can be measured. As such the signal is very noisy and imprecise when reading the passive current draw of the microcontroller. This is mitigated via the use of software low pass filters which allow reasonably accurate measurements down to approximately 20mA.
- Current draw from the CAN bus using the same architecture used on all other RocketCAN boards.
- Remote arming parses the UART altitude stream from the Stratologger altimeter and transmits it over the CAN bus so that the altitude can be monitored live during flight. The level shifting circuit can be seen in Figure 10.24.

#### 10.7.6 Remote Arming Testing

Remote Arming undergoes full system testing under bench-top conditions. It also undergoes a series of simulated flights where the complete recovery electronics system is put in a vacuum chamber.

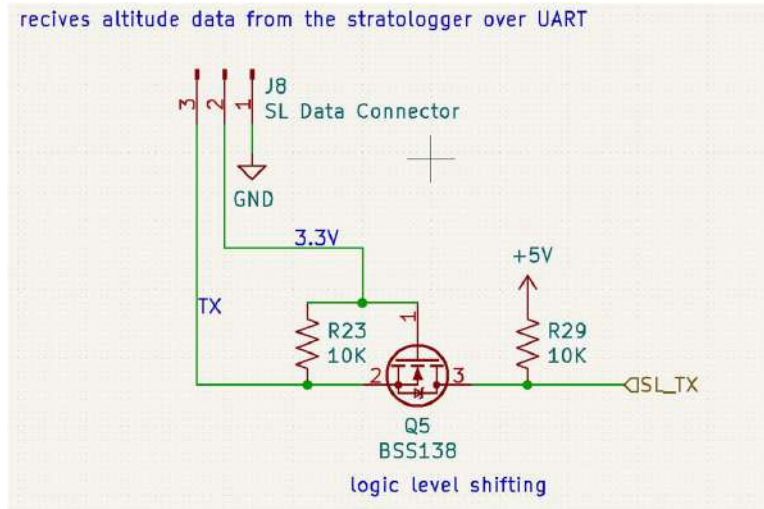


Figure 10.24: Stratologger telemetry level shifting circuit

In this test, a partial vacuum is pulled to simulate an increasing altitude, then air is slowly introduced back in to simulate apogee and descent. Referencing an aircraft altimeter, the test should confirm the drogue channel fired at apogee, and the main channel fired at a reading of 1500 ft. Throughout the process, the telemetry is also verified for correctness. Unfortunately, this test only works with the Stratologger altimeter, since its altitude measurement is solely barometric, while the Raven 4 uses an accelerometer along with the barometer. Both the Raven and Stratologger altimeters are tested with Remote Arming by connecting them to a computer and using their built-in, simulated flight tests.

The system uses a common power bus supplied by two redundant 9 V batteries. The single bus provides power to both redundant altimeters. This allows for a single 9 V failure as well as a single altimeter failure without a failure of the recovery system. While a joined power bus is deemed valuable for added reliability, this adds an additional failure mode. It is possible that a short-circuited e-match could cut power to both altimeters, leading to a failure. To test this during development, the main parachute pyro line was intentionally short circuited on one altimeter and that channel was fired while monitoring the status of the other altimeter. This test was then conducted with the two altimeters in opposite roles. This test confirmed that the brownout protection capacitors on each altimeter allow them to keep their state in the event of a drop of bus voltage due to a short-circuited e-match on the other altimeter. Therefore, this failure mode does not affect the operation of the other altimeter. As an extra safety measure, the single point of connection between the two circuits is a 4A PTC fuse. The fuse value was chosen heuristically from testing current draw of the e-matches while firing. This will prevent a short in one battery from taking out both systems, maintaining dual redundancy.

The copies of Remote Arming being flown Aurora are the same as those used on Borealis and the 2025 test flight, after undergoing re-verification and testing post-flight. For this reason, and due to multiple rockets worth of flight heritage for earlier, very similar designs, the team is extremely confident in the reliability of this system.

### 10.7.7 Recovery Electronics Sled

The recovery electronics, which comprise the COTS altimeters, Remote Arming Board, Rocket Power Board, Logger Board, LTT, and GPS Board are located on a compact sled attached to a plate beneath the parachute canister using custom L brackets. Care is taken to ensure proper strain relief and electrical routing to components and allow for ease of access for assembly and disassembly.

In order to increase accessibility to electronics boards and reduce the required disassembly in the event of replacement or maintenance, the structure of the recovery electronics sled was changed from a parallel plate to circular fibre-reinforced polymer (FRP) plates bridged using three fibreglass C-channels. These provide vertical mounting space as well as structural rigidity, as shown in Figure 10.25.

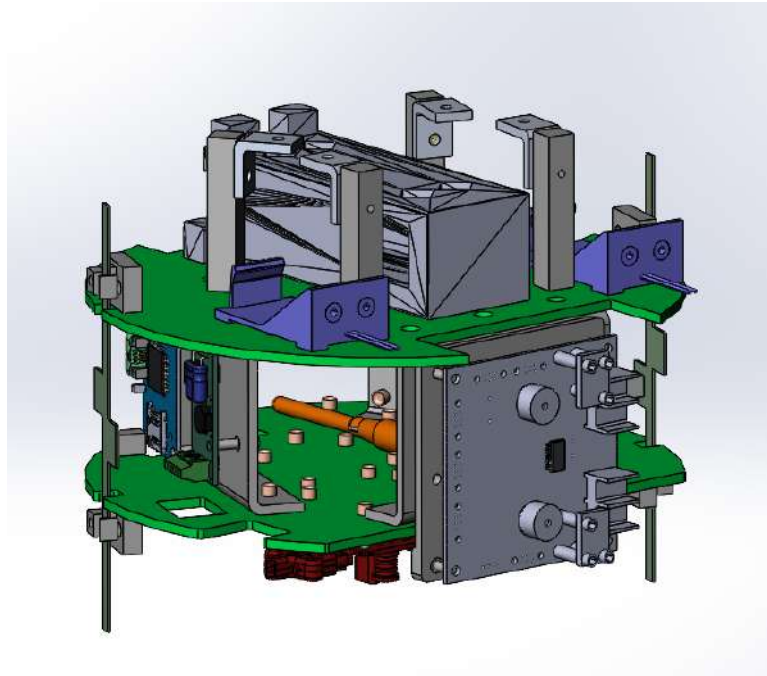


Figure 10.25: Recovery electronics sled

Additionally, to accommodate the change in telemetry antenna configuration, new mounting features were designed in order to vertically secure the PCB antennas. Mounts are 3D printed from PETG and bonded to the sled plates using West Systems epoxy. Matching adapters are bonded to the LTT antennas, allowing them to be mounted using M3 screws interfacing with heatset inserts on the sled side. The complete assembly mounted to the sled can be seen in Figure 10.26.

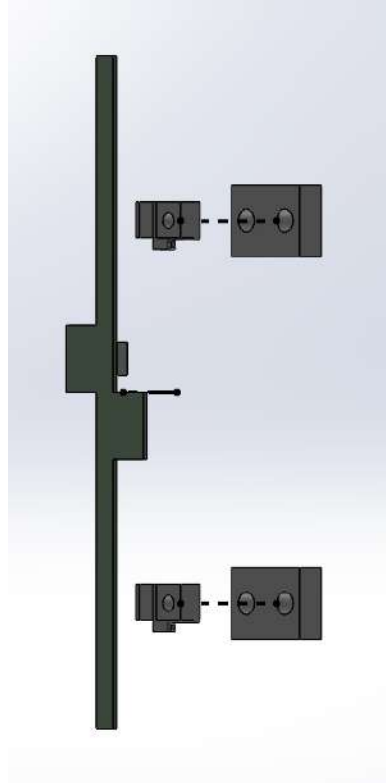


Figure 10.26: Antenna mounting exploded view

## 10.8 Risks and Failure

When considering the new recovery system, it is critical to try and predict any new potential sources of failure and what effect they would have on the system in flight. Three main sources of failure were identified for the new design. The main risks of the recovery section can be broadly categorized in two sections, recovering too quickly or too slowly. If the system does not deploy properly, the rocket will come down much more quickly than designed. This will harm the rocket and may cause a risk to LC competitors and staff if the rocket comes down near a populated area. If the system deploys the main prematurely, the rocket may drift much further than anticipated with a worst case scenario of the rocket breaching the flight waiver.

### 1. Tangles in the Rigging

The most unpredictable source of failure is a tangle in the rigging. From past experience, it has been determined that this can come from one of three places. Interactions with the nosecone, interactions of the parachutes, and incorrect deployment. The severity of a tangle involving the parachute is quite high, having the potential to prevent either main or drogue chute inflation. Since the nosecone has its own recovery system, and given testing with test flight it is unlikely that the nosecone will tangle with the drogue parachute. The nosecone contains no edges for the parachute to catch on, further reducing the probability of failure. As the main deploys, there is the possibility of the drogue tangling, as its airflow is choked. Test flight revealed that the main is sufficiently large as to ensure that the drogue will not reach

the suspension lines mitigating this failure. To ensure correct deployment, all aspects of the rigging are held in its proper deployment bag, reducing the chance of tangles.

## 2. 2-Ring Release Severing Prematurely

A potential source of failure is the movement or grinding of the 2-ring release line on the pyrocutter body abrading it to the point it breaks mid flight leading to a main deployment before the selected altitude. The most likely source are the pyrocutters. The material selected for the reefing line (cypress line) is very durable and the reefing line is made out of new material prior to competition, so the risk is already quite small. To minimize this risk further, the pyrocutters are being tested extensively to ensure any sharp edges are removed, to ensure all edges are bevelled or filleted and ultimately by attempting to use the pyrocutters to cut the cypress line manually.

## 3. Pyrotechnics Disconnect Electrically Before Activation

This is a moderate risk failure mode that has been tested through test flight. Additionally, the team has already successfully routed cabling up a shock cord to allow for skirt reefing in previous years. By using similar harnessing to that flown in previous year, and in test flight, higher confidence can be gained in the electrical connect. All pyrotechnics are also dual redundant ensuring that if any individual component fails (mechanically or electrically) the system will function regardless.

## 11 GROUND SUPPORT EQUIPMENT

The team has significant SRAD and COTS ground support equipment (GSE) which will be used during the launch of Aurora. The proposed layout of the launch pad is presented in Figure 11.1.

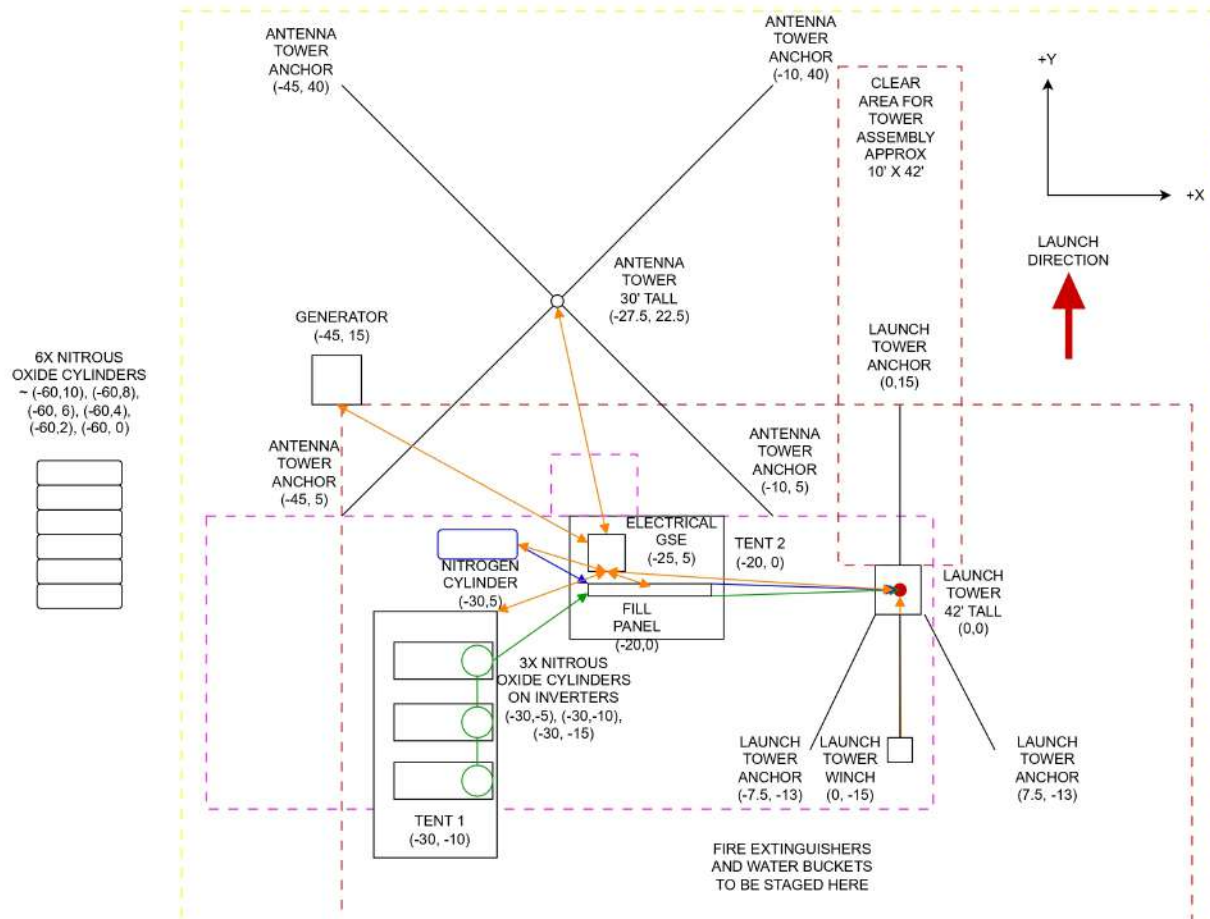


Figure 11.1: Proposed site layout

### 11.1 EGSE Network

The EGSE is split between the pad and mission control. At the pad, individual electrical systems communicate over a local area network (LAN) via weatherproof Ethernet cables. A pair of Ubiquiti Litebeam 5AC antennas, mounted on extendable carbon fibre towers, are used to extend the network from the pad to mission control. These antennas have been fully qualified at multiple cold flows, static fires, and competitions. Appendix B shows the complete EGSE network.

### 11.2 Remote Launch Control System

The Remote Launch Control System (RLCS) is the primary means of interfacing with the rocket and controlling the fill system during test and launch operations. The objective of RLCS is to allow

remote operation of the rocket from up to 3 000 ft from the tower during all phases of operation. Once the RLCS operator takes control of the launch process, no human intervention is required at the launch site at any time when the SRAD fluid systems are pressurized. In the event of total failure, the system places all engine and fill systems into a predetermined safe state so that personnel can approach the rocket without placing themselves in danger.

RLCS is made up of two halves, Clientside and Towerside, which communicate over the EGSE network. Towerside is located beside the launch tower, and controls valve actuation and engine ignition. Clientside is located at mission control and houses switches that map to the Towerside actuators and an LCD to display data to the operator. Both halves are built into robust, weather-proof cases to protect them from the elements.

### 11.2.1 Clientside

Clientside (Figure 11.2) is used by the Control operator to control motorized valves and ignition. Clientside is composed of an Arduino Mega, a LCD module, several missile switches, and a custom Arduino breakout to regulate power and extend I/O pins to screw terminals. Additionally, it exposes a USB port which allows Clientside to send data to a computer for plotting and logging.

Clientside contains a set of missile switches, each matched to a motorized ground-side valve or rocket onboard valve. There is also a button for ignition paired with an arming switch for controlling the current that passes through the engine ignition coil. The LCD module displays the state of all motorized valves (open, closed, and not connected), the voltage of the LiPo batteries, and the ignition coil current. Clientside dumps all RLCS sensor data periodically through the USB link to the DAQ operator laptop.



Figure 11.2: RLCS Clientside

### 11.2.2 Towerside

Towerside (Figure 11.3) receives commands from Clientside and actuates its output ports accordingly. It is made up of a set of standard relay boards and two high-current relay boards (for tank

heating) connected over an I2C bus to a master Arduino Mega and custom shield.

Each relay board is connected in a daisy-chain configuration. In addition to the two I2C data lines, SDA and SCL, there is a regulated 5 V line, an unregulated 12 V line, and a ground line. The 5 V line powers the MCUs on the boards and the 12 V line is used to drive the relay coils. The standard relay boards have a secondary power connection which is used exclusively to power the actuators (through the relay contacts). This ensures that the high current draw of the actuators does not cause brownouts on the MCU power lines. The tank heating relay boards are connected to dedicated car batteries, and do not draw power from the actuator power line.

Figure 11.3: RLCS Towerside

### 11.2.3 Towerside Power Board

This board is designed to provide 5 V to the Arduino, power output, a UART link for communication to mission control, a keylock switch connector, and I2C connection. A seven segment display on the board allows the status of each actuator channel to be viewed directly, with each bit of the output value representing an individual actuator.

### 11.2.4 RLCS Relay Board

The purpose of Relay Board is to control the motorized valves on the ground-side plumbing system. Each board is connected to one motorized valve. The board also detects the states of limit switches built into the valves, which are activated whenever the motor shaft arrives at a fully closed or fully open state. This information is provided to operators so that they are continually aware of the current position of every motorized valve in the system. In addition to operating motorized valves, the board is also used to supply current to the ignition coil used to ignite the engine. This year, the pyro valve contains the same type of ignition coil, which is actuated in the same way. The typical ignition current is 4 A. The relay board is equipped with a current-sense amplifier which continually measures the output current. This is used, among other criteria, to determine when the engine has ignited and the injector valves should be opened.

Relay board uses a pair of relays to control actuation direction and power to the actuator independently. This requires two actions to be taken in order to actuate a valve or fire an ignition coil (where the coil is wired to the normally open contacts of the direction relay).

### 11.2.5 System Safety

RLCS is designed to prevent unintended actuation of valves and fail safely. Both Clientside and Towerside have keyed-alike arming and disarming switches respectively, both of which retain the key when turned. Whenever the pad is approached, the key is removed from Clientside, disarming it, and then inserted into Towerside, also disarming it. In this configuration it is physically impossible to arm Clientside while personnel are at the pad since the key is also physically with them, and even if a fault caused either Clientside or Towerside to unintentionally arm, the other half would still be disarmed.

Within Towerside, two relays are required to actuate in order to trigger any action. The relays are wired in series such that one provides power to the actuator and the second determines which direction the actuator should move. The plumbing system is also set up such that if any individual actuator fails the system can still be safely vented.

Clientside and Towerside continually send command and sensor data messages to each other. This means that if either one unexpectedly fails, or the radio link between them drops, both can detect this by noticing silence on the line. If Towerside does not hear from Clientside for 10 seconds, it will automatically set all actuators to safe states that are predefined in firmware. This means opening all vent valves and closing or de-energizing all others in order to make the system safely approachable by personnel. Clientside will also report any silence of at least 3 seconds to the operator, which could indicate an intermittent radio issue or an issue with Towerside.

Furthermore, Towerside continually sends the commanded states from Clientside to the respective output boards, meaning that if a state is flipped in one message due to a communication error, this will not cause the system to enter an incorrect state. Also, Towerside will only change its commanded state to the output boards once it has received two identical messages from Clientside in a row, preventing a single incorrect message from causing an output from changing states. The output boards similarly wait to receive two identical messages from Towerside before changing state for the same purpose.

RLCS controls the following actuators necessary for fill, engine start, and abort:

- Oxidizer Fill Valve
- Oxidizer Drain Valve
- Oxidizer Vent Valve
- Nitrogen Purge Valve
- Fill Disconnect Solenoid
- Two nichrome coils inside the engine ignition puck
- One nichrome coil inside the Pyro Valve ignition puck
- Two sets of tank heaters

Moreover, RLCS uses sensors to collect the following data, and report that data back to the operator:

- The current state of all motorized valves (open/closed)
- The amount of current flowing through each coil inside the ignition puck
- Voltage, current and temperature sensed from tank heating
- Voltage of all LiPo batteries
- All error codes

### 11.3 Data Acquisition System

The purpose of the Data Acquisition System (DAQ) system is to obtain ground-side sensor data during fill and launch operations. It also allows data to be plotted and logged in real time on a computer in a more user-friendly visualization than the LCD on Clientside.

The heart of the DAQ system is a National Instruments USB-6218 Multifunction I/O Device (NI module). It supports up to 32 analog input channels with a sensitivity down to  $4.8 \mu\text{V}$ . This makes it suitable for both 0-5 V and 4-20 mA sensors and mV/V strain gauges such as load cells with no external amplification.

Once the sensor voltages are collected by the NI module, they are passed over USB to the Framework Motherboard, a compact single-board computer running the necessary software to send the data to mission control. At startup, the motherboard automatically runs the DAQ server in preparation to connect and send data to mission control.

### 11.3.1 DAQ Power Board

Power to sensors is delivered by DAQ Power Board. Three copies of this board power the 5 V, 10 V, and 12 V power rails within the DAQ system. DAQ Power board is designed for 1 A output at a configurable voltage between 5 V and 15 V.

Power to the integrated computer is delivered by a COTS USB-C PD DC-DC charger. This module is able to accept voltage from the 12 V power rail and convert it to the appropriate operating voltage.

### 11.3.2 DAQ Patch Panel

The sensor ports on the DAQ box are connected to the NI module through the DAQ Patch Panel boards. They allow for the input voltage for each sensor type to be selected individually. To prevent shorting between the header pins when selecting voltages, a star design for the header pins with selection in the middle was adopted to only allow connection to one voltage rail at a time.

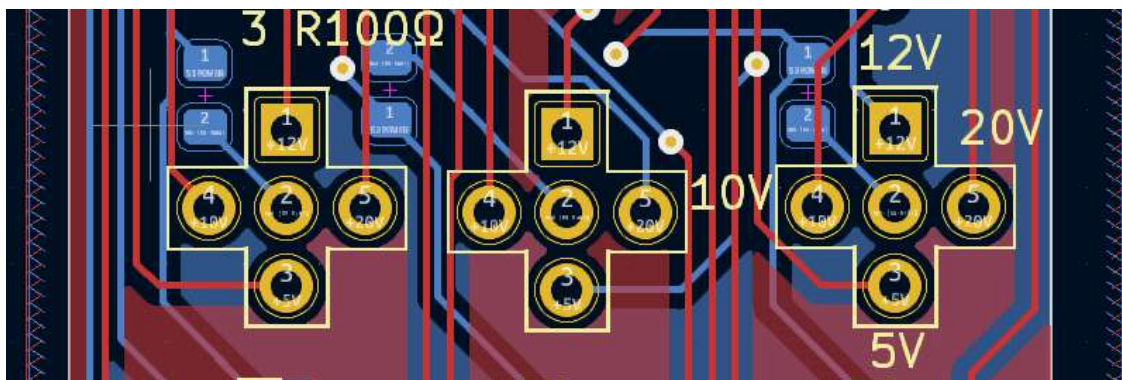


Figure 11.4: Patch Panel star-shaped voltage headers

To allow for the use of 4-20 mA and resistive sensors without an external output resistor, an additional jumper set for output resistor selection is included. Furthermore, when using 4-20 mA sensors, the ground port can be set to a secondary voltage input to allow for two sensors to run from one sensor port, doubling the maximum number of 4-20 mA sensors without increasing the number of ports. These jumpers allow configuration of a total of three sensor ports per board. To allow for all four copies of the board to be installed and draw from the same voltage supply, the supply rails and ground are daisy-chained between boards, similar to the RLCS relays.

## 11.4 Omnibus

Omnibus is a unified data bus which manages various data "sources" (such as DAQ and RLCS) and "sinks" (such as plotting and logging) and connects them. This allows real-time data to be sent between devices at the launch pad and mission control.

The DAQ and RLCS systems act as Omnibus sources, which package their data, serialize it, and broadcast it on the EGSE network. At mission control, a host laptop runs Omnibus sinks (such as the Dashboard). For example, a pressure transducer feeding into DAQ will have its data transmitted through the Omnibus source for the NI module running on the DAQ Mainboard, sent over the Wi-Fi antennas, then received by the Omnibus Dashboard sink on the laptop. This allows mission control to see the pressure visually on a graph that updates in real time.

In addition to DAQ and RLCS data, which is read-only, Omnibus is also used for bidirectional communication with the avionics. Using the wireless and redundant ground-side CAN links, the telemetry operator has full visibility of the avionics' status and can issue manual commands, such as to remotely arm the altimeters or actuate the control system.

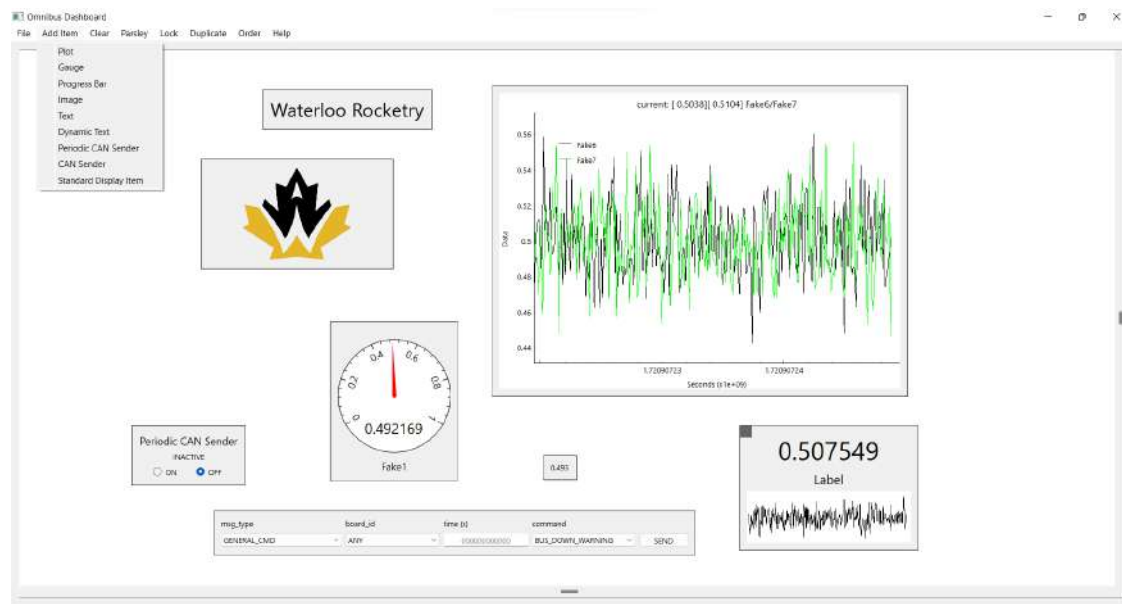


Figure 11.5: Omnibus dashboard

The Omnibus Dashboard is designed to allow for easy modifications to allow DAQ operators to make quick changes as necessary. Dashboard items can be locked and resized, with keyboard shortcuts to simplify common actions. Dashboard configurations can be saved and loaded. Data visualization features including an analog gauge, progress bar, and sparkline display provide clear updates.

## 11.5 Ground Side Power Distribution

Ground Side Power Distribution (GSPD) supplies power to all EGSE at the pad: DAQ, RLCS, the router box, and the antenna. GSPD takes power from either car batteries or a 120 VAC source, usually the generator while in the field. The system takes in 12V from the car batteries directly or

uses an ATX 430W power supply to rectify the AC supply and convert it down to 12 VDC. The 12 V is then fed through a 5 V and 24 V converter and filtered. The 5 V, 12 V, 24 V and GND lines along with voltage, current, and temperature sense outputs are distributed to the rest of the EGSE stack via an array of M12 connectors and cables. The components of GSPD are housed in a water and dust-proof case, modified for ease of usage and cooling. A detailed design and analysis of GSPD is provided in [17].

### 11.5.1 48 V Boost Board

In 2024, the team acquired a network video recorder (NVR) and security cameras. These are used at the launch pad and at tests to visually monitor the plumbing system and the rocket, and record test and flight footage. The NVR normally runs from a COTS 120 VAC to 48 VDC adapter, which necessitates plugging it into a generator while in the field. In order to make EGSE totally independent of the generator, it was required to power the NVR from the GSPD main 12 V supply. 48 Boost Board exists to meet this requirement. It is mounted inside the GSPD case, and is composed of a boost converter that takes in 12 V and provides 48 V at up to 2 A , which meets the current requirement of the NVR. The converter was designed using TI WEBENCH, and dissipates approximately 4.2 W at max load. The board is also equipped with input and output current sensing, and both the input and output lines are appropriately fused.

## 11.6 Tank Heating

Due to the climate at the launch site, it is necessary to actively heat the propellants to reach firing pressure. The tank heater is a single-layer flexible PCB with adhesive, which is glued to the exterior of the oxidizer tank. The heater has a resistance under room temperature of approximately  $1\ \Omega$ , and a power draw of 625 W. The heater's resistance increases with temperature; when the heater reaches  $75\ ^\circ\text{C}$ , the resistance is approximately  $1.2\ \Omega$ . This change in resistance is used to estimate the surface temperature of the tank. Two of these heaters are used in parallel to quickly and evenly heat the propellant.



Figure 11.6: Tank heater flex PCB

Power to the heater is connected via an XT-30, with the female side soldered to the flex PCB. The male connector is connected via a pair of 12 AWG wires to power and a pair of 22 AWG wires to tank heating relay board for voltage sensing. The extra voltage sensing line is required to avoid inaccurate data caused by voltage drop on the power wires. There is a thermistor on the heater which is used for redundant temperature sensing. The thermistor connector is a standard 2-pin Dupont connector. Both connectors are friction fit and pointing downward such that they separate at launch.

### 11.6.1 Tank Heating Relay Board

Tank Heating Relay Board is similar to Relay Board, except it only has one high current relay for controlling power to a tank heater. The board takes 24 V in from two standard 12 V car batteries connected in series. The 24 V line is fed through the relay and a 30 A automotive blade fuse to the output terminals. The ground path contains a 1 mΩ shunt resistor used for current sensing. The board is also responsible for measuring the heater voltage and the the thermistor resistance.

## 11.7 Electrical Umbilical

The rocket is connected to EGSE while on the pad by the electrical umbilical. It consists of 3D printed housings containing spring loaded pins and matching contacts. These two housings are held together by magnets on either end, which are polarized such that the connector can only be attached in one orientation. The ground-side is wired into DAQ, which supplies the charge line, ground, CANH/CANL pair, and unregulated 12V. The rocket side is mounted inside the injector section fairing, and is connected to the rest of the avionics harness. When the rocket lifts off, the umbilical passively separates from the rocket. This design has been validated on both LOTS and Borealis. Because the electrical umbilical disconnects after liftoff, this backup link is fully sufficient to launch the rocket in the event of a live telemetry failure.



Figure 11.7: Rocket electrical disconnect

### 11.7.1 Ground-Side Charging Board

As described in the rocket power architecture (Sec. 9.1.6), rocket battery charging functionality has been moved from the rocket to EGSE. GSCB takes in a 12 V supply, and outputs a voltage-limited constant-current 1 A supply, which is used by avionics boards to charge their batteries.

It consists of two stages. The first is a 12 V to 18 V boost converter based on the LM3478MA controller (Figure 11.8), which provides the necessary headroom to the battery charge circuit. The LT1510 (Figure 11.9) is an integrated battery charge controller suitable for LiPo cells. The safe charge voltage of a 3S lipo is approximately 12.6 V. To provide some safety margin, the target battery voltage is 12.4 V. Each battery charge input uses a Schottky diode (see Figure 9.11), which is designed to have a low forward voltage drop (and thus dissipate minimal power), in series with the battery. Using the PMEG3030EP on Rocket Power Board as an example, the typical forward voltage drop at 1 A is 260 mV [33]. The output voltage limit of the charge circuit must be increased to compensate for this forward voltage drop, and so is configured to 12.7 V.

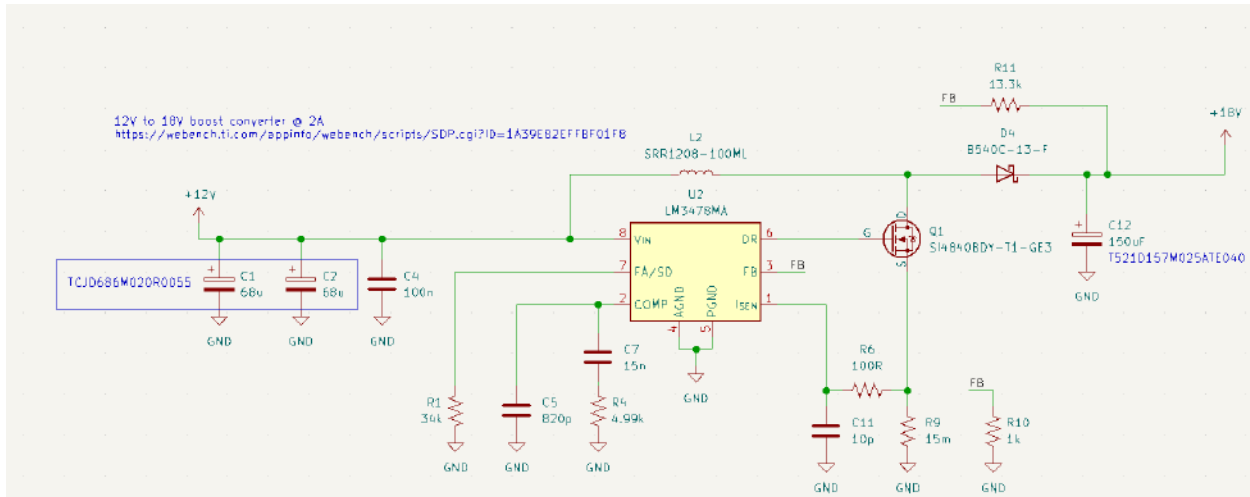


Figure 11.8: GSCB boost converter

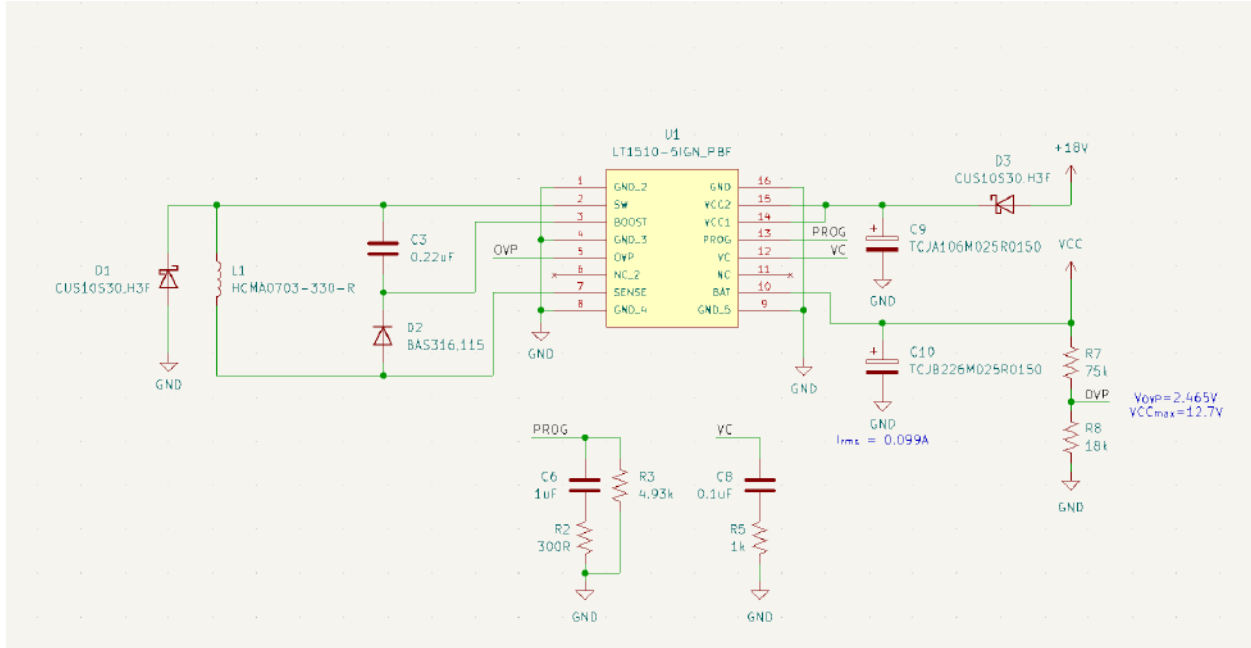


Figure 11.9: GSCB charge controller

### 11.7.2 Pyro Valve Igniter

With the addition of the pyro valve, it is necessary to run two additional wires from EGSE into the vent section of the rocket. A direct connection from ground to the section was considered, but would have required another disconnect point. It was decided to simply expand the main electrical disconnect with two additional pins. The existing pin and contact pair can accommodate the current requirements for pyro valve ignition. Suitably sized wires are attached to both sides of the disconnect and run into the pyro valve ignition coil from the injector section, along the raceway.

### 11.7.3 Payload Umbilical

This year, the deployable payload has its own independent electrical umbilical. The pinout is identical to the main rocket umbilical (with the exception of pyro valve), and the DAQ box has a second set of hardware to provide the charge line and CAN connections. The main rocket and payload CAN busses are entirely independent, which avoids complications with the termination resistors. Because the payload must further separate from the nosecone, its umbilical has two separation points: one on the exterior of the nosecone that separates in the same way as the main disconnect at launch, and an internal disconnect embedded inside the 3D printed payload-nosecone spacer (Figure 11.10).

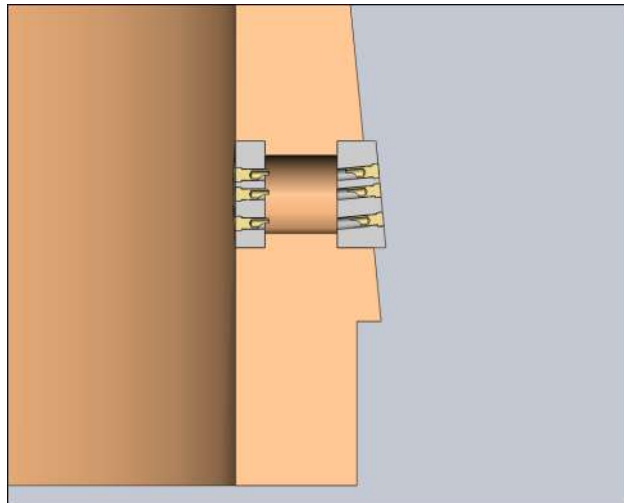


Figure 11.10: Payload disconnect internal pass-through (spacer in orange), wires not shown

## 11.8 Launch Tower

The team's launch tower consists of four 10 ft segments of triangular aluminum truss, connected to a steel base plate. The plate is connected to a larger frame via a hinge, allowing the frame to be secured to the ground before the tower is raised. A 32 ft launch rail made up of 1.5 in aluminum extrusion segments is mounted onto the tower using clamps that wrap around the vertical tubes of the aluminum truss. The rail interfaces with two launch lugs on the rocket, which slide through the slot profile of the extrusion. The launch rail is sized to ensure adequate off-rail-velocity for a large range of rocket TWPs.

Once the rocket has been railed, the tower and rocket are raised using a gin pole. This is attached to the tower base and connected to an electric winch powered by a car battery. This is an improvement over the previous winch, which was driven by a handheld cordless drill. The electric motor allows for much faster raising, while the car battery is more reliable than the previous drill battery. One downside to the new system is that the new winch can be back-driven; the weight of the tower alone can cause the winch to unwind, whereas the old winch had a worm gear system which prevented this. This is mitigated by operators securing the tower throughout the raising procedure. The system was used successfully at LC in 2024, and improvements are planned for the future to address the back-driving issue. When raised, the tower is angled 6 degrees from vertical as per DTEG R10.1.1, and secured by three guy wires. The guy wires are sized to ensure a FOS of at least 1.5 on tipping at the maximum wind speed recorded in Timmins during the launch period, 60 km/h.

The tower is secured using arrowhead anchors attached to the guy wires via aircraft cable and turnbuckles. The anchors interface with a long metal rod, which is used to hammer them into the ground. In 2024, the 3 in arrowheads, embedded 2 ft deep, could be pulled out of the ground with some effort. To address this, new sizing requirements were studied on "solid classification 2 - Silty and Clayey Sand" [34]. The result of this study was to move to 4 in arrowheads. They achieve higher load capacity, and are driven 4 ft deep to improve performance in loose soil.

The launch tower base has been used by the team for over 10 years. Given the increase in mass of Aurora compared to previous vehicles, there was considerable risk of the current base failing.

FEA simulations were conducted on the existing base. The boundary conditions include an external force applied to the tower base, assumed on the y-axis for simplicity. This includes loads from the weight of the rocket, and an overall worst case load considering materials, height of the tower trusses, wind speeds, and guy wire tension force. The legs of each tower base were fixed at each hole, where rebar stakes are placed. Guy wires were discarded as constraints for simplicity. This yielded a minimum safety factor of 1.09, which was deemed untrustworthy considering how much the loading and constraints were simplified. Based on these results, additional support pieces were added at the bottom of the base, where the simulation suggested it would likely fail. Simulations were conducted on the modified tower base (Figure 11.11) after the supports were added to verify they would improve the strength as expected. The analysis yielded a minimum factor of safety of 1.87, a maximum of 15, and an average of 14.97. This was considered acceptable.

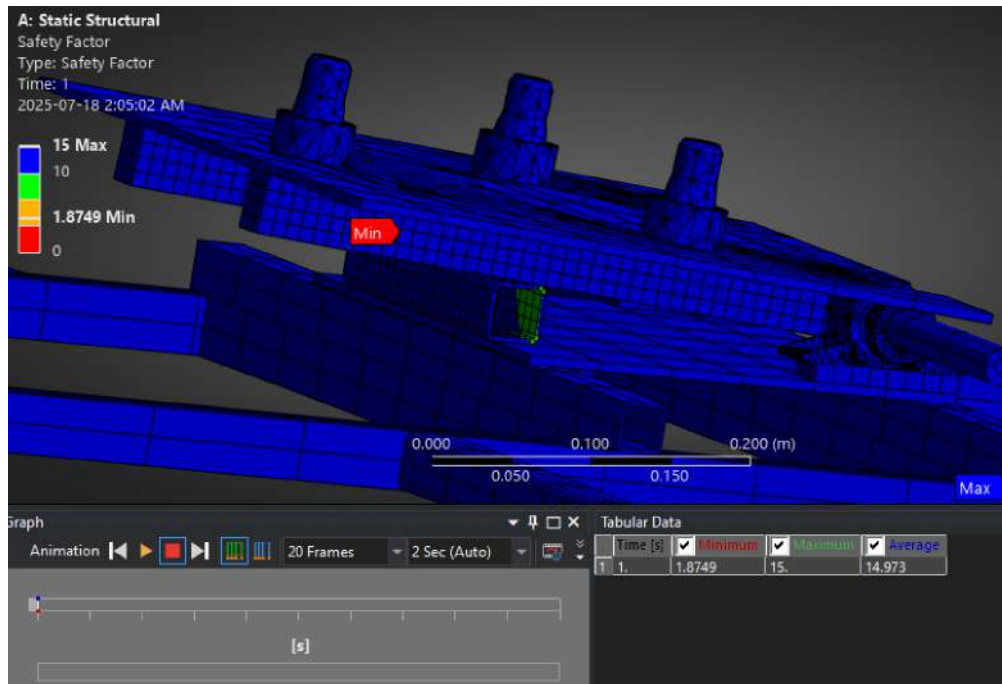


Figure 11.11: Launch tower base stress analysis

## 11.9 Antenna Towers

At competitions in 2022 and before, the antenna at the launch site was mounted on the launch tower, and the antenna at mission control was affixed to a shovel or vertical piece of wood. This created issues when connecting the antennas, as the tower-side antenna needed to be rotated independent of the launch tower in two axes, horizontally to point towards base camp, and vertically as the antennas were at different elevations. The low elevation of the mission control antenna also presented connectivity issues as signals were blocked by surrounding vegetation or the terrain.

In 2023, two identical towers with metal extendable bases and telescoping carbon fibre masts were sourced so that the antennas can be mounted independently and at a high enough elevation to be clear of any obstructions. The towers can be raised to a maximum height of 33 ft, and the height can be adjusted as desired by extending some or all the telescoping mast segments to properly align

the antennas vertically. The telescoping masts can also be rotated once they are raised, allowing fine tuning of antenna pointing to improve connection. The towers are secured by four guy wires similar to the launch tower, and were used successfully at IREC 2023 and LC 2024.

## 11.10 Fill Plumbing

For competition in 2023, a panelized approach to ground-side plumbing was implemented to reduce pad setup time and increase plumbing standardization and reliability. The team has continued to use this system at all subsequent engine tests and launches, including the launch of Borealis at LC 2024. The fill plumbing stand has two panels, one for loading nitrous oxide into the rocket, and one for operating pneumatics. The complete fill system and rocket P&ID is presented in Figure 8.1.

The panel includes many features to make operations easier and safer. Remote valves and pressure transducers at key locations allow for the system to be monitored and operated at a distance, and mean that operators only need to open supply cylinders and set the nitrogen regulator before retreating. This means no operators are near the rocket when it is filled with propellant. Additionally, manual bypass valves with ropes attached are located so that there is no point where there can be pressure trapped without a way to vent it from a distance. The panel also includes a pressure gauge, as well as a pressure relief valve set to 1 000 psi for safety. To allow the panel to be used without full sanitation after each use, a swappable filter element is included at the inlet of the panel to catch debris. Additionally, an inlet for a nitrogen purge is included to remove remaining nitrous oxide vapour after use. Quick disconnects interface from hoses to the panel, for rapid assembly in the field. Tubing is used for as much of the panel as possible to allow for easy assembly without the clocking issues caused by NPT fittings. Additionally, it is easy to modify the tubing if changes are required. Both JIC flared connections and Swagelok are used on the panel to connect tubing and interface with NPT components. The fully assembled panel is shown in Figure 11.12.



Figure 11.12: Assembled nitrous oxide fill panel

## 12 CONTROLS

The Controls subsystem was established in 2023 to develop active control systems for the team's launch vehicles, beginning with the airbrakes implemented on Borealis. Although the airbrakes yielded limited flight performance, the project confirmed strong team interest in control systems and laid the groundwork for further development.

This year, the focus shifted from apogee control to active roll control. Roll control offers several advantages, including improved stability through reduced coning motion (see subsubsection 6.7.5), enhanced trajectory accuracy, and improved onboard video quality. Roll motion becomes increasingly pronounced with higher altitudes and velocities, making active control particularly valuable as the team advances toward more ambitious flight profiles.

To meet these objectives, the Controls subsystem has implemented an active roll control system on Aurora using steered canard surfaces. These consist of two mechanically linked aerodynamic surfaces mounted above the tank. By rotating the canards, the system generates a rolling moment, enabling precise control of the rocket's roll rate during ascent.

### System Architecture Overview

The canard system is a self-contained package which includes the canard surfaces, the gear system and servo motor, the Motor Control Board (MCB) to power the servo, Processor Board to perform the necessary controller calculations, and two inertial measurement units (IMUs) with accelerometers, gyroscopes, magnetometers, and barometers. The canard control software interfaces with the rocket through these sensors and actuator commands, as shown in Figure 12.1. Sensor data informs control decisions, while servo signals actuate the canards to produce the desired roll response.

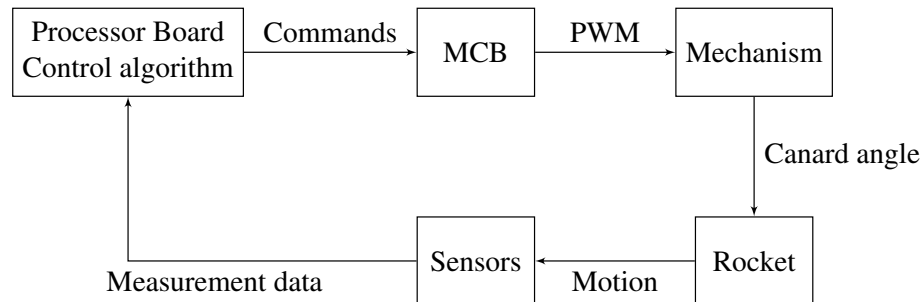


Figure 12.1: Diagram of the canard system architecture

### 12.1 Canard Mechanism

The canards mechanism is responsible for mechanically linking the two aerodynamic control surfaces as well as providing rigid mounting and connections between those control surfaces and the servo which drives them. The controls avionics, battery, and flight cameras are also mounted to it.

### 12.1.1 System Location

At the beginning of the canards project, two options for the location of the canards were proposed. They could either go in the vent section, immediately above the tank and in front of both the CP and CG of the rocket, or they could go in the injector section, aft of both the CP and CG. Each of these options had trade-offs, and created different risks and requirements. They also affected the amount of work required from different groups within the team, and this complicated the decision-making process.

After significant discussion with major stakeholders, it was decided to place the canards at the top of the tank (see subsubsection 8.4.4 for implementation details). This design decision significantly reduced the mechanical complexity of the system and made the integration constraints on Aurora nearly identical to the test flight launch [35].

### 12.1.2 Mechanism Design Details

The canards mechanism flown on Aurora is mostly unchanged from what flew on the test flight, with the exceptions noted in subsubsection 12.1.3. It is also described more thoroughly in the design report cited throughout this section [35].

The canards mechanism incorporates three shafts geared together using bevel gears as shown in Figure 12.2. This design was specifically created to meet the requirement of mechanically linking the canards together so that they can never actuate separately. These three sub-assemblies, along with other components such as the battery mount, camera mounts, and avionics are bolted to a single base-plate. This allows for full integrated testing of the system without requiring other rocket components, and enables easier integration into any vehicle the assembly is launched on [35].

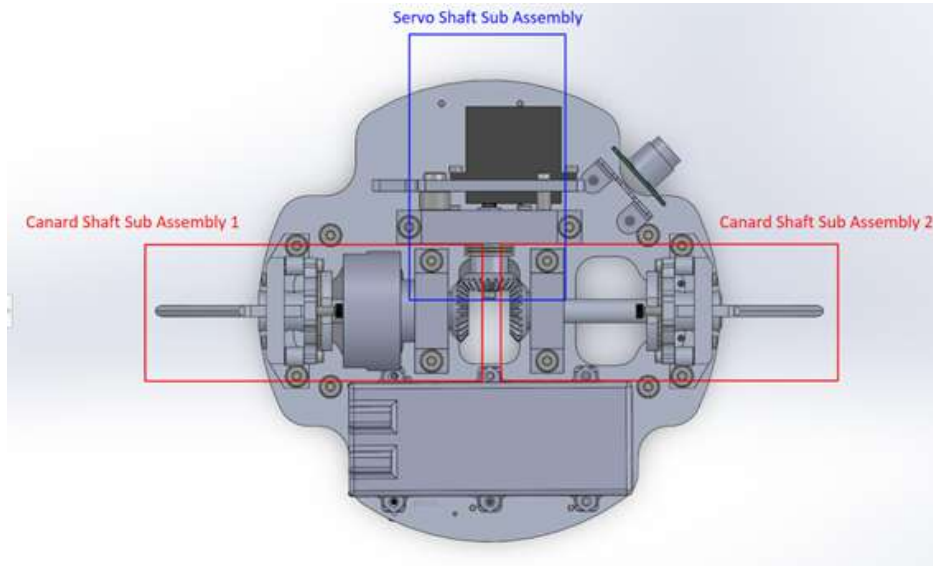


Figure 12.2: Canard mechanism top view

The canard shaft subassembly has several functions. It provides secure mounting for the canard control surfaces, maintains the exact position of the gear to minimize backlash, and connects the

two rigidly. A through-hole potentiometer is also mounted on one of the canard shafts with a set screw. To retain the shaft, a mounting block with a bearing is located at each end. The outer end uses an ultra-thin bearing to fit around the control surface mounting geometry, while the inner end uses a standard bearing to save cost. Each mounting block is positioned onto the base-plate using locator pins, although because of the difficulty in retaining them some were removed after assembly. The full sub assembly can be seen in Figure 12.3.

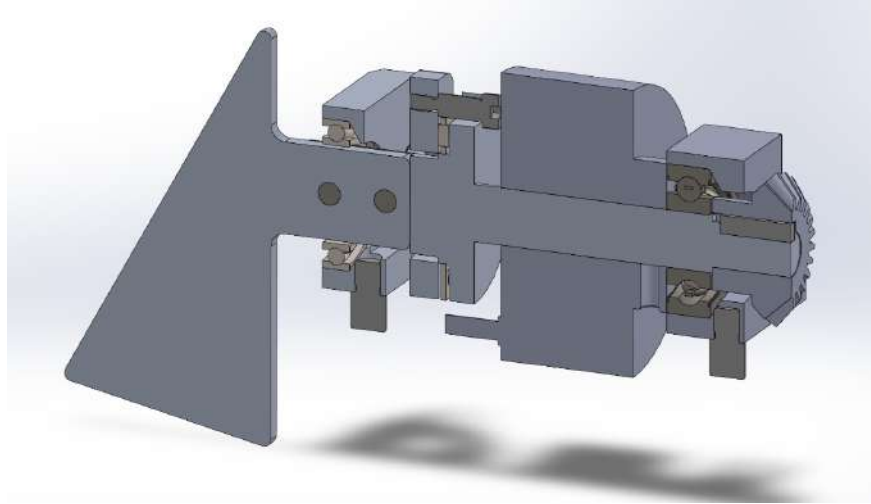


Figure 12.3: Canard shaft sub-assembly section view

To mount the canard aerodynamic surfaces, two shoulder bolts pass through one side of the shaft, the canard, the other side of the canard shaft, and into a tight space nut. This both locates the canards repeatably using the shoulder, and fixes them using the shoulder and clamping forces. This, along with the canard profile for Aurora can be seen in Figure 12.4. The canard surface aerodynamic design, including size and shape, is covered in subsection 6.8.

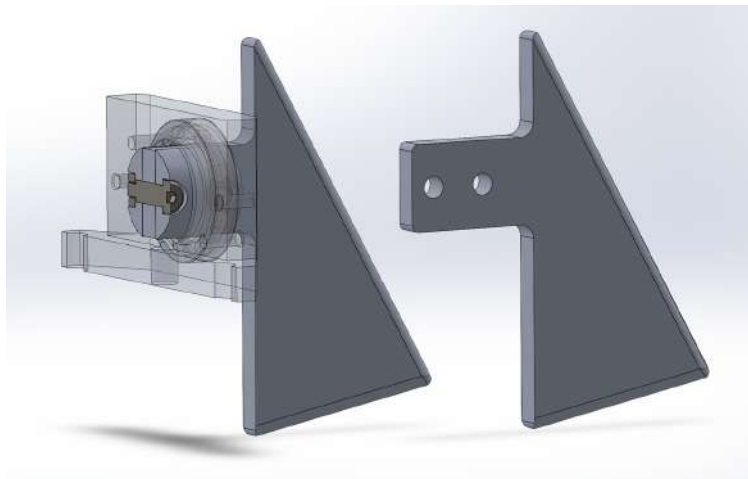


Figure 12.4: Canard aerodynamic surface mounting and profile

To control the backlash of the gears, and therefore minimize any negative impacts the backlash could have on the control loop stability, a shim system was used. Figure 12.5 shows the force

path through which the gear is located and how changing the number of shims changes the axial position of the gear. Multiple 0.002 inch shims can be used, nominally five.

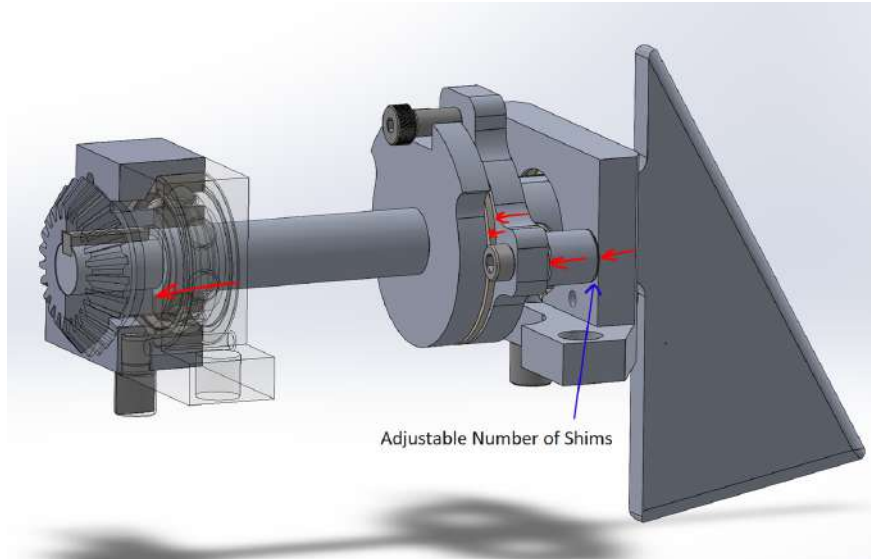


Figure 12.5: Shim adjustment force path

The servo shaft sub-assembly, depicted in Figure 12.6, is similarly structured with a shaft running through a bearing and mounting block to a gear at the centre. The servo shaft has only one mounting block because it is significantly shorter and because the bushing in the servo also helps maintain its position. The shaft was turned down from a hex servo shaft to allow it to both connect to the servo and fit through the specific diameter parts on it.

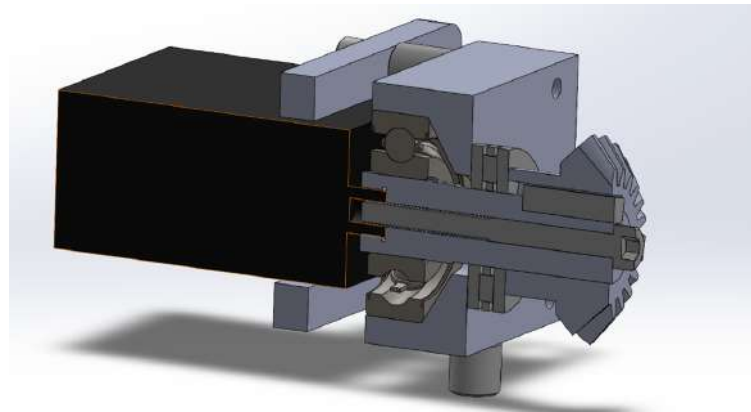


Figure 12.6: Servo shaft sub-assembly section view

### 12.1.3 Final System and updates since Testflight

Broadly, the canard system remains unchanged between test flight and Aurora. The changes were minimized for several reasons. Even though the mechanism actuation is untested on flight, as they did not actuate during test flight, the other aspects of the system have been verified to function as

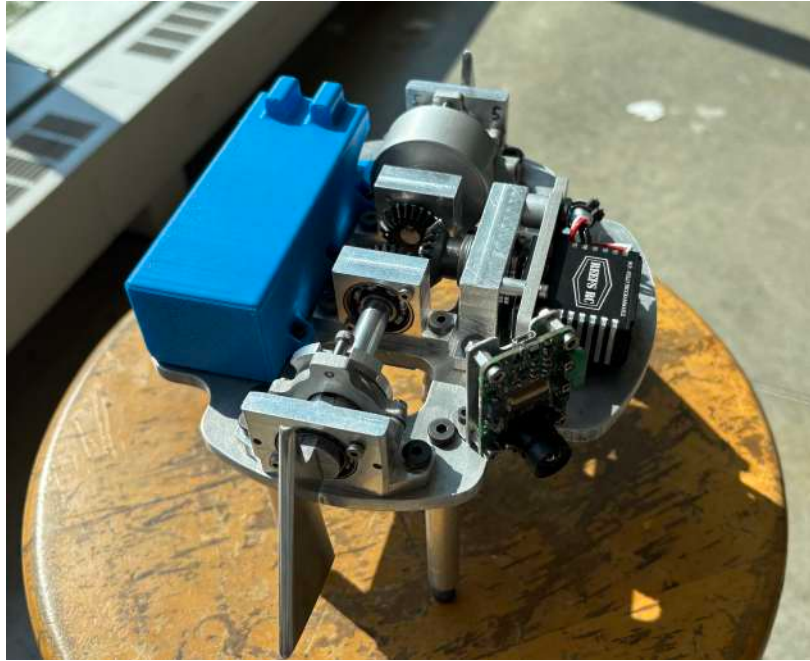


Figure 12.7: Assembled canards

designed. Importantly the canards have actuated on the ground with the required performance for the controller stability, and any changes would require revalidation. Minimizing the changes also reduced the total cost and required work for the full design cycle, while allowing for more in-depth analysis and testing.

Some changes were still required for Aurora. The control surfaces' area is reduced to account for the increased air speed of Aurora compared to the test flight, while keeping the control authority similar [36]. The inner diameter of the bodytube which the canards sit inside is slightly smaller than on test flight, and therefore some components of the canards have been filed or otherwise slightly modified to fit within the new tube. Camera mounting has also been updated to fit around components of the vent section with which the canards now integrate.

## 12.2 Flight Simulation

The Controls flight simulation is documented in the design report [37]. The simulation is developed in Matlab/Simulink and the codebase is available on GitHub in the simulation repository [38].

The team has existing infrastructure for flight simulations, with the Flight Dynamics subsystem primarily using OpenRocket, a proven rocket simulation software. However, OpenRocket does not support movable aerodynamic surfaces, such as canards.

To address this limitation and enable realistic testing of the canard-based roll controller, the Controls subsystem developed a new, custom-built simulation environment. Implemented in Matlab/Simulink, the new simulation framework was specifically designed to support closed-loop control and to integrate seamlessly with the controller logic. Simulink was chosen for its flexibility in modelling complex, nonlinear dynamical systems, and its robust numerical solvers. Unlike previous tools, this simulation is capable of modelling actuator behaviour, dynamic aerodynamics with moving surfaces, and sensor characteristics, allowing for a high-fidelity representation of the

rocket's response to control inputs. The development of the simulation occurred in parallel with the flight dynamics design cycles and the canard control system itself, enabling close collaboration and co-design between subsystems. This ensured that both the aerodynamic models had consistent physical representation, and that the controller could be tested in simulation.

The simulation environment is also capable of performing Monte-Carlo simulations, where flight parameters such as wind speed, engine performance, sensor failures, and actuator backlash can be varied randomly. This flight simulation framework marks a step forward in the team's simulation capabilities, transforming the role of simulation from purely predictive trajectory analysis to a tool for controller development and system validation.

### 12.2.1 Simulation Architecture

The Controls simulation was developed in Simulink, as this makes the numerical time integration of highly complex dynamics very easy. To maintain modularity and improve maintainability (due to binary Simulink .slx files) the simulation is structured as a hierarchical, modular architecture as shown in Figure 12.8.

Each major plant component, such as flight dynamics, actuators, environmental conditions, or sensor emulation, is encapsulated in its own subsystem. The major subsystems are then further structured into layers, e.g. flight dynamics → forces → normal forces → canard forces. Each layer computes a specific aspect of the physical model, aggregating contributions from lower-level components. This layered modularity improves traceability, simplifies debugging by isolating the impact of individual forces or effects (e.g., lift from fins, body, or canards), and allows for isolated development and testing. Intermediate results such as local force contributions can be verified against theoretical values or simulation baselines. Furthermore, components like aerodynamic models or actuator dynamics can be upgraded independently without disrupting the overall architecture.

### 12.2.2 Implementation Details

To lower implementation effort and reduce the chance of mathematical errors, many standard components such as the 6DOF equations of motion and the atmosphere models are sourced from the Matlab Aerospace Blockset. Simulation parameters such as mass distribution and thrust are implemented using lookup tables derived directly from OpenRocket exports, ensuring consistency between tools. While aerodynamic moments and normal forces are computed independently within the Controls simulation, other data such as mass, thrust curves, and Mach-dependent drag remain synchronized with OpenRocket for maximum parity.

The simulation is configured via initialization scripts. A rocket-specific script (e.g., aurora.m) loads relevant trajectory and performance data from a .csv export of an OpenRocket simulation. This includes time-series data for thrust, mass, and drag coefficients. Rocket geometry and other parameters, such as launch location and rail angle, can also be configured here. A separate script handles sensor configuration, including settings for noise density, bias instability, and saturation limits, based on datasheets and experimental characterization. Wind disturbances can be configured in an environment script. The configuration scripts automatically perform pre-processing of the data in preparation for the simulation, such as calculating fin parameters from the input geometry.

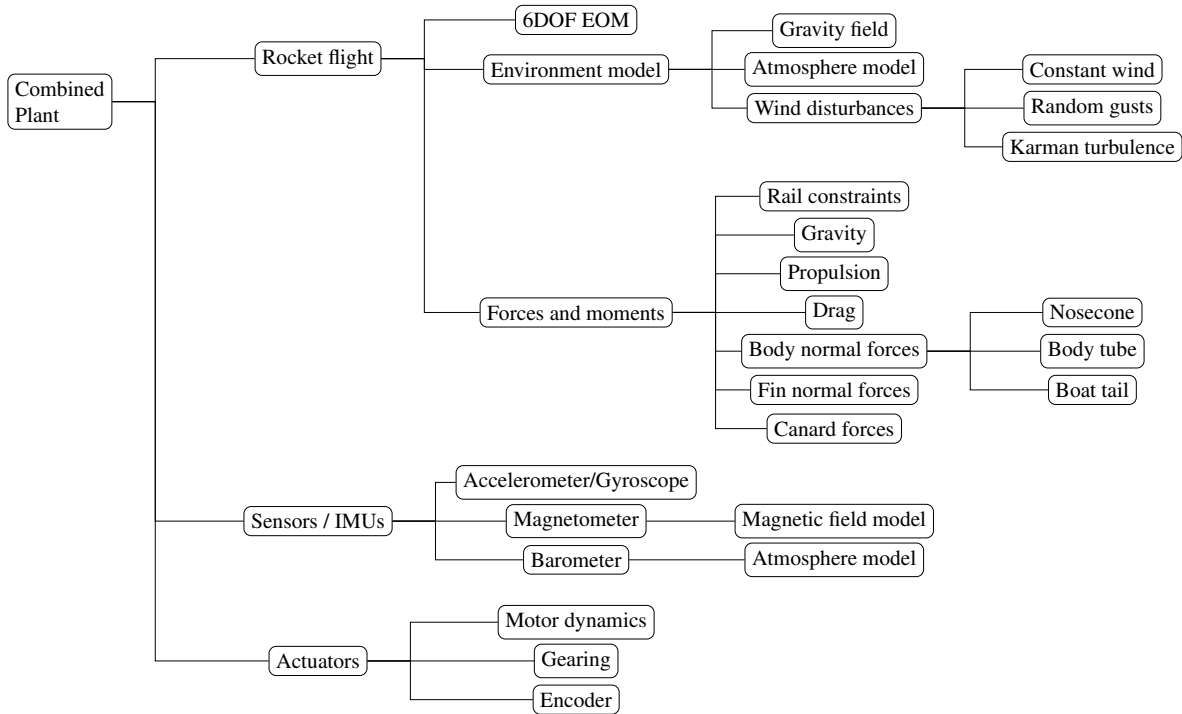


Figure 12.8: Diagram of the Controls flight simulation architecture, hierarchical tree

The sensor subsystem has two custom implemented IMU subsystems to simulate the actual IMUs on Aurora. All sensors are subject to noise and bias, which can be set in the subsystem mask, and output data at the processor sampling rate. The magnetometer and barometer use standard models of Earth's magnetic field and atmosphere, respectively. The accelerometer and rate gyroscope are implemented with dynamic behaviour and limits. The actuator component simulates the nonlinear dynamics of a motor, with dead time and angle/rate limits. Gearing behaviour is included with backlash and misalignment, and the encoder measurements are also modelled with noise.

Aerodynamic force and moment calculations follow the Barrowman method [39], with dynamic computation of coefficients and centres of pressure for the rocket body, fins, and canards at each timestep. This allows the model to account for nonlinear aerodynamic effects, including those from supersonic flow and high angle-of-attack behaviour. Particular emphasis was placed on accurate modelling of canard aerodynamics to ensure fidelity for control testing. At this time the drag force is calculated with Mach/ $C_D$  lookup tables, and the mass and thrust curves are taken from engine tests. The equations of motion are implemented via the variable mass quaternion block from the Aerospace Blockset.

### 12.2.3 Comparison with OpenRocket

The model dynamics implemented in Simulink were validated by comparing the simulated trajectories of both Simulink and OpenRocket. The comparison is shown in Figure 12.9, both simulations are computed without wind disturbances, as these are partly stochastic models. The simulations line up quite well, the most significant difference is the recovery deployment of OpenRocket after

apogee as recovery events are not yet implemented in the Controls simulation.

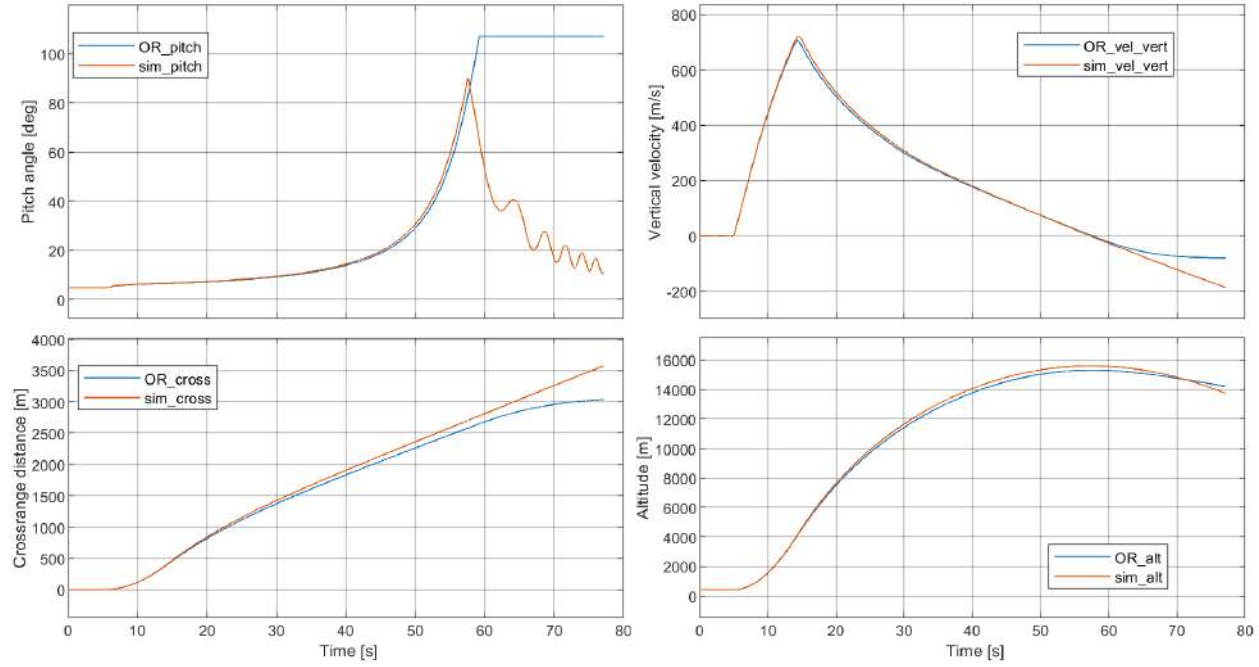


Figure 12.9: Comparison of the developed flight simulation to OpenRocket, simulation in red, OpenRocket in blue. Top left: pitch angle magnitude, top right: Vertical velocity, bottom left: crossrange distance, bottom right: altitude.

## 12.3 Controller and Estimator design

The theoretical background and design rationale are detailed in the design report [37]. The control algorithm is implemented in Matlab, with all design and simulation code available in the design repository [38].

With the introduction of active roll control on Aurora, a robust control system was required to stabilize the rocket's roll motion. This section outlines the design of the controller responsible for regulating the canard-induced roll dynamics. The control system was developed under constraints, most notably the facts that the canards only generate torque about the roll axis, and that the rocket flight is highly dynamic and partly nonlinear. The following subsections describe the Controller and Estimator in detail, including modelling, control laws, and state estimation algorithms.

### 12.3.1 Controller architecture

The controller is responsible for stabilizing the rocket state, attenuating any disturbances, and driving it to some desired value. In their mechanical configuration the canards can only provide a torque around the roll axis of the rocket. This imposes some constraints on the controller design, as it renders the whole rocket system under-actuated with respect to 3DOF attitude, velocity, altitude, etc.

The controller chosen for the canards is linear state feedback, where the feedback gains  $K$  are computed by the *Linear Quadratic Regulator* (LQR) method [40]. The current rocket state is determined by the state estimation algorithm (the Estimator is treated in Sections 12.3.4, 12.3.5, 12.3.6). This estimated state  $\hat{x}$  is projected onto the controllable subspace  $\hat{x}_R$  and the roll model parameter space  $\hat{x}_{FC}$ . The control loop is a two-degree-of-freedom design, where the reference signal is prescaled by a feedforward gain  $K_{pre}$ , as seen in Figure 12.10. To account for the non-linearity of the rocket dynamics, the control gains are selected from a gain schedule, which is a look-up table of gains for different model parameters.

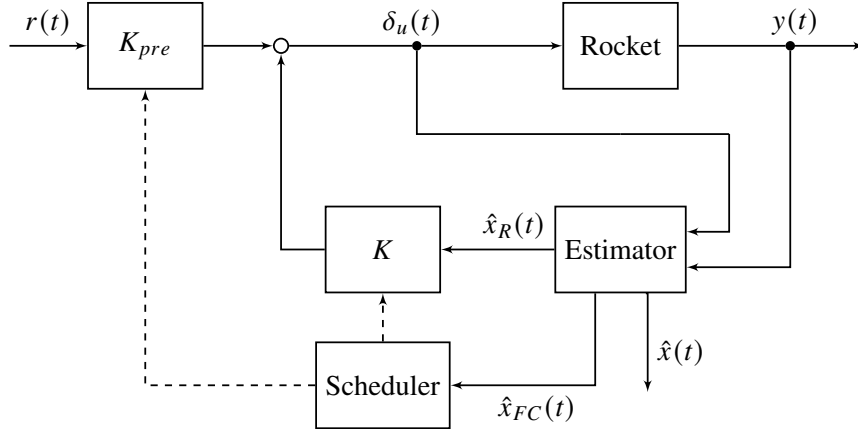


Figure 12.10: Control loop block diagram, gain scheduled two-degree-of-freedom Estimator-based state feedback.

### 12.3.2 Controller roll model

The roll dynamics of the rocket are modelled as a linear parameter varying system using a state-space realization. The state variables are the roll angle  $\phi$ , the roll rate  $\omega_x$ , and the canard actuation angle  $\delta$ . The state  $x_R$  for the roll model and the flight condition  $x_{FC}$  are then

$$x_R = [\phi \quad \omega_x \quad \delta]^T \quad x_{FC} = [\bar{p} \quad C_L] \quad (12.1)$$

where the dynamic pressure  $\bar{p}$  and the canard coefficient  $C_L$  are the scheduling variables of the controller. The state-space model with the servo command signal  $\delta_u$  is

$$\dot{x}_R = A x_R + B \delta_u \quad y_R = C x_R \quad (12.2)$$

with the matrices

$$A(x_{FC}) = \begin{bmatrix} 0 & 1 & 0 \\ 0 & L_{\omega_x} & L_\delta \\ 0 & 0 & -\tau \end{bmatrix} \quad B = \begin{bmatrix} 0 \\ 0 \\ \tau \end{bmatrix} \quad C = [I_3] \quad (12.3)$$

where the roll control derivative is  $L_\delta(\bar{p}, C_L)$ , the roll damping derivative is  $L_{\omega_x}(\bar{p}, C_L)$ , and the actuator time constant is  $1/\tau$ . The matrix  $C$  combines the states of the system to an output signal. The states are assumed to be well known by the Estimator, so the output can be set arbitrarily for response analysis. For the case  $C = [I_3]$ , the output signal is the entire state vector  $y(t) = x_R(t)$ , for the case  $C = [1 \ 0 \ 0]$  the output signal is  $y(t) = x_{R,1}(t) = \phi$ . The open-loop eigenvalues are simply

$$\lambda_1 = 0 \quad \lambda_2 = L_{\omega_x} \quad \lambda_3 = -\tau \quad (12.4)$$

The rocket in open-loop is only marginally stable due to the free integrator from the roll rate to roll angle ( $\omega_x \rightarrow \phi$ ). Additionally, when using a spin can the damping derivative  $L_{\omega_x}$  is very small compared to the control derivative  $L_\delta$ . When assuming  $L_{\omega_x} \approx 0$  the open-loop is quadratically unstable.

To determine if pole placement is possible, which is a necessary condition for LQR [40], the roll model is checked for controllability. The controllability matrix is

$$C = [B \ AB \ A^2B] \quad (12.5)$$

which has full rank for all  $L_\delta \neq 0$ , i.e. there exists a feasible feedback gain for every flight condition, except for zero dynamic pressure ( $\|v\| = 0$  or  $\rho = 0$ ) or a zero coefficient of lift ( $C_L = 0$ ).

### 12.3.3 Roll control law design

The control law is a two-degree-of-freedom state feedback controller, with the reference gain  $K_{pre}$  and the feedback gains  $K = [K_\phi \ K_{\omega_x} \ K_\delta]$  being adjusted by a gain schedule. The control law is

$$\delta_u(t) = K\hat{x}_R(t) + K_{pre}r(t) \quad (12.6)$$

The gain scheduler interpolates the gain matrices linearly between design points of the flight condition  $x_{FC}$ . The collection of gains for the design points and a linear interpolation over them results in the scheduling surfaces shown in Figure 12.11. The dependence of the gains on the dynamic

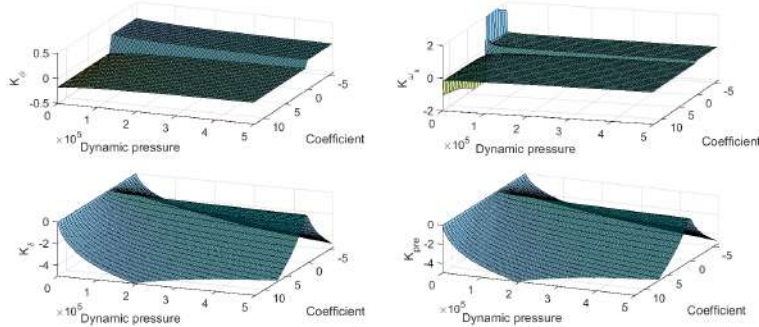


Figure 12.11: Controller gain scheduling surfaces

pressure and canard coefficient are clearly visible. The cases of  $\bar{p} = 0$  and  $C_L = 0$  result in unfeasible feedback gains, so the design points are cut off for these values. Negative dynamic pressure is not possible by definition, and the gains are interpolated over a zero coefficient (resulting in a characteristic ridge shape). If the flight condition is outside of the design point envelope, the gains are set to  $K = 0$  and  $K_{pre} = 0$ .

The feedback gains are computed by performing the LQR method on the system matrices of each design point, using the `lqr` function in Matlab as

$$K = -\text{lqr}(A, B, Q, R) \quad (12.7)$$

The LQR method minimizes the cost function

$$\min \int_0^{\infty} (x^T(t)Q_c x(t) + u^T(t)R_c u(t))dt \quad (12.8)$$

which is the accumulated weighted squared state error and control effort [40]. The reference gain is chosen to achieve a zero steady-state error (with  $C = [1 \ 0 \ 0]$  the roll angle is tracking the reference) under ideal conditions, so

$$K_{pre} = \frac{1}{-C [A + BK]^{-1} B} \quad (12.9)$$

## Tuning and responses

The state error and control effort weighting matrices,  $Q_c$  and  $R_c$ , are chosen as

$$Q_c = \begin{bmatrix} 9 & & \\ & 4 & \\ & & 4 \end{bmatrix} \quad R_c = 300 + 0.003 \frac{\bar{p}}{1\text{Pa}} \quad (12.10)$$

which places the highest error weight on the roll angle error. The control effort weight is scaled affine linear to stiffen up for higher dynamic pressures. This was found to be necessary in later simulations, as the simulated actuator behaviour is nonlinear and a reduced bandwidth at higher dynamic pressures reduces the impact of the actuator rate limit.

The open loops  $\mathcal{L}(x_{FC}) = K_{pre}K I(sI - A)^{-1}B$  have the loop shapes shown in Figure 12.12. The amplitudes curves should be outside the blue and red boxes for proper disturbance rejection and noise attenuation, respectively [41]. Especially the high frequency gain should be below  $-40$  dB to reduce aliasing behaviour in the control loop. For good robustness, the curves should crossover the  $0$  dB line with a slope of  $-20$  dB to  $-30$  dB, the slopes are shown as green cones [41]. The plant without controller is shown on the rightmost side which clearly violates the crossover cone. This corresponds to the marginally stable behaviour expressed by the eigenvalues  $\lambda_1$  and  $\lambda_2$ . The open-loop amplitudes with the controller mostly satisfy all requirements, and show good robustness behaviour in the crossover region. At low dynamic pressure the canards have reduced control authority and the loop will have slower tracking. The plot is extended to a frequency of  $200$  Hz, which is chosen as the control processing rate due to the high frequency gain requirement. If the Processor Board struggles to achieve a  $200$  Hz control cycle, the bandwidth can be lowered to accommodate slower processing.

The (approximately in continuous time) closed loop is

$$\dot{x}_R = (A + BK)x_R + BK_{pre}r \quad y_R = Cx_R \quad (12.11)$$

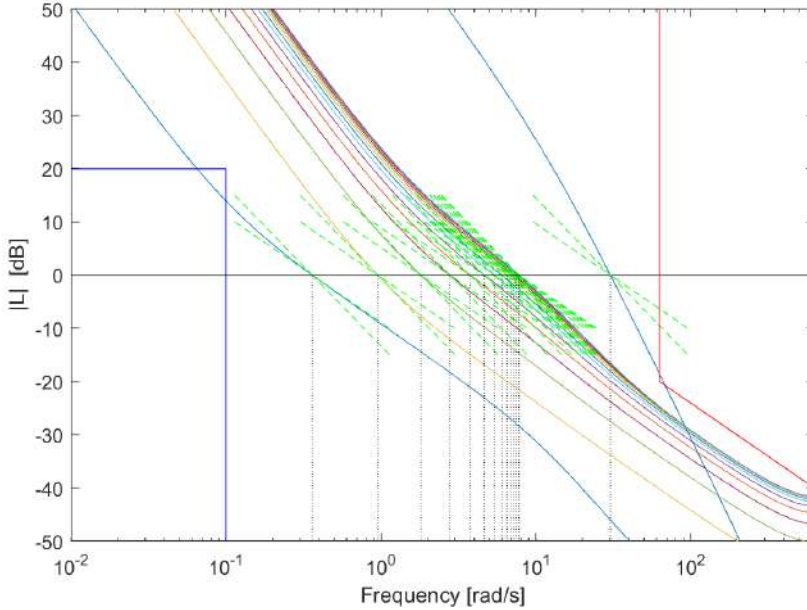


Figure 12.12: Open loop Bode plot (amplitude only), for different dynamic pressures. Constraints are blue and red boundaries, crossover slope should be in the green cones. Uncontrolled plant is the rightmost curve.

which has the responses shown in Figure 12.13. The step responses in Figure 12.13a show smooth behaviour of the closed loop, as the roll angle has no peak overshoot and no oscillations are visible. At low dynamic pressures, the roll responses are much slower due to decreased control authority, even though the actuation angle is the largest there. The roll rate dampens out within a few seconds, and the actuation angle stays always well within the maximum allowable angle of  $10 \text{ deg} = 0.1745 \text{ rad}$  imposed by the Flight Dynamics subsystem. The Bode diagram in Figure 12.13b shows a cutoff at the discrete processing frequency of  $200 \text{ Hz}$  of the control loop. The low frequency gain of  $0 \text{ dB}$  means that there is no slow roll angle increase. The bandwidth is lower for lower dynamic pressures, as expected from previous analysis.

#### 12.3.4 Estimator architecture

The state estimation algorithm is responsible for accurately determining the current rocket state  $\hat{x}$ , describing the rocket attitude, rate, velocity, altitude, and canard coefficient and angle [37]. Because the underlying dynamics are partly nonlinear, an *Extended Kalman Filter* (EKF) is used to estimate the current state. The EKF algorithm uses these modelled dynamics to

1. predict the current state from the last state and control inputs to the rocket
2. correct the state using measurements from onboard sensors, including rate gyroscopes, magnetometers, accelerometers, barometers.

The process is a Bayes filter, where the state estimate has an associated belief  $P$  in the accuracy of the estimate. As the EKF employs nonlinear models, it needs an accurate initial state estimate for later linearization. For this reason, the *Pad Filter* determines the initial rocket orientation and sensor biases while the rocket is idle on the launch rail [37].

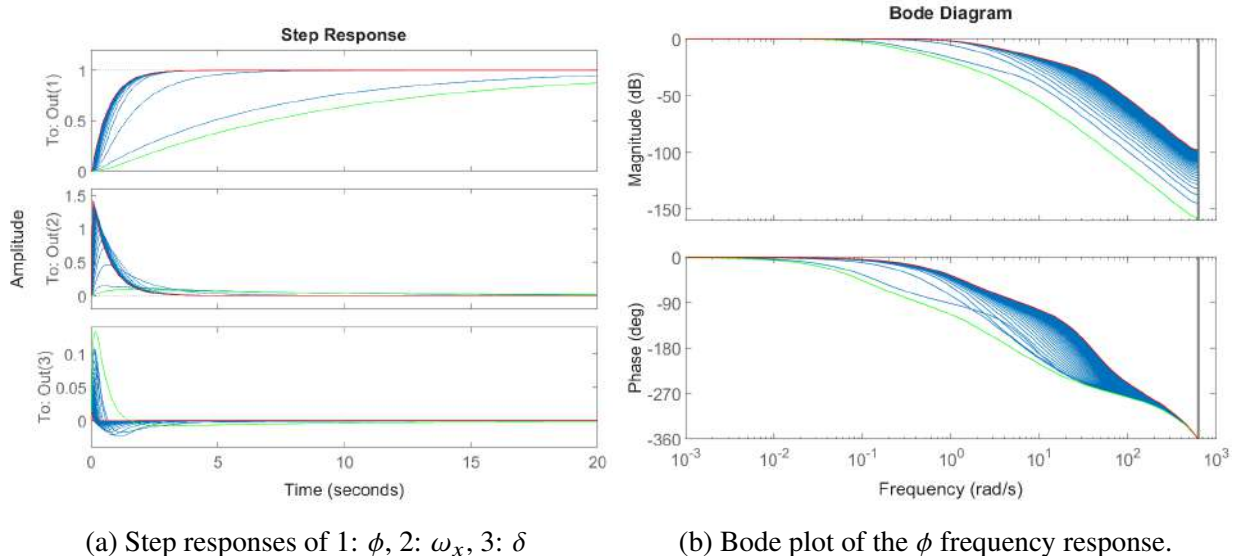


Figure 12.13: Responses of the closed-loop system, for different dynamic pressures. Response at airspeed  $V = 20 \frac{m}{s}$  in green, airspeed  $V = 900 \frac{m}{s}$  in red.

### 12.3.5 Estimator models

Dynamical models of the rocket flight are needed for the estimator algorithm. The rocket model is made up of a system of algebraic and differential equations, which describe the rocket motion and the sensor measurements.

#### Kinematics and dynamics

The ground frame  $f^G$  is assumed to be the earth-flat geographic frame, with an up-crossrange-downrange orientation. The origin is located below the launch rail at sea level. The body-fixed frame  $f^B$  is oriented along the main axes of the rocket body, namely forward-starboard-rail ( $x^+$  is forward). The origin of the body-fixed frame is located at the dry centre of gravity. The sensor frames  $f^S$  are aboard the rocket, but rotated and translated against the body frame. To simplify the following notations, the velocities, the angular rates, and the external forces and torques are given in the body-fixed frame, and the index  $B$  is omitted.

The attitude quaternion is defined as

$$q = [q_w \quad q_x \quad q_y \quad q_z]^T = \begin{bmatrix} q_w \\ q_v \end{bmatrix} \quad (12.12)$$

To describe rotations the attitude quaternion is normed to  $|q| = q^T q = 1$ . This unit constraint is enforced in the filter process by norming  $q$  after modification [42]. The inverse of a unit quaternion is simply the conjugate  $q^{-1} = [q_w, \quad q_v]^{-1} = [q_w, \quad -q_v]$ . The time derivative of the quaternion

attitude with angular rates  $\omega$  described in the body-fixed frame is [42, 43, 44]

$$\dot{q} = \frac{1}{2}q * \begin{bmatrix} 0 \\ \omega \end{bmatrix} = \frac{1}{2}\tilde{Q} \cdot \begin{bmatrix} 0 \\ \omega \end{bmatrix} \quad \text{with} \quad \tilde{Q} = \begin{bmatrix} q_w & -q_x & -q_y & -q_z \\ q_x & q_w & -q_z & q_y \\ q_y & q_z & q_w & -q_x \\ q_z & -q_y & q_x & q_w \end{bmatrix} \quad (12.13)$$

For integration to a discrete time update, multiple approaches can be used. The simplest method to implement is explicit Euler with posteriori norming, which assumes small time steps such that the quaternion norm does not deviate far from 1. The rotation matrix  $S = S_G^B$  is used to transform a vector from the ground frame  $G$  to the body-fixed frame  $B$ . It can be computed directly from the quaternion as [43]

$$S = \begin{bmatrix} q_w^2 + q_x^2 - q_y^2 - q_z^2 & 2q_wq_z + 2q_xq_y & 2q_xq_z - 2q_wq_y \\ 2q_xq_y - 2q_wq_z & q_w^2 - q_x^2 + q_y^2 - q_z^2 & 2q_wq_x + 2q_yq_z \\ 2q_wq_y + 2q_xq_z & 2q_yq_z - 2q_wq_x & q_w^2 - q_x^2 - q_y^2 + q_z^2 \end{bmatrix} \quad (12.14)$$

$$= 2q_vq_v^T + (q_w^2 - q_v^T q_v)I_3 - 2q_w\tilde{q}_v$$

As the rotation matrix is orthogonal the inverse transformation is  $S^{-1} = S^T$ , and thus  $S_B^G = S^T$ . The inverse rotation matrix is the rotation matrix of the inverse quaternion  $S^T(q) = S(q^{-1})$ . The Euler angles *yaw*  $\psi$ , *pitch*  $\theta$ , and *roll*  $\phi$  can be recovered from the rotation matrix elements. For the rotation sequence yaw → pitch → roll (order  $z \rightarrow y' \rightarrow x''$ ) the Euler angles are [43]

$$\psi = \text{atan2}(S_{12}, S_{11}) \quad \theta = \arcsin(-S_{13}) \quad \phi = \text{atan2}(S_{23}, S_{33}) \quad (12.15)$$

The change of velocity  $v = [v_x \ v_y \ v_z]^T$  in the rotating body-fixed frame is [44, 43]

$$\dot{v} = [A - \dot{\omega} \times d_A - \omega \times (\omega \times d_A)] - \omega \times v + Sg^G \quad (12.16)$$

which accounts for the derivation in the rotating frame with the transport term  $-\omega \times v$ , and corrects the measured acceleration  $A$  of the IMU for centrifugal and angular accelerations. The gravity vector  $g^G \approx [-9.81 \ 0 \ 0]^T \frac{\text{m}}{\text{s}^2}$  is transformed to the body-fixed frame to account for the gravitational acceleration, as the ground frame  $G$  is not truly inertial.

The position change in the ground frame is

$$\dot{r}^G = S^T v \quad (12.17)$$

The change in angular rate  $\omega = [\omega_x \ \omega_y \ \omega_z]^T$  of a rigid body is [43, 44]

$$\dot{\omega} = J^{-1}(\mathcal{T} - \omega \times J\omega) \quad (12.18)$$

with the external torques  $\mathcal{T}$  described in the body-fixed frame, and the gyroscopic moment. The inertia tensor  $J$  is determined from CAD or experimentally. If the coupling inertia moments are very small, they may be neglected to fill the tensor diagonally as  $J = \text{diag} [J_x \ J_y \ J_z]$ , where in a rocket cruciform typically  $J_x < J_y = J_z$  [37].

## Measurements

The accelerometer measures the apparent acceleration  $A$  relative to the inertial frame. The gyroscope measures the angular rates directly in the body-fixed frame  $\Omega \approx \omega$ . The magnetometer measures the magnetic field vector aboard the rocket  $M$ , which consists mostly of the earth magnetic field  $M_E^G$ . This relation is approximately (as there are field distortions by onboard irons)

$$M \approx S(q) M_E^G \quad (12.19)$$

and can be used to correct the attitude drift accrued by the gyroscope rate integration. The barometer measures the static air pressure  $P$ , an estimate of which is computed with the US standard atmosphere model [45]

$$P \approx \text{atmosphere}(altitude, constants) \quad (12.20)$$

The canard shaft encoder directly measures the canard angle  $\delta_e \approx \delta$ .

## Aerodynamics

The aerodynamic forces acting on the rocket are measured by the accelerometer. However the aerodynamic torques can be used to infer accurate behaviour of the canards. The main effects of rocket flight are pitch/yaw torques due to normal forces caused by the tail fins and rocket body, and roll torques caused by the canards and canard/fin interaction. The normal torques and the roll torque are

$$\mathcal{T}_{\text{normal}} = \begin{bmatrix} 0 \\ \bar{p} C_{N_\alpha} \alpha A^{\text{ref}} d^{\text{ref}} \\ \bar{p} C_{N_\beta} \beta A^{\text{ref}} d^{\text{ref}} \end{bmatrix} \quad \mathcal{T}_{\text{canard}} = \begin{bmatrix} \bar{p} C_{L_\delta}^{\text{can}} \delta A^{\text{can}} d_y^{\text{can}} \\ 0 \\ 0 \end{bmatrix} \quad (12.21)$$

with the dynamic pressure  $\bar{p} = \frac{1}{2} \rho \|v\|^2$ , the reference and canard planform areas  $A^i$ , and the lever arms from the respective centre of pressure to the respective inertia axes  $d^i$ . The coefficient derivatives  $C_{i,j}$  depend on the rocket and canard geometries and can be predicted using Barrowman's method [39, 46], and thin airfoil theory [47]. The local incidence angles are the angle of attack of the rocket  $\alpha$ , and the canard actuation angle  $\delta$ . The theoretical canard coefficient  $C_{L,\text{th}}$  is calculated according to Equation 6.16 from subsection 6.8. As the canard coefficient is a state, it can be estimated to a more accurate value if the theoretical value is wrong. This is the case, when for example supersonic roll reversal occurs.

## State space realization

The nonlinear state-space realization has the state vector  $x$  consisting of attitude  $q$ , rates  $\omega$ , velocity  $v$ , altitude  $l$ , and the canard coefficient  $C_L$  and actuation angle  $\delta$  [37]

$$x = [q \ \omega \ v \ l \ C_L \ \delta]^T \quad (12.22)$$

and the input and measurement vectors, consisting of the controller command  $\delta_u$  and the encoder measurement  $\delta_e$ , as well as the IMU package measurements acceleration  $A$ , rates  $\Omega$ , magnetic field  $M$ , and barometric pressure  $P$

$$u = [A \quad \delta_u]^T \quad y_{IMU} = [\Omega \quad M \quad P]^T \quad y_{encoder} = [\delta_e] \quad (12.23)$$

The state and measurement equations are [37]

$$\dot{x} = f(x, u) = \begin{bmatrix} \text{Equation 12.13} \\ \text{Equation 12.18} \\ \text{Equation 12.16} \\ \text{Equation 12.17} \\ \tau_c(C_{L,th} - C_L) \\ \tau_\delta(\delta_u - \delta) \end{bmatrix} \quad y_{IMU} = h_{IMU}(x) = \begin{bmatrix} \omega \\ S(q) M_E^G \\ \text{atmosphere}(l) \\ \delta \end{bmatrix} \quad (12.24)$$

As the Estimator process runs on the embedded processor in discrete time, the state equation  $f$  has to be integrated to a discrete state update equation  $f_D$ . The integration method used is *explicit Euler* as it is simple to implement and to partially differentiate

$$x_{k+1} = \int_0^{t+dt} f(x(t), u(t)) dt \approx x_k + dt \cdot f(x_k, u_k) = f_D(x_k, u_k) \quad (12.25)$$

The EKF requires linearizations of the state update and measurement functions to propagate the covariance, the Jacobians of the state update and the measurement functions are

$$F_D(x, u) = \frac{\partial f_D}{\partial x} \quad H(x) = \frac{\partial h}{\partial x} \quad (12.26)$$

The Jacobians are derived analytically to reduce computational effort of the processor, the derivations are given in [37].

To check if the filter can converge at a given state, the linearized system is examined for observability. The observability matrix (with the number of states  $n = 13$ ) is

$$O = \begin{bmatrix} H \\ HF_D \\ HF_D^2 \\ \vdots \\ HF_D^n \end{bmatrix} \quad (12.27)$$

which has rank 13 for almost all randomly tried state combinations, except for a rank loss to 12 at  $\delta = 0$  which leads to the coefficient being undetermined. This turns out not to be an issue in simulation, as  $C_L$  quickly converges near its actual value when the canard is actuated.

### 12.3.6 EKF algorithm

In flight the Estimator runs the EKF with the models derived above, propagating the state estimate  $\hat{x}$  and the covariance  $P$ . One complete iteration of the algorithm of the discrete EKF is [48, 40]

Predict:

$$\hat{x}_k^- = f_D(\hat{x}_{k-1}^+, u_{k-1}) \quad (12.28)$$

$$P_k^- = F_D(\hat{x}_k^-, u_{k-1}) P_{k-1}^+ F_D^T(\hat{x}_k^-, u_{k-1}) + Q_e \quad (12.29)$$

Correct:

$$K_k = P_k^- H^T(\hat{x}_k^-) [H(\hat{x}_k^-) P_k^- H^T(\hat{x}_k^-) + R_e]^{-1} \quad (12.30)$$

$$\hat{x}_k^+ = \hat{x}_k^- + K_k [y_k - h(\hat{x}_k^-)] \quad (12.31)$$

$$P_k^+ = [I - K_k H(\hat{x}_k^-)] P_k^- [I - K_k H(\hat{x}_k^-)]^T + K_k R_e K_k^T \quad (12.32)$$

Here the prediction part consists of the discrete-time dynamics (Equation 12.28) and the associated covariance in discrete-time (Equation 12.29). The correction part computes the filter gain  $K_k$  using the covariance of the estimate  $P$  and the sensitivity of the measurement model  $H$  (Equation 12.30). As the measurement model is discrete, the computation of the predicted measurements ( $\hat{y} = h(t, \hat{x}_k^-)$ ) and the correction of the state estimate (Equation 12.31) is straightforward. The covariance of the estimate is updated (Equation 12.32) using the Joseph stabilized form to ensure the covariance remains positive semidefinite, even if the gain  $K_k$  is suboptimal [48].

The EKF is tuned using the weighting matrices  $Q_e$  and  $R_e$ , which represented the expected noise covariances of dynamics and measurement.

Nominally the correction step is performed sequentially multiple times as multiple sensors are available for feedback. All sensors have their own measurement model (and bias), Jacobian, and weighting.

The weighting matrices of the state prediction and the measurement correction,  $Q_e$  and  $R_e$ , are set to

$$Q_e = \text{diag} [[1 1 1 1]E^{-10} \quad [1 1 1]E^{-2} \quad [1 1 1]E^{-2} \quad 1E^{-3} \quad 30 \quad 0.5] \quad (12.33)$$

$$R_{e, IMU1} = 2 \text{diag} [[1 1 1]E^{-8} \quad [1 1 1]E^{-3} \quad 1] \quad (12.34)$$

$$R_{e, IMU2} = 3 \text{diag} [[1 1 1]E^{-8} \quad [1 1 1]\frac{1}{3}E^{-3} \quad 1] \quad (12.35)$$

$$R_{e, encoder} = 0.002 \quad (12.36)$$

### Pad Filter calibration and initialization

While the rocket is stationary on the launch rail, the *Pad Filter* computes average sensor values with a low-pass filter to determine

1. Sensor biases
2. Initial rocket attitude relative to the ground
3. Earth magnetic field vector

The sensor bias determination is especially important for the rate gyroscope integration, as it reduced dependence of the filter on the noisy magnetometer. As the rocket acceleration off the rail may exceed the accelerometer limits, the initial barometer bias is also important to get accurate altitude and velocity estimates in the boost phase.

The initial attitude is computed using the accelerometer as an inclinometer, and defining the roll angle as zero. With this orientation the measured magnetic field is referenced to the zero attitude, this way the state estimation is not dependant on high-fidelity magnetic field models.

### 12.3.7 Simulation results

The designed control loop is tested in the Controls flight simulation described in subsection 12.2.

#### Single simulation

The closed-loop simulated step responses of the rocket roll angle are shown in Figure 12.14. The roll stability of the rocket is good, with the rocket smoothly tracking the roll program reference. The steps show a non-zero steady-state error, which is due to the simulated backlash in the canard gearing. The rocket loses control authority near apogee, as air density and airspeed are low.

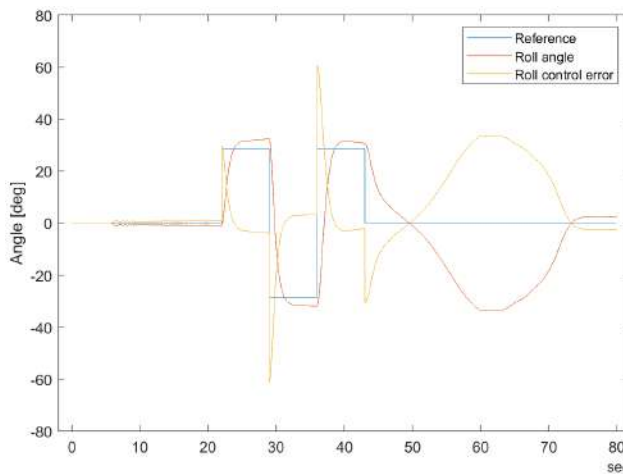


Figure 12.14: Controlled roll angle

The Estimator results are shown in Figure 12.15. This plot shows the actual simulated rocket states, and the estimated states computed from simulated sensor measurements. The estimation of the attitude, rates, altitude, and canard angle is almost exactly the same as the simulated values, indicating good Estimator performance. The velocity estimate deviates from true near apogee, as the airspeed is low and the aerodynamic effects used for estimation are not as pronounced. The canard coefficient estimation shows the largest deviations from the true value, which is mostly due to the canard angle being zero most of the time.

The estimation error, i.e. the difference between simulated actual and estimated state, is shown in Figure 12.16. For the attitude, rates, and canard angle, the error is within one percent of the maximum value. The same is true about the altitude, as a maximum error of 30 m is quite small given the apogee of about 15 km. The maximum velocity error is quite large with 50 m/s, to note

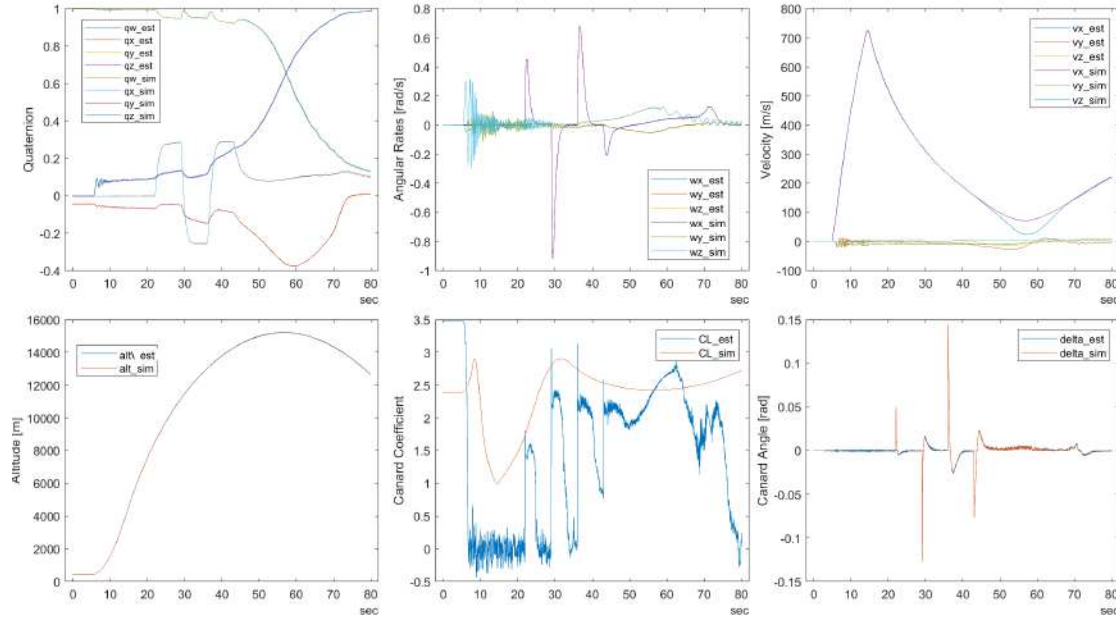


Figure 12.15: Simulated vs. estimated states. Top from left: Attitude quaternion, body rates, velocity. Bottom from left: Altitude, canard coefficient, canard angle.

is however that the air density and thus dynamic pressure is about five times lower than sea level when this occurs. The velocity error presents the biggest issue in further tuning the Estimator. As noted above, the canard coefficient error is quite large. However, the roll stabilization is quite smooth as can be seen in Figure 12.14, so this does not present a large issue.

### Monte-Carlo simulations

The simulation is run 200 times with swept parameters to analyze the Estimator and Controller behaviour. The closed-loop simulated step responses of the rocket roll angle are shown in Figure 12.17. To note is the spin up of the rocket during the boost phase, as the actuator is deactivated there. Additionally, the rocket loses control authority near apogee, as air density and airspeed are low. During the coast phase, the rocket roll angle follows the roll program smoothly for the majority of simulations. The simulated and actual states are shown in Figure 12.18. The estimation error is shown in Figure 12.19. The errors of angular rate, altitude, and canard angle are low as expected. The attitude deviates slightly from

## 12.4 Motor Control Board

Motor Control Board (MCB) is an SRAD board developed specifically to control the canards servo. It replaces Charging Board, which was used to control the airbrakes servo on Borealis but suffered from significant design and integration challenges. MCB actuates a single servo motor using PWM signals, in accordance with commands received from Processor Board via RocketCAN. In addition, MCB measures the servo current and battery voltage and reads the position of the canard shaft from

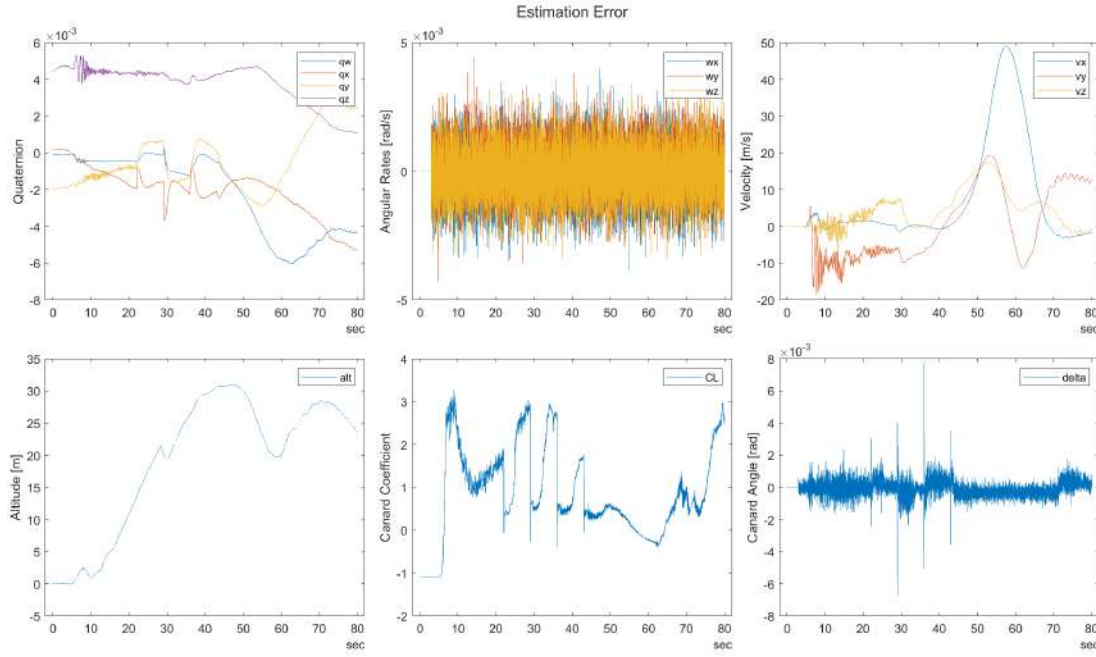


Figure 12.16: Simulation estimation error

an angular encoder. This positional data is relayed back to Processor Board, where it is used in the flight control loop and assists with servo dynamics and backlash characterization during testing.

In line with other RocketCAN boards, MCB utilizes PIC18F26K83 MCUs. It is powered by a dedicated 3S LiPo battery using the new standard charging interface (see subsubsection 9.2.1). This design reduces dependency on the main power system, increasing reliability and isolating the servo's high current draw. The encoder is sampled at 1 kHz, low-pass filtered to 200 Hz, and transmitted to the Processor Board. Servo commands are nominally received every 5 ms, but this interval is flexible and non-blocking. If no command is received within 100 ms, MCB returns the canards to 0 degrees (their neutral state) until communication is reestablished. The PWM frequency is set to 300 Hz, which is well above the servo drive frequency but below the 300 Hz servo limit. Current and voltage are logged at 5 Hz and 1 Hz, respectively.

## 12.5 Processor Board

Processor Board was originally designed to control the airbrakes system onboard Borealis, and has since been updated to serve a similar purpose for canards. The board interfaces with RocketCAN, as well as two IMUs and a dedicated SD card. The purpose of the board is to run the control loop by reading IMU data, computing state estimation and controller output (described in subsection 12.3), and sending the control command to MCB.

### 12.5.1 Electrical

The board saw two major hardware changes this year, with the first being the replacement of the VN-300 IMU that was previously flown with three new IMUs:

1. (Movella), and XSENS MTi-630 DK IMU from Movella

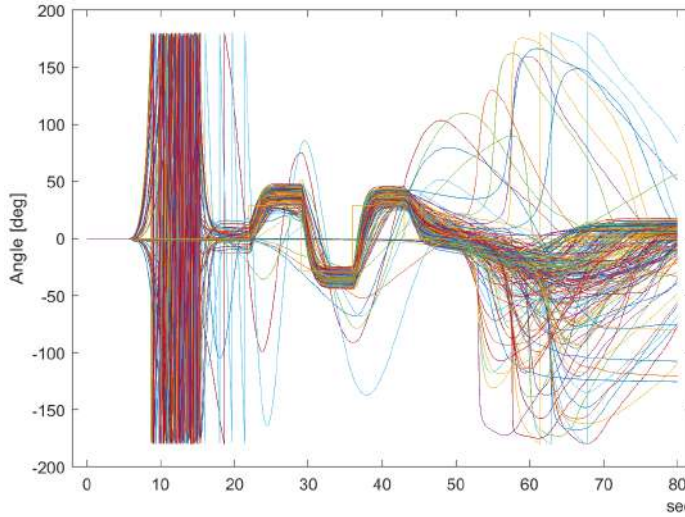


Figure 12.17: Monte-Carlo controlled roll angle, 200 simulations

2. (AltIMU), a combination of LSM6DSO, LIS3MDL, and LPS22DF from ST mounted on an AltIMU-10 v6 circuit board from Pololu
3. (LSM), an LSM6DSV16XTR from ST mounted directly on the processor board

It was determined that due to the higher risks associated with flying canards and the requirement to also fly it on the Testflight, it was no longer justifiable to have the VN-300 on board due to its cost. The AltIMU and Movella offer low noise and high sensitivity for both the accelerometer and gyroscope, which is essential for accurate measurements during flight, while adding the LSM provides a backup IMU during flight should the others fail, and also another point of comparison to detect errors during bench-top testing and potentially even flight. Unfortunately, due to an error in electrical design, the LSM was determined to be unusable without a rework of the board. As such, only the AltIMU and the Movella are in use on Aurora. The second change is replacing the 5-3.3 V LDO with a buck converter, which improves the power conversion efficiency of the board from 66% to 95% and reduces the load on the RocketCAN 5 V line.

Figure 12.20 shows the front side of a fully assembled processor board. At the time of writing, the processor board has been assembled in its flight condition and tested with firmware.

### 12.5.2 Firmware

The STM32H723 MCU runs the 200 Hz control cycle using C firmware on FreeRTOS. It uses a layered architecture which decouples hardware drivers (I2C, ADC, etc.) from application modules (controller, state estimation, etc). FreeRTOS was chosen for its success on Borealis. C++ was briefly considered, but C was chosen for its simplicity, which aligns with the relatively simple scope of this firmware project.

A major goal for this design cycle was to improve the reliability of the firmware by implementing stronger testing and safety-critical practices in anticipation of future controls projects. A new initiative of this design cycle was adopting the BARR-C:2018 coding standard [49] with the goal of improving code safety and consistency. This standard was enforced through code review with

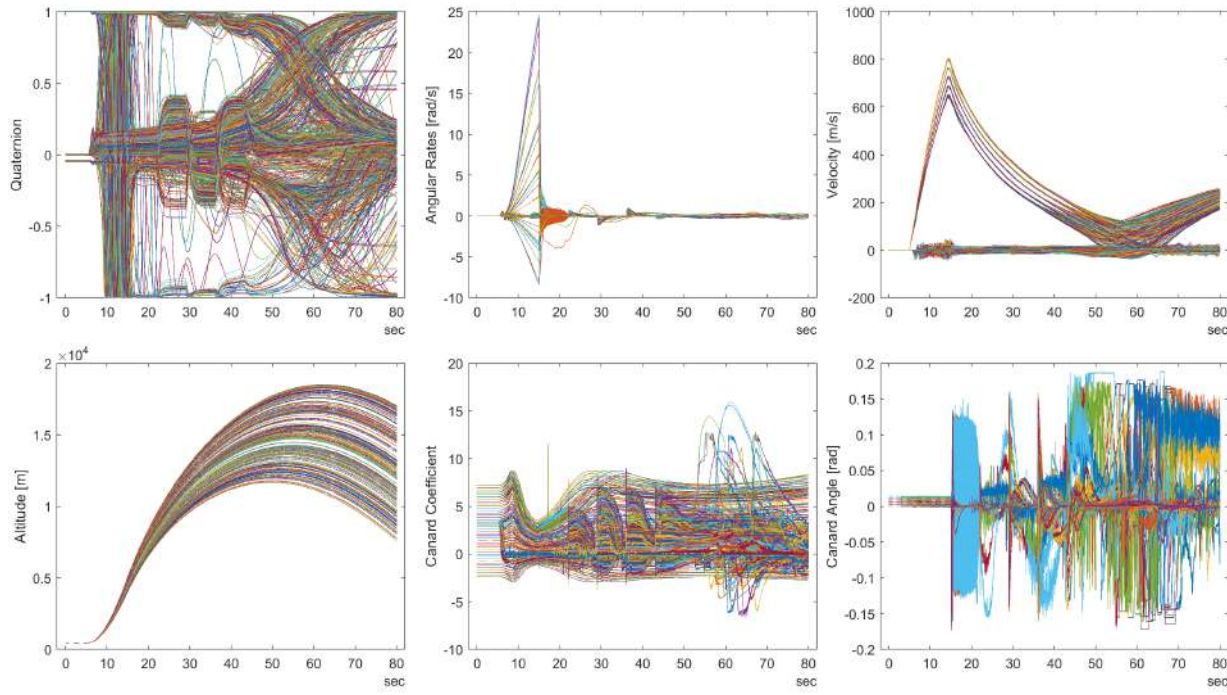


Figure 12.18: Monte-Carlo estimated vs simulated state, 200 simulations

some success, but more importantly served as a useful reference when making code implementation decisions.

A necessary improvement from Borealis was to allow higher logging bandwidth given the faster control cycle and more data to log. The system still uses FATFS and an onboard SD card. Using flash memory was considered, but for ease of access and historical success on the team, it was decided to still use SD cards. To allow logging IMU data, state estimation, and controller outputs at 200 Hz, raw binary data would provide more freedom with post-flight analysis than the human-readable strings used on Borealis. Furthermore, logging raw C structures was determined to be better than using an encoding system (Protocol Buffers, etc.) due to increased simplicity and efficiency. String-based logging exists still partially for non-repeating events such as errors. The logger module uses ping-pong buffers to allow tasks to write messages into one buffer while the other buffer is written to the SD card. A Python script is then used to parse the raw binary logs for data processing.

The timing and data flow for the main control loop tasks are described in Table 12.1. Task priorities were set on the principle of prioritizing producers over consumers, with IMU Handler, Estimator, Controller having increasing priorities respectively. This way, the IMU Handler task cannot collect new data (and thus start a new cycle) until the Estimator and Controller tasks complete. Merging the above three tasks into one task was considered but decided against to decouple each module and allow injecting data at different stages of the control loop for testing.

As the Estimator and Controller were designed in Matlab, one critical challenge was implementing the design in C. A key decision was whether to use Matlab C code generator or translate

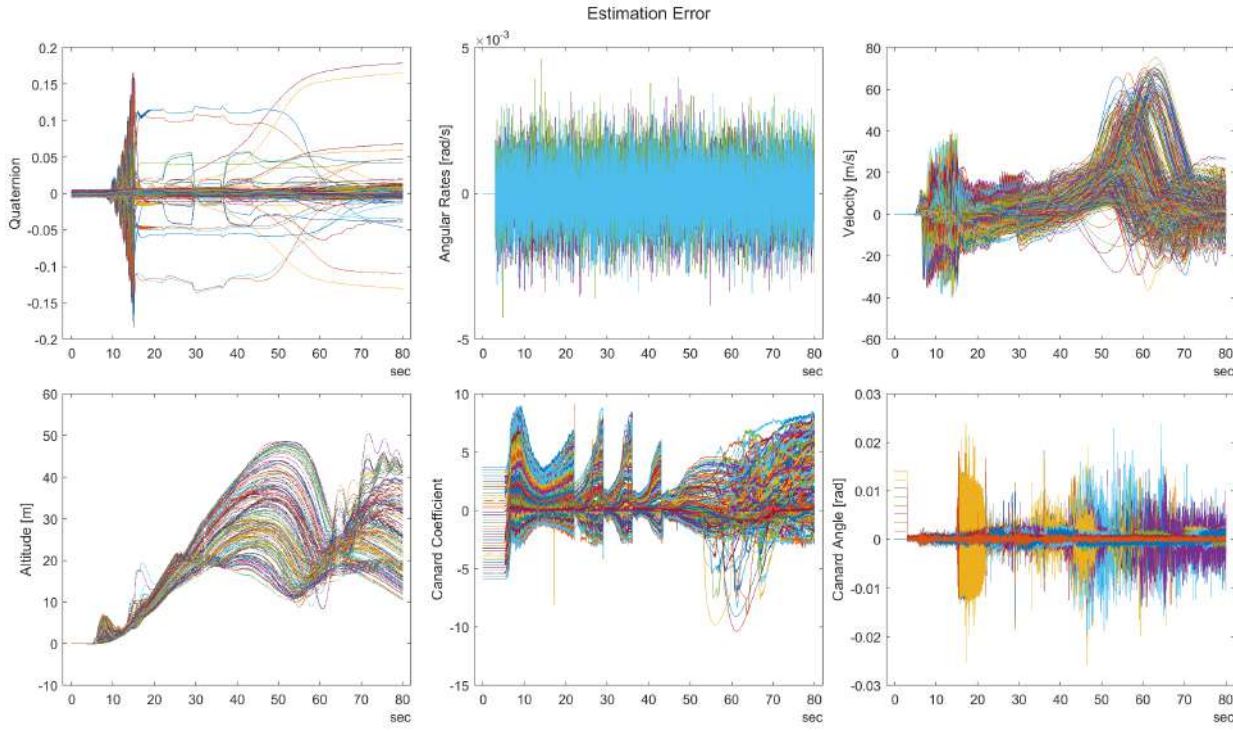


Figure 12.19: Monte-Carlo estimation state error, 200 simulations

the Matlab design into C by hand. It was determined that the code style generated by Matlab would result in worse runtime. It was also determined by the team to be more error-prone, since the generated code is difficult to read, and hence difficult to optimize for our chip architecture, like using the STM32 hardware trigonometry accelerator. As such, all the C code for state estimation and controller was translated by hand one-to-one from the Matlab design, with the exception that the Matlab file structure was altered to accommodate the nature of C. Each state estimation and controller function from Matlab was translated into a corresponding C function, preserving most of the structure and logic of the Matlab design as closely as it deemed possible. To implement advanced math operations, the CMSIS-DSP library was chosen for its easy-to-use matrix and interpolation operations, as well as its adaptability with our chip. Double-precision floating point was required over single-precision to reduce compounding errors in consecutive sequence of operations. The STM32H7 floating-point unit made the performance trade-off negligible.

The Estimator and Controller modules operates during different subsets of flight phase, shown in Figure 12.21. During the pad filter phase, the Estimator runs pad filter calculations each cycle while the controller is idle. To meet DTEG R7.4.1, the controller does not run any calculations except during the actuation-allowed phase. The risk of this lockout failing was deemed very low. This is because the flight phases are timer-controlled; timer hardware failure is very unlikely.

### 12.5.3 Testing

Unit testing was a new initiative of this design cycle. It was critical for the success of Matlab to C translation. All Estimator and Controller code and supporting math-related functions were

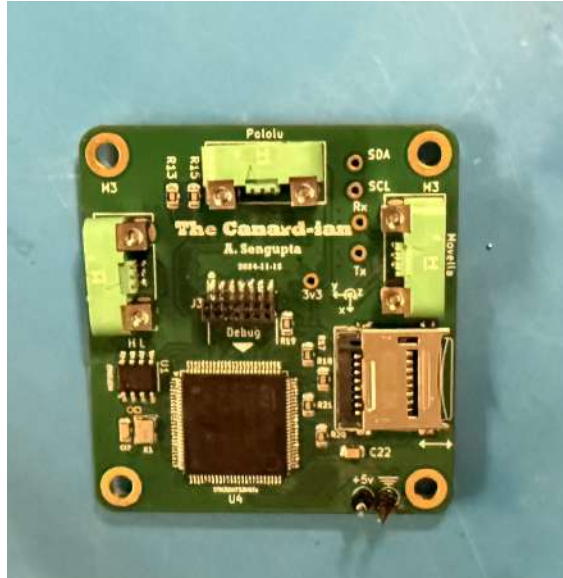


Figure 12.20: Assembled processor board

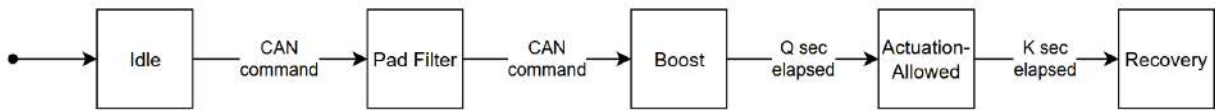


Figure 12.21: Flight phase states and transitions.  $Q$  and  $K$  are hard-coded based on the latest flight simulations.

unit tested. For each translated function, Matlab was used to generate expected output values for various input parameters. These parameters were then used to write unit tests for the corresponding C functions.

Processor responds to firmware failures by sending no command (rather than commanding 0 degrees), using the fact which the MCB fail-safes to 0 degrees if no commands from Processor are sent for 100 ms. A single recoverable failure of the control cycle (such as an IMU communication miss) sends an error status via CAN, but does not send any actuation commands. However, errors deemed unrecoverable, such as peripheral initialization failures or hard faults, are handled by calling a fatal error handler which loops infinitely to prevent further running of the program.

Since 0 degrees actuation is determined to be the system safe-state, the main risk occurs to be potential canard oscillations and control instability resulting from the control module sending undesirable sequences of non-zero commands. This risk is mitigated by the strict verification of the Controller and Estimator code, with the assumption that the Matlab simulations are sound. By running unit tests and hardware-in-the-loop (HIL) tests using flight-representative simulations, there is high confidence the design implementation functions as expected and complies with safety requirements.

Another possible source of failure is when IMU data is collected incorrectly. To mitigate this risk, the IMU values are manually sanity-checked during testing. The crew collectively decided to avoid hard-coded validation of IMU readings during flight, to instead allow out-of-bounds data to

Task	Description
<b>Main Control Loop</b>	
IMU Handler	Reads each IMU and places the data in a queue for the Estimator task. Timing of the control loop propagates from this since the following tasks are blocked until this completes.
Estimator	Waits for new IMU data from the IMU Handler. Runs one cycle of the EKF (see subsubsection 12.3.6) and places the estimated state in a queue for the Controller.
Controller	Waits for new state estimates. Computes the desired canard angle (see subsubsection 12.3.3) and sends the command to MCB via CAN.
<b>Background</b>	
CAN Handler	Processes incoming CAN messages and transmits outgoing ones.
Logger	Writes log message buffers to the SD card when full.
Health Checks	Periodically polls each firmware module for error statuses and broadcasts overall system health via CAN.
Flight Phase	Runs the flight phase state machine (Figure 12.21): idle, pad filter (see subsubsection 12.3.6), boost, actuation-allowed, and recovery. The pad filter and boost phases are triggered via CAN. Flight phases are based on hard-coded simulation timings from Open-Rocket, rather than sensor-based detection, for increased reliability.

Table 12.1: FreeRTOS tasks and descriptions

be rejected by the controller, in which the scheduling fails if the data are out of bounds.

## 12.6 Results

### 12.6.1 hardware-in-the-loop

While unit tests validated individual functions, the hardware-in-the-loop (HIL) system shown in Figure 12.22 was essential for testing end-to-end functionality such as FreeRTOS interactions. The Simulink simulation connects to Processor using Serial Send/Receive blocks which communicate through the ST-Link debugger UART. To avoid the risk of mixing HIL changes with flight firmware it was decided to keep HIL-related firmware changes in a separate Git branch instead of options like using compiler macros or build configurations.

The simulation is configured to send input data packets every 1 ms of simulated time. The firmware was modified to increment the FreeRTOS tick count upon receiving a new packet (normally incremented using the hardware timer). Each packet contains simulated sensor and encoder readings that would normally be processed by the IMU Handler task. The firmware was modified to parse the Simulink packet format and inject it into the IMU Handler task to run a control cycle. The controller task was modified to send the canard command to Simulink via UART (in

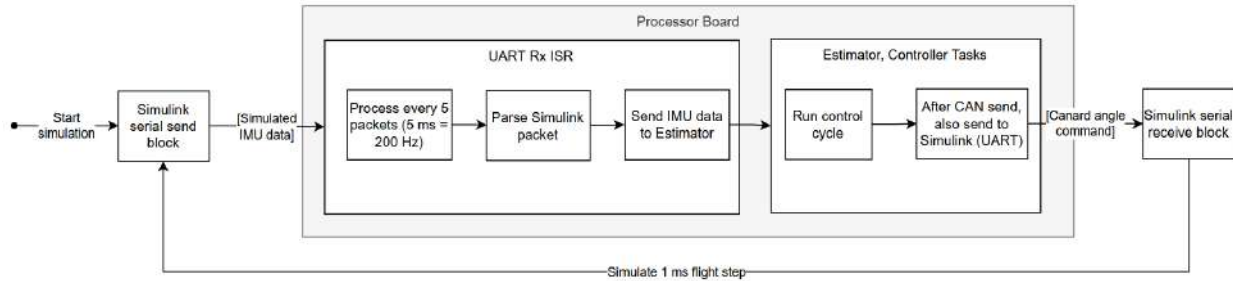


Figure 12.22: Flowchart of the hardware-in-the-loop process.

addition to sending it over CAN). When the Simulink serial receive block receives a canard angle commands from Processor, it simulates the effect accordingly.

### 12.6.2 Testflight

The Testflight launch was conducted on May 10th 2025 near Louisville, Kentucky.

The resulting state estimation data is shown in Figure 12.23. Due to an error with SD card logging only the telemetry data is available. This data was transmitted by Processor Board to the rocket CAN bus, sent over radio telemetry, and logged by the ground station computer. Due to the telemetry bandwidth and lossy connection, data points were only recorded intermittently at irregular intervals, and in some cases bits were dropped resulting in larger jumps of the recorded data (e.g. at about  $t = 8\text{s}$ , the altitude jumps from 250m to 512m instead of 256m).

Due to unaccounted differences between the Testflight launch and the expected Aurora launch, a safety lockout was triggered prematurely which caused the canards to be commanded to zero for the entirety of the flight. Therefore the rocket had no control authority, and some misalignment of the canards and fin cant led to a slow roll rate with a peak of about 2 rad/s, as can be seen in Figure 12.23c.

The rocket lifts off at about  $t = 8\text{s}$ , and reaches apogee at about  $t = 28\text{s}$ . At  $t = 31\text{s}$  the recovery system is deployed, at which point the mission of the Controls subsystem ends. After recovery deployment the state estimation becomes unreliable, as descent under parachutes is not modelled. Overall the Estimator performed as expected, as simulations line up well with the actual test flight.

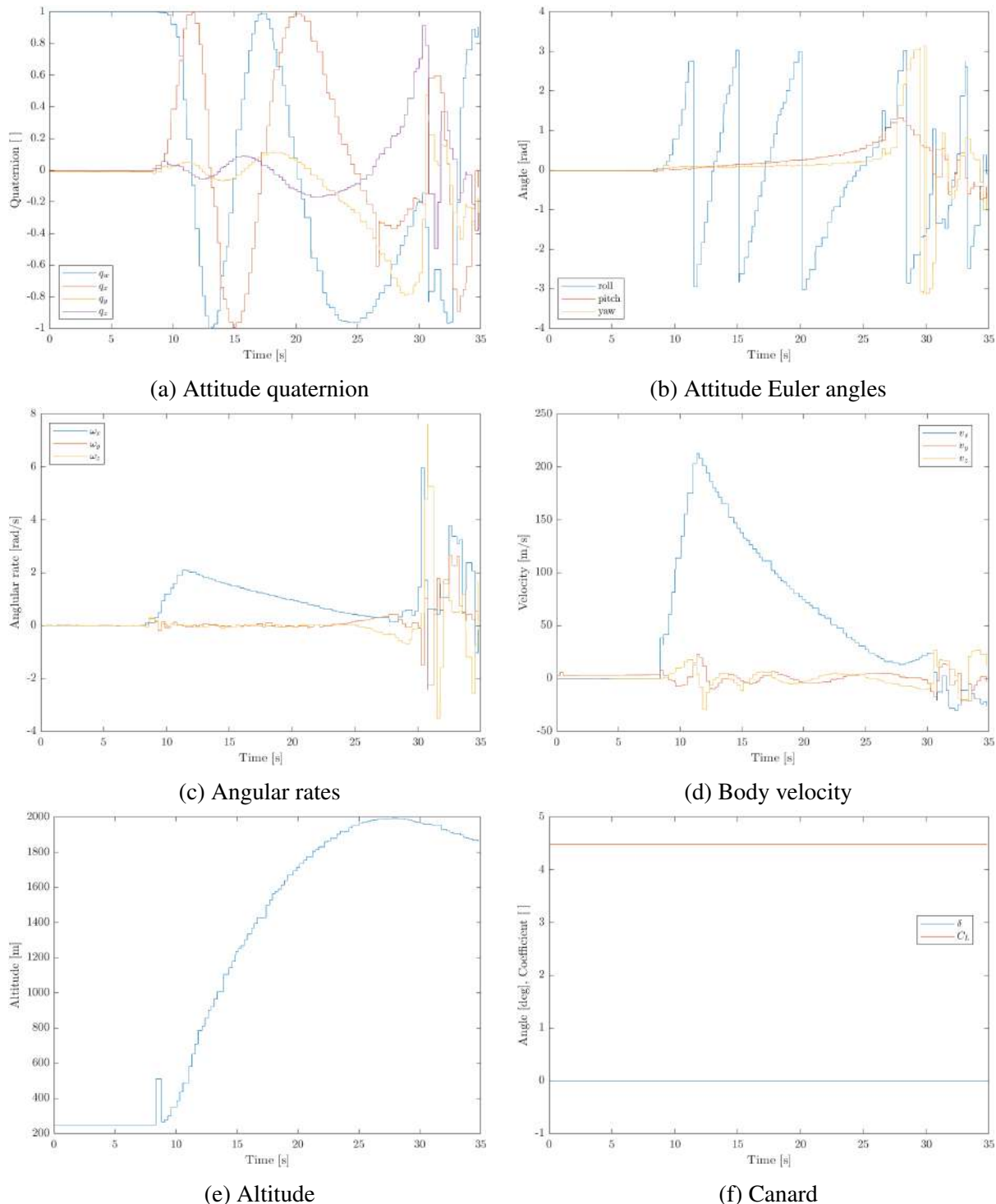


Figure 12.23: Testflight telemetry, estimated state

## 13 PAYLOAD

### 13.1 Payload Experiment

A mid-infrared (MID-IR) Fourier-transform spectrometer was chosen as the payload experiment for this design cycle. Its purpose is to monitor the wavelengths of infrared light being transmitted and absorbed through the troposphere to identify the presence of greenhouse gases by comparing experimental results with known absorption spectra. Specifically, due to the range of infrared light this spectrometer can detect, this experiment aims to remotely sense levels of carbon dioxide ( $\text{CO}_2$ ), nitrous oxide ( $\text{N}_2\text{O}$ ), and methane ( $\text{CH}_4$ ) concentrations in the troposphere.

### 13.2 Deployable Payload Recovery System

To reach the desired environmental conditions for this year's experiment, an independent recovery system was designed for the nosecone to allow the payload to deploy and descend separately from the main rocket body. This occurs in two stages. The first is a flat-spin descent, experimentally determined to have a terminal velocity of 150 ft/s below 6000 ft. The second is descent under main parachute, experimentally determined to reach a terminal velocity of 27 ft/s at sea level. Dispersion analysis has been performed for this system by the Waterloo Rocketry Flight Dynamics subsystem [50], and the system has been demonstrated to be functional through a fully representative test flight.

## 14 TESTING

### 14.1 Engine tests

Below is a list of major tests that Waterloo Rocketry will undergo during development of this engine and vehicle. It is a summary of critical milestones and integration tests the team will perform. For more information on the testing plans of any individual system, reference that system's section.

**Date:** 2024-09-21

**Type:** Cold Flow - Seven Element (EV2-LCFs 1-3)

**Description:** This test involved flowing simulated propellants (Carbon Dioxide and Water) through a seven element coaxial shear injector to validate propellant mass flow rates and mixing.

**Status:** Complete

**Date:** 2024-11-01

**Type:** Cold Flow - Full Injector (EV2-LCF4)

**Description:** This test involved flowing simulated propellants through a complete injector, comprised of 35 coaxial shear elements. This test validated propellant flow rates and mixing, as well as ground support equipment and procedures that will be used in future static fires.

**Status:** Complete

**Date:** 2024-11-23

**Type:** Static Fire - Development (EV2-LSF3)

**Description:** In this test, propellants (liquid nitrous oxide and ethanol) were loaded into concentric tanks using the same ground support equipment that will be used for launch. The engine was then ignited with the intention of allowing it to burn for approximately 4 seconds before all propellants are expended. Unfortunately, an issue with the combustion chamber's design led to a hard start and rapid unscheduled disassembly of the combustion chamber. This is theorized to be due to an undersized nozzle causing over pressurization of the combustion chamber and backflow into the injectors. The static fire anomaly is explored in further detail in the Liquid Static Fire 3 Anomaly Report [51]. No persons were injured or endangered during the test. Additionally, no critical hardware beyond the combustion chamber and injectors were damaged.

**Status:** Complete

**Date:** 2025-03-22

**Type:** Coldflow - Full injector (EV2-LCF5)

**Description:** This test involved flowing simulated propellants through a complete 3D printed injector. Preliminary versions of the new piloted injector valves were also used in this test. This test validated propellant flow rates and mixing, as well as the new 3D printed injectors and piloted injector valves.

**Status:** Complete

**Date:** 2025-04-19

**Type:** Static Fire - Development (EV2-LSF4)

**Description:** In this test, propellants (liquid nitrous oxide and ethanol) were loaded into concentric

tanks using the same ground support equipment that will be used for launch. The engine was then ignited with the intention of allowing it to burn for approximately 5 seconds before all propellants are expended. The static fire was successful. However, the observed maximum thrust was only 7.5 KN, well below the expected 14 KN. This was theorized to be due to the injectors being undersized. Some electrical issues were encountered during setup, but all operations were nominal.

**Status:** Complete

Videos of the two static fire tests can be found at <https://www.youtube.com/watch?v=ZWvHEy1VRlg>.

**Date:** 2025-07-13

**Type:** Coldflow - Full injector (EV2-LCF6)

**Description:** This test involved flowing simulated propellants through a complete 3D printed injector. Flight versions of the piloted injector valves, vent valve, tanks, and piston were also used. This test validated the tanks and piston. A pneumostatic test was also performed to 950 psi to proof the flight tanks.

**Status:** Complete

**Date:** 2025-07-19

**Type:** Static Fire - Flight like (EV2-LSF5)

**Description:** In this test, propellants (liquid nitrous oxide and ethanol) were loaded into concentric tanks using the same ground support equipment that will be used for launch. The engine was then ignited with the intention of allowing it to burn for approximately 8 seconds before all propellants are expended. The flight injectors, injector valves, vent valve, quick disconnect mechanism, tanks, piston, and bulkheads (where possible) were used during this test. This test validated the flight architecture and procedures of the rocket. The test was successful, however, the ablatives underperformed.

**Status:** Complete

## 14.2 Wet Dress Rehearsal

The first wet dress rehearsal (WDR) test is scheduled for July 26th. The purpose of the first WDR is to verify all flight critical rocket avionics work as desired, all sensors are operational and provide sensible data, and practice a nominal abort scenario. All engine and critical avionics components will be assembled with the exception of the combustion chamber internals (liners, ignition puck, and nozzle). The test will be conducted using nitrogen to fill the oxidizer tank and water to fill the fuel tank in order to minimize risk to personnel and allow this test to be safely conducted outside the building where the team's design bay is located, allowing for easy access to tools and supplies to fix any issues that may occur.

**Status:** Planned

An additional WDR may be performed during the week depending on the results of the first WDR.

## 14.3 Competition Simulator

The "competition simulator" test will be the final dress rehearsal test of the rocket once any and all issues discovered during WDRs have been fixed. This test will start with the rocket in the state it will be in after the conference days. The team that will be responsible for setting up the launch

pad at competition will be sent in the morning to assemble all launchpad infrastructure, while a second team works to assemble the rocket (minus ignition and recovery pyrotechnics). Once the pad infrastructure and rocket are prepared, the rocket will be brought out to the 'pad', railed, and raised. The team will then conduct a wet dress rehearsal following the nominal operations procedure (minus ignition) which will conclude by flowing CO<sub>2</sub> through the injectors. The goal of this test is to give team members practice for what they will be doing during the competition, and to identify and solve any issues that come up or delays that occur during the test so that competition will go as smoothly as possible. This test is scheduled for August 2nd.

**Status:** Planned

## 14.4 Testflight

On May 10<sup>th</sup>, 2025, Waterloo Rocketry successfully launched a test vehicle to validate several new subsystems intended for use on the 2025 competition vehicle *Aurora*. The vehicle reached an apogee of 5,700 ft AGL, a peak speed of approximately 800 ft/s, and experienced a maximum acceleration of 12 g during ascent.

The primary objectives of the flight were to test and validate:

- A new single-separation dual-deploy recovery system;
- Recovery of a deployable payload (non-experimental);
- A mechanically linked canard system for active roll control.

The recovery system performed as expected, with both the main and drogue parachutes deploying nominally. The deployable payload was also recovered successfully. The roll control system encountered minor software issues during flight, but collected valuable data that has since been used to inform design refinements.

This testbed flight served as a critical step in reducing risk ahead of the Aurora flight. More detailed information about the subsystems flown, as well as changes made as a result of the test, are provided in their respective sections.

For video footage and a summary of the launch, see: <https://www.youtube.com/watch?v=XtJAorsHZNg>.

## 15 PROGRAMMATIC/TECHNICAL RISKS AND MITIGATION STRATEGIES

Technical risks have been explored in each system's relevant section. As such, this section will explore programmatic and organizational risks to a successful launch and successful flight. The tables below summarises the most severe or likely programmatic risks associated with development and testing of the vehicle.

Table 15.1: Likelihood and Severity Categories for overall programmatic risks

Likelihood	Explanation	Severity	Explanation
Low	Event is unlikely to occur.	Low	Event is unfavourable, but relatively easy to recover from.
Medium	Event may occur; unclear.	Medium	Event is severe, but primary mission goal is still possible.
High	Event is likely to occur.	High	Event is detrimental; team will be unable to compete.

Table 15.2: Team-wide programmatic risks

Risk	Likelihood	Severity	Mitigation Strategy
Team funds deplete	Low	High	Careful financial planning and seeking of outside funding sources
Shipping / Lead times make parts unavailable	Medium	Low	The majority of parts on the rocket are SRAD, leading the team to not often have to deal with shipping times. This means that the team can keep track of those that do require lead times more effectively and order them well in advance. The team also has the skill to manufacture things if something will not arrive on time, even if it will not be as effective as the purchased part
Critical illness/Injury incapacitating team members	Medium	Medium	Commonly known as the "bus factor", the team is careful to not be too reliant on any singular person, and to crosstrain as much as possible. The team is also careful to finish things early so that illness does not affect timelines

Spring Term Exams using team time	High	Low	Waterloo has exams that most in-person students will be participating in for the 2-3 weeks before Launch Canada. The team is including this in the relevant timelines, and ensuring there exists a flight ready vehicle before team members must focus on school
Packing errors or forgotten items (e.g. tooling, spare electronics, N <sub>2</sub> tank)	Medium	Medium	Use detailed packing lists. Assign a team member to verify every bin/toolset. Do a full kit laydown before departure.
Vehicle condition degrades during transport (e.g. vibration, moisture, loose bolts)	Low	Medium	Rigidly secure all assemblies. Use padded cases. Conduct full post-transport inspection and re-torque all fasteners.
Damage critical hardware during handling or testing	Low	Medium	The team treats all flight hardware carefully during bench testing and integration. Spares are built for as many components as possible (valve seats, boards, etc) to avoid damage ruining flight opportunities.

## REFERENCES

- [1] Joel Godard. *Increasing Rocket Apogee by 23% Through Iterative Design*. Waterloo Rocketry. Jan. 2024. URL: <https://drive.google.com/file/d/1CygsVuvnB14k3kH8S6ockkXLsafdzxK7/view>.
- [2] Joel Godard and Thomas Fairhead. *Increasing Apogee by 23% Through Iterative Design Approach*. Waterloo Rocketry, 2024. URL: <https://www.youtube.com/watch?v=fDDOLux1RgE>.
- [3] C. E. Rogers. *RASAero II Aerodynamic Analysis and Flight Simulation Program - User Manual*. Rogers Aeroscience. 2019. URL: <https://www.rasaero.com/dloads/RASAero%20II%20Users%20Manual.pdf>.
- [4] Patrick Gu. *OpenRocket Airbrakes Plugin Repository*. Waterloo Rocketry. 2024. URL: <https://github.com/waterloo-rocketry/or-airbrake-plugin>.
- [5] Charles Hoult. *Rocket Science and Engineering Technologies*. 2013. URL: <http://www.rsandt.com/reports.html#StruLoad>.
- [6] D. J. Martin. *Summary of Flutter Experiences as a Guide to the Preliminary Design of Lifting Surfaces on Missiles*. Tech. rep. NASA, 1958.
- [7] Theodore Theodorsen and I. E. Garrick. *Mechanism of Flutter - A Theoretical and Experimental Investigation of the Flutter Problem*. Tech. rep. NACA, 1940.
- [8] MatWeb. *Overview of Materials for Epoxy/Carbon Fiber Composite*. URL: [https://www.matweb.com/search/datasheet\\_print.aspx?matguid=39e40851fc164b6c9bda29d798bf3726](https://www.matweb.com/search/datasheet_print.aspx?matguid=39e40851fc164b6c9bda29d798bf3726).
- [9] J. K. Bennett. *Fin Flutter Analysis Revisited (Again)*. 2023. URL: <https://www.apogeerockets.com/education/downloads/Newsletter615.pdf>.
- [10] J. Keith Nisbett Richard G. Budynas. *Shigley's Mechanical Engineering Design*. 2015.
- [11] Tim Van Milligan. *The Corrective Moment Coefficient*. Apogee Rockets. 2007. URL: <https://www.apogeerockets.com/education/downloads/Newsletter193.pdf>.
- [12] Tim Van Milligan. *Radial Moment of Inertia and the Natural Frequency*. Apogee Rockets. 2007. URL: <https://www.apogeerockets.com/education/downloads/Newsletter196.pdf>.
- [13] J. G. Leishman. *An Introduction to Aerospace Flight Vehicles*. Pressbooks, 2024.
- [14] R. F. Stengel. *Flight Dynamics*. Princeton University Press, 2004.
- [15] A. H. Shapiro. *The Dynamics and Thermodynamics of Compressible Flow, Vol. 1*. Ronald Press, 1953.
- [16] Open-Meteo. *Accurate Weather Forecasts for Any Location*. URL: <https://open-meteo.com>.
- [17] *Leviathan of the Sky Hybrid Rocket Project Technical Report*. Waterloo Rocketry. URL: <https://drive.google.com/file/d/1y9teKByS1LoSF9aj4fo1byQsZomRpGke/view>.
- [18] Zachariah Mears. "Optimization and Characterization of Laser Powder Bed Fusion of AlSi10Mg for Complex Aerospace Structures". MA thesis. University of Waterloo, 2025.

- [19] nTopology Inc. *nTop*. URL: <https://www.ntop.com/>.
- [20] *Spin Can.* (Accessed: 2025/05/25). Portland State Aerospace Society. Dec. 2010. URL: <https://archive.psas.pdx.edu/lv2cspincan/>.
- [21] Half Cat Rocketry. *CHAMBERSAFE*. URL: <https://www.halfcatrocketry.com/chambersafe>.
- [22] G. S. Gill and W. H. Nurick. *NASA SP 8089 Liquid Rocket Engine Injectors*. 1976. URL: <https://ntrs.nasa.gov/api/citations/19760023196/downloads/19760023196.pdf> (visited on 01/29/2025).
- [23] Matthew Gordon. *Design of a Remotely Operated Fill/Dump Valve*. Waterloo Rocketry. May 2024. URL: [https://drive.google.com/file/d/1bzky83p\\_3DFZrT0OoN1y\\_qT1im5U-eZw/view?usp=sharing](https://drive.google.com/file/d/1bzky83p_3DFZrT0OoN1y_qT1im5U-eZw/view?usp=sharing).
- [24] Benjamin Waxman. “An Investigation of Injectors for use with High Vapor Pressure Propellants with Applications to Hybrid Rockets”. PhD thesis. Stanford, 2014. URL: <https://purl.stanford.edu/ng346xh6244>.
- [25] *Difference between Standard CAN and Extended CAN frame explained*. Automotive Vehicle Testing. URL: <https://automotivevehicletesting.com/standard-can-and-extended-can-frame/>.
- [26] *Borealis Project Technical Report*. Waterloo Rocketry. URL: [https://www.waterloorocketry.com/pdfs/2024\\_project\\_report.pdf](https://www.waterloorocketry.com/pdfs/2024_project_report.pdf).
- [27] *Team 139 Project Technical Report for the 2022 IREC*. Waterloo Rocketry. URL: [https://www.waterloorocketry.com/pdfs/2022\\_project\\_report.pdf](https://www.waterloorocketry.com/pdfs/2022_project_report.pdf).
- [28] T.W. Knacke. *Parachute Recovery Systems: Design Manual*. Para Pub., 1992. ISBN: 9780915516858. URL: <https://books.google.ca/books?id=5pzgAAAAMAAJ>.
- [29] *U.S. Standard Atmosphere: Temperature, Pressure, and Air Properties vs. Altitude*. URL: [https://www.engineeringtoolbox.com/standard-atmosphere-d\\_604.html](https://www.engineeringtoolbox.com/standard-atmosphere-d_604.html).
- [30] Catherine Mollmann. *Design and Testing of CPAS Main Deployment Bag Energy Modulator*. Tech. rep. NASA, 2015.
- [31] David Schultz. *Pressure lag*. July 2025. URL: <http://home.earthlink.net/~david.schultz/rnd/pressurelag/parachute.html>.
- [32] *Drag Separation*. MIT Rocket Team. Dec. 2017. URL: <https://wikis.mit.edu/confluence/display/RocketTeam/Drag+Separation>.
- [33] Nexperia. *PMEG3030EP product data sheet*. 2025. URL: <https://assets.nexperia.com/documents/data-sheet/PMEG3030EP.pdf>.
- [34] American Earth Anchors. *Load Capacity and Pullout Strength*. 2025. URL: [https://americanearthanchors.com/load-capacity/?srsltid=AfmB0orq6\\_2WtDvuTr5v81HVir2GTNb1etLY](https://americanearthanchors.com/load-capacity/?srsltid=AfmB0orq6_2WtDvuTr5v81HVir2GTNb1etLY).
- [35] Ben Pickens. *Mechanical Design of Roll Control Canards for a Sounding Rocket*. Waterloo Rocketry. July 2025.

- [36] Luca Scavone. *Canards Aerodynamic Design for an Active Roll-Control System*. Waterloo Rocketry. Mar. 2025.
- [37] Finn Breuer. *Roll Control Design and Simulation of a Canard-controlled Sounding Rocket*. Waterloo Rocketry. July 2025.
- [38] Finn Breuer et al. *Roll Control Simulation and Design repository*. Waterloo Rocketry. July 2025. URL: <https://github.com/waterloo-rocketry/simulink-canards>.
- [39] James S. Barrowman. “The practical calculation of the aerodynamic characteristics of slender finned vehicles”. M.Sc. thesis. USA – Washington, D.C.: The Catholic University of America, 1967. URL: <https://ntrs.nasa.gov/api/citations/20010047838/downloads/20010047838.pdf>.
- [40] Herbert Werner. *Control Systems Theory and Design: Lecture Notes*. Hamburg University of Technology, Institute of Control Systems, 2021.
- [41] Julian Theis. *Flight Control Law Design: Lecture Notes*. Hamburg University of Technology, Institute of Aircraft Systems (FST), 2023.
- [42] Joan Solà. *Quaternion kinematics for the error-state Kalman filter*. Technical University of Catalonia, Institut de Robòtica i Informàtica Industrial, 2017.
- [43] Brian L. Stevens, Eric N. Johnson, and Frank L. Lewis. *Aircraft Control and Simulation: Dynamics, Controls Design, and Autonomous Systems*. Third edition. Hoboken, New Jersey: Wiley, 2015. ISBN: 9781119174882. DOI: [10.1002/9781119174882](https://doi.org/10.1002/9781119174882).
- [44] Peter H. Zipfel. *Modeling and Simulation of Aerospace Vehicle Dynamics*. 2nd. Reston: American Institute of Aeronautics and Astronautics, 2007. ISBN: 978-1-56347-875-8. DOI: [10.2514/4.862182](https://doi.org/10.2514/4.862182).
- [45] United States Committee on Extension to the Standard Atmosphere. *U.S. Standard Atmosphere, 1976*. NOAA Document S/T 76-1562. Washington, D.C.: National Oceanic and Atmospheric Administration (NOAA), 1976. URL: <https://ntrs.nasa.gov/citations/19770009539>.
- [46] Sampo Niskanen. “Development of an Open Source model rocket simulation software”. M.Sc. thesis. Finland – Helsinki: Helsinki University of Technology, 2009. URL: <https://openrocket.sourceforge.net/thesis.pdf>.
- [47] Robert F. Stengel. *Flight Dynamics*. Princeton, NJ: Princeton University Press, 2004. ISBN: 9781400866816. DOI: [10.1515/9781400866816](https://doi.org/10.1515/9781400866816).
- [48] Frank L. Lewis, Lihua Xie, and Dan Popa. *Optimal and Robust Estimation*. 2nd. CRC Press, Taylor & Francis Group, 2008. ISBN: 978-0-8493-9008-1.
- [49] Michael Barr and Barr Group. *Embedded C Coding Standard*. 2nd. Barr Group. 2018. URL: <https://barrgroup.com/Embedded-Systems/Books/Embedded-C-Coding-Standard>.
- [50] Waterloo Rocketry. *Launch Canada 2025 Challenge: Final Design Report for Aurora*. Tech. rep. University of Waterloo, 2025.

- [51] Matthew Gordon. *Liquid Static Fire 3 Anomaly Report*. Waterloo Rocketry. 2025. URL: [https://docs.google.com/document/d/1RyLiovhaGRAygKT\\_Ui01IBN\\_F5iqJ2aHMDEiq2dpIGg/edit?usp=sharing](https://docs.google.com/document/d/1RyLiovhaGRAygKT_Ui01IBN_F5iqJ2aHMDEiq2dpIGg/edit?usp=sharing).
- [52] *Aluminum 6061-T6; 6061-T651*. Aerospace Specification Metals inc. 2024. URL: <https://asm.matweb.com/search/SpecificMaterial.asp?bassnum=ma6061t6>.

# A APPENDIX - Calculations

## A.1 Coupler Loads Analysis

A sample calculation is provided for the avionics forward coupler at MaxQ, which has the following geometry and loads:

Axial Load (P)	-270.2 lbf
Bending Moment (M)	734.2 lbf-in
Coupler Inner Diameter (CID)	7.63 in
Coupler Outer Diameter (COD)	7.77 in
Coupler Edge Distance (CED)	0.3 in
Bolt Diameter	0.25 in
Number of Bolts	6
Bearing Yield Strength, 6061-T6	56000 psi [52]
Shear Yield Strength, 6061-T6	30000 psi [52]

Table A.1: Sample Calculation for Avionics Forward Coupler

$$\text{Additional axial load from bending (worst case)} = \frac{M}{4 \times 2\text{in} \times \sqrt{3}} = \frac{734.2\text{lbf-in}}{4 \times 2\text{in} \times \sqrt{3}} = 53\text{lbf}$$

$$\text{Maximum axial force per bolt}(F) = \frac{P}{6} \pm \text{Additional axial load from bending} = \frac{-270.2\text{lbf}}{6} \pm 53\text{lbf} = 8\text{lbf}, -98\text{lbf}$$

- For bearing, take largest magnitude. For tearout, take positive.

$$\text{Coupler Thickness (CT)} = \frac{(\text{COD} - \text{CID})}{2} = \frac{(7.77\text{in} - 7.63\text{in})}{2} = 0.07\text{in}$$

$$\text{Bearing area } (A_{\text{Bearing}}) = \text{BD} \times \text{CT} = 0.25\text{in} \times 0.07\text{in} = 0.0175\text{in}^2$$

$$\text{Bearing Stress } (\sigma_{\text{Bearing}}) = \frac{F}{A_{\text{Bearing}}} = \frac{98\text{lbf}}{0.0175\text{in}^2} = 5600\text{psi}$$

$$\text{Bearing FOS} = \frac{\text{Bearing yield strength}}{\sigma_{\text{Bearing}}} = \frac{56000\text{psi}}{5600\text{psi}} = 10$$

$$\text{Tear out area } (A_{\text{Tear}}) = 2 \times \text{CT} \times \left( \text{CED} - \frac{\text{BD}}{2} \right) = 2 \times 0.07\text{in} \times \left( 0.3\text{in} - \frac{0.25\text{in}}{2} \right) = 0.0245\text{in}^2$$

$$\text{Tear out stress } (\sigma_{\text{Tear}}) = \frac{F}{A_{\text{Tear}}} = \frac{8\text{lbf}}{0.0245\text{in}^2} = 326.5\text{psi}$$

$$\text{Tear out FOS} = \frac{\text{Shear yield strength}}{\sigma_{\text{Tear}}} = \frac{30000\text{psi}}{326.5\text{psi}} = 91.9$$

## B APPENDIX - Electrical References

### B.1 Electrical Architecture

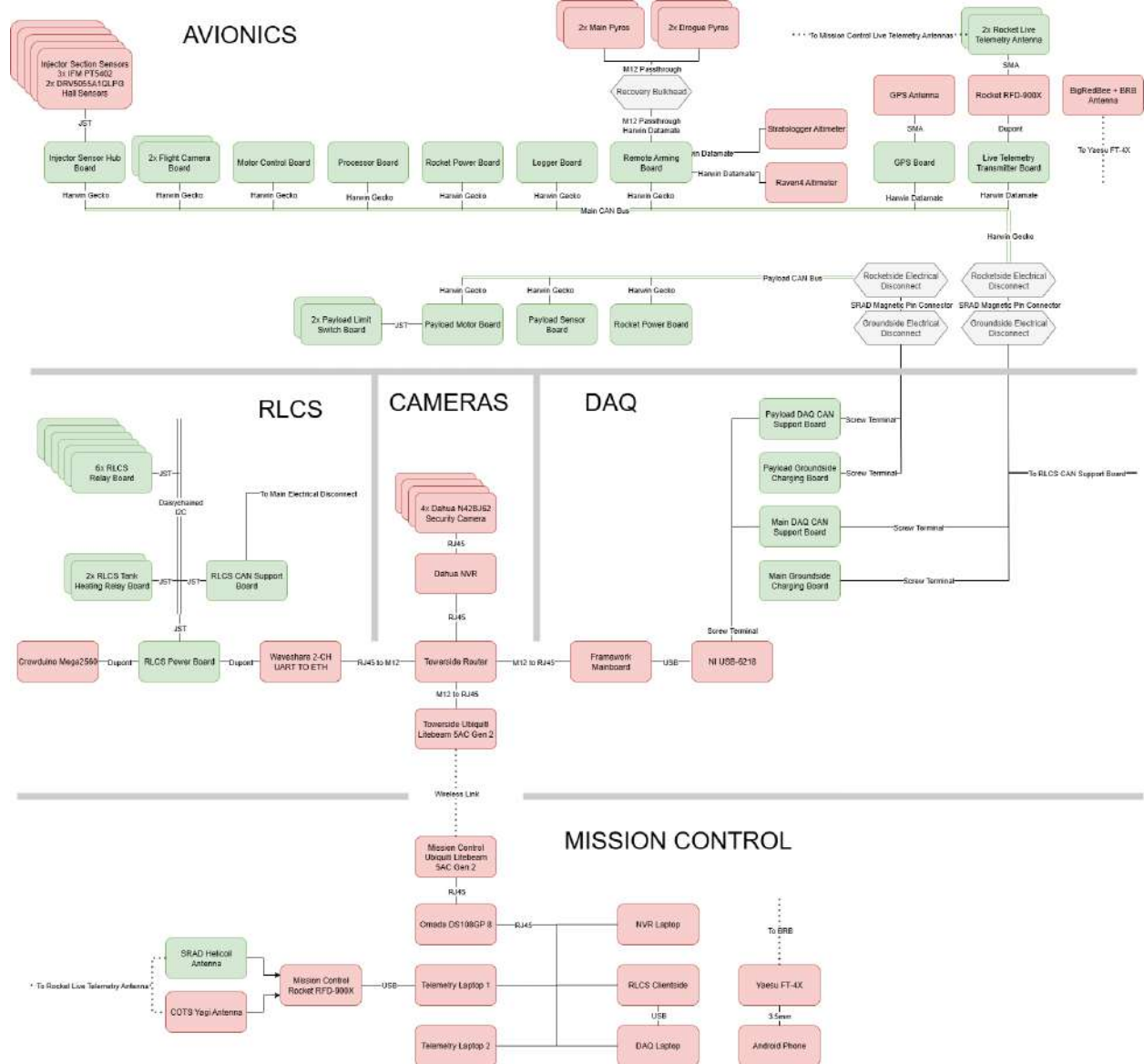


Figure B.1: Aurora electrical architecture diagram